2017

Studies of Energy-Relevant Materials by Nuclear Magnetic Resonance

Jinfang Cui
Iowa State University

Studies of energy-relevant materials by nuclear magnetic resonance

by

Jinfang Cui

A dissertation submitted to the graduate faculty

in partial fulfillment of the requirements for the degree of

DOCTOR OF PHILOSOPHY

Major: Chemistry

Program of Study Committee:
Yuji Furukawa, Co-major Professor
Gordon Miller, Co-major Professor
Paul Canfield
James Evans
Theresa Windus

The student author and the program of study committee are solely responsible for the content of this dissertation. The Graduate College will ensure this dissertation is globally accessible and will not permit alterations after a degree is conferred.

Iowa State University

Ames, Iowa

2017

DEDICATION

This work is dedicated to my parents Xin Cui and Mo Zhang, who offered their unique way of support and love, by letting me recognize that I have got to be my own hero at each breathing place of my life.

TABLE OF CONTENTS

LIST OF TABLES

LIST OF FIGURES

ACKNOWLEDGEMENTS

First and foremost, I would like to express my deep and sincere gratitude to my advisor, Professor Yuji Furukawa. It has been truly a privilege and honor to become his graduate student. I appreciate all his contributions of time, effort, ideas, and motivation, to teach me personally, patiently and make my last three years of Ph.D. experience joyful and productive. Meantime, I would like to say Thank You, for everything, to my co-advisor Professor Gordon Miller, for your support all the way through. I am also thankful to Professor Klaus Schmidt-Rohr, for the excellent example as a dedicated and well-respected scientist. He has taught me the clear vision to see what is really important in life.

I am also indebted to my committee members Dr. Paul Canfield, Dr. James Evans, Dr. Edward Yu and Dr. Theresa Windus for being supportive of my research work and guiding in my thesis writing.

I thank Dr. Paul Canfield, Dr. Sergey Bud'ko, Dr. Sheng Ran, Dr. Tai Kong, Mr. William Meier, Dr. Ruslan Prozorov and Dr. Makariy Tanatar for providing the high quality samples on which we had done the NMR measurements and for the precious insights for the resistivity measurements.

The members of Furukawa group have contributed immensely to my professional and personal development. Dr. Beas Roy had patiently trained me with the implementation of basic condensed matter NMR experiments when I first started. Dr. Paul Wiecki, Dr. Qingping Ding had lent me hands with technical difficulties I encountered in my research. I also enjoyed the encouraging conversations with Dr. Evgenii M. Levin and the pleasant company of Dr. Robert Johnson in the Schmidt-Rohr group. Dr. Feili Qin in the Chemistry Department had helped me a lot when I was fulfilling my teaching role for the course of physical chemistry and instrumental analysis of chemicals.

The warm support and love from all my friends helped me survive humid summer in Ames. I

will never forget those delightful moments and surely miss those delicious dinners accompanied with Dr. Weiwei Xie, Dr. Tuo Wang, Dr. Tai Kong, Dr. Peng Xu, Dr. Dapeng Jing, Dr. Yang Li, Dr. Yang Sun, Mr. Peng Zhang and Mr. Zhuoran Wang.

Special thanks to Dr. Chen Liu, for his helpful advice to all the troubled situations I got myself into, for his steely determination forcing me grow into a strong and independent person.

ABSTRACT

In this thesis, we have used nuclear magnetic resonance (NMR) as a local probe to microscopically study three different families of energy-relevant complex materials, namely the 122 Fe-based superconductors $Ca(Fe_{1-x}Co_x)_2As_2$, GeTe-based thermoelectric tellurides GeTe and detonation nanodiamond.

In Chapter 3, we investigated the Co substitution effects on static and dynamic magnetic properties of the single-crystalline $Ca(Fe_{1-x}Co_x)_2As_2$ (x = 0, 0.023, 0.028, 0.033, 0.059) via ^{75}As NMR and resistivity measurements. Robustness of the Fe magnetic moments was evidenced by only slight decreases of $H_{\rm int}$, although $T_{\rm N}$ is strongly suppressed with Co substitution in antiferromagnetic (AFM) state. In the paramagnetic (PM) state, the temperature dependence of Knight shift K for all crystals shows similar T-dependence of magnetic susceptibility χ. The spin fluctuations with the $q = 0$ components are suppressed with $\Delta/k_{\rm B}$. On the other hand, the growth of the stripe-type AFM fluctuations with $q = (\pi, 0)$ or $(0, \pi)$ upon cooling in the PM state for all samples is evidenced by the T-dependence of $(1/T_1T\chi)$. A pseudogap-like phenomenon, i.e., suppression of the AFM spin fluctuations, was discovered with decreasing temperature below a x-independent characteristic temperature T^* ($\sim$ 100 K) in samples with $x \geq 0.028$. In addition, clear evidence for the coexistence and competition of the stripe-type antiferromagnetic and ferromagnetic (FM) spin correlations was given by modified Korringa ratio analysis in Chapter 4.

In Chapter 5, we have carried out ^{125}Te NMR measurements to study the electronic properties of $Ge_{50}Te_{50}$, $Ag_2Ge_{48}Te_{50}$ and $Sb_2Ge_{48}Te_{50}$. NMR shift K and $1/T_1T$ of $Ge_{50}Te_{50}$ are nearly temperature independent at T $<$ 50 K and both increase slightly with increasing temperature at high temperatures. A two-band model, where one band overlaps the Fermi level and the other band is separated from the Fermi level by an energy gap, has been used to explain these behaviors. The first-principle calculation revealed that the metallic band originates from

the Ge vacancy while the semiconductor-like band may be related to the fine structure of the density of states near the Fermi level. At low temperature, we found conduction carriers are free carriers with no significant electron correlations, while Korringa ratio increases slightly at high temperature, suggesting the slight enhancement of the electron correlation.

In Chapter 6 and Chapter 7, we have used ^{13}C NMR spectral editing technique to accurately analyze the surface composition of pristine purified, heat-treated (at 800 °C), and air-oxidized detonation nanodiamond. We have resolved ten peaks of C=O, COO, C=C, O–C–O, C–OH, C–N, CH, subsurface C, core C, and C–C–N. The aromatic fraction is only ∼1.1%, which corresponds to less than 1/20 of an aromatic surface layer. We have also shown that other surface functional groups (CH, COH, etc.) accounts for most of the surface sites, making up ∼11.5% of all C in pristine nanodiamond. The signal of carbon bonded to nitroge was observed selectively based on increased chemical-shift anisotropy due to breaking of the local symmetry. Furthermore, we used modified ^{13}C{^{1}H} REDOR experiments to observe the signals from carbons at different depths from the surface and estimate their quantities.

CHAPTER 1. BACKGROUND OF ENERGY-RELEVANT MATERIALS

1.1 Overview

The imminent depletion of fossil fuels (e.g. petroleum, coal and natural gas) and negative environmental impacts (e.g. pollution and global warming) have become profound global challenges. These issues have to be addressed in two aspects: to transit to renewable energy sources (e.g. solar power, wind power, and hydropower, etc.), and to increase the efficiency of energy usage. Improvements in energy efficiency are generally achieved by adopting high performance materials which hold the key in efficient energy production process or by application of commonly accepted methods to reduce energy losses. Better lubricants that decreases fuel consumptions, thermoelectric energy conversion devices, superconductors for energy storage system, are crucial factors for environmentally sound and sustainable future technologies.

Materials used in systems for energy generation or conversion can be very complex both chemically and in terms of structure with significant disorder on the 1-nm scale that prevents full characterization from diffraction or microscopy techniques. This high level of complexity can also apply to their synthesis process or to the operation of the materials. Therefore, scientific tools to gain insight into the synthesis, structure and operation of such materials —generally called "energy-relevant" in this paper —are highly desirable. Using nuclear spins as local probes, advanced solid-state nuclear magnetic resonance (NMR) can make important contributions to the elucidation of the structure and of structure-property relations in such complex materials.

This thesis presents applications of NMR to the characterization of energy-relevant materials. The systems investigated include: (i) high temperature iron-based superconductors $Ca(Fe_{1-x}Co_x)_2As_2$, (ii) GeTe-based thermoelectric tellurides, and (iii) detonation nanodia-

mond. In the following, I will provide background information on the portfolio of complex materials selected for detailed characterization by NMR.

1.2 Iron-based Superconductors

1.2.1 Historical overview of superconductivity

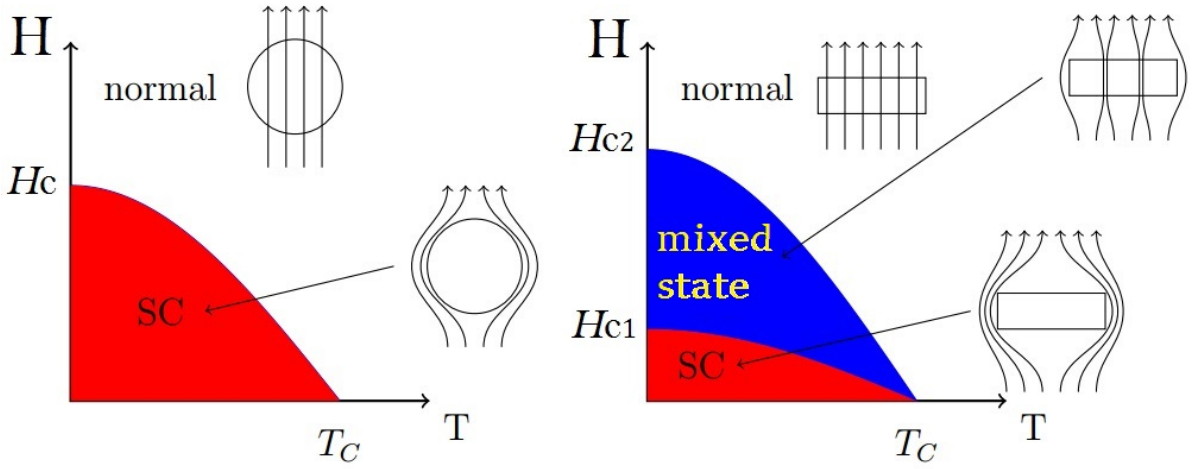

(a) Type I superconductor (b) Type II superconductor

Figure 1.1 The temperature dependence of the critical magnetic fields of type I and type II superconductors.

The phenomenon of superconductivity was discovered by Heike Kamerlingh Onnes [1] in 1911. Below a finite critical temperature, T_c, of 4.2 K the electrical resistance of mercury falls to zero. In 1933 another property of superconductors was discovered, the Meissner effect, which is now considered a defining feature of superconductors (to distinguish them from perfect conductors). Meissner and Ochsenfeld [2] found that a superconductor in an applied field will exclude the magnetic flux from its interior and becomes a perfect diamagnet. This leads to the most popular demonstration of superconductivity by levitating a magnet above a superconductor or vice versa. However, this stays true until the critical magnetic field, H_c is reached and the magnetic field starts to penetrate into the superconductor, which destroys superconductivity.

For the case of conventional superconductivity found in a Type I superconductor (e.g., mercury, lead, aluminum), the magnetic field is completely expelled from the interior for $H < H_c$. When the applied field exceeds the critical value H_c the entire sample reverts to the normal state and the magnetic field completely penetrates. On the other hand, two different critical magnetic fields exist in the case of Type II superconductors. For $H < H_{c1}$ the magnetic field is completely expelled, when $H_{c1} < H < H_{c2}$ the magnetic field partially penetrates through the material in the form of vortices (referred as mixed state), the number density of vortices increases with increasing applied field until $H > H_{c2}$, where superconductivity is completely destroyed and the field penetrates the entire sample. The temperature dependence of these critical fields is shown in Fig. 1.1.

Although the discovery of superconductivity was made in 1911, it took over half a century to unravel this mystery of the underlying microscopic mechanism to be achieved. In 1957, Bardeen, Cooper and Schrieffer published a theory of superconductivity in which electrons form ′Cooper pairs′ through interactions of electrons and phonons [3]. The electron pairs condense with their spins anti-aligned (i.e. in a singlet state in the quantum ground state) and this creates an energy gap between the ground state and the lowest quasiparticle excitation state. This description, known as BCS theory, explains why these pairs can travel through the material without scattering. It was a triumph in the field as it explained all of the superconductors known at that time, and for all the "conventional" superconductors discovered since then. Unfortunately, however, BCS theory puts a limit on the maximum T_c of ∼30–40 K.

In 1979 the first unconventional superconductor, which is not described by BCS theory, $CeCu_2Si_2$ was reported, with a T_c of 0.5 K [4]. Superconductivity in most unconventional materials is caused by the formation of electron pairs, but physical properties were not explained by BCS theory. The most important breakthrough was the discovery of high-T_c superconductivity in a layered copper-oxide compound—"cuprates", in 1986 by Alex Müller and Georg Bednorz [5]. One particular example, $YBa_2Cu_3O_{7-x}$ (YBCO) as shown in Fig. 1.2 (a), where the yttrium and barium are in between copper-oxide (CuO_2) layers, is the first superconductor exhibiting a $T_c = 93$ K above liquid nitrogen temperature (77 K) [7]. The undoped parent compounds of cuprates are generally described as Mott insulators, in which strong local-coulomb

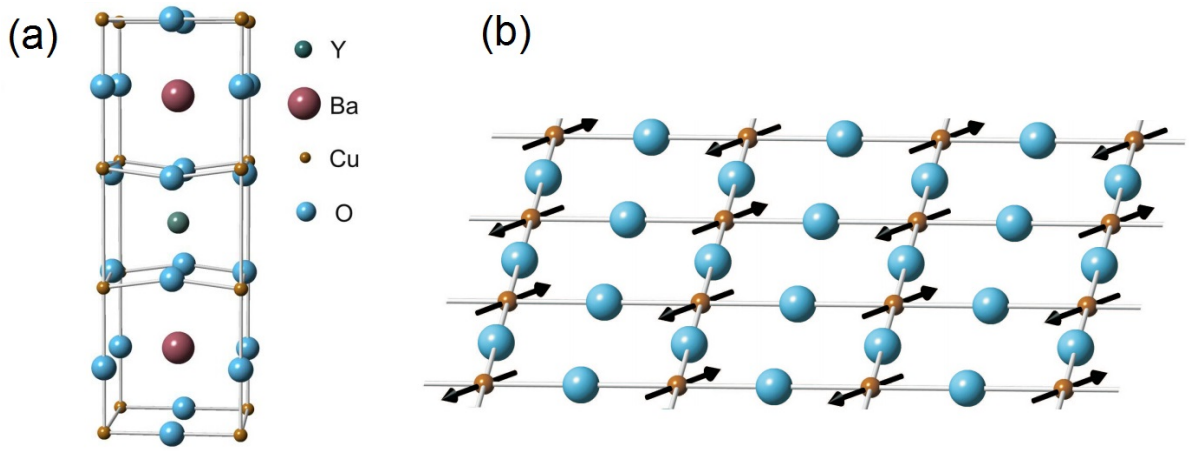

Figure 1.2 (a)Unit cell demonstrating the crystal structure of YBCO for the stoichiometric undoped material. (b) Simple representation of the AFM order in a CuO_2 layer in a cuprate material. Arrows represent the spin on a cooper ion. [6]

interactions cause the material to be insulating instead of metallic. Within this Mott-insulator state, antiferromagnetic (AFM) ordering of the copper spins ($S = 1/2$) within the copper-oxygen planes is found, as depicted in Fig. 1.2 (b)).

The phase diagram of a cuprate superconductor in Fig. 1.3 illustrated how the properties of such materials evolve with both temperature and chemical substitution. The AFM ordering is only present in a narrow region of the phase diagram and is quickly suppressed by carrier doping. Superconductivity only emerges if the static AFM order has been suppressed. Strong AFM fluctuations, however, are still expected in regions of the phase diagram close to magnetic order. This suggests that proximity to the magnetic phase might be essential to the superconducting electron pairing and that superconductivity may be mediated by AFM spin fluctuations in the cuprates [8, 9].

Before 2008, all known "high-T_c" superconductors exhibited two essential properties: copper-oxygen planes and magnetic moments on the copper atom. It was hence thought that high-T_c superconductivity was reserved for the cuprates. Then a T_c of 26 K was discovered in $LaFeAsO_{1-x}F_x$ by Hideo Hosono and colleagues [10]. This new iron-based superconductors (FeSC) opened up a new area for the investigation of unconventional high-T_c superconductivity and magnetism. This discovery was followed by the revelation of an even higher T_c of 43 K for

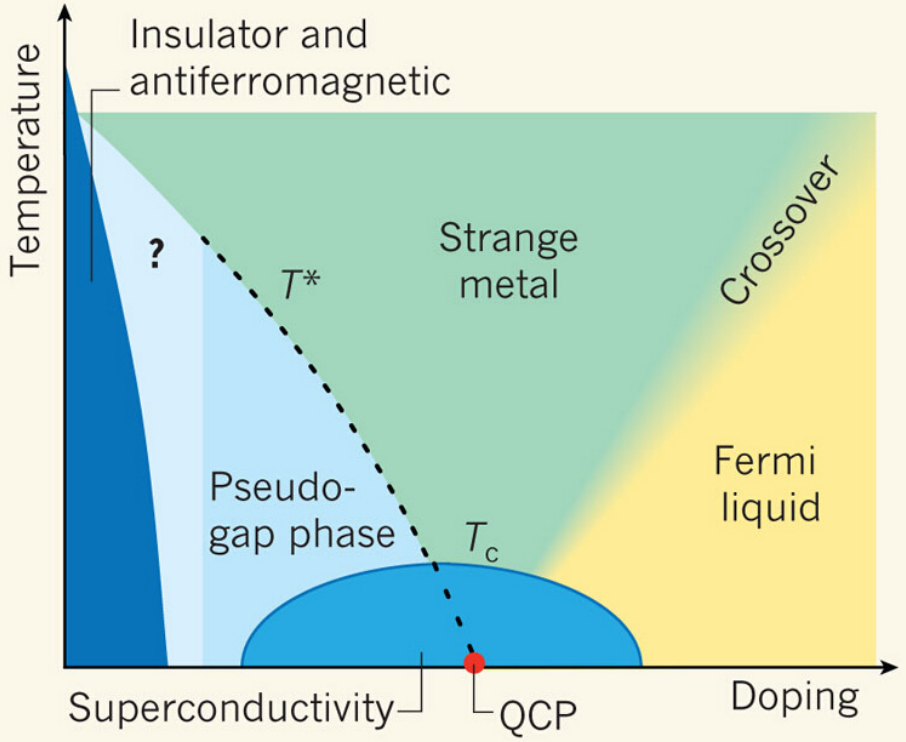

Figure 1.3 The generalised temperature against hole doping phase diagram of the cuprate superconductors. At low levels of substitution, cuprates are insulating and antiferromagnetic. With increased doping levels, they become conducting. At temperatures below T_c, they become superconducting, and at temperatures above T_c but below T^* they fall into the pseudogap phase. The boundary of the pseudogap region at low doping levels is unknown. The transition between the Fermi-liquid phase and the strange-metal phase occurs gradually (by crossover). QCP denotes the quantum critical point at which the temperature T^* goes to absolute zero. [21]

the same compound under applied pressure [11] or replace La with Sm [12]. Many iron-pnictide and iron-chalcogenide compounds were soon found to lead to T_c up to 56 K [13].

These T_cs cannot be explained by a phonon-mediated electron-pairing mechanism. The iron-based systems were shown to have parent phases of antiferromagnetic ordered state. [14] These materials present a novel playground for investigating the magnetic interactions that may be the cause of the superconducting pairing process. The presence of iron immediately hints that strong magnetic correlations could be dominant in the materials, so the field of research was quickly directed to investigating magnetic order and dynamics. This thesis adds to the body of evidence indicating the importance of magnetic fluctuations in FeSCs, which

may ultimately be accounted for in a theory of the systems. Having much higher H_cs than cuprates and high isotropic critical currents, FeSC materials would be good candidates of electricity generators, cheaper medical imaging scanners, and extremely fast levitating trains, since superconductors with higher T_cs do not require expensive coolants to reach the critical transition temperature. Moreover, the coexistence of magnetism and superconductivity makes them promising for spintronics. Therefore, research in FeSCs are not only important for fundamental condensed matter physics but also quite attractive in the application community.

1.2.2 Structural properties

The common crystallographic structural form of iron-based superconductors consists of layers containing iron pnictogen (Fe with As or P) or iron chalcogen (Fe with Se or Te), nominally in a 1:1 ratio, in a tetrahedral arrangement with pnictogen or chalcogen ions arranged above and below the square iron-plane. These layers (we will focus more on FeAs layers) are usually separated by other ions (alkali, alkaline earth or rare earth and oxygen/fluorine)—the "blocking layers", which provide a quasi-two-dimensional character in the crystal structure, with minimal electronic coupling along the *c*-axis. Physical properties of these materials are expected to have a highly two-dimensional character, as that in cuprates, which are also layered systems. However, CuO_2 layers in cuprates are nearly flat while layers in FeSCs are much more three-dimensional as shown in Fig. 1.4. Blocking layers have ionic bonds to the FeAs layer, while the FeAs layer itself possess Fe-As covalent bonding and Fe-Fe metallic bonding as well. [15]

It is widely believed that the interaction that leads to superconductivity is initiated from FeAs layers, similar as cuprates where CuO_2 layer is responsible for high temperature superconductivity. FeSC compounds exhibit tetrahedral coordination of Fe and As, where T_c depends on the height of tetrahedral or, equivalently, the As–Fe–As bond angle. [16, 17] In particular, T_c tends to maximize close to the perfect tetrahedral geometry, i.e. for an As–Fe–As bond of $\approx$ 109.47°. [15] Besides, the length of the c-axis is thought to affect the two-dimensionality of the systems and therefore the structurally driven modification of the Fermi surface, rather than charge-carrier doping, may be key to superconductivity [18, 19].

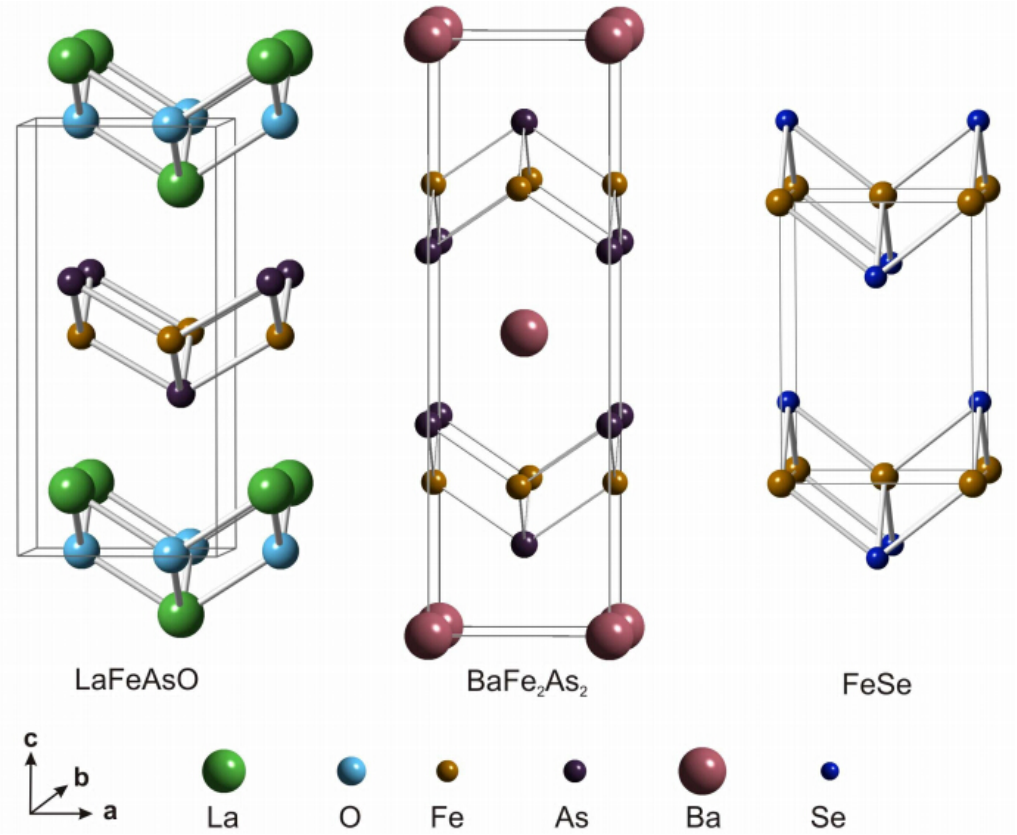

Figure 1.4 Structures of LaFeAsO, BaFe2As2 and FeSe. Crystallographic unit cells of the undoped materials are shown, for tetragonal ($T > T_s$) structures. The solid lines mark one unit cell for each material. The common structural unit of all iron-based compounds is the Fe-As tetrahedral layer, with the adjacent layers either co-aligned out-of-plane or alternating in orientation. [20]

Based on this FeAs-layered framework, the electronic structure calculated using the local density approximation (LDA) [22–24] shows a high density of states at the Fermi energy, and electronic structure in the vicinity of the Fermi energy is dominated either by Fe-d bands, or strongly hybridized Fe-d and As-p orbitals, The predominantly Fe-d bands crossing the Fermi level form two hole pockets at the Γ point and two electron pockets centered at (0, π) and (π,0), the X point of 1-Fe Brillouin zone. The crossings produce the complex multiband Fermi surface of iron-base compounds. Techniques sensitive to the geometry and topology of the Fermi surface, such as angle-resolved photoemission spectroscopy (ARPES), have confirmed its multiband and quasi-two-dimensional character in the FeSC compounds, and consistent

with the theoretical calculations. As mentioned above, the two-dimensionality of the electronic structure is widely believed to be one of the essential prerequisites for high-temperature superconductivity [25], mostly due to the drastic enhancement of electronic instabilities and fluctuations in lower dimensions.

The FeSCs are classified based on their crystallographic structure. Classes are usually denoted by the chemical formula of the parent, often nonsuperconducting, compounds, e.g. '1111' for the parent compounds REFeAsO (RE = rare earth elements like La, Ce, Sm, Gd, ...) and AFeAsF (A = Ba, Sr...), '122' for AFe_2As_2 (A = Ba,Sr, Ca...), '111' for AFeAs (A=Li, Na, K...), and '11' for FeSe(Te). Some examples are illustrated in Fig. 1.4, showing the parent phases of LaFeAsO (1111), $BaFe_2As_2$ (122) and FeSe (11) systems, all of which have tetragonal crystal symmetry at room temperature. The iron in these systems is divalent with electronic configuration $3d^6$. 1111, 111 and 11 families belong to the tetragonal P4/nmm space group. 11 class is especially simple, only consists of layers of $FeSe_4$ edge-sharing tetrahedra. The parent undoped compound of 122 class, such as $BaFe_2As_2$, crystallizes in a $ThCr_2Si_2$-type structure (Fig. 1.4) with a tetragonal crystallographic symmetry in the I4/mmm space group.

1.2.3 Magnetic properties and phase diagram

Upon cooling, most of the undoped iron-based compounds undergo structural distortions from the structures shown in Fig.1.4, to orthorhombic below T_s, accompanied simultaneously or followed by an antiferromagnetic(AFM) transition, similar to the cuprates [26]. However, the former are semimetals with all five $3d$ orbitals of Fe contribute to the states around the Fermi level, rather than Mott insulators involving the Cu $3d_{x^2-y^2}$ orbital and the oxygen $2p$ orbital in cuprates. All of the FeAs-based superconductors share a similar magnetic structure of long range magnetic order. As shown in the iron plane of Fig. 1.5, the iron sublattice undergoes magnetic ordering with an arrangement of spins aligning ferromagnetically along one chain of nearest neighbors, and antiferromagnetically along the other direction. Although displayed on a tetragonal lattice, this only occurs after the system undergo an orthorhombic deformation as explained above.

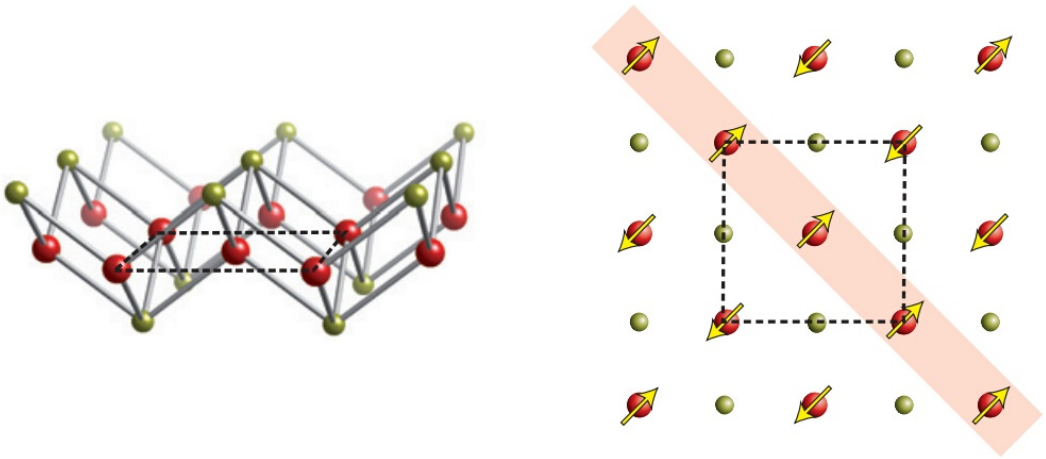

Figure 1.5 Depiction of the active planar iron layer common to all superconducting compounds, with iron ions in red and pnictogen/chalcogen anions in gold. The dashed line indicates the size of the unit cell of the FeAs-type slab that includes two iron atoms due to two nonequivalent As positions. The ordered spin arrangement for FeAs-based materials is indicated by arrows (not shown for FeSe). [15]

The long range magnetic order could result from ordering of local moments on the ironsites, or be due to itinerant electron ordering. Localised magnetism occurs via interactions between magnetic moments of the electrons that are confined to particular magnetic sites. These moments are usually large because each unpaired electron spin contributes 1 μ_B to the total moment. Localised magnetism is often seen in insulating compounds because of localization of electrons. As mentioned above, the parent compound of the cuprates, being intrinsic Mott insulators, where its insulating behavior arised from very strong electron-electron correlations, is a good example of local antiferromagnets. On the other hand, itinerant electron magnetism occurs in magnetic states in which the electrons can move throughout the crystal, thus form the spontaneous spin density into a periodic magnetic structure, i.e., spin-density wave. The values of the ordered magnetic moment are often much smaller than in the localized electron systems.

The situation in the iron-based compounds is significantly more complex. It is currently believed that antiferromagnetism in these compounds is located between purely local magnets (e.g. cuprates) and purely itinerant magnets (e.g. elemental chromium) [27] with the characters of both local and itinerant magnetic moments. For example, it has been predicted by first-

principles calculations and also confirmed by extensive ARPES measurements that most of iron-based compounds, such as $Ba_{1-x}K_xFe_2As_2$ [28], FeTe [29], exhibit rather good nesting between hole- and electron-like pockets of the Fermi surface, making them prone to a spin-density-wave instability. The observed ordered antiferromagnetic moments, though, show quite small values of 0.3–1.0 μ_B [30], even there are six electrons in the Fe-3d orbital.

The generic phase diagram of the FeSC systems is shown in Fig. 1.6. The parent compounds of FeSCs are semimetals at room temperature, while at lower temperatures the antiferromagnetic ground state in these compounds is a spin-density wave (SDW) state arising from itinerant electrons due to the relatively small and variable values of ordered moment observed for the parent compounds, in contrast to cuprates where the antiferromagnetism is associated with strong electron correlation. In FeSCs, such as LaFeAsO and $BaFe_2As_2$, parent compounds are not superconducting themselves under ambient conditions, but charge carriers doping or application of pressure induce superconductivity. [10, 31] In the case of $Ba(Fe_{1-x}Co_x)_2As_2$ system, AFM state is suppressed with substitution and SC phase is more or less centered near the critical concentration where AFM order is destroyed. The proximity of superconductivity to the antiferromagnetism gives rise to strong antiferromagnetic spin fluctuations (AFMSF) once the long-range order has been suppressed, which are currently believed to be the most plausible candidate for the superconducting pairing mediator. [32–35, 55, 74]

The issue of phase separation/coexistence has been of particular interest in the iron-based compounds showing overlapping AFM and SC regions. In F-doped 1111 systems such as $LaFeAsO_{1-x}F_x$ [36],$CeFeAsO_{1-x}F_x$ [26], AFM and SC phases are completely separated as a function of doping and do not overlap, however, with the exception of $SmFeAsO_{1-x}F_x$ [37], where the coexistence of AFM and SC phases is reported. In the case of 122 system, $Ba(Fe_{1-x}Co_x)_2As_2$ show microscopic coexistence of AFM and SC [38], whereas $Ca(Fe_{1-x}Co_x)_2As_2$, undergo intrinsic phase separation [40]. Whether the coexistence of these two order parameters evolve from the same electrons, since they are often homogeneously throughout the bulk of the crystal and intertwined strongly with each other, is still under debate, making it possible to study the properties of one via the other. In particular, researchers have been interested in the quantum critical point (QCP) that might be hidden at the boundary of the AFM phase inside

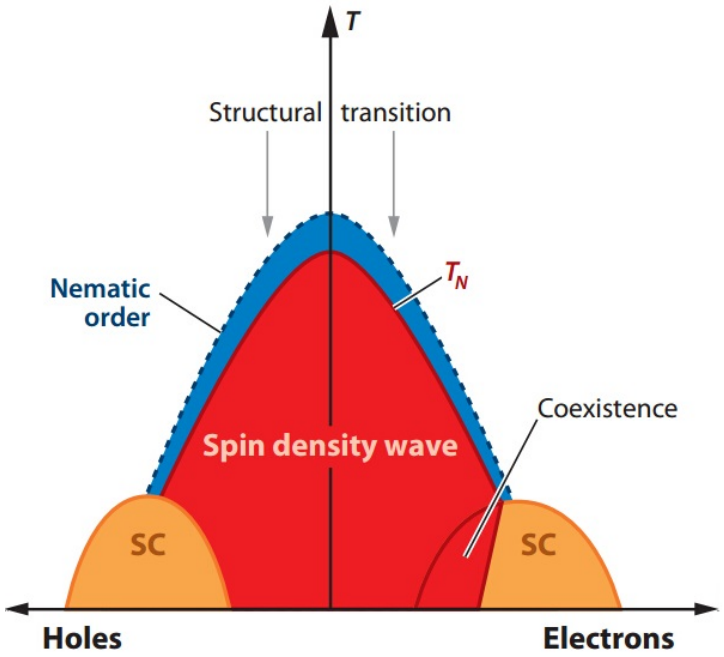

Figure 1.6 General schematic phase diagram of iron-based superconductors. The crystal structure changes from tetragonal to orthorhombic below T_s. There is antiferromagnetic order (spin-density wave state) below T_N. Shaded region shows the coexistence of superconductivity (SC) and antiferromagnetism. Superconductivity has also been found to occur in the extremely overdoped regime either disconnected from the optimally-doped region or as a part of a ubiquitous superconducting phase. The nematic phase above T_N is still under debate. [25]

the superconducting dome, where QCP marks the position of a quantum (zero-temperature) phase transition driven by quantum fluctuations. [15] Recent study of $BaFe_2(As_{1-x}P_x)_2$ with phase coexistence, has revealed a strong peak in the doping dependence of the zero-temperature London penetration depth $\lambda_L(0)$ at the doping level corresponding to the maximum of T_c at the boundary of the coexistence phase. [41] The increase of the penetration depth may result from the increase in the scattering of electrons which make Cooper pairs heavier and thus their screening of external magnetic fields less effective. Meantime, the concomitant critical enhancement of AFMSF leads to the stronger binding of electrons into Cooper pairs and leads to a higher T_c.

The anisotropy of in-plane resistivity above the structural transition temperature in the parent and Co-doped $BaFe_2As_2$ [47,48] has raised the question of the possible existence of a more

exotic and elusive phase —nematic phase (blue areas in Fig. 1.6), which shows no magnetism but breaks the *C4* rotational symmetry of the high-temperature tetragonal phase in a second-order phase transition. This new phase has been confirmed in both the Co-doped compound [49] and $BaFe_2(As_{1-x}P_x)_2$ [50]. Fernandes *et al.* [51, 52] have explained this nematic phase by anisotropic spin fluctuations above the antiferromagnetic transition temperature. However, in $BaFe_2(As_{1-x}P_x)_2$, nematic phase was found to exist even in the overdoped regime, distant from long-range antiferromagnetic order. Recent ARPES measurements on $Ba(Fe_{1-x}Co_x)_2As_2$ [53] suggest that, in addition to the spin fluctuations, orbital anisotropy might also play an important role for the occurence of nematic phase.

So far, we have mentioned two keys for high-temperature superconductivity , including the two-dimensionality of the Fermi surface and the proximity of superconductivity to strong antiferromagnetism, observed in both the cuprates and FeSCs. In both cuprates and FeSCs, superconductivity is strongest where the antiferromagnetic long-range order has just disappeared completely, although the antiferromagnetic phases are quite different in two systems. This suggests that SC is actually driven by the fluctuations of electron spins, which are strongest at the edge with the AFM state, although SC is destroyed by long-range AFM order. Inelastic neutron scattering (INS) revealing a resonance mode at the value of the antiferromagnetic ordering vector in all iron-based superconductors [30], in fact, strongly support this result. This makes the study of the dynamic magnetic properties, fluctuations, of the FeSCs indispensable to a complete understanding of their superconducting pairing mechanism.

In an itinerant paramagnet, statistical fluctuations of electron-spin density may still be significant even the ordered magnetic moment is zero. [54] Various techniques, such as INS, NMR, Muon spin relaxation/rotation (μSR), can be applied to detect these fluctuations depending on the energy scale. In FeSCs, such spin fluctuations have been shown to occur at the same wave vector in the Brillouin zone as the static magnetism of the respective parent compounds. [55] In this thesis, we focus on the study of magnetic fluctuations in normal state of $Ca(Fe_{1-x}Co_x)_2As_2$ compounds (Ca122) using techniques of NMR.

1.2.4 Superconducting properties

Similar as the cuprates, the Cooper-pairing mechanism that causes the high temperature superconductivity in FeSCs is one of the most challenging problems in condensed matter physics field. Although the exact nature of the pairing is not known in FeSCs, many experiments have been performed to determine the pairing symmetry of the superconducting order parameter. For the FeSCs, the symmetry was predicted theoretically to have s-wave symmetry, but with a sign reversing that occurs between different bands in the complex multi-band electronic structure, the so called "$s_{\pm}$" symmetry. [56–58] The $s_{\pm}$ wave-symmetry, together with another possible scenario, d-wave symmetry for the superconducting order parameter symmetry in FeSCs, is shown in Fig. 1.7. In the $s_{\pm}$ model, the superconducting gaps which open at each Fermi surface upon entering the superconducting state are isotropic and similar in magnitude, but differ in their sign ($+\Delta$ and $-\Delta$ on the hole and the electron pocket, respectively). [56] Modulation of the gap amplitude in $s_{\pm}$-wave symmetry may be present allowing plentiful low-energy excitations even at temperatures much below the energy of the gap, explaining the node observed in LaFePO [59], $BaFe_2(As_{1-x}P_x)_2$ [41] and KFe_2As_2 [62].

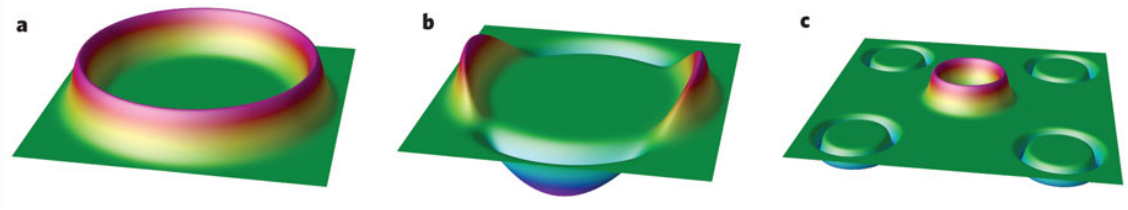

Figure 1.7 Schematic representation of the superconducting order parameter. (a) a uniform s wave. (b) d wave, with nodes in the order parameter. (c) $s_{\pm}$ wave symmetry. [63]

NMR technique is powerful to determine symmetry of superconducting order parameter. In the case of conventional superconductors, nuclear spin-lattice relaxation rate ($1/T_1$) is known to show the Hebel-Slichter peak just below T_c. [64] The singlet paring can also be indicated by the sharp drop of Knight shift below T_c. The temperature dependence of the $1/T_1$ below T_c are frequently used to discriminate conventional from unconventional pairings with absence of the Hebel-Slichter peak. For a single Fermi surface, nuclear spin-lattice relaxation rate of

superconductors with line node and point node order parameters would follow the power-law behavior, $1/T_1 \sim T^3$ and T^5, respectively [65], which for singlet pairing correspond to the d- and a special $s+g$-wave state.

Early NMR results of line-node pairing symmetry [66–70] based on this T^3 dependence of $1/T_1$ in the superconducting state were not consistent with the results of various other experiments, such as ARPES and thermal conductivity κ, which indicated that the superconducting gap is nodeless on each Fermi surface pocket. [71–73] Moreover, INS experiments observed a peak at the antiferromagnetic wave vector $\vec{Q}$ and $\omega = \omega_{res}$ below T_c in various compounds [31,74,75], supporting a $s_{\pm}$-wave symmetry. Soon it was found by NMR there is no universal behavior for the power-law dependencies of $1/T_1 \propto T^n$, values of n between 1.5 and 6 have been observed in different pnictides. [31,66–71,71–73,75–82] Therefore in these multiband compounds, besides the possibility of a simple line-node gap, $s_{\pm}$ wave symmetry model [56,57,83,84] and inclusion of two superconducting gaps with different amplitudes [67, 77, 81, 85] has been adopted to explain the NMR data especially in the presence of additional impurity scattering effects [56, 57, 83, 84] and thus can reconcile NMR and ARPES results.

1.2.5 NMR studies of 122 families of FeSCs

In the last section, I mentioned the studies of NMR on the paring symmetries of superconductors. Actually, NMR is quite versatile. It can detect the onsite hyperfine field originating from the electronic bath. Therefore, it is very sensitive to static electronic spin susceptibility, magnetic order, and low-energy magnetic excitations. In this section, I will summarize NMR studies on several 122 compounds of FeSCs.

As seen from the phase diagram, the structural transitions in iron pnictides are strongly coupled to the magnetic properties. Fig. 1.8(a) displays the temperature dependence of the quadrupole resonance frequency ν_q of ^{75}As in $BaFe_2As_2$, reported by Kitagawa *et al.* [86] ν_q directly measures the quadrupole interaction between the nuclear quadrupole moment and crystalline EFG, which is determined by the lattice structure. With temperature increasing, the ν_q^c gradually decreases and shows a sudden jump at $T_s \sim 135K$, indicating the structural transition. Correspondingly, the asymmetry parameter increases abruptly from zero in the

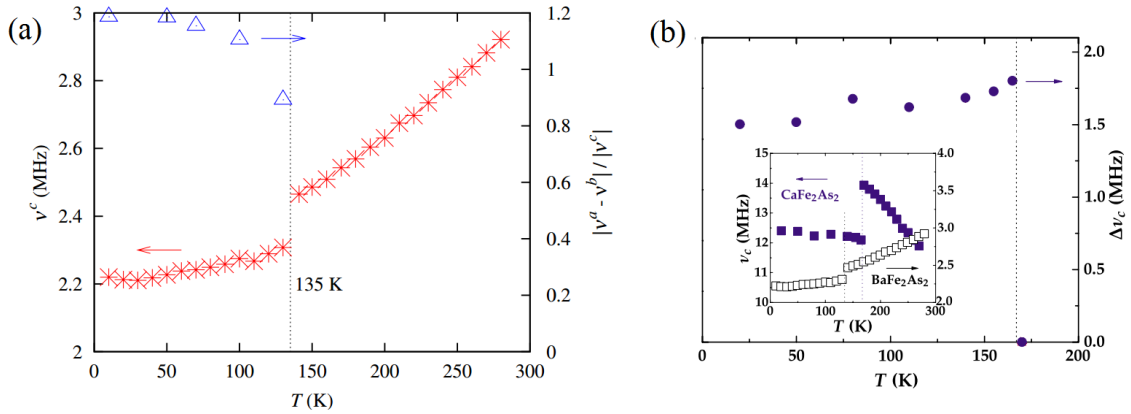

Figure 1.8 (a) Temperature dependence of the quadrupole frequency ν_q at As site with $\vec{H}||c$, and the in-plane EFG asymmetry parameter in $BaFe_2As_2$. [86] (b) Temperature dependences of the order parameters in the ordered state for $\vec{H}||c$ in $CaFe_2As_2$. $\Delta\nu_c \equiv |\nu_c(T) - \nu_c(T_N)|$ is a measure of the structural distortion. The inset shows the temperature dependences of quadrupole frequency for both compounds. Adapted from [87]

tetragonal phase to a finite value just below the transition temperature, consistent with the first order tetragonal-to-orthorhombic transition.

The temperature dependence of the asymmetry parameter η of EFG at As site and ν_q^c have important implications for the structural transition. The relation, $|\nu_q^a - \nu_q^b|/|\nu_q^c| > 1$ in the low temperature region, indicates that the principal axis of EFG has been rotated by 90° across the transition. Compared with the little difference between a and b axis, this big change of EFG may come from the substantial change of the charge density distribution around the As sites. Therefore a high anisotropy in the band structure is suggested in the ab plane.

The T-dependence of quadrupole frequency in $CaFe_2As_2$ (where ν_c increases upon cooling) behave contrasts sharply with that observed in $BaFe_2As_2$, however, the discontinuous decrease in ν_c at T_N and a measure of the structural distortion $\Delta\nu_c$ was also observed in $CaFe_2As_2$, indicating the structural transition.

Figure 1.9 shows the temperature dependence of ^{75}As NMR spectra across the AFM transition in $BaFe_2As_2$ [86] and $CaFe_2As_2$ [87]. In the paramagnetic state, both spectra are composed of a sharp central line and two satellites, as a result of the quadrupole interaction. Below the Néel temperature, the spectrum for $H||c$-axis was split due to the internal field ($\vec{H}_{int}$) along

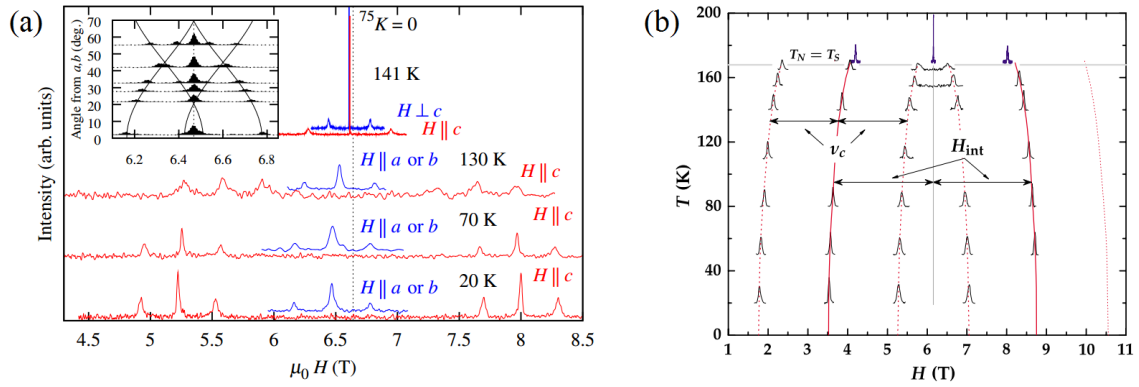

Figure 1.9 (a) Temperature dependences of field-swept ^{75}As spectra in $BaFe_2As_2$ with different field orientations. The inset shows angular variation of the spectrum at 20 K for the field rotated in the ab-plane. [86] (b) Temperature dependences of ^{75}As NMR spectra in $CaFe_2As_2$ for $\vec{H}||c$. The red/gray solid and dotted lines represent the split central lines and the satellites associated with each central line, respectively. One of the satellites at highest fields was not measured due to the limited maximum field 9 T. [87]

the c-axis; on the other hand, spectrum for $H||ab$-plane shifted to lower fields (not shown in $CaFe_2As_2$). Observation of the $\vec{H}_{int}||c$-axis in the AFM state suggests that the configuration for the hyperfine coupling between ^{75}As nucleus and Fe moments is an stripe-type structure with the AFM moment perpendicular to the stripe, as shown in Fig. 1.10.

As a local probe, NMR is very useful to investigate microscopically the competition between antiferromagnetic order and SC, as well as their coexistence, which is important for the understanding of high-T_c superconductivity in iron pnictides. As shown in Fig. 1.11, Iye *et al.* [88] reported on their NMR evidence for the microscopic coexistence of AFM and SC in power of underdoped $BaFe_2(As_{1-x}P_x)_2$. Fig. 1.11(a) shows the temperature dependence of ^{31}P-NMR spectrum. Above T_N, a single sharp peak is observed in the powdered sample without quadrupole broadening for ^{31}P nuclei ($I = 1/2$). Below T_N, a broad NMR spectrum with gaussian shape gradually develops and coexists with a sharp peak. The broadened spectrum indicates the magnetic broadening in the underdoped sample, with the magnetic moments displayed in Fig. 1.11(b). The internal field on ^{31}P sites increases steeply below T_N, and is strongly suppressed below T_c^*. As shown in Fig. 1.11(c), $1/T_1T$ measured at the broad magnetic ordered spectrum decreases at T_c^*, indicating the opening of superconducting gap in the

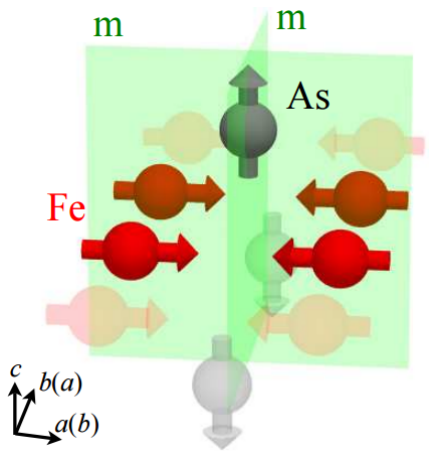

Figure 1.10 The stripe type AFM ordered state in $BaFe_2As_2$, which is compatible with the ^{75}NMR results. The internal field at the As sites are shown by grey arrows. [86]

AFM region of the sample. The suppressed moment in the AFM region below superconducting transition is a direct evidence for the competition between these two orders. As shown in Fig. 1.11(d) and (e), the values of $1/T_1T$ are measured at different frequencies across the broad spectrum at $T = 5$ and 20 K, showing that the values of $1/T_1T$ in all regions of the spectrum at 5 K are smaller than at 20 K, which confirms the SC in the entire region of the sample. The above measurements indicate the microscopic coexistence of and strong competition between SC and AFM in underdoped $BaFe_2(As_{1-x}P_x)_2$, suggesting that these two orders originate from the same Fermi surface.

The microscopic coexistence is also observed in underdoped $Ba_{1-x}K_xFe_2As_2$ single crystals, reported by Li *et al.* [89]. As shown in Fig. 1.12(a), the AFM is monitored by the peak splitting for $H||c$ and peak shifting to a higher frequency for $H||a$ below $T_N \sim 46$ K. No evidence for residual paramagnetic phase is seen below T_N. Fig. 1.12(b) displays the temperature dependence of spin-lattice relaxation rate measured at the central peak for $H||a$. Above T_N, $1/T_1$ shows an upturn behavior with temperature decreasing due to strong spin fluctuations in a system near the magnetic instability. Below T_N, $1/T_1$ begins to drop for the gradually suppressed spin fluctuations in an ordered state. When the SC sets in below T_c, $1/T_1$ shows another sharp drop and follows a T^3 power law behavior, which is clear evidence for the

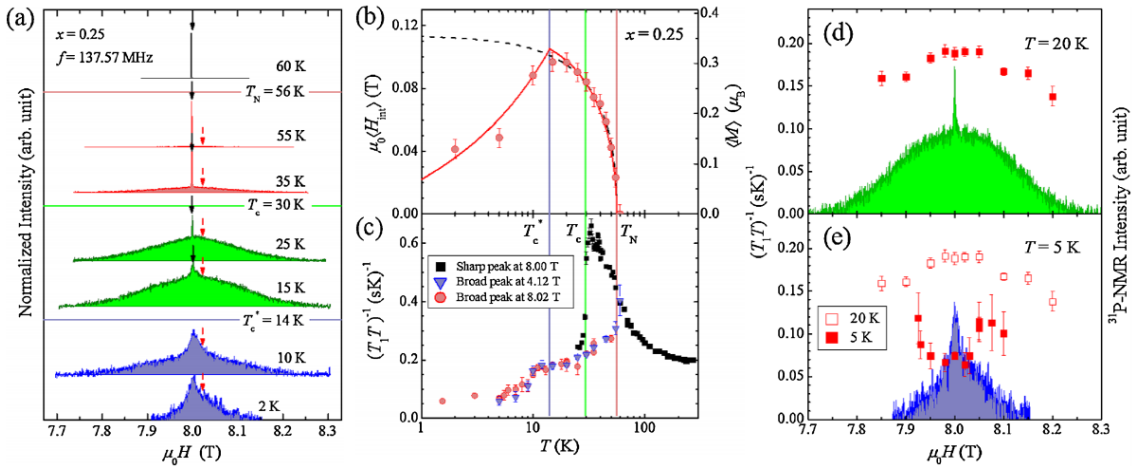

Figure 1.11 (a) $BaFe_2(As_{0.75}P_{0.25})_2$: Field-swept ^{31}P NMR spectra of various temperatures. (b) Temperature dependence of averaged internal field on ^{31}P sites $\langle H_{int} \rangle$, as obtained by the second moment of the spectrum. (c) Temperature dependence of $1/T_1T$ measured at the sharp paramagnetic NMR signal (closed squares) and the broad antiferromagnetic signal (triangles and circles). Plots of $1/T_1T$ across the spectra (d) above and (e) below the T_c in the magnetically ordered phase. [88]

microscopic coexistence of AFM and SC.

NMR, as a low energy probe, is very sensitive to low energy excitations in condensed matter system. Anisotropic $1/(T_1T)$ can give the information about the momentum dependence of spin fluctuations, as we will discuss in next chapter. Ning *et al.* [90] reported on their NMR study on the evolutions of the spin fluctuations in $Ba(Fe_{1-x}Co_x)_2As_2$ single crystals for various values of x, as shown in Fig. 1.13. The $1/(T_1T)$ data show an upturn characteristic upon cooling in samples with $x \leq 0.12$, indicative of the development of low-energy spin fluctuations. Actually, $1/(T_1T)$ can be fitted by $\frac{1}{T_1T} = \frac{C}{T+\theta} + \alpha + \beta e^{-\frac{\Delta}{k_BT}}$, where the first term refers to the low-energy spin fluctuations from interband scattering based on Moriyas theory for weakly antiferromagnetic itinerate system, and the second and third terms represent the phenomenological activation forms. The low-energy spin fluctuation strength can be quantitatively analyzed by the θ value or the value of $1/(T_1T)$.

Figure 1.13(b) and (c) display the variations of $1/(T_1T)$ ($T = 25$ K) and θ value with doping level. The θ value is negative for $x \leq 0.05$, indicative of the antiferromagnetic ground state for samples, as shown in Fig. 1.13 (c). At the same time, the large value of $\theta \approx 119$ K for

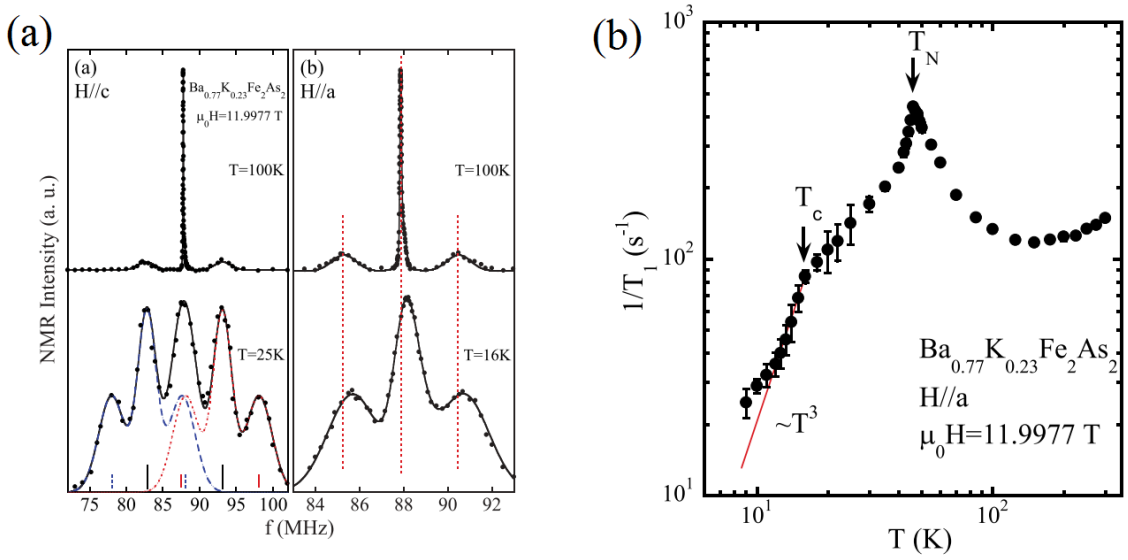

Figure 1.12 (a) ^{75}As NMR spectra of $Ba_{1-x}K_xFe_2As_2$ above and below T_N for (a) $\vec{H}||c$ and (b) $\vec{H}||ab$, respectively. The blue dashed curve and the red dotted curve are the simulated two sets of spectra that are split by the internal magnetic field, and the black curve is the sum of the two sets of spectra. The short lines designate peak positions. (b) Temperature dependence of the ^{75}As $1/T_1$. The straight line indicates the $1/T_1 \propto T^3$ relation. [89]

$x = 0.12$ overdoped sample indicates that it is far from the magnetic instability. The small positive $\theta \approx 31$ K for $x = 0.08$ optimally doped sample is an indication for the fact that the optimally doped superconductivity is slightly beyond the quantum critical point ($\theta = 0$). This work also suggests that the low-energy antiferromagnetic spin fluctuations play an important role in high-T_c superconductivity in the iron-based materials.

1.2.6 Motivation

Figure 1.14 shows typical phase diagram of $Ba(Fe_{1-x}Co_x)_2As_2$ and $Ca(Fe_{1-x}Co_x)_2As_2$. A universal finding is that they both undergo a transition from paramagnetic (PM) tetragonal phase to an AFM orthorhombic phase. Nevertheless, differences between Co-doped Ca122 and Ba122 system observed by experiments still cannot be well-understood. The $Ba(Fe_{1-x}Co_x)_2As_2$ system exhibits a clear splitting of structural and magnetic phase transition lines upon Co substitution, and the coexistence of AFM and SC has been found. [38, 39] $Ca(Fe_{1-x}Co_x)_2As_2$,

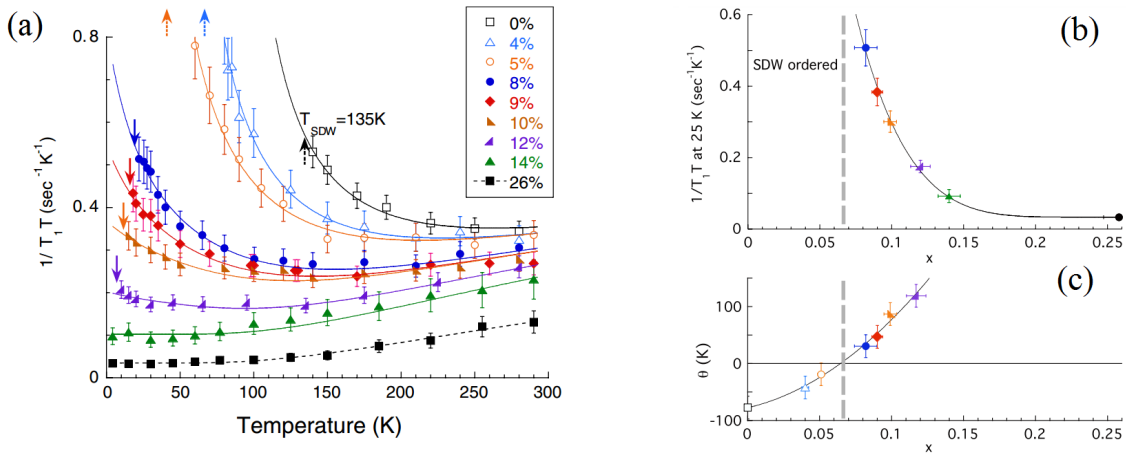

Figure 1.13 (a) ^{75}As NMR $1/T_1T$ measured in $Ba(Fe_{1-x}Co_x)_2As_2$ for various concentrations x with $\vec{H}||ab$. T_c and T_N are denoted by the solid and dashed arrows. Solid and dashed curves are the best fits. (b) The concentration dependence of the strength of paramagnetic spin fluctuations as measured by $1/T_1T$ observed at 25 K. (c) Weiss temperature θ. [90]

however, shows a coincident structural and magnetic phase transition at the same temperature and does not show any splitting of the transitions lines. No coexistence of the AFM and SC has been reported either in $Ca(Fe_{1-x}Co_x)_2As_2$. [40]

In addition, Ca122 is particularly sensitive to pressure: with pressure larger than 0.35 GPa, $CaFe_2As_2$ experiences another exceptional transition from AFM orthorhombic state to a new nonmagnetically ordered but collapsed tetragonal ($c\mathcal{T}$) state in which the distance between two FeAs layers is strongly reduced. [91–93].

So far, NMR has been applied to investigate the spin correlations in normal state and the low-temperature $c\mathcal{T}$ phase in $CaFe_2As_2$. [94] Baek *et al.* [95] also reported temperature-dependence of ^{75}As NQR spin lattice relaxation rates ($1/T_1$) in $Ca(Fe_{1-x}Co_x)_2As_2$, showing a gradual decrease of ($1/T_1T$) below a crossover temperature (T^*) in the underdoped and optimally doped regions. However, no systematic NMR data on Co-substituted $CaFe_2As_2$ have been reported up to now.

Therefore, in this thesis, we will shed new light on the physical properties of $Ca(Fe_{1-x}Co_x)_2As_2$ through a microscopic NMR investigation. In Chapter 3, details of the static spin susceptibility, magnetic order and stripe-type AFM fluctuations in Ca122 system with different Co-doping

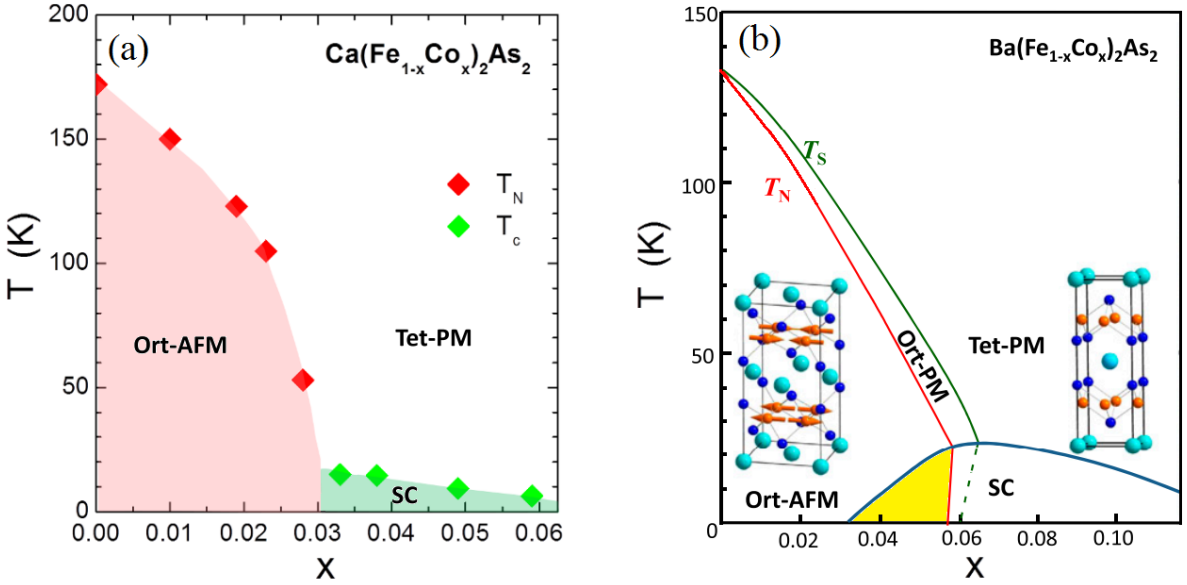

Figure 1.14 Temperature-doping (T-x) phase diagram for (a) $Ca(Fe_{1-x}Co_x)_2As_2$ [40] and (b) $Ba(Fe_{1-x}Co_x)_2As_2$, adapted from ref. [96] and [97]. Insets shows the orthorhombic structure with in-plane Fe spin marked by arrows (left) and tetragonal structure of 122 compound (right). Yellow shaded area shows the coexistence of AFM and SC phase.

concentration will be given. We found a sudden drop of antiferromagnetic spin fluctuations just below T_N [98] in Ca122 system in constrast to the clear divergent behavior and a gradual suppression of fluctuations in the case of Ba122 system. Furthermore, our results of Co-doping independent internal field in Ca122 system suggests a robust Fe-ordered moments in contrast of monotonic decreased Fe ordered moments with Co substitution in Ba122 by neutron scattering measurements. [96] Based on our NMR data, we also found a gradual decrease of the AFM spin fluctuations below a crossover temperature $T*$ that was nearly independent of Co-doping concentration, and it is attributed to a pseudogaplike behavior.

In Chapter 4, we will discuss the competition of antiferromagnetic spin fluctuations and ferromagnetic fluctuations in this system. From the measurements of ^{75}As NMR shift and nuclear spin-lattice relaxation rate $1/T_1T$, we did the Korringa ratio analysis and found clear evidence for the coexistence of stripe-type AFM and FM spin correlations.

1.3 Thermoelectric Tellurides

Home heating, automotive exhaust, and industrial processes lose over 60% of unused waste heat that could be converted to electricity by using thermoelectric generators. [99, 100] In a global drive for clean energy sources to replace carbon-based fossil fuels, thermoelectric materials will play an important role in energy storage, conversion, recovery, and transfer. The emerging and prospective areas of application of thermoelectric materials include: automotive waste heat power generation, direct solar thermal energy conversion, and superconducting electronics. Thermoelectric generators are solid-state devices with no moving parts; lacking of noise, reliable and scalable, making them ideal for small, distributed power generation [101,102]. However, the low efficiency of thermoelectric devices (which still remains below 5%) has limited their spread in commercial applications. It is therefore necessary to develop advanced thermoelectric materials displaying higher efficiency, better performance and chemical and thermal stability at the appropriate operating temperatures for the lower cost of devices [103].

1.3.1 Thermoelectric material properties

The fundamental process responsible for thermoelectric power generation is known as the Seebeck effect (Fig. 1.15). Metals and semiconductors contain charge carriers carrying heat that are free to move much like gas molecules. In the presence of a temperature gradient, the mobile charge carriers at the hot end tend to diffuse to the cold end of the material. At equilibrium, an electrostatic potential (voltage) will be generated due to the build-up of charge carriers, thus to balance the chemical, diffusive driving force provided by the temperature difference. A thermoelectric generator uses heat flow across this temperature gradient to power an electric load through the external circuit. The Seebeck coefficient α is defined as the ratio of the measured voltage across the sample to the temperature difference, $\alpha = \triangle V/\triangle T$. For metals or degenerate semiconductor, the Seebeck coefficient is given by:

$$\alpha = (\frac{8\pi^2 k_B^2}{3eh^2}) m^* T (\frac{\pi}{3n})^{2/3} \tag{1.1}$$

where n is the carrier concentration and m^* is the effective mass of the charge carrier. Mixed n-type and p-type conduction will lead to both charge carriers moving to the cold end, cancelling

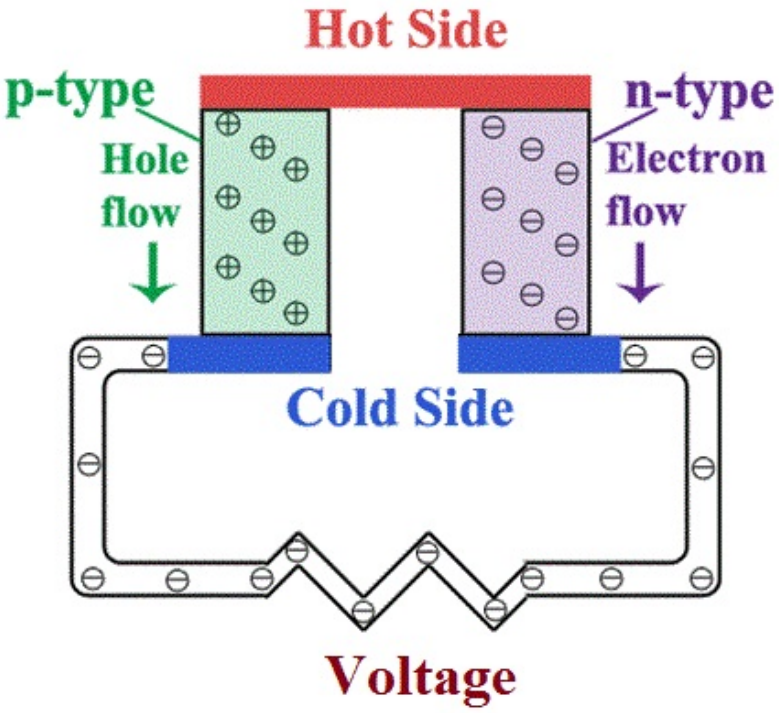

Figure 1.15 Schematic picture of the Seebeck effect in which charge carriers flow towards the cold end of a heated material– the resulting voltage that develops determines the Seebeck coefficient: $\alpha = \triangle V/\triangle T$.

out the induced Seebeck voltages. Therefore, only single type of carrier should be present to ensure a large Seebeck coefficient. [104]

The maximum efficiency of a thermoelectric material for power generation is determined by its figure of merit zT:

$$zT = \frac{\alpha^2 \sigma T}{\kappa} \tag{1.2}$$

where zT depends on Seebeck coeffcient α, absolute temperature T, electrical conductivity σ, and thermal conductivity κ. The electrical conductivity σ is related to n through the carrier mobility μ, $\sigma = ne\mu$. Low carrier concentration insulators and even semiconductors should give rise to large Seebeck coefficients, according to equation (1.1). However, low carrier concentration also results in low electrical conductivity.

There is no theoretical limit for the thermoelectric zT. Therefore, to maximize the power generation effciency and performance of thermoelectric materials, zT should be as high as pos-

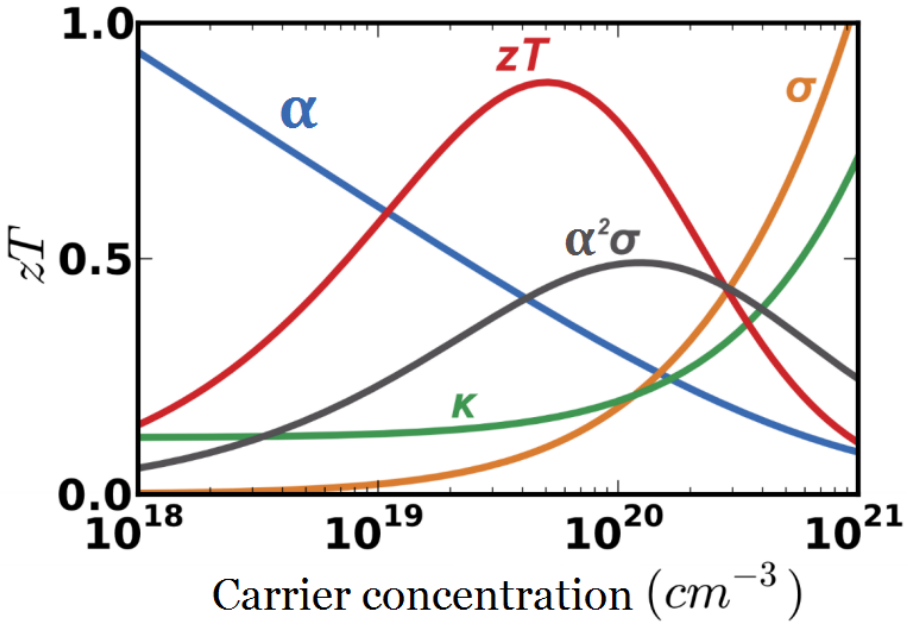

Figure 1.16 Maximizing zT of a thermoelectric involves a compromise of thermal conductivity (κ; 0 to 10 $Wm^{-1}K^{-1}$) and Seebeck coefficient (α; 0 to 500 μVK^{-1}) with electrical conductivity (σ; 0 to 5000 $\Omega^{-1}cm^{-1}$). Adapted from [104].

sible. A variety of conflicting properties need to be optimized: a large thermopower (absolute value of the Seebeck coefficient) leads to a high voltage across the device; high electrical conductivity minimizes resistive losses due to Joule heating, and low thermal conductivity allows large possible temperature gradientare. Fig. 1.16 shows the compromise between large thermopower and high electrical conductivity in thermoelectric materials that must be struck to maximize the figure-of-merit zT. This peak typically occurs at carrier concentrations between 10^{19} and 10^{21} carriers per cm^3, which falls in between common metals and semiconductors that are so heavily doped their transport properties resemble metals.

The thermal conductivity parameter κ describes heat transfer. [105] It is defined with respect to the steady-state flow of heat down a long rod with a temperature gradient, $J_u = -\kappa dT/dx$, where J_u is the flux of thermal energy. [106] κ is contributed by two sources, i.e., carriers transporting heat (κ_e) and phonons travelling through the lattice (κ_l): $\kappa = \kappa_e + \kappa_l$. Electrical thermal conductivity κ_e is directly related to the electrical conductivity through the Wiedemann-Franz law: $\kappa_e = L\sigma T = ne\mu LT$, where L is the Lorenz factor, $2.4\times10^{-8}J^2K^{-2}C^{-2}$

for free electrons and varies particularly with carrier concentration. It reveals an inherent materials conflict for achieving high zT requiring high electrical conductivity but low thermal conductivity. For materials with very high electrical conductivity or very low κ_l, the Seebeck coefficient alone primarily determines zT:

$$zT = \frac{\alpha^2/L}{1 + \frac{\kappa_l}{\kappa_e}} \tag{1.3}$$

where $\kappa_l/\kappa_e \ll 1$.

Thermal conductivity due to lattice can be expressed as $\kappa_l = \frac{Cv\lambda}{3}$, where C is the phonon heat capacity per unit volume, v is the average phonon velocity, and λ is the phonon mean free path. [107] An effective way to reduce lattice thermal conductivity is through enhancement of the phonon scattering. For example, creating rattling structures or point defects such as interstitials, vacancies or by alloying [108] increase the scattering of phonons within the unit cell, causing interruptions of phonons with large mean free path at interfaces and boundaries. However, the distortion introduced above inevitably blocks charge transport, showing lower mobility due to increased electron scattering, which may reduce electrical conductivity.

It is noteworthy that good thermoelectrics should be crystalline materials that manage to scatter phonons without deleterious effect on the electrical conductivity. Therefore, a commonly used model for desirable thermoelectric materials is "phonon-glass electron-crystal". [109] This means that an ideal thermoelectric material needs to act as crystalline materials, with respect to meeting electronic properties, and as a glass, having as low lattice thermal conductivity as possible.

1.3.2 State-of-the-art high-zT thermoelectrics and advanced approaches

The complex parameter relationships make the approach of tuning one factor alone difficult to enhance zT. However, over the past few decades, great progress has been made in thermoelectric field encompassing diverse strategies to enhance the power factor and reduce thermal conductivity, promoting the development of thermoelectrics. Fig. 1.17 summaries the figure-of-merit zT as a function of temperature for current commercial thermoelectric materials. According to the optimal working temperature, thermoelectric materials can be divided into

three ranges [104]: Bi_2Te_3- based low-, PbTe-based middle- and SiGe-based high-temperature ranges, with typical temperatures varying from <400 K, 500 K–900 K and >900 K, respectively. For near-room-temperature applications, Bi_2Te_3 alloys have been proved to possess the greatest zT for both n- and p-type thermoelectric systems. Peak zT values for these materials are typically in the range of 0.8 to 1.1 with p-type materials achieving the highest values. For mid-temperature power generation, group-IV tellurides, such as PbTe, GeTe or SnTe are typically used. [110–113] The peak zT in optimized n-type material is about 0.8. Only the p-type alloy $(GeTe)_{0.85}(AgSbTe_2)_{0.15}$ (called TAGS), with a maximum zT greater than 1.2 [114], has been successfully used in long-life thermoelectric generators. zT of silicon-germanium alloys, typically used in high-temperature thermoelectric generators, is fairly low for the p-type material, due to the relatively high lattice thermal conductivity of the diamond structure. Adjusting the carrier concentration will alter the temperature where zT peaks, enabling the materials for specific applications.

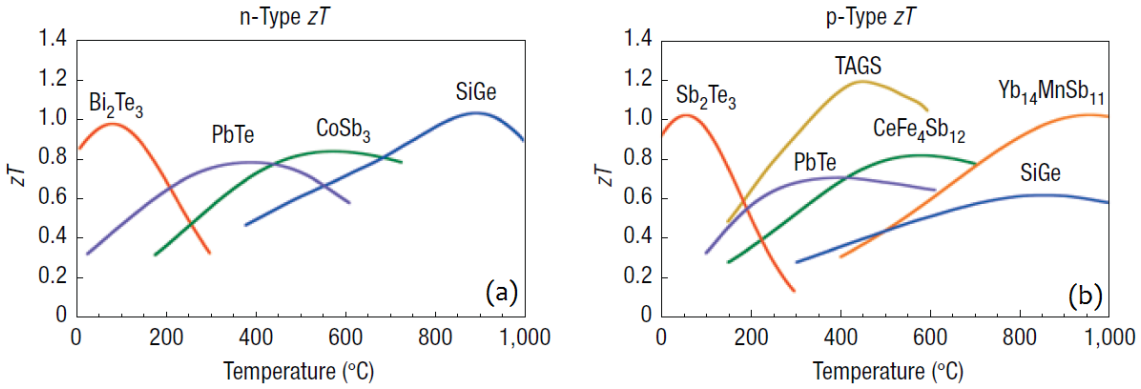

Figure 1.17 Figure-of-merit zT of state-of-the-art commercial thermoelectric materials for thermoelectric power generation. (a) p-type. (b) n-type. Most of these materials are complex alloys with dopants. [104]

To date, diverse advanced approaches to enhance zT emerged aim to maintain a high power factor and/or reduce the lattice thermal conductivities. For example, doing Tl to PbTe has increased effective carrier mass and pronuanced higher Seebeck coefficient through density-of-states (DOS) distortion, leading to a zT as high as 1.5 at 773 K. [115, 116] Such a situation can occur when the valence or conduction band of the host semiconductor resonates with the

localized impurity energy level. Theoretical predictions also suggested that the thermoelectric efficiency could be enhanced by quantum confinement of the electron charge carriers. [117,118] In a quantum confined structure, the electron energy bands are progressively narrower as the confinement increases and the dimensionality decreases. These narrow bands would produce high effective masses and therefore large Seebeck coefficients.

Additional effective methods to enhance thermoelectric performance include nanostructuring and all-scale hierarchical architecturing to reduce the lattice thermal conductivity. [119,120] For example, clathrates [121], which contain large cages that are filled with rattling atoms; skutterudites [122] such as $CoSb_3$, contain corner-sharing $CoSb_3$ octahedra, creating void spaces that may also be filled with rattling atoms. [123] Other materials include various intermetallics and Zintl phases (e.g., $Yb_{14}MnSb_{11}$) [124], complex transition metal oxides (e.g. BiCuSeO) [125, 126], nanostructured tellurides and selenides (e.g. $AgPb_xSbTe_{x+2}$) [127], as well as other types of semiconductors and semimetals (e.g. $AgSbTe_2$, $AgSbSe_2$) [128, 129].

1.3.3 NMR studies of thermoelectric tellurides

The disorder resulting from doping and alloying, in terms of point defects, vacancies, lattice distortions, minor phases and nanoinclusions, as well as electronic inhomogeneity [130], makes a complete structural analysis by diffraction and microscopy methods difficult. Whereas NMR using nulear spins as local probes of composition, defects, and charge-carrier concentration can make important contributions to elucidating the structure of thermoelectric tellurides and establishing structure-property relations. NMR can characterize (i) the local chemical composition [130]/ various phases present (whether crystalline or amorphous), by observing isotropic chemical shifts [131, 132], heteronuclear correlation, and indirect effects of bonding to abundant quadrupolar nuclei such as Sb and Bi; (ii) the distribution of the charge-carrier concentration (whereas the Hall effect or thermopower provides only an average) [130, 133], according to the distribution of longitudinal relaxation and Knight shift [134–136]; (iii) the presence and composition of nanoinclusions via T_1 of matrix and inclusions, and spin diffusion; (iv) the local symmetry from anisotropic chemical shifts; and (v) the presence of abundant or dynamic defects in cubic structures by analyzing line broadening and anisotropic chemical

shifts. Particularly, NMR is unique to detect various types of disorder, often characterized by a distribution in observables like charge-carrier concentration or local composition.

One example, GeTe-based materials with ∼30% Ag+Sb on the Ge sublattice, the aformentioned TAGS (TAGS-x: $(GeTe)_x(AgSbTe_2)_{100-x}$), are among the highest-performance p-type thermoelectrics. Their p-type conductivity is due to vacancies on the cation sublattice, whose concentration can be varied via the Ge:Te ratio. Extremely high values of $p = 15\text{–}40 \times 10^{20} cm^{-3}$ from Hall effect measurements have been reported. [138, 139] However, the corresponding 6-

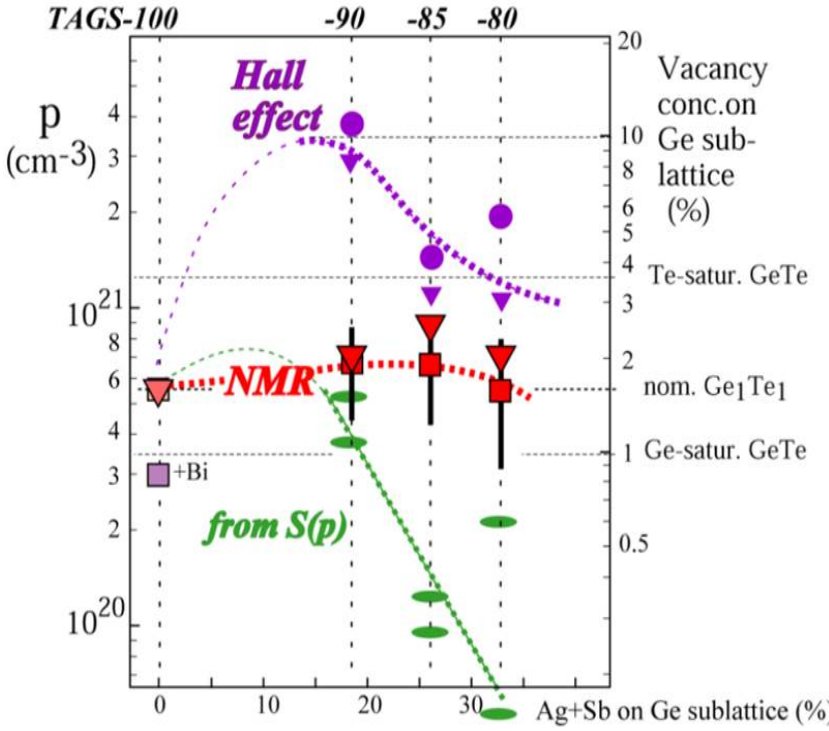

Figure 1.18 Red squares: Knight shift NMR data; red inverted triangles: T_1 NMR data from ref. [130, 137] purple circles: Hall-effect data of refs. [138, 139]; green ellipses: estimates obtained using the Seebeck S(p) curve of ref. [140]

fold increase in hole concentration from TAGS-100 (= GeTe) to TAGS-90 and gradual decrease to TAGS-80 (with 33% Ag+Sb on the Ge sublattice) is not reflected in the transport properties. Carrier concentration in TAGS-80 to TAGS-100 have been reassessed based on ^{125}Te NMR Knight shifts and spin-lattice relaxation [137]. The NMR data were calibrated using nominally stoichiometric GeTe, Te-rich GeTe, and TAGS-x with increased vacancy and carrier

concentration, and Bi-doped GeTe with reduced carrier concentration. NMR data indicate that the hole concentration in TAGS-90 and TAGS-85 is actually much lower than reported based on the Hall effect measurements, as shown in Fig. 1.18. For TAGS-90, it is about 5 times smaller than the previous Hall effect measurements, which would have corresponded to a high vacancy concentration of >16% on the cation sublattice. It also demonstrate how the carrier concentration in these complex thermoelectric materials can be tuned by doping with Te and Bi. This paves the way for a search of the optimum charge carrier concentration in TAGS materials.

In addition, distortions of the local lattice structure from the nominal cubic symmetry in SnTe, GeTe, and PbTe, have been observed by ^{125}Te chemical-shift anisotropy (CSA) measurements using broad-band recoupling approaches. Based on correlation with the density of charge carriers generated by vacancies, these CSAs of 10 – 200 ppm are attributed to distortive effects of vacancies on the cation sublattice, acting over multiple bonds. Doping with Na, I, Sb, Ge, etc. also produces local distortions at most Te sites in PbTe. The average distortion per defect (Sn/Ge/Pb-vacancy, Te-vacancy, or dopant) correlates with the maximum concentration of the defect.The distortions throughout the lattice appear to be larger than the rhombohedral lattice tilt in GeTe.

1.3.4 Motivation

Up to now, most of NMR works on tellurides thermoelectrics have been performed at room temperature. However, it is important to get insights of carrier concentration changes based on density of states of the band structure, and of the origin of the metallic conductivity, from the temperature dependence of the NMR shift (K) and nuclear spin lattice relaxation rate ($1/T_1$), Therefore, we investigated the electronic and magnetic properties of GeTe-based thermoelectrics in a wide temperature range ($4.3K - 294K$) using NMR, aiming to correlate with thermoelectric properties and eventually develop materials with enhanced figure-of-merit. As we report the NMR results in Chapter 5, we have found that two bands contribute to the physical properties of the materials based on the temperature dependence of the NMR shift and $1/T_1$. We also found that one band overlaps the Fermi level providing the metallic state

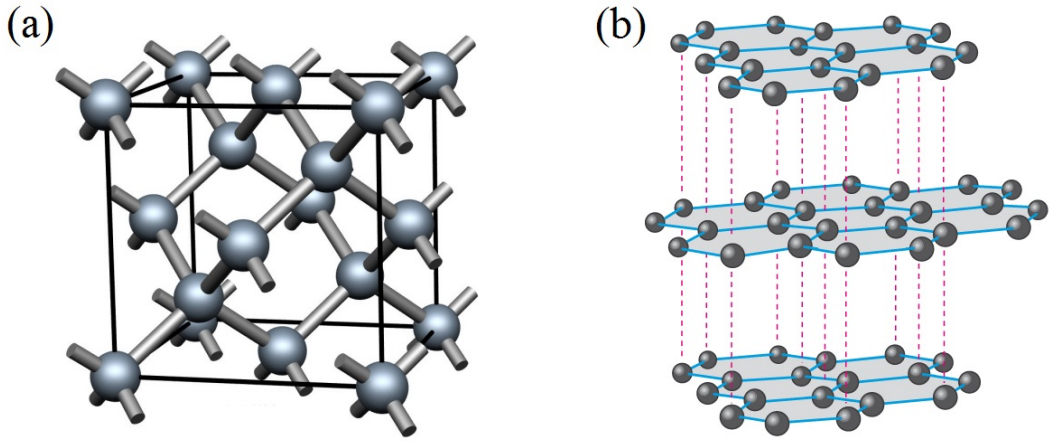

Figure 1.19 (a) Diamond (b) Graphite

without strong electron correlations, originating from the Ge vacancy. Furthermore, the other band is found to give rise to semiconductorlike properties, related to the fine structure of the density of states near the Fermi level.

1.4 Detonation Nanodiamond

Diamond is one of the well-known allotropes of carbon in nature, where carbons arrange themselves in sp^3 chemical bonds. Due to the incompressible C–C bonds and the three-dimensional stability of the tetrahedral bonding, diamond has a Mohs hardness of 10, harder than any other known materials. It is unaffected by chemical corrosion and can tolerate radiation and compressive forces. It also demonstrates higher electrical resistance and better thermal conductivity than any other solids at room temperature. Besides high strength and rigidity, diamond has the highest atom-number density of any material. [141] Fig. 1.19(a) gives the cubic lattice structural model of diamond where each atom bonds to four others tetrahedrally to form a 3-dimensional network. At pressures above 60 kbar, diamond is the thermodynamically stable form of carbon. [142] The density of diamond ranges from 3.15 to 3.53 g/cm^3, almost twice the density of graphite (Fig. 1.19(b)).

Nanodiamonds are characterised by nanometer scale particle sizes and have chemically inert cores and reactive, functionalized surfaces, which become more dominant with decreas-

ing particle size. Inherited the unique lattice structure of bulk diamond, nanodiamonds are of great interest of potential applications in energy storage [143], nanocomposites [144–148], catalysis [150, 151] and biomedicine [152–154] due to the possibility of sophisticated surface functionalization without compromising the superior properties of the diamond core.

1.4.1 Detonation synthesis of nanodiamond and purification

Nanodiamonds are produced in ton quantities by detonation approach. During this process, nanodiamond particles are formed from carbon atoms contained within the organic explosive molecules, such as a mix of TNT ($C_6H_2(NO_2)_3CH_3$) and hexogen ($C_3H_6N_6O_6$). The explosion takes place in an nonoxidizing atmosphere of either gas (N_2, CO_2 or Ar) or water/ ice. The product of detonation synthesis —detonation soot —contains a mixture of up to 80 wt% diamond particles [155, 156] 4–6 nm in diameter with graphitic carbons and impurities (metals and oxides) [156, 157] from metal debris of the detonation chamber and due to the incomplete combustion of the explosives.

Metallic impurities, which cause nanodiamond particles to agglomerate and degrades the stability of nanodiamond suspensions [158], are eliminated by an acidic treatment (e.g. concentrated HCl) while non-diamond carbon species are removed through liquid-phase oxidation prepared from high-boiling acids (e.g. $HClO_4$, H_2SO_4) with an addition of active oxidant (e.g. HNO_3, $NaClO_4$, CrO_3, $K_2Cr_2O_7$) or aqueous solutions of alkali (e.g. KOH, Na_2O_2). [159] However, these traditional ways of purification are hazardous and expensive, since the process is complicated to be conducted at high temperature and pressure and requires special equipment. [147] For example, poisonous chromium, resulting from multiple washings of nanodiamond from CrO_3 in sulfuric acid, need to be got rid of in biomedical application. Alternatively, air-oxidation at elevated temperatures has been introduced as a more environmentally friendly and less costly purification approach to remove non-diamond carbon [157,160], capable of increasing the diamond content from ∼25 wt% to >95 wt%. [147]

Nanodiamonds with sizes between 4 and 6 nm and their narrow size distribution are very attractive for nanotechnology.However, they tend to aggregate for reducing their high surface energy and the micro-sized agglomerates can withstand the standard ultrasonic treatment. This

property represents a severe obstacle for potential of nanodiamond in certain applications. To overcome this limitation, considerable deaggregation into individual primary particles have been developed. One of the most common techniques, bead-assisted sonic disintegration (BASD) [161, 162], uses ZiO_2 microbeads to crush the nanodiamond aggreates and yields stable single-digit nanodiamond colloidal solutions of individual particle 4–5 nm in diameter [163]. However, ZiO_2 is too hard to be crushed during milling or sonication and thus maintain their initial sizes during the deaggregation. In addition, bead materials get worn in this procedure, leaving behind debris contaminants and genarating graphitic layers on the nanodiamond surface that need additional strong base or acid to remove [164, 165].

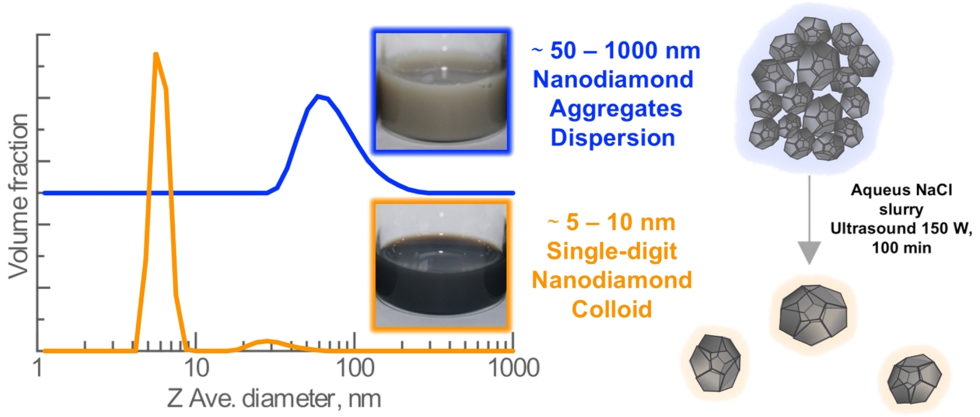

Figure 1.20 Particle size distribution before and after deaagregation of detonation nanodiamond using SAUD method. [166]

Recently, Turcheniuk et al. [166] demonstrated a salt-assisted ultrasonic deaggregation (SAUD) process, using sodium chloride (NaCl) crystals to produce nanodiamond colloids in water without difficult-to-remove impurities. In contrast of ZiO_2, NaCl can be completely washed out from the nanodiamonds due to its high solubility in water while providing sufficient hardness to destroy nanodiamond agglomerates. Particle size distribution and photographs of initial and SAUD nanodiamond aqueous dispersions are shown in Fig. 1.20. The nanodiamond slurries were subjected to ultrasound as the core aggregates disintegrated to form colloids of primary 5–10 nm nm particle.

1.4.2 Surface chemistry and modification

Surface of detonation nanodiamond can be modified by attaching many different functional groups without compromising the useful properties of the diamond core. [167] Introducing this feature of surface functionalization, which differenciates the nanodiamonds from other carbon-based materials (e.g. graphitic nanoparticles and carbon nanotubes), allows applications of nanodiamond in various fields. The nature of these groups, though, strongly influences the stability of the individual nanodiamond particles in solution and leads to agglomeration. It is therefore desirable to modify the surface of nanodiamond not only for adding functionalities but also to reduce or prevent aggregation of nanodiamond particles.

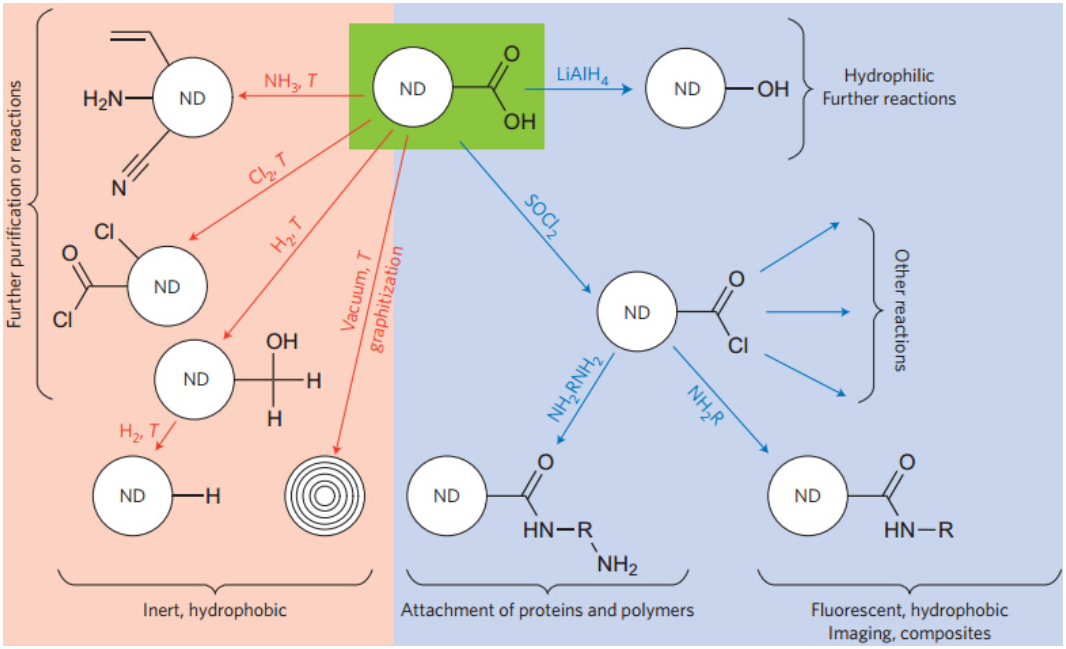

Figure 1.21 Different routes of nanodiamond surface modification. COOH-terminated nanodiamond (green) is a common starting material (produced by oxidation or ozone purification of nanodiamond). Red region: high-temperature gas treatments. Blue region: ambient-temperature wet chemistry treatments. [147]

Figure 1.21 presents various schemes for the surface modification of nanodiamond. Reaction of nanodiamond with gaseous ammonia (NH_3) results in the formation of a variety of different surface groups including NH_2, C≡N and C=N contained groups. [168, 169] Heating in chlorine (Cl_2) produces acylchlorides while fluorine (F_2) and hydrogen treatment forms C–F groups.

[170–172] Fluorinated nanodiamond can be further functionalized using alkyl-lithium reagents, diamines to produce C–N or C–C groups.

Nanodiamond can also be modified through surface graphitization by annealing in N_2, Ar or vacuum above 1300 °C to remove the functional groups and form carbon onions [173,174], which can act as an efficient lubricant [175] due to the microscopic ball-bearing action. The graphitic shells of nanodiamond can been further grafted of organic moieties using Diels-Alder reactions, where a stable C–C coupling of aromatic moieties with nanodiamond can be achieved. [176]

In addition to the gas treatment, wet chemistry are available as well to produce a wide range of surface groups to functionalize nanodiamonds as shown in Fig.1.21. Hydroxylated nanodiamond can react with silane-linker molecules to form an amine-terminated surface, which could be further covalently grafted with peptides, biotin or used as initiators/ monomers for polymerization. [154,177] For example, Li et al. [178] have attached a radical initiator to oxidized nanodiamond and initiated the growth of methacrylate monomers by atom transfer radical polymerization. Nanodiamonds are then terminated with methacrylate-based polymer brushes, which improved solubility and tailored hydrophilic/hydrophobic properties of the nanoparticle.

Nanodiamond provides numerous options for surface functionalization, the outcome, though, strongly depends on the purity and uniformity of the surface chemistry of the starting material. As mentioned before, the surface of sp^3 carbons must be either reconstructed into sp^2 carbons or stabilized through termination with functional groups. Therefore, in addition to size and shape, surface functionalization also affects the stability of nanodiamond particles. [179,180] So far, most of the characterization methods can only present qualitative data of surface groups. It is thus important to develop techniques for quantitative analysis, such as solid state NMR, of various surface groups of nanodiamond.

1.4.3 Structure and characterization

The exact nature of the structure of nanodiamond is under debate. It is necessary, however, to account for the shape of the particle, the presence of sp^2 carbons, and distinct surface functional groups. Fig. 1.22 (a) shows a transmission electron microscopy (TEM) image of detonation nanodiamond powder, containing diamond nanoparticles with an average size of

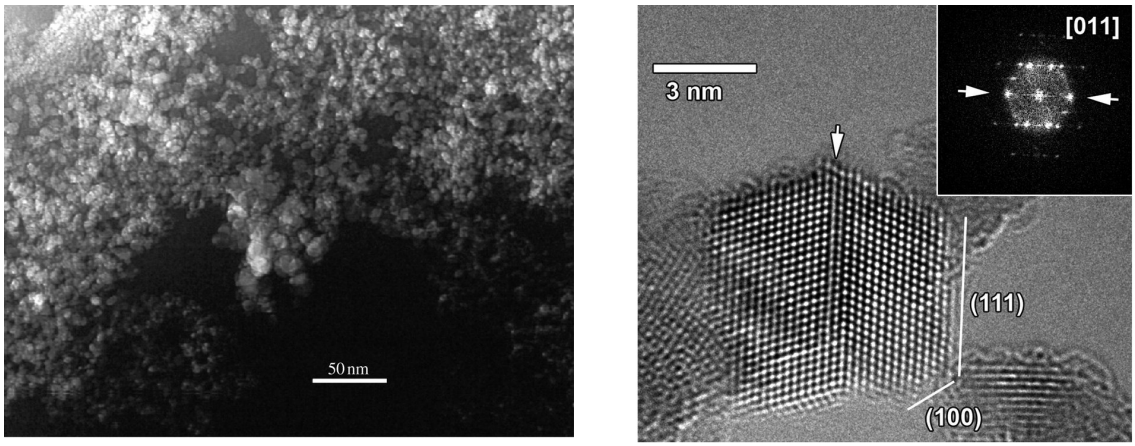

Figure 1.22 (a) TEM image of commercial 5nm detonation nanodiamond powder. [151] (b) HRTEM of nanodiamond from ozone purification showing the presence of a {111} twin plane indicated by an arrow. The main surface of particles show only a minimal presence of non-sp^3 carbon. [160]

5 nm, forming aggregates up to several micrometres in dimension though. Observations by neutron diffraction and high-resolution TEM (Fig. 1.22 (b)) show presence of twins and grain boundaries [160] and that the core of nanodiamond is built up of sp^3-bonded carbons, the former can be responsible for the broadening of the X-ray diffraction peaks that was earlier attributed to disordered sp^3 carbon. X-ray photoelectron spectroscopy (XPS) [181] shows other composition includes approximately 10–20% oxygen, and 2–3% nitrogen impurities. The small amount of nitrogen may either be present as surface NH_2 groups introduced during the acid washing stage, as shown by FTIR spectroscopy [182, 183] where nitrogen defects demonstrate two broad bands in the region of 1100–2500 cm^{-1}, or within the core of the nanodiamond particles, originating from the explosives.

Several models have been proposed based on experimental results or theoretical calculations. For examples, the "bucky-diamond" (Fig. 1.23(a)), where Raty et al. [184] claimed that a full single-layer graphitic, or a fullerene sheet, is formed on the surface of nanodiamond particle by applying ab initio calculations. Based on large-Q neutron diffractionmeasurements, another model [185] (Fig. 1.23(b)) was proposed where the sp^3 ordered diamond core, which has a lower compressibility, was surrounded by a shell of compressed diamond and a non-crystalline outer

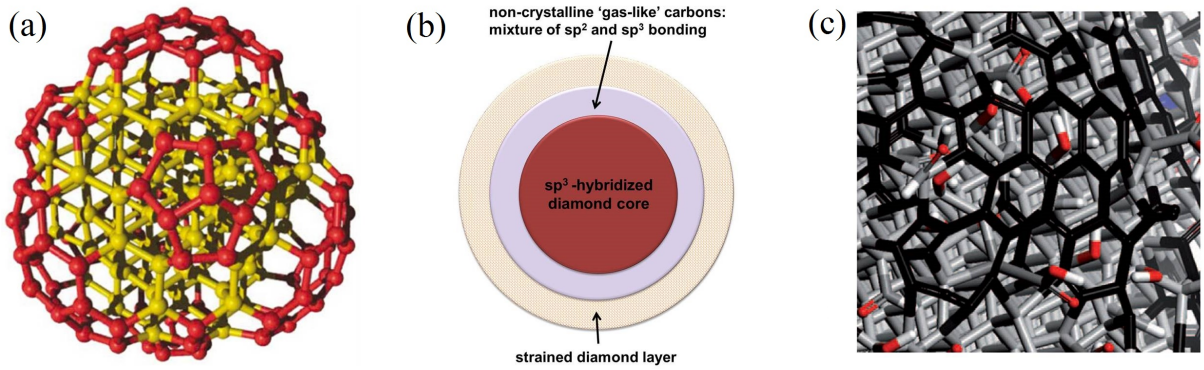

Figure 1.23 (a) Fully reconstructed, C275 cluster. Diamond core (yellow) and a fullerenelike reconstructed surface (red). [184] (b) Nanodiamonds have a pure sp^3-hybridized diamond core and gradually distorted outer layers and non-crystalline layers. [147] (c) Close-up views of two regions of the schematic model in ref. [185] of a single ∼5-nm nanodiamond after oxidative purification. The diamond core is covered by a layer of surface functional groups, which stabilize the particle by terminating the dangling bonds. (oxygen atoms are shown in red, nitrogen in blue). The sp^2 carbon (black) forms chains and graphitic patches. (c) is adapted from [185]

layer of 'gas-like' with a mixture of sp^2 and sp^3 carbons. Recently, Mochalin et al. [147] has proposed that nanodiamond consists of a pure sp^3-hybridized diamond core which is partially coated by aromatic shell with dangling bonds terminated by oxygen-containing groups, as shown in Fig. 1.23(c). This is similar to the commonly accepted "onion-shell" model [186], where a crystalline diamond core is coated by a fractal structure formed from a gradually distorted outer layers and graphite-like platelets. The ratio of sp^2 to sp^3 carbons, the thickness, and atomic arrangement of nanodiamond will depend strongly on the cooling conditions employed during synthesis. [187] This may explain the different sp^2 characters on the surface of nanodiamond observed by Auger, Raman and XPS spectroscopy. [191]

Depending on the purification methods used, the surface of detonation nanodiamonds can be terminated by a variety of functional groups, including hydroxyls, carboxylic groups, anhydride, ketones, and lactone moieties. [183,188–190] The characterization of nanodiamonds has involved various methods. In addition to the aforementioned transmission electron microscopic (TEM) and X-ray photoelectron, [157, 160, 362] vibrational spectroscopies [182, 183, 192, 193], such as FTIR and Raman, also provide insights into phase composition and surface terminations of

nanodiamonds. For example, absorption bands of C=O stretch (1720–1790 cm^{-1}), O–H stretch (1640, 3400 cm^{-1}) and C–H stretch (2,850–3,000 cm^{-1}) have been exhibited in IR spectra of the nanodiamond after oxidative purification.

One important feature to characterize is the distribution of unpaired electrons (paramagnetic centers) and their origin in the nanodiamond particles. NMR has been attempted because of the sensitivity of ^{13}C relaxation times to paramagnetic ions. Fang et al. [194] showed that unpaired electrons in nanodiamond with a diameter of ∼5 nm are mainly distributed within a disordered shell, at distances between 0.4 and 1 nm from the surface. Presti et al. [195] also investigated functionalized nanodiamond using electron paramagnetic resonance (EPR). They confirmed the unpaired electrons are centered on dangling bonds as well as a few nitrogen defects, and the nitrogen paramagnetic centers are mostly located in the disordered shell of nanodiamonds.

In the presence of paramagnetic centers, NMR shows shorter spin-lattice relaxation times of ∼150 ms and broadened spectra due to the hyperfine interaction of carbons with unpaired electrons. The broadening prevents the observation of nuclei distant by less than a few angstroms from paramagnetic centers. [196] The hyperfine coupling also decreases the efficiency of cross-polarization (CP), since the nucelar coherences decay faster and the coherence transfer is often ineffective in the presence of paramagnetic centers. [197, 198] However, NMR signal can be enhanced by transferring the high polarization of unpaired electrons to the nearby nuclei via hyperfine interactions. This polarization transfer in diamond has been achieved by dynamic nuclear polarization (DNP) [199–201], using continuous-wave or pulsed microwave (μw) irradiation near EPR frequency and by optical pumping with visible light of the electronic transition of nitrogen-vacancy (NV) centers. [202, 203]

1.4.4 Properties and application prospects of detonation nanodiamond

Detonation nanodiamond inherits most of the superior properties of bulk diamond and delivers them at the nanoscale. These properties include superior Youngs modulus and mechanical strength, high thermal conductivity and electrical resistivity, chemical stability and the resistance to harsh environments, optical properties and fluorescence. Besides, nanodiamond

exhibits ultra-dispersibility, solid-lubricating ability (which bulk and micronsized diamonds never have), high adsorption ability and biocompatibility. The present research and development trends of the detonation nanodiamond are as follows:

Mechanical applications. Purified nanodiamond provides enhanced tribological performance when dispersed alone or with polytetrafluoroethylene (PTFE) or metal nanoparticles in greases or oils [204]. Lubricants containing a few percent of detonation nanodiamonds decreases fuel consumption of ships, aircraft, and automobiles up to 8% and makes engines last longer. [156]

By dispersing the purified and well-dispersed nanodiamond into polymers, metals and ceramics, new nanocomposite with improved mechanical strength [144, 148, 149, 205], thermal conductivity [144,145], adhesion [206], electromagnetic shielding [146] and wear resistance [207] can be obtained.

Electrical and electrochemical applications. Nanodiamond additives have been used for electrolytic and electroless metal plating for many years. [156] More recently, they have been used as a seeding material for chemical vapour deposition (CVD) synthesis of nanocrystalline diamond films. [160] Nanodiamond films can be coated on the electrode and surface-modified with glucose oxidase for semiconductor device applications. Undoped non-conducting nanodiamond also demonstrates redox activity in electrochemical systems. [151] Furthermore, detonation nanodiamond has been considered as qubits for quantum computing [209] due to the presence of nitrogen-vacancy (NV) defect center —a nitrogen atom next to a vacancy, which has an $S = 1$ spin ground state that can be spin-polarized by optical pumping and a long spin coherence time.

Biomedical applications. The detonation nanodiamond combined many required assets for biomedical applications: biocompatibility, surface chemistry allowing both covalent and non-covalent grafting, stable core, tunable size (from 100 nm down to 5 nm) and extremely low cytotoxicity. The aforementioned NV centers leads to useful fluorescence properties of nanodiamonds. Fluorescent nanodiamonds can act as biomarkers for tumor imaging or tracking as a non-toxic alternative of semiconductor quantum dots. [153,210] Nanodiamond functionalized by drugs elements is a promising candidate for targeted drug delivery systems and disease di-

agnostics. [211–214] Applications in biomedical technology is expected to advance considerably in the near future.

1.4.5 Motivation

Many challenges remain in fundamental questions and applications for nanodiamonds. In terms of chemical reactivity and interparticle interactions, the composition of the surface is clearly most important. [215] The structure of the diamond surface also has major effects on friction [216, 217] and surface conductivity [218, 219]. For example, do they have a fullerenic ("bucky-diamond") [184, 220] or disordered graphitic surface as has been widely concluded? [186, 191, 221, 222, 227–229] Is there an amorphous graphitic component, [223, 224] or are they fully sp^3-hybridized with a hydrogenated surface? [225, 226] Are there dangling bonds at the surface? [227] Are there many OH groups at the diamond surface, [216, 217] or is the O-H vibration in Raman spectroscopy just from adsorbed water? [226] Is the nitrogen at the surface or in the core? [162, 220] Is the diamond lattice distorted? [228] Better understanding of their structure and surface chemistry will lead to greater control over their properties, and also help to solve the problems in potential practical applications.

Previous NMR studies have touched on some of these issues, [227, 230, 231] but we will show that important spectral features have not been attributed correctly and several proposed conclusions have to be revised. For example, earlier ^{13}C NMR analyses of detonation nanodiamond [194,227,230–235] did not identify the aromatic-carbon signal and signals of C=O groups seen in XANES and IR spectra were not detected. Most importantly, the surface and structure model of detonation nanodiamond is still a matter of an ongoing debate. Models with more than 40% of the particle surface covered by an aromatic shell, containing $>$ 10% of all carbon atoms, are still being put forward. [147, 150]

In Chapter 6, we show that NMR can detect and quantify small amount of sp^2-hybridized carbons in nanodiamond, and that sp^2 surface carbon (C=O, COO, and aromatic carbons) has a fraction of up to 2.4 $\pm$ 0.5% of all carbon atoms. In Chapter 7, we analyzed air-oxidized nanodiamond using ^{13}C NMR spectra editing and long-range $^{13}C\{^1H\}$ dephasing. The signal of carbon bonded to nitrogen has been observed selectively based on the breaking of the lo-

cal symmetry and the resulting increased chemical-shift anisotropy. Signals from carbons at different depths from the surface have been observed selectively through modified $^{13}C\{^1H\}$ rotational echo double resonance (REDOR) experiments, and their quantities estimated. We confirmed the NMR-based model based on the quantification of functional groups on surface, shell and core of nanodiamond. Our accurate analysis of the surface composition of nanodiamond particles will be useful for guiding rational functionalization of nanodiamond materials.

CHAPTER 2. BASICS OF NUCLEAR MAGNETIC RESONANCE

2.1 Overview

The first successful observation of NMR signals in the condensed phase was reported by Purcell and Bloch on probing protons in paraffin wax and water. [236–238] NMR has rapidly evolved to become a powerful, versatile analytical technique applied in different fields of fundamental science as well as in medicine and industry. It is capable of probing nearly any state of matter, as far as the nuclei has non-zero spin (I $\neq$ 0) present, thus allows researchers to see the otherwise invisible world with traditional characterization methods. Generally, chemists apply regular NMR spectroscopy in liquid state to characterize, for example, compounds and to control chemical reactions, where the nuclear dipole-dipole interaction is motionally averaged resulting in extremely narrow resonance lines. On the other hand, in the solid molecular systems and composites, the NMR line shapes can be quite broad due to dipolar, quadrupolar, and magnetic interactions of the nuclei with their surroundings. Particularly, in strongly correlated electron materials, these interactions make NMR a low energy technique for probing the static and dynamic electronic and magnetic properties microscopically.

Some of the most useful features of NMR include: (i) bulk probe that investigates the entire sample, barring of course penetration depth problems for conducting or even superconducting systems; (ii) non-destructive since only radio frequency (rf) pulses are employed (with frequencies from $\sim 10^1$ to $\sim 10^3$ MHz and average powers typically well below $0.1mW$); (iii) site-selective and sensitive, providing the structural detail from the atomic scale to a range of tens of nanometers, that is over two orders of magnitude in length scale; (iv) capable of probing magnetic (for $I > 0$) and electric (for $I > 1/2$) properties. (v) quantitative, as the integrated areas of a NMR signal is proportional to the actual fractions of nuclei investigated;

There are abundant literatures for thorough introduction to NMR. [239–241] This chapter will be limited to an outline of basic concepts and principles, with some more elaboration on the particulars of the NMR of quadrupolar nuclei ($I > 1/2$) that are relevant for this work.

2.2 Nuclei in the External Magnetic Field

When an isolated nucleus with magnetic moment $\vec{\mu} = \gamma_N \hbar \vec{J}$ (where $\vec{J}$ is the angular momentum of the magnetic moment, γ_N is the gyromagnetic ratio) is exposed to an external magnetic field $\vec{H}_0$, the field will induce a torque on the magnetic moment $\vec{\mu}$. The magnetic moment will obey the equation of motion:

$$\tau = \frac{d\vec{J}}{dt} = \vec{\mu} \times \vec{H} \tag{2.1a}$$

$$\frac{d\vec{\mu}}{dt} = \vec{\mu} \times (\gamma_N \hbar \vec{H}) \tag{2.1b}$$

which indicates that the nuclear moment $\vec{\mu}$ precesses around $\vec{H}$ at a constant frequency $\omega = -\gamma_N \vec{H}$. In NMR experiments, the external magnetic field is generally assumed to be oriented along the z direction, $\vec{H} = H_0 \hat{z}$, and the corresponding precession frequency is called the Larmor frequency ω_0. Therefore, for a nucleus with gyromagnetic ratio γ_N in a fixed magnetic field:

$$\omega_0 = -\gamma_N H_0 \tag{2.2}$$

To conveniently describe the NMR experiments, the so-called rotating frame of reference is usually employed. For the observer in the laboratory frame, the coordinates of the rotating frame are rotating with the Larmor frequency, in the same sense. Thus, the precessing motions of the nuclear magnetic moments are frozen in the rotating frame, if only an external magnetic field is applied.

While it is possible to glean a great deal of understanding from the above classical treatment of NMR, quantum mechanically one can explain the same in the following manner. For an isolated nulear spin in a static, homogenous magnetic field, the response of the spin can be described by Zeeman interaction, Hamiltonian $\mathcal{H}$ is then given by:

$$\mathcal{H}_Z = -\vec{\mu} \cdot \vec{H}_0 = -\gamma_{\rm N} \hbar \hat{I} \cdot \vec{H}_0 \tag{2.3}$$

where $\hat{I} = \hat{x}I_x + \hat{y}I_y + \hat{z}I_z$, is the nuclear spin operator. In the simplest case we consider the static field is applied along the $\hat{z}$-direction, i.e., $\vec{H}_0 = H_0\hat{z}$, then the interaction Hamiltonian can be written as :

$$\mathcal{H}_Z|m\rangle = -\gamma_{\rm N}\hbar H_0 I_z|m\rangle = E_{\rm m}|m\rangle \tag{2.4}$$

The energies of the nuclear spin states are given by the eigenvalues of the Hamiltonian $E_{\rm m} = \gamma_{\rm N}\hbar H_0 m$. In this situatioin there are $(2I+1)$ non-degenerate energy levels corresponding to the $(2I+1)$ values of $m = -I, -I+1, .., I-1, I$.

The NMR resonances we observed correspond to allowed transitions between these energy levels, i.e., between these eigenstates ($|m\rangle$), labeled by the quantum number m. These transitions can be induced by radio frequency (rf) magnetic field. Such transitions will be governed by the Bohr frequency condition, whereby energy is transferred when ΔE, the gap between the energy levels, is equal to the frequency of the radiation. Thus for NMR transitions between eigenstates $|m\rangle$ and $|m'\rangle$ of a single nucleus,

$$\Delta E = E_{\rm m} - E_{\rm m'} = \omega_{m,m'} = \gamma_{\rm N}\hbar H_0 \Delta m \tag{2.5}$$

The selection rule governing such transitions is $\Delta m = \pm 1$, meaning only $m' = m \pm 1$ satify a non-zero transition probability ensuring the occurence of the transition [239], so Eqn.(2.5) reduces to

$$\Delta E = \omega_{m,m'} = \gamma_{\rm N}\hbar H_0 \tag{2.6}$$

Consider the simplest case $I = 1/2$, the two states are $|-1/2\rangle$ and $|1/2\rangle$ with quantum numbers $m = -1/2$ and $1/2$ respectively. Transitions are possible between these two states $|-1/2\rangle \leftrightarrow |1/2\rangle$ with an exchange of energy $\Delta E = E_{|-1/2\rangle} - E_{|1/2\rangle}$. We will observe a resonant frequency of $\omega_0 = \gamma_{\rm N} H_0$ as shown in Fig. 2.1.

2.3 Nuclear Spin Hamiltonian

The Zeeman interaction of a lone nuclear spin with an applied external field is the dominant part of the Hamiltonian. However, the Zeeman interaction term alone is not sufficient to de-

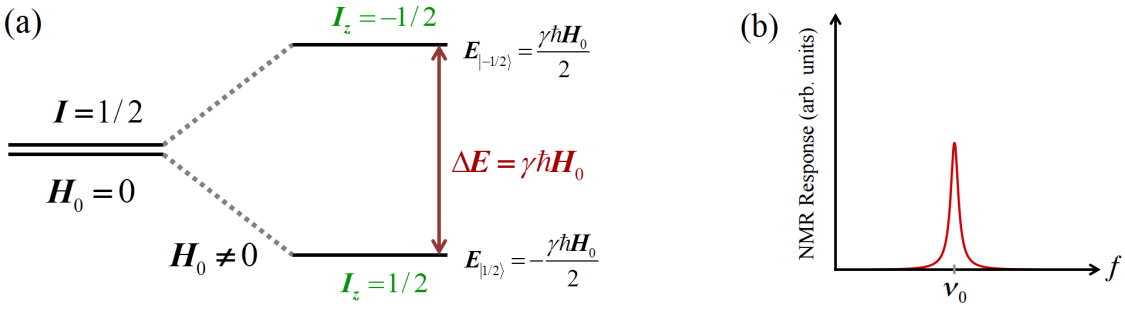

Figure 2.1 (a) Zeeman energy levels for $I = 1/2$ with $\nu_0 = \gamma_N H_0/2\pi$. (b) The corresponding NMR response of the system as a function of frequency.

scribe the physical arrangement, spin polarization, and dynamics of the electrons in condensed matter systems. It is thus vital to investigate the influence of the surrounding electrons on the nuclear energy levels.

2.3.1 Hyperfine interaction

Interaction of a nucleus spin with the surrounding electrons, referred to as the hyperfine interaction:

$$\mathcal{H}_{hf} = \gamma_N \hbar \hat{I} \cdot \mathbb{A} \cdot \hat{S} \tag{2.7}$$

where $\mathbb{A}$ is the hyperfine coupling tensor and $\hat{S}$ is the electron spin operator. This general form can be broken down into contact, dipolar, and orbital terms, as shown below:

$$\mathcal{H}_{hf} = \hbar\gamma_N g\mu_B \cdot \left[\frac{8\pi}{3}\delta(\vec{r})\hat{I}\hat{S} - \left(\frac{\hat{I}\hat{S}}{r^3} - 3\frac{\hat{I}\cdot\vec{r}(\hat{S}\cdot\vec{r})}{r^5}\right) + \frac{\hat{I}\vec{L}}{r^3}\right] \tag{2.8}$$

where μ_B is the Bohr magneton, g is g-factor of the electron spin, $\hat{L}$ and $\hat{S}$ are the orbital and the spin angular momentum of the electrons, respectively. The Fermi contact interaction term arises from unpaired s electron states which have a non-zero probability of being found at the nucleu (i.e., have a finite wavefunction at $r = 0$). The dipolar term describes the interaction between the nuclear and the electronic spin moments, if these two are at a finite distance from each other, typically prevalent in case of p- and d-electrons; however it is often neglected since its contribution is much smaller than the other two terms. This term is responsible for the anisotropic Knight shift K_{aniso} in absence of cubic symmetry and at times even at cubic sites

if spin-orbit coupling is present. The orbital term represents the magnetic interaction between the nuclear spin $\hat{I}$ and the electronic orbital angular momentum $\vec{L} = \vec{r} \times \vec{p}$. In some transition metals this term can be important, but in most cases $\vec{L}$ is generally quenched.

2.3.1.1 Knight Shift

If we just consider s-state electrons, only the Fermi contact term will survive after taking an average over the electron wave function. Assuming the external field ($H_0 = \nu_0/\gamma_N$) is along the z direction, the effective Fermi contact interaction can be written as

$$\mathcal{H}_{Fermi} = -\gamma_N \hbar I_z \frac{8\pi}{3} \langle |\psi_s(0)|^2 \rangle_{FS} \chi_p H_0 \tag{2.9}$$

where χ_p is the Pauli paramagnetic spin susceptibility per atom, $\psi_s(0)$ is the Bloch wavefunction measured at the site of nucleus and $\langle |\psi_s(0)|^2 \rangle_{FS}$ is the probability density of electron wavefunctions averaged over the Fermi surface. [242] This energy can be treated as a small perturbation ($\Delta\vec{H}$) of the external field and will lead to a small resonance frequency shift. The total effective field at the nucleus sums to $\vec{H}_{eff} = \vec{H}_0 + \Delta\vec{H}$. Knight shift ($\mathcal{K}$), measures this effective field at the nucleus,

$$\mathcal{K} \equiv \frac{\Delta H}{H_{eff}} \tag{2.10}$$

In metallic systems, the main contribution of Knight shift comes from the hyperfine interaction of the conduction electrons in contact with the nuclei, according to the theory first proposed by Townes, Herring and Knight [243, 244], is given by

$$\mathcal{K}_{Fermi} = \frac{8\pi}{3} \langle |\psi_s(0)|^2 \rangle_{FS} \chi_p \tag{2.11}$$

In addition to this, there is contribution from the orbital magnetic moment of the conduction electrons [245]:

$$\mathcal{K}_{orb} = 2\chi_{orb} \langle \frac{1}{r^3} \rangle \tag{2.12}$$

and also a diamagnetic contribution [246] :

$$\mathcal{K}_{dia} = \frac{8\pi}{3} \chi_{dia} \tag{2.13}$$

where χ_{orb} and χ_{dia} are the orbital and the diamagnetic contributions to the magnetic susceptibility. The T dependence of the total Knight shift might change sign depending on the

magnitude and sign of the different contributions. The anisotropic component in the Knight shift, which is present in case of nucleus in non-cubic symmetry, does not contribute to the shift of the centroid of the NMR resonance. [242]

For a Fermi gas of noninteracting spins,

$$\chi_p = \frac{1}{2}\gamma_e^2\hbar^2\rho(E_F) = \frac{1}{2}g^2\mu_B^2\rho(E_F) \tag{2.14}$$

where $g \approx 2.00$ is the spectroscopic splitting factor (g-factor) of the electron spin and μ_B is the Bohr magneton. Also the nuclear spin-lattice relaxation rate $1/T_1$ (to be discussed in the next section) for metallic materials with substantial s-character in the wavefunction at the Fermi surface, is given by, [239]

$$\frac{1}{T_1} = \frac{64}{9}\pi^3\hbar^3\gamma_e^2\gamma_N^2 \ \langle|\psi_s(0)|^2\rangle_{FS}^2\rho^2(E_F)k_BT \tag{2.15}$$

where $\rho(E_F)$ is the density of states at the Fermi energy for one spin direction. Therefore, for metallic systems, where conduction electrons will control the relaxation mechanism and only electrons at the Fermi level be considered, we can derive following relation from the Fermi contact interaction, combining eqns.(2.11), (2.14) and (4.4):

$$\mathcal{K}^2T_1T = \frac{\hbar}{4\pi k_B}\frac{\gamma_e^2}{\gamma_N^2} = S \tag{2.16}$$

where γ_e is the electron gyromagnetic ratio and k_B is the Boltzmann constant. This equation is known as the *Korringa relation*. [247] The ratio $S/(\mathcal{K}^2T_1T)$ is known as the *Korringa ratio*, which be affected by a number of sources, such as electron-electron interactions, and exchange enhancement. For an uncorrelated electron system (fermi liquid), the ratio is one. For anti-ferromagnetic correlations when $\vec{q} \neq 0$ fluctuations are dominant, this ratio is greater than 1 and for ferromagnetic correlations, the ratio is less than one. Therefore, Korringa ratio plays an important role in determining the nature of spin fluctuations in a metallic system. We will discuss in detail of Korringa ratio analysis in Ca122 system in Chapter 4.

Conduction electrons cause a change in the effective field as seen by the nucleus through the hyperfine interaction. In the tensor notation:

$$\mathcal{K}_{\alpha\alpha}(\equiv \mathcal{K}_\alpha) = \frac{H_{hf,\alpha\alpha}}{N_A\mu_B}\chi_{\alpha\alpha} \tag{2.17}$$

where $H_{hf,\alpha\alpha}$ is the hyperfine field at the nucleus, α is assumed to be along one of the principal axes of the hyperfine field tensor. This equation is widely used to estimate the hyperfine field from the $\mathcal{K} - \chi$ plot.

2.3.2 Quadrupole interaction

While a nucleus with a magnetic moment interacts with the magnetic field via the Zeeman interaction, a nucleus with $I > 1/2$ also possesses a finite electric quadrupole moment Q, and can interact electronically with electric field gradient created by the electronic charges.

A nucleus with the positive charge distributed in the shape of a ellipse will naturally orient as shown in Fig. 2.2(a). It is perpendicular to the direction of the external positive charge —attracted to the negative charges and repelled by the positive charge, due to electrostatic force. The charge distribution is no longer spherical, giving rise to a electric field gradient (EFG) which is responsible for the finite Q. The phenomenon is named nuclear quadrupole interaction and is able to probe the local electronic structure of a material directly.

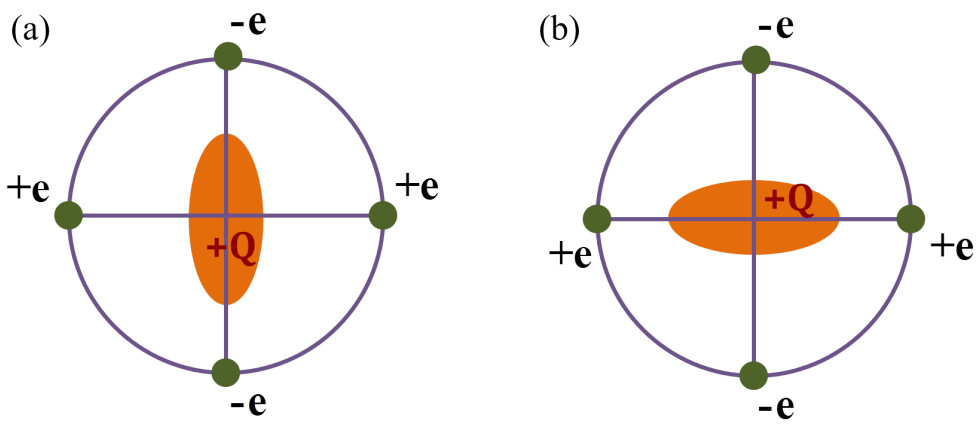

Figure 2.2 Illustration of electric quadrupole moment residing in a location with a non-zero EFG

The quadrupolar interaction results in the shift of the otherwise equidistant energy levels. Fig. 2.2(a) would be in a lower energy state compared to the Fig. 2.2(b). This shift is proportional to the square of the quantum number m. Thus for nucleus with $I = 3/2$, the energy states with $m = \pm 1/2$ shift identically and those with $m = \pm 3/2$ shift identically, as

shown in Fig. 2.3 (a). The energy difference can be measured via nuclear quadrupole resonance (NQR), with zero applied field, as shown in Fig. 2.3 (c). The electric quadrupole moment Q can interact with electric field to produce a change in the energy levels in addition to the Zeeman effect, as shown in Fig. 2.3 (b, d).

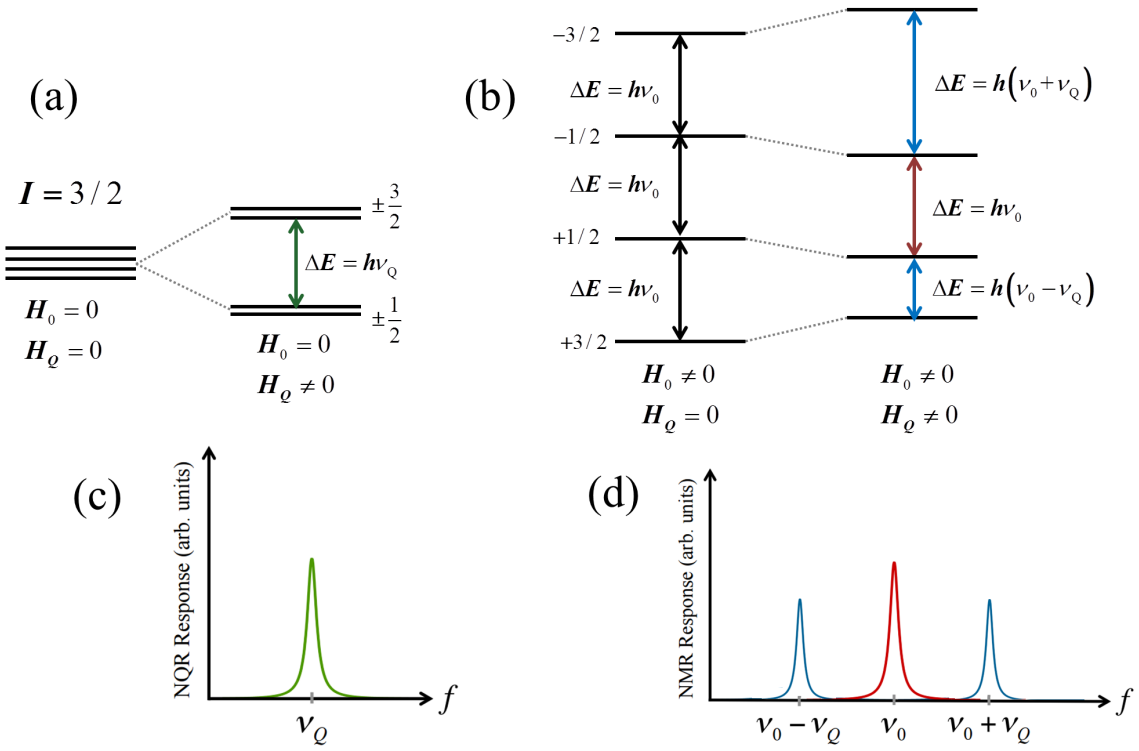

Figure 2.3 Exemplifying scheme of energy levels (a, b) and corresponding spectra (c, d) for nucleus with $I = 3/2$ spin. (a) Degeneracy of energy levels at zero applied field altered by the presence of EFG; (b) NMR (applied field $H_0 = 2\pi\nu_0/\gamma$) energy levels and allowed transitions with a non-zero EFG at the nuclear site; corresponding NQR (c) and NMR (d) responses as a function of frequency.

Formally, the electrostatic energy of a charge distribution can be expressed as:

$$E_Q = \int \rho(\vec{r})V(\vec{r})d\tau \tag{2.18}$$

where $\rho(\vec{r})$ is the charge density, $V(\vec{r})$ is the electrostatic potential, $d\tau$ is an element of volume. If we introduce the quadrupole tensor $Q_{a,b}$,

$$Q_{a,b} = \int (3x_a x_b - \delta_{ab} r^2)\rho d\tau \tag{2.19}$$

where $Q_{a,b} = \delta^2 Q/\delta x_a \delta x_b$ and a and $b \equiv x, y$ and z, and with the condition that V satisfies the Laplaces equation ($\nabla^2 V = 0$), it can be shown that the quadrupole energy is given by:

$$E_{\mathrm{Q}}^{(2)} = \frac{1}{6}\sum_{a,b} V_{a,b} Q_{a,b} \tag{2.20}$$

where $V_{\mathrm{a,b}} = \delta^2 V/\delta x_a \delta x_b$. Thus, if nucleus is in a cubic environment $V_{XX} = V_{YY} = V_{ZZ}$ and with $\nabla^2 V = 0$, the quadrupole interaction would vanishes. [239]

Quantum mechanically, the quadrupole operator $\hat{Q}_{a,b}$ for a point charge e, will then be defined as,

$$\begin{aligned}\hat{Q}_{a,b} &= \int (3x_{ab} - \delta_{ab} r^2)\hat{\rho}(\vec{r}) d\tau \\ &= e\sum_{\mathrm{k}} \int (3x_a x_b - \delta_{ab} r^2)\delta(\vec{r} - \vec{r}_k) d\tau \\ &= e\sum_{\mathrm{k}} (3x_a x_b - \delta_{ab} r^2)\end{aligned} \tag{2.21}$$

where k is the number of protons since neutrons have 0 charge. Thus, the contribution of the quadrupole interaction in the Hamiltonian is:

$$\mathcal{H}_{\mathrm{Q}} = \frac{1}{6}\sum_{a,b} V_{a,b}\hat{Q}_{a,b} \tag{2.22}$$

Thus, from eqns. (2.21) and (2.22), we have,

$$\mathcal{H}_{\mathrm{Q}} = \frac{eQ}{4I(2I-1)}[V_{ZZ}(3I_z^2 - I^2) + (V_{XX} - V_{YY})(I_x^2 - I_y^2)] \tag{2.23}$$

With introduction of two quantities η and q [239] such that

$$\text{Electric field gradient} : eq \equiv V_{ZZ} \tag{2.24a}$$

$$\text{Assymetry parameter} : \eta \equiv \frac{V_{XX} - V_{YY}}{V_{ZZ}} \tag{2.24b}$$

The subscripts X, Y, and X correspond to the principal axes of the EFG in the crystalline basis. The nuclear quadrupole Hamiltonian is given by:

$$\mathcal{H}_{\mathrm{Q}} = \frac{e^2 qQ}{4I(2I-1)}[3I_z^2 - I^2 + \eta(I_x^2 - I_y^2)] \tag{2.25}$$

A good example would be ^{75}As nucleus with $I = 3/2$. We expect a single resonance in zero field as shown in Fig. 2.3 (c). Upon application of an external field, the nuclear spin energy

levels will lose all degeneracy, resulting in three resonances (Fig. 2.3 (d)). These are referred to as the central resonance ($m = +1/2 \leftrightarrow -1/2$), the upper satellite ($m = +3/2 \leftrightarrow +1/2$), and the lower satellite ($m = -1/2 \leftrightarrow -3/2$). And corresponding nuclear quadrupole frequency is $\nu_Q = \frac{e^2qQ}{4I(2I-1)}\sqrt{1+\frac{\eta^2}{3}}$. Only states that differ in angular momentum of one are allowed by the selection rules due to conservation of angular momentum of the nuclear spin and the photon (of spin 1).

2.4 Relaxation Phenomena

Dynamical properties of condensed matter systems can be gained from the study of its nuclear relaxation mechanisms with nuclei serving as a local probe of the electron spin dynamics. The relaxation of the nuclear system following population inversion by a radio frequency pulse can probe the density of electron states, spin fluctuations above a magnetic phase transition, and spin wave excitations in the magnetically ordered state. Since NMR can probe the density of states at the fermi energy, it is also a powerful tool for studying the symmetry of the energy gap in superconducting materials. [3, 64, 248, 249] In fact, the Hebel-Slichter peak in the spin-lattice relaxation rate just below the superconducting transition temperature is predicted to occur due to the coherence factors in the BCS theorys. [3] The relaxation processes are the spin-lattice relaxation, longitudinal to applied field $\vec{H}_0$ and characterized by the time constant (T_1), and the spin-spin relaxation, transverse to $\vec{H}_0$ and characterized by the time constant (T_2).

2.4.1 Bloch equations

In 1964, F. Bloch proposed a set of phenomenological equations to describe the behavior of nucleus in the presence of external magnetic field. Bloch's approach was macroscopic and classical, which is complementary to the use of a spin Hamiltonian. It mainly concerns with dynamic processes and lineshapes. In the following discussion, the sample is assumed to contain many identical nucleus, and the total magnetic moment or magnetization $\vec{M}$ is the resultant of the nuclear moments $\vec{\mu}$.

The classical motion of the nuclear magnetization for an ensemble of spins is given below, similar as that of nuclear moments discussed in (2.1):

$$\frac{\mathrm{d}\vec{M}}{\mathrm{d}t} = \gamma\vec{M} \times \vec{H}_0 \tag{2.26}$$

Bloch assumed that the components of $\vec{M}$ decay to $\vec{M}_0$ (nuclear magnetization in equilibrium) exponentially, but he allowed the components of $\vec{M}$ parallel and perpendicular to $\vec{M}_0$ to decay with different time T_1 and T_2, so that with the z axis chosen along $\vec{H}_0$:

$$\frac{\mathrm{d}M_z}{\mathrm{d}t} = -\frac{M_z - M_0}{T_1} \tag{2.27a}$$

$$\frac{dM_x}{dt} = -\frac{M_x}{T_2} \quad \text{and} \quad \frac{dM_y}{dt} = -\frac{M_y}{T_2} \tag{2.27b}$$

where T_1 and T_2 is the longitudinal and transverse relaxation time, respectively, emphasizing the relatioship of M_z and the applied field.

In the NMR experiment, an small oscillating rf field in addition to the static field, is applied such that there is a finite component of nuclear magnetization at right angles to the static field. Combining the effects of static field and a rf field together we obtain:

$$\frac{dM_{x,y}}{dt} = \gamma(\vec{M} \times \vec{H})_{x,y} - \frac{M_{x,y}}{T_2} \tag{2.28a}$$

$$\frac{dM_z}{dt} = \gamma(\vec{M} \times \vec{H})_z - \frac{M_z - M_0}{T_1} \tag{2.28b}$$

where $\vec{H}$ is total field (static and rf field). The approach to thermal equilibrium is known as relaxation and T_1 and T_2 are relaxation times. The decay of the longitudinal component (M_z) differ from the decay of the transverse components (M_x and M_y). We will discuss the relaxation characterizing these two types of decays in the following sections.

2.4.2 Nuclear spin-lattice relaxation rate $(1/T_1)$

The spin-lattice relaxation rate T^{-1} characterizes the interaction of the spin system with the exterior (the 'lattice') which functions as a 'heat-bath' in the thermodynamic sense, allowing for an energy exchange with the spin system and thereby establishing a thermodynamic equilibrium.

As discussed before, for $I = 1/2$, under a static magnetic field H_0, the two adjacent nuclear energy levels with populations $N_\uparrow$ and $N_\downarrow$ are separated by $\Delta E = \gamma_{\rm N}\hbar H_0$. The equilibrium state is described by Boltzmann-statistics, where the nuclei would distribute themselves in the two energy levels such that the ratio of their population will be,

$$\frac{N_\downarrow}{N_\uparrow} = \exp(-\frac{\Delta E}{k_{\rm B}T}) \tag{2.29}$$

At equilibrium, with more number of nuclei in the lower energy level ($N_\uparrow$), there is a net equilibrium nuclear magnetization of a spin-system of $N_{\rm A}$ nuclear spins along the applied field direction, given by the Curie Law,

$$M_0 = M_{0z} = H_0\frac{\hbar^2\gamma_N^2 I(I+1)N_{\rm A}}{3k_{\rm B}T} \tag{2.30}$$

This macroscopic magnetization M_0 is essentially what NMR probes, indicating that the NMR signal intensity is not only field- but also temperature-dependent.

2.4.2.1 T_1 in terms of dynamical susceptibility

The fluctuations in the hyperfine field produce nuclear relaxation making transition between adjacent nuclear levels. Generally, $1/T_1$ can be expressed in terms of correlation fuction of fluctuating hyperfine fields.

$$\frac{1}{T_1} = \frac{\gamma_N^2}{2}\int_{-\infty}^{\infty}\left\langle\{H_{hf}^+(t),\ H_{hf}^-(0)\}\right\rangle\exp(i\omega_0 t) \tag{2.31}$$

where $\omega_0 = \gamma_N H_0$ is the Larmor nuclear frequency, $\{PQ\} = (PQ + QP)/2$ and $\langle..\rangle$ is the time average. The bilinear coupling Hamiltonian between the nuclear spin $\vec{I}$ at $\vec{r} = 0$ and the electronic spin $\vec{S_i}$ at the electronic site $\vec{r} = \vec{r_i}$ is given by,

$$\mathcal{H}_{hf} = \sum_i \hat{S}_i \cdot \mathbb{A} \cdot \hat{I} = \sum_i\sum_{\alpha\alpha'} S_{i,\alpha}\mathbb{A}_{\alpha\alpha'}(\vec{r_i})I_{\alpha'} \tag{2.32}$$

where $\alpha, \alpha' \equiv x, y, z$, $\mathbb{A}$ is the hyperfine coupling tensor and $\sum_i$ runs over all the neighboring electronic spin sites. In terms of the hyperfine field H_{hf}, the Hamiltonian $\mathcal{H}_{hf}$ is :

$$\mathcal{H}_{hf} = -\gamma_N\hbar\hat{H}_{hf}\cdot\hat{I} = -\gamma_N\hbar\sum_\alpha H_{hf,\alpha'}I_{\alpha'} \tag{2.33}$$

Combining the above equations, $1/T_1$ can be expressed in terms of the electronic spin-spin correlation function perpendicular to the applied magnetic field,

$$\frac{1}{T_1} = \frac{1}{2\hbar^2} \sum_i \sum_\alpha \sum_{\alpha' \equiv x,y} \mathcal{A}^2_{\alpha\alpha'}(\vec{r_i}) \int_{-\infty}^{\infty} \left\langle S^+_{i,\alpha}(t) S^-_{i,\alpha}(0) \right\rangle \exp(i\omega_0 t) \tag{2.34}$$

In electronic systems, the fluctuation-dissipation theorem [250] is used to relate the spin-spin correlation function to the spin susceptibility. Therefore, eqn. (2.34) can be recast in terms of the dynamical susceptibility χ'',

$$\frac{1}{T_1} = \frac{k_B T}{N\hbar^2 N_A g^2 \mu_B^2} \sum_{\vec{q}} \sum_\alpha \sum_{\alpha \equiv xy}, |\mathcal{A}_{\alpha\alpha'}(\vec{q})|^2 \frac{\chi''_\alpha(\omega_0, \vec{q})}{\omega_0} \tag{2.35}$$

where N is the number of lattice points in the system, $\sum_{\vec{q}}$ is over all the q values in the first Brillouin zone and χ'' is the imaginary part of the magnetic susceptibility. $\mathcal{A}_{\alpha\alpha'}(\vec{q}) = \sum_i \mathcal{A}_{\alpha\alpha'}(\vec{r_i}) e^{-i\vec{q}\cdot\vec{r_i}}$ is the Fourier transform of $\mathcal{A}_{\alpha\alpha'}(\vec{r_i})$.

2.4.3 Nuclear spin-spin relaxation rate $(1/T_2)$

The nuclear spin-spin or the transverse relaxation rate $1/T_2$, measures how fast the magnetization decays in the xy plane. T_2 is the dephasing time in which the nuclear spin ensemble loses its coherence due to a distribution of local magnetic fields experienced by the spins.

One of mechanisms by which these fields are formed is dipole-dipole interactions among the nuclei. A nucleus starts to experience a local field H_{loc} due to the neighboring nuclei. The z-component of the local field produced at a position $\vec{r}$ by the nuclear dipole $\mu_N = \gamma_N \hbar I$ can be expressed as,

$$H_{loc,z} \propto \frac{\mu_N}{r^3}(3\cos^2\theta - 1) \propto \frac{\gamma_N \hbar I}{r^3}(3\cos^2\theta - 1) \tag{2.36}$$

This field $H_{loc,z}$ alters the field (H_0) experienced by the nucleus thereby causing it to precess slower or faster, resulting in the dephasing of the nuclei with the T_2 mechanism. If at $t = 0$ the nuclei were all precessing in-phase (coherent) then as a result of this dipolar interaction they will get out of phase. If in a time which we identifty with T_2 such that $\gamma_N H_{loc} T_2 \approx 1$, they will be completely phased out and the vector sum of moments ≈ 0, then,

$$\frac{1}{T_2} \approx \gamma_N H_{loc} \propto \frac{\gamma_N^2 \hbar}{r^3} \tag{2.37}$$

T_2 is also affected by $H_{\mathrm{hf,z}}$, the z-component of the fluctuating field at the nucleus, which increases or decreases the rate of precession. It does not affect the T_1 process (relevant to longitudinal magnetization) but causes decay of transverse magnetization leading to the T_2 effect. In the limit of the rapid fluctuations ($\omega_0\tau_0 << 1; \omega_0$ is the Larmor frequency and τ_0 is the correlation time of the longitudinal fluctuating field) the resonance becomes narrower (*motional narrowing*) due to the first term in the equation (2.38). The spin-lattice relaxation results in the finite lifetime of a spin in an eigenstate ($\Delta E = \hbar\Delta\omega = \frac{\hbar}{T_1}$) , thus contributing to the broadening of the resonance. Therefore, these two effects must be incorporated in the definition of T_2:

$$\frac{1}{T_2} = \gamma_{\mathrm{N}}^2 \langle H_{\mathrm{hf,z}}^2 \rangle \tau_0 + \frac{1}{2T_1} \tag{2.38}$$

Apart from the dynamic time variational fluctuations in the field, there can be static spatial fluctuations in the field having a more macroscopic origin such as inhomogeneity (ΔH) in the applied field. It would contribute a term $\gamma_{\mathrm{N}}\Delta H$ in the expression for T_2. The analysis of transverse relaxation can be quite complicated due to the abundance of contributions, inhomogenity of the applied magnetic field, distribution of the static local field at nucleus caused by electrons, nuclear dipole-dipole coupling, T_1 process resulting in a finite lifetime of energy states, and also EFG which lifts the degeneracy of the energy levels, result in the broadening of the absorption line of resonance.

2.5 Effects of Radio Frequency Pulses

Pulsed NMR, as opposed to continuous wave (CW) NMR, encompasses a broad class of techniques that have evolved into the standard of modern NMR. The application of radiofrequency (rf) pulses allows for a time domain offset of the high voltage necessary for nuclear spin excitation and the extremely low voltage response thereof. As a result, pulsed NMR techniques, especially those employing the spin echo, are ideal for low signal-to-noise ratio experiments. The combination of signal averaging with phase coherent pulse sources and phase sensitive detection has also contributed to the takeover of pulsed NMR.

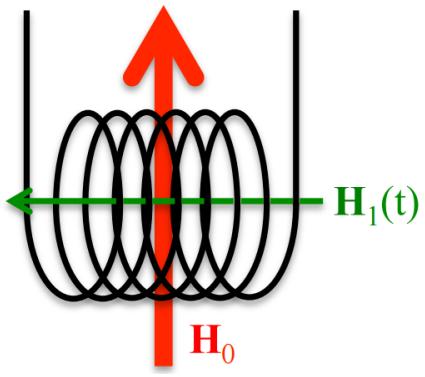

Figure 2.4 The experimental configuration of a standard NMR experiment. $\vec{H}_0$ is the external polarizing field which is typically on the order of many Tesla. $\vec{H}_1(t)$ is the applied rf field which excites the nuclei when on resonance and can be on the order of tens of Gauss.

2.5.1 Free induction decay

The free induction decay (FID) is the coherent precession of the nuclear magnetization following a $\frac{\pi}{2}$ pulse, which is then detected via faraday induction of a voltage in the pickup coil, which in the following experiments is the same coil used to apply the excitation pulses. To visualize the dynamics of the nuclear magnetization, the experiment can be set up as shown in Fig. 2.4, consisting of a sample inside of an excitation/pickup coil and two applied magnetic fields: the static field $\vec{H}_0$ polarizes the nuclei, and the perpendicular rf field $\vec{H}_1(t)$ produced by the coil is used to excite the nuclei.

Initially, the thermally equilibrated nuclear magnetization will be aligned with the static external magnetic field and we choose this to be the $\hat{z}$ axis by convention. We can turn on an rf field H_1 for time t_1 such that $\gamma H_1 t_1 = \pi/2$. This $\frac{\pi}{2}$ pulse will bring the magnetization in to the $x-y$ plane, which then induces a signal voltage, i.e., the FID signal, after the switch-off of the rf field.

The nuclei in a real sample experience other fields from extrinsic sources in addition to the dominant dipolar fields, such as local inhomogeneities in the magnet. Therefore, as time progresses the nuclear magnetization (and thus Faraday-induced voltage across the coil) will dephase naturally at an intrinsic rate T_2^{-1} (known as the spin-spin relaxation rate), and the

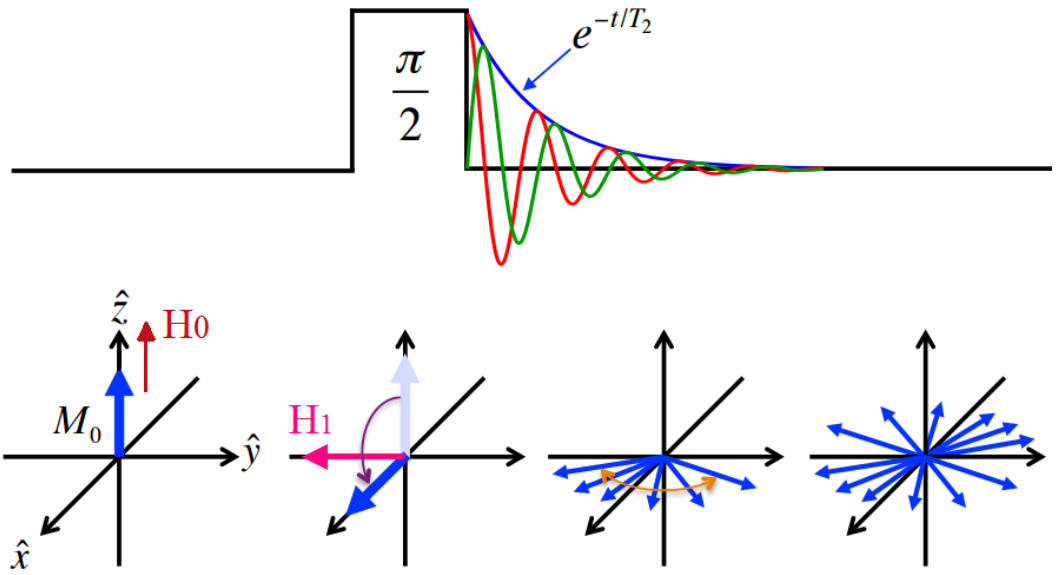

Figure 2.5 Schematic representation of nuclear magnetization of a free induction decay

eventual result is a net zero magnetization, as depicted in Fig. 2.5. The total decay rate of magnetization, with extrinsic effects included, is often referred to as T_2^{*-1},

$$\frac{1}{T_2^*} \approx \frac{1}{2T_1} + \frac{1}{T_2} + \gamma \Delta H_0 \tag{2.39}$$

where ΔH_0 is the inhomogeneity of the z-component of the magnetic field across the sample. For solid state samples, the main contribution to T_2^* comes from the second and third terms, since the dipolar field contribution to T_2 from neighboring spins does not cancel out. [251]

Therefore, if we consider an FID signal $S(t) = S_0 \exp(-t/T_2)$ (here we neglect the T_1 effects for simplicity), and transform it from the time domain to the frequency domain via Fourier transform (FT), we have

$$\begin{aligned} \tilde{S}(\omega) &= \frac{1}{2\pi} \int_{-\infty}^{\infty} \exp(-t/T_2) \exp(-i\omega t) \mathrm{d}t \\ &= \frac{(1/T_2)}{2\pi[(1/T_2)^2 + \omega^2]} - i \frac{\omega}{2\pi[(1/T_2)^2 + \omega^2]} \end{aligned} \tag{2.40}$$

The real and the imaginary parts correspond to the absorptive and the dispersive mode respectively (Fig. 2.6). The absorption mode yields a Lorentzian line shape of linewidth $1/\pi T_2$ in Fourier space.

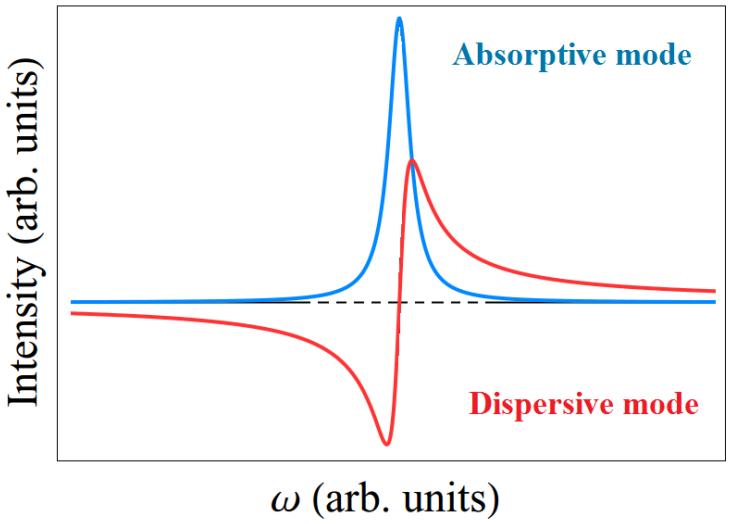

Figure 2.6 Fourier transform of Free Induction Decay (FID) Absorptive and Dispersive Lorentzian.

2.5.2 Spin echo

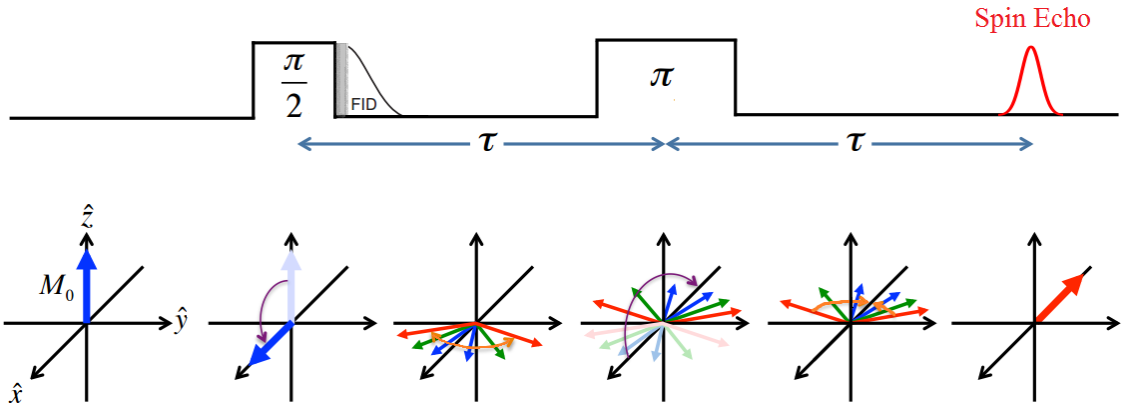

Figure 2.7 Formation of a Spin echo by a Carr-Purcell pulse sequence. The gray portion just after the first $\pi/2$-pulse is the *dead time*.

Due to the dead time (the finite recovery time of the receiver), the initial part of the FID cannot be observed. In the extreme case (esp. in solids) when T_2 is shorter than the dead time, it is difficult to observe an FID quickly after the high voltage pulses. To resolve this constraint, Spin Echo (also known as Hahn echo) was developed in 1950 by Erwin Hahn. [252]

A $\frac{\pi}{2} - \pi$ pulse sequency proposed by Carr-Purcell [253] was used, as elaborated in Fig. 2.7, where the refocussing of spins after the π-pulse results in a spin echo. Prior to the pulses, the equilibrium nuclear magnetization is aligned with the $\hat{z}$ axis. The first $\frac{\pi}{2}$ pulse rotates the nuclear magnetization to the $x - y$ plane as in the FID. The spins decohere for some amount of time τ. They are rotating with different rotational velocities due to different local field strengths, thus some are precessing faster and others slower. In the rotating frame there is a spreading of the nuclear spins and causes a decay of the detected NMR signal. A π pulse is then applied, which flips the spins such that they recohere in the $x - y$ plane, the faster spins are now behind and slower spins are ahead. As a result, all the spins will eventually refocus at a time τ after the π pulse and form the spin echo.

The spin echo intensity is proportional to the number of nuclei precessing inside the coil. This is because the echo is really just the induced voltage in the coil, which is in turn proportional to the nuclear magnetization and therfore the number of nuclei participating in the spin echo. Pulse sequences utilizing the spin echo abound and are used to measure NMR spectra, T_1, and T_2.

2.5.3 Saturation recovery measurements of T_1

One method to measure the spin-lattice relaxation time T_1 with spin echoes is given in Fig. 2.8 (a). There are two sets of pulses: the saturation and the detection pulses. The saturation pulse is usually a $\frac{\pi}{2}$ pulse which knocks the spins down on the $x - y$ plane. After a certain delay time τ_{delay} which allows some part of the longitudunal magnetization to grow, a $\frac{\pi}{2} - \pi$ spin-echo pulse sequence, detects the magnitude of the NMR signal for a particular delay time. Thus a plot of the integrated spin-echo intensity versus delay time is generated in Fig. 2.8 (b), which reflects the growth of the z-component of the magnetization.

The rate at which the longitudinal component of the magnetization M_z goes back to thermal equilibrium can be expressed as $\frac{\mathrm{d}M_z}{\mathrm{d}t} = -\frac{M_z - M_0}{T_1}$. Solve the function we can get the growth of the longitudinal magnetization $M_z(t)$:

$$M_z(t) = M_0(1 - e^{-t/T_1}) \tag{2.41}$$

where t is the delay time, M_0 is the equilibrium value of the magnetization, and T_1 is the spin-lattice relaxation time. A good single exponential recovery of the magnetization looks like an S curve in a semi-logarithmic plot shown in Fig. 2.8 (b). In some cases, multiple exponential or stretched exponential fitting ($M_z(t) = M_0(1 - A \cdot e^{-(t/T_1)^\beta})$) is used if there is more than one relaxation mechanism. For $I > 1/2$, for example ^{75}As with $I = 3/2$, the central transition recovery curve for the magnetic contribution is given as,

$$M_z(t) = M_0[1 - (0.1e^{-t/T_1} + 0.9e^{-6t/T_1})] \tag{2.42}$$

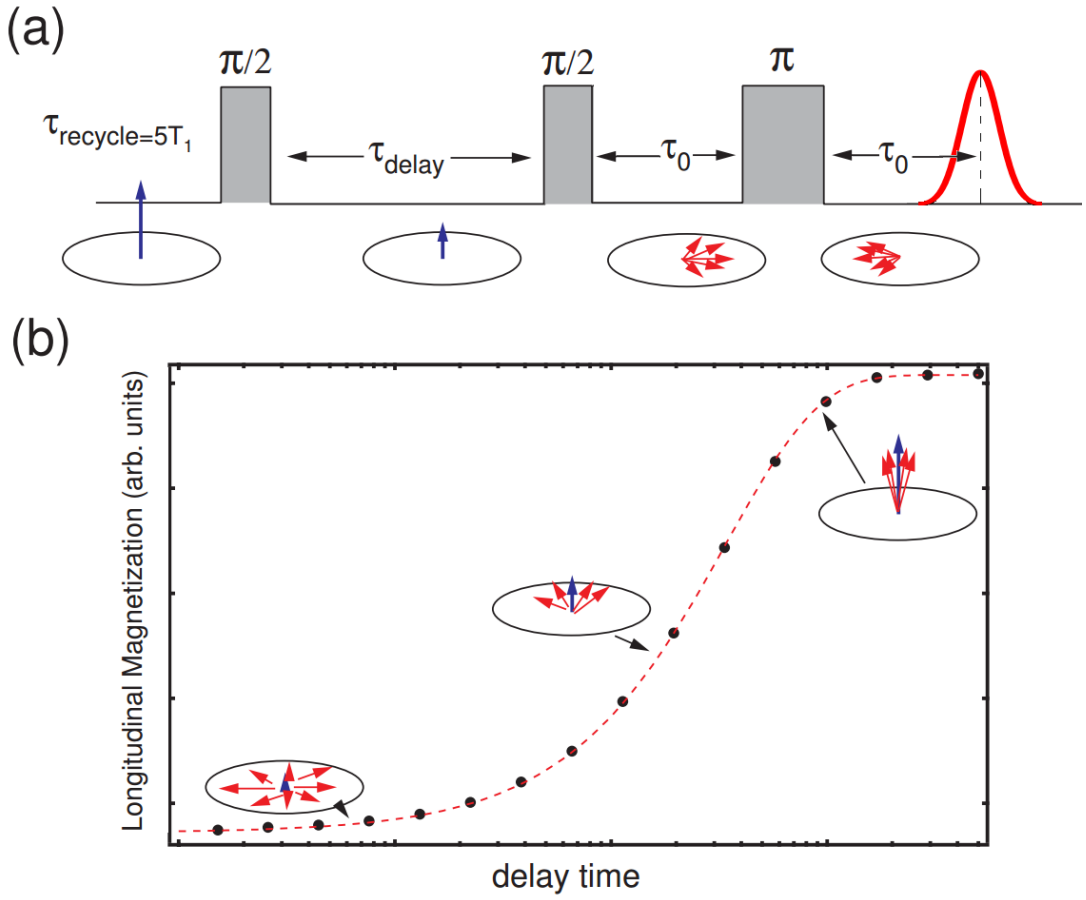

Figure 2.8 Measurment of T_1 by using a single saturation pulse method. (a) a $\frac{\pi}{2}$ "saturation" pulse is followed by a variable delay time which allows the growth of longitudinal magnetization M_z as it increases. The $\frac{\pi}{2} - \pi$ spin-echo sequence "inspect" the recovery of this magnetization which is reflected in (b) where the constant of the exponential growth is T_1.

2.5.4 Echo decay measurements of T_2

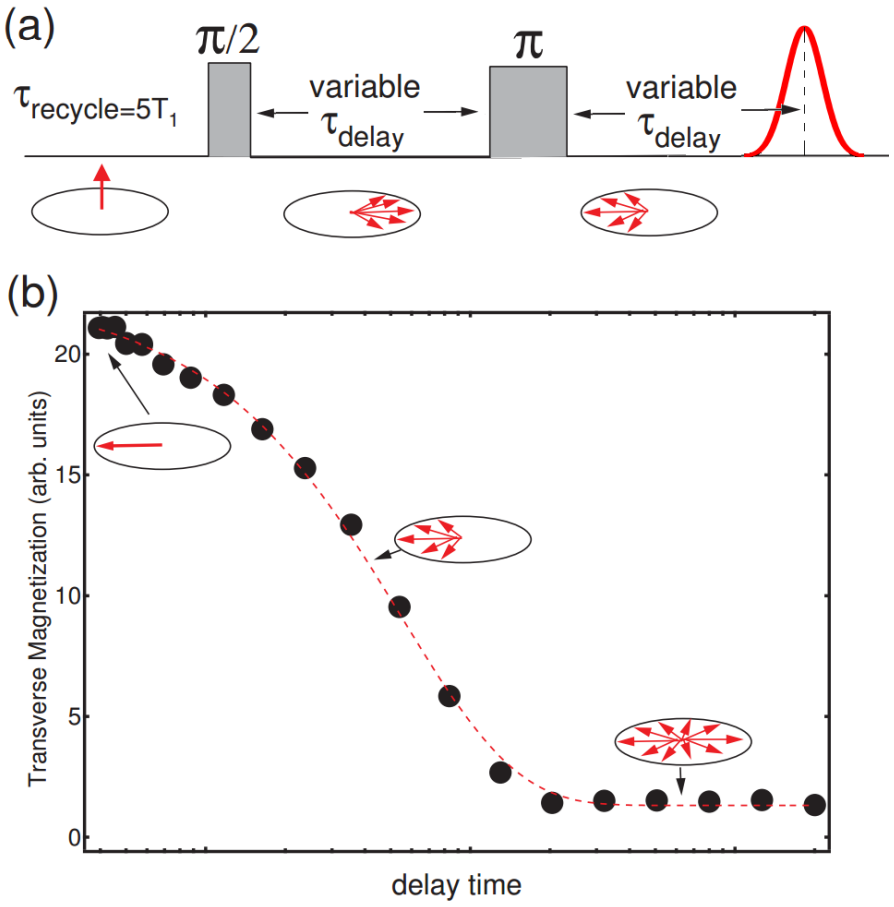

Figure 2.9 Measurement of spin-spin relaxation time T_2: (a) the variable delay time τ_{delay} after each pulse in the sequence $\frac{\pi}{2} - \pi$ is increased. (b) T_2 is the constant of the exponential decay of the transverse magnetization M_{xy}.

Figure 2.9(a) shows the echo decay sequence to measure the T_2. After the magnetization is knocked down on $x-y$ plane by the $\frac{\pi}{2}$ pulse, the spins lose their coherence or "fan out" as the delay time increases and the π pulse flips the fanned-out spins where they refocus giving a spin echo signal. As the delay time τ_{delay} increases, the more the transverse magnetization decays and the smaller the integrated spin echo will be. T_2 can be obtained by fitting the echo areas using equation,

$$M_{xy}(t) = M_{xy}(0)e^{-t/T_2} \tag{2.43}$$

where t is the delay time, and $M_{xy}(0)$ is the equilibrium value of the magnetization. A good

single exponential fit of the $x-y$ magnetization decay is a reversed S curve in a semi-logarithmic plot illustrated in Fig. 2.9(b). The echo decay sequence truly measures the intrinsic spin-spin relaxation time T_2 and not T_2^*.

CHAPTER 3. ANTIFERROMAGNETIC SPIN CORRELATIONS AND PSEUDOGAP-LIKE BEHAVIOR IN $CA(FE_{1-X}CO_X)_2AS_2$ STUDIED BY ^{75}AS NUCLEAR MAGNETIC RESONANCE AND ANISOTROPIC RESISTIVITY

A paper published in Physical Review B, **92**, 184504 (2015)

J. Cui,[1,2] B. Roy,[1,3] M. A. Tanatar,[1,3] S. Ran,[1,3] S. L. Bud'ko,[1,3] R. Prozorov,[1,3] P. C. Canfield,[1,3] and Y. Furukawa[1,3]

1 Ames Laboratory, U.S. DOE, Ames, Iowa 50011, USA

2 Department of Chemistry, Iowa State University, Ames, Iowa 50011, USA

3 Department of Physics and Astronomy, Iowa State University, Ames, Iowa 50011, USA

3.1 Abstract

We report ^{75}As nuclear magnetic resonance (NMR) measurements of single-crystalline $Ca(Fe_{1-x}Co_x)_2As_2$ ($x = 0.023$, 0.028, 0.033, and 0.059) annealed at 350 °C for 7 days. From the observation of a characteristic shape of ^{75}As NMR spectra in the stripe-type antiferromagnetic (AFM) state, as in the case of $x = 0$ ($T_N = 170$ K), clear evidence for the commensurate AFM phase transition with the concomitant structural phase transition is observed in $x = 0.023$ ($T_N = 106$ K) and $x = 0.028$ ($T_N = 53$ K). Through the temperature dependence of the Knight shifts and the nuclear spin lattice relaxation rates ($1/T_1$), although stripe-type AFM spin fluctuations are realized in the paramagnetic state as in the case of other iron pnictide superconductors, we found a gradual decrease of the AFM spin fluctuations below a crossover temperature T^* which was nearly independent of Co-substitution concentration, and is attributed to a pseudogap-like behavior in the spin excitation spectra of these systems. The T^* feature finds correlation with

features in the temperature-dependent inter-plane resistivity, $\rho_c(T)$, but not with the in-plane resistivity $\rho_a(T)$. The temperature evolution of anisotropic stripe-type AFM spin fluctuations are tracked in the paramagnetic and pseudogap phases by the $1/T_1$ data measured under magnetic fields parallel and perpendicular to the c axis. Based on our NMR data, we have added a pseudogap-like phase to the magnetic and electronic phase diagram of $Ca(Fe_{1-x}Co_x)_2As_2$.

3.2 Introduction

After the discovery of superconductivity in substituted transition metal pnictides, much attention has been paid to understanding of the interplay between magnetism and superconductivity in these new materials. [10,30,254,255] Among the iron pnictide superconductors, AFe_2As_2 (A = Ca, Ba, and Sr), known as "122" compounds with a $ThCr_2Si_2$-type structure at room temperature, has been one of the most widely studied systems in recent years. [30,39,43,93,254,255] Application of pressure and carrier doping are considered to play an important role in the suppression of the antiferromagnetic (AFM) ordering and the appearance of the high temperature superconducting (SC) phase. These tuning parameters produce the well-known phase diagram of the Fe-based superconductors: an AFM ordering temperature T_N is suppressed continuously with doping or pressure application, and an SC state emerges with the transition temperature T_c varying as a function of the tuning parameters. [30,39,43,254,255]

Among the 122 compounds, $CaFe_2As_2$ is known to be extremely sensitive to an application of pressure and is considered to be a system with strong coupling of the magnetic and structural phase transitions exhibiting an AFM ordering of the Fe moments at T_N = 170 K with a concomitant structural phase transition to a low temperature orthorhombic phase. [39,42,93] Under ambient pressure, substitutions of Fe by Co, Ni and others induce superconductivity in $CaFe_2As_2$ with T_c up to ~15 K. [40,93,256,257] Under a pressure of just a few kilobars, the orthorhombic AFM phase was replaced by a non-magnetic, collapsed tetragonal phase. [92,93,258,259] The collapsed tetragonal phase in $CaFe_2As_2$ is characterized by a ~10 % reduction in the tetragonal c lattice constant, from the value in the high temperature tetragonal phase, along with the absence of AFM ordering. [91,260,261]

Recently it was shown that, by careful combination of Co substitution and post growth

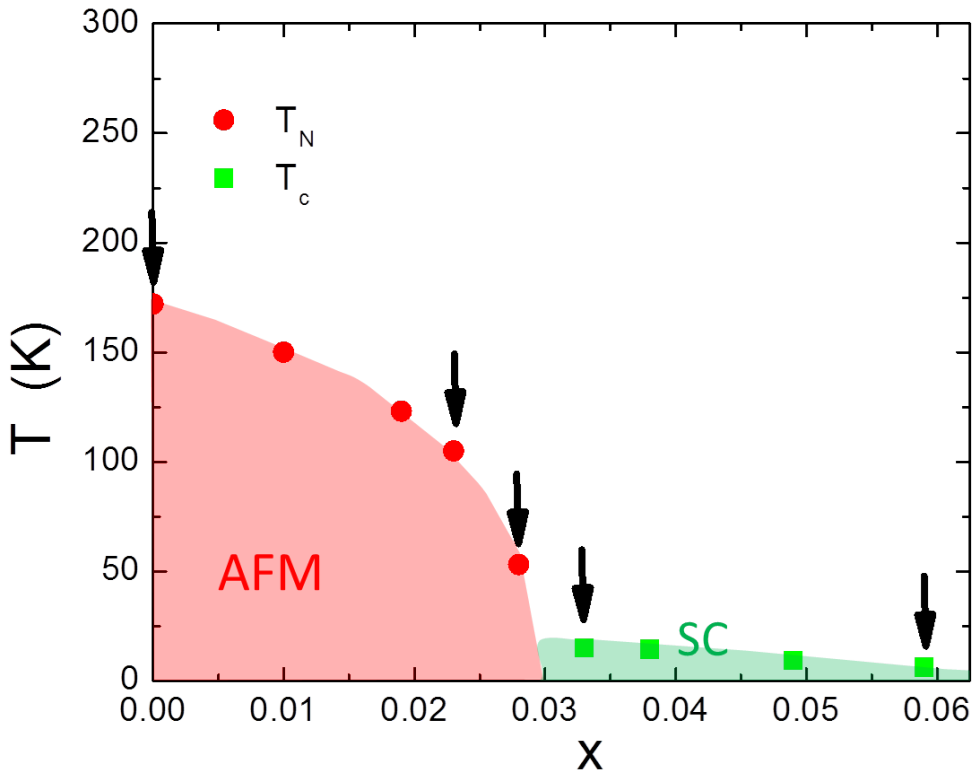

Figure 3.1 Phase diagram of $Ca(Fe_{1-x}Co_x)_2As_2$ in the case of the crystals annealed at T_a = 350 °C for 7 days and then quenched. [40] T_N and T_c are from Ref. [40]. AFM and SC represent the antiferromagnetic ordered state and superconducting phase. Arrows indicate the Co substituted samples used in the present work.

annealing and quenching, $Ca(Fe_{1-x}Co_x)_2As_2$ can be systematically tuned to have one of four different ground states: orthorhombic AFM, superconducting, tetragonal paramagnetic and collapsed tetragonal states. [40,261] Fig. 3.1 shows the typical phase diagram of $Ca(Fe_{1-x}Co_x)_2As_2$ in the case of the crystals annealed at T_a = 350 °C for 7 days and then quenched. [40] With Co substitution, the AFM state with T_N = 170 K at $x = 0$ is suppressed to 53 K at $x = 0.028$ and then an SC phase shows up with a highest $T_c \sim 15$ K at $x = 0.033$. Although the phase diagram is, in some ways similar to the case of $Ba(Fe_{1-x}Co_x)_2As_2$, $Ca(Fe_{1-x}Co_x)_2As_2$ shows a coincident, first order, structural and magnetic phase transition at the same temperature and

does not show any splitting of the phase transitions upon Co substitution, and no coexistence of the AFM and SC has been reported, [40] while $Ba(Fe_{1-x}Co_x)_2As_2$ system exhibits a clear splitting of those transition lines, and the coexistence of AFM are SC has been found. [38, 39]

Nuclear magnetic resonance (NMR) has been known to be a microscopic probe suitable to investigate static spin susceptibility, magnetic order and low energy spin excitations for Fe pnictides superconductors. [30, 262, 263] The NMR spectrum gives us information on static magnetic properties through the hyperfine interactions of the nuclei with Fe spins while the nuclear spin lattice relaxation rate $(1/T_1)$ is related to the power spectrum of the hyperfine field fluctuations produced by the Fe spins. [30, 262, 263] Previous ^{75}As NMR studies of the parent material $CaFe_2As_2$ showed clear splittings of ^{75}As NMR lines due to a hyperfine field produced by Fe moments below Néel temperature $T_N = 170$ K, demonstrating a phase transition from a high temperature paramagnetic state to a low temperature stripe-type AFM state. [87, 264, 265] Suppression of the Fe spin correlations in the collapsed tetragonal phase in $CaFe_2As_2$ was also revealed by ^{75}As NMR. [94, 266]

In the case of Co substituted $CaFe_2As_2$, Baek *et al.* reported nuclear spin lattice relaxation rates $(1/T_1)$ of ^{75}As nuclear quadrupole resonance (NQR) as a function of temperature in $Ca(Fe_{1-x}Co_x)_2As_2$ grown out of Sn flux, showing a gradual decrease of $1/T_1T$ below a crossover temperature (T^*) in the under- and optimally-substituted regions. [95] The decrease in $1/T_1T$ has been attributed to pseudogap-like phenomenon and the crossover temperature T^* shows a strong substitution dependence, falling to zero near optimum substitution. Pseudogap-like behavior has been reported in the isostructural Co substituted $BaFe_2As_2$ from temperature dependence of Knight shift and $1/T_1T$ of ^{75}As NMR measurements [90] which provide important information about static and dynamical magnetic properties, in addition to NQR measurements. Furthermore, NMR measurements, in particular $1/T_1$ measurements under different magnetic field directions, provide more detailed information about magnetic fluctuations. [262] Thus, using NMR techniques, detailed studies of Co substitution effects on static and dynamical magnetic properties in $CaFe_2As_2$ are important and of a great deal of interest. However, no systematic NMR data on Co substituted $CaFe_2As_2$ have been reported up to now.

It was found previously, [267] that the temperature-dependent NMR Knight shift in sub-

stituted Ba122 compounds shows a correlation with the temperature-dependent resistivity, particularly for the inter-plane transport direction, $\rho_c(T)$. This correlation was interpreted as evidence for magnetic character of scattering in the compounds [268] and indication of a partial charge gap (pseudogap) [267, 269, 270] developing at high temperatures. The pseudogap-like behavior has been also reported in iron pnictides by other experimental techniques such as angle-resolved photoemission spectroscopy and optical measurements. [271–273] Change of alkali earth element in the 122 family from Ba to Ca, leading to inevitable change of the Fermi surface, [274,275] can bring additional insight into the origin of pseudogap and its dependence on material properties.

In this paper, we report a comprehensive study of the ^{75}As NMR in $Ca(Fe_{1-x}Co_x)_2As_2$ and its comparison with inter-plane transport properties. Here we used single crystals grown out of a FeAs/CoAs flux since the effects of Co substitution on the crystals grown out of Sn flux have issues with solubility, reproducibility, and inhomogeneity, [276–278] while one can minimized these problems in Co substituted $CaFe_2As_2$ grown out of an FeAs/CoAs flux by systematically control annealing/quenching temperatures. [40,261] We present the temperature and the x dependence of NMR spectra from which we derive information about the hyperfine and quadrupole interactions at the ^{75}As sites exhibiting microscopic evidence of a simultaneous stripe-type AFM and structural phase transition in Co substituted $CaFe_2As_2$. We also report the temperature and x dependence of nuclear relaxation rates that provide the pseudogap-like phase in the phase diagram as shown in Fig. 3.12 where the crossover temperature T^* is found to be nearly independent of x, in contrast to the previous report. [95] We support this interpretation by observation of features in the temperature-dependent inter-plane transport.

3.3 Experimental

The single crystals of $Ca(Fe_{1-x}Co_x)_2As_2$ (x = 0.023, 0.028, 0.033 and 0.059) used in this study were grown out of a FeAs/CoAs flux, [40,261] using conventional high temperature growth techniques. [279, 280] Subsequent to growth, the single crystals were annealed at T_a = 350 °C for 7 days and then quenched. For $x = 0$, we used the single crystal annealed at T_a = 400 °C for 24 hours. The Co substitution levels of the single crystals used in this study were determined

by a wavelength dispersive x-ray spectroscopy, and the crystals are characterized by magnetic susceptibility, [40] resistivitity [40] and thermal expansion [281] measurements. Details of the growth, annealing and quenching procedures are reported in Refs. [40] and [261].

NMR measurements were carried out on ^{75}As ($I = 3/2$, $\gamma/2\pi = 7.2919$ MHz/T, $Q = 0.29$ Barns) by using a lab-built, phase-coherent, spin-echo pulse spectrometer. The ^{75}As-NMR spectra were obtained by sweeping the magnetic field at a fixed frequency $f = 53$ MHz. The magnetic field was applied parallel to either the crystal c axis or the ab plane, and the direction of the magnetic field on the ab plane was not controlled. The origin of the Knight shift, $K = 0$, of the ^{75}As nucleus was determined by the ^{75}As NMR measurements of GaAs. The ^{75}As $1/T_1$ was measured with a recovery method using a single $\pi/2$ saturation rf pulse. The $1/T_1$ at each T was determined by fitting the nuclear magnetization M versus time t using the exponential functions $1 - M(t)/M(\infty) = 0.1e^{-t/T_1} + 0.9e^{-6t/T_1}$ for ^{75}As NMR, where $M(t)$ and $M(\infty)$ are the nuclear magnetization at time t after the saturation and the equilibrium nuclear magnetization at $t \to \infty$, respectively. In the paramagnetic states, the nuclear magnetization recovery curves were well fitted by the function in all Co-substituted crystals within our experimental uncertainty. On the other hand, below T_N or T_c, we observed a slight deviation due to short T_1 components with unknown in origin. A part of NMR data for the parent compound ($x = 0$) annealed at 400 °C has been reported previously. [94]

The in-plane resistivity measurements were made in four-probe configuration on samples cut into bars with typical dimensions $1\times0.2\times0.2$ mm^3 ($a\times b\times c$). Contacts to the samples were made by Sn soldering 50 μm diameter Ag wires. Inter-plane resistivity measurements were made in the two-probe sample configuration. [282] Contacts were covering the whole ab plane area of the c axis samples, typically 0.5×0.5 mm^2, while current was flowing along c axis (short dimension typically 0.1 mm). A four-probe scheme was used to measure the resistance down to the contact to the sample, i.e. the sum of the actual sample resistance R_s and contact resistance R_c was measured. These measurements were relying on ultra-low contact resistance on soldered Sn contacts. [283,284] Taking into account that $R_s \gg R_c$, contact resistance represents a minor correction of the order of 1 to 5%.

The drawback of the measurement on samples with a (or b) $\gg c$ is that any inhomogeneity

in the contact resistivity or internal sample connectivity admixes in-plane component due to redistribution of the current. To minimize this effect, we performed measurements of ρ_c on at least 5 samples of each composition. In all cases we obtained qualitatively similar temperature dependences of the electrical resistivity, as represented by the ratio of resistivities at room and low temperatures, $\rho_c(0)/\rho_c(300)$. The resistivity value, however, showed a notable scatter and at room temperature was typically in the range 1 to 2 mΩcm. For the sake of comparison we selected the samples with the temperature dependence of resistivity least similar to that of $\rho_a(T)$. Typically, these samples had the lowest value of electrical resistivity, as described in detail in Ref. [282]. This is important since partial exfoliation increases resistivity values. [282]

Because Sn contacts are covering the whole ab-plane area of the samples, they can potentially create uncontrolled stress/strain. Due to strong sensitivity to strain, this can lead to non-negligible effect on the features observed in $CaFe_2As_2$ compositions. For some compositions we performed measurements using Montgomery technique, [285,286] in which contacts are located at the sample corners, see discussion below. We have not observed any significant effect of the contact-related stress, similar to measurements in parent $BaFe_2As_2$ under pressure. [268]

3.4 Results and discussion

3.4.1 ^{75}As NMR spectra

In the paramagnetic state of $CaFe_2As_2$, the ^{75}As NMR spectrum exhibits a typical feature of a nuclear spin $I = 3/2$ with Zeeman and quadrupolar interactions. This results in a sharp central transition and two satellite lines split by the quadrupolar interaction of the As nucleus with the local electric field gradient (EFG). [87,94] Just below T_N, when H is applied parallel to the c axis, each NMR line splits into two lines due to internal field H_{int} (parallel or antiparallel to H) which is produced by the Fe spin ordered moments with the stripe-type spin structure. [86]

In the case of Co substituted crystals with $x = 0.023$ and 0.028, similar splittings of the NMR lines are observed below T_N. Figure 3.2(a) shows a typical example of temperature evolution of the field-swept ^{75}As-NMR spectra of the $x = 0.028$ Co substituted $CaFe_2As_2$ crystal for a magnetic field $H \parallel c$ axis. Just below $T_N = 53$ K, the spectra split into the two sets of three

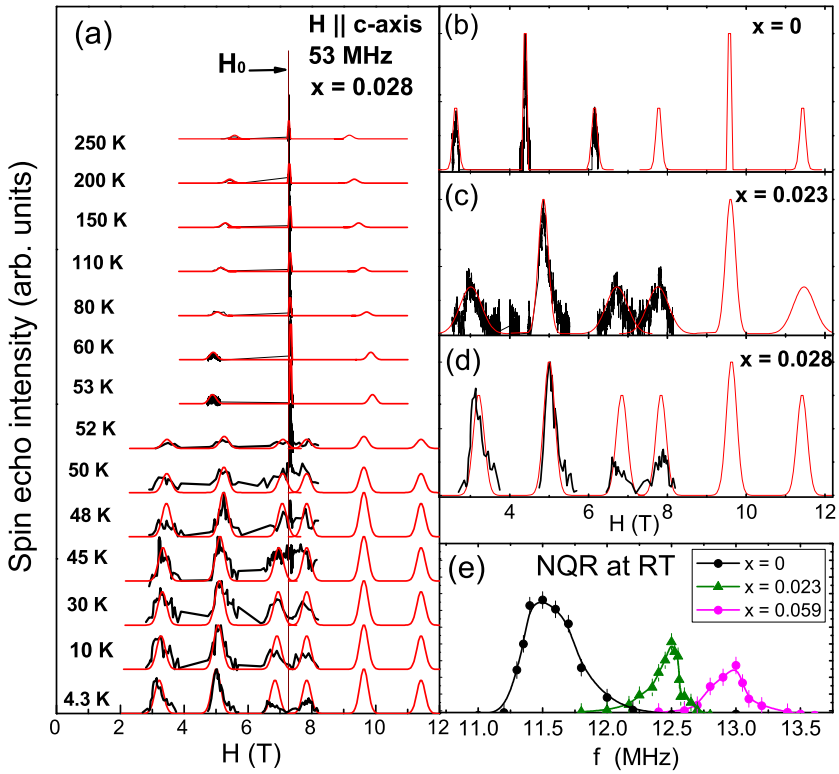

Figure 3.2 (a) Temperature variation of field-swept ^{75}As NMR spectra for the $x = 0.028$ Co substituted $CaFe_2As_2$ crystal (annealed at $T_a = 350$ °C for 7 days) at $f = 53$ MHz for magnetic field parallel to the c axis. The black and red lines are observed and simulated spectra, respectively. Expected lines above 8.5 T are not measured due to the limited maximum magnetic field for our SC magnet. Field-swept ^{75}As NMR spectra in antiferromagnetic state are shown in (b) for $x = 0$ ($T = 4.3$ K), (c) $x = 0.023$ ($T = 4.3$ K) and (d) $x = 0.028$ ($T = 4.3$ K), together with the simulated spectrum for each. (e) ^{75}As NQR spectra measured at room temperature.

lines due to the internal field as in the case of $CaFe_2As_2$. The observed spectra are reproduced well by a simple nuclear spin Hamiltonian $\mathcal{H} = -\gamma\hbar\vec{I}\cdot\vec{H}_{\rm eff} + \frac{h\nu_Q}{6}\,[3I_z^2\text{-}I(I+1) + \frac{1}{2}\eta(I_+^2 + I_-^2)\,]$, where $H_{\rm eff}$ is the effective field at the As site (summation of external field H and the internal field $H_{\rm int}$), h is Planck's constant, and ν_Q is nuclear quadrupole frequency defined by $\nu_Q = eQV_{ZZ}/2h$ where Q is the quadrupole moment of the As nucleus, V_{ZZ} is the EFG at the As site, and η is an asymmetric parameter of EFG. [239]

From the simulated spectra shown by red lines in Fig. 3.2(a), we extracted the temperature dependence of ν_Q and $H_{\rm int}$ for $x = 0.028$, which are shown in Fig. 3.3 together with the data

for $x = 0$ and 0.023. For $x = 0.028$, with decreasing temperature, ν_Q increases from 12.2 MHz at $T = 250$ K to 17.5 MHz at 53 K, shows a sudden jump to 13 MHz just below 53 K and levels off in the antiferromagnetic state at low temperatures. This clearly indicates the first-order structural phase transition at $T_s = 53$ K. In our experiment, we do not observe clear hysteresis within our experimental uncertainty. Similarly $H_{int} = 2.25$ T at $T = 4.3$ K decrease slightly with increasing T and then suddenly disappears above 53 K. These results indicate that, even for the Co substitution level of $x = 0.028$, the crystal exhibits the AFM ordering at T_N= 53 K with a concomitant structural phase transition as in the case of $CaFe_2As_2$ ($T_N = 170$ K). This is in sharp contrast to the case of $Ba(Fe_{1-x}Co_x)_2As_2$ where the two phase transitions separate ($T_S > T_N$) upon Co substitution. [38, 39] These results suggest that couplings between lattice and magnetism in $CaFe_2As_2$ are much stronger than in other pnicitdes such as $BaFe_2As_2$. H_{int} and ν_Q in a temperature range of $T = 50$ – 100 K for $x = 0.023$ were not measured because of poor signal intensities.

Figure 3.2(b)-(d) show a comparison of ^{75}As NMR spectra in the stripe-type AFM state for $x = 0$, 0.023 and 0.028. With Co substitution, each line broadens but is still well separated, implying that ν_Q and H_{int} can be well defined. This is in contrast to the case of $Ba(Fe_{1-x}Co_x)_2As_2$ where very broad and featureless ^{75}As NMR lines were observed in antiferromagnetic state for x = 0.02 and 0.04. [287] Clear split lines observed even for $x = 0.028$ indicate that the stripe-type AFM structure is commensurate upon Co substitution in $CaFe_2As_2$. Similar splitting of ^{75}As NMR lines in the AFM state in 2 % Co substituted $BaFe_2As_2$ has been observed recently, [288] consistent with commensurate AFM state.

Figure 3.2(e) shows the ^{75}As NQR spectra in crystals with different Co-substitution levels at room temperature. The line width (∼0.5 MHz) of the spectrum is nearly independent of x, which indicates that no significant increase of inhomogeneity in distribution of electronic field gradient (EFG) with the Co substitutions. In the case of the $Ca(Fe_{1-x}Co_x)_2As_2$ crystals grown with Sn flux, the line width of NQR spectrum increases from 0.4 MHz at $x = 0$ to 0.95 MHz at $x = 0.09$ (Ref. [95]). The smaller line widths indicate a higher degree of homogeneity in crystals grown with FeAs/CoAs flux than that with Sn flux, consistent with the previous report. [278]

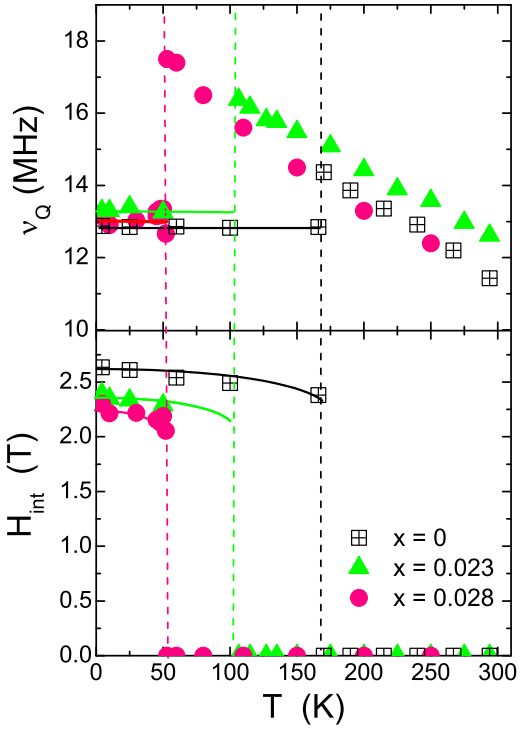

Figure 3.3 (top) Temperature dependence of quadrupole frequency ν_Q for $x = 0.023$ and 0.028. (bottom) Temperature dependence of H_{int}. The vertical broken lines correspond to $T_N = T_s$ for each crystal determined by the magnetic susceptibility measurements. [40] H_{int} and ν_Q in a temperature range of $T = 50 - 100$ K for $x = 0.023$ were not measured because of poor signal intensities. The solid lines are guides for eyes.

As shown in Fig. 3.3, the saturated values of H_{int} decrease slightly from 2.64 ± 0.05 T at $x = 0$ to 2.35 ± 0.1 T for $x = 0.023$ and to 2.25 ± 0.1 T for $x = 0.028$, although T_N changes drastically from 170 K for $x = 0$ to 106 K for $x = 0.023$ and to 53 K for $x = 0.028$. This is in contrast to the case in Ni substituted $Ba(Fe_{1-x}Ni_x)_2As_2$ where $H_{int} = 1.5$ T at $x = 0$ at As sites decreases upon Ni substitution with a similar reduction of T_N. [289] The H_{int} at the As sites in the stripe-type AFM state in AFe_2As_2 (A = Ca, Ba, and Sr) is known to be expressed as $H_{int} = 4\ B_c\langle s\rangle$ where B_c is an off-diagonal term in the hyperfine coupling tensor and $\langle s\rangle$ the ordered magnetic moments. [86] Using the value $\langle s\rangle = 0.8\ \mu_B$ from neutron scattering measurements [290] and $H_{int} = 2.64$ T, B_c is estimated to be 0.82 T/μ_B/Fe, which is in good agreement with the previously reported value. [265, 291]

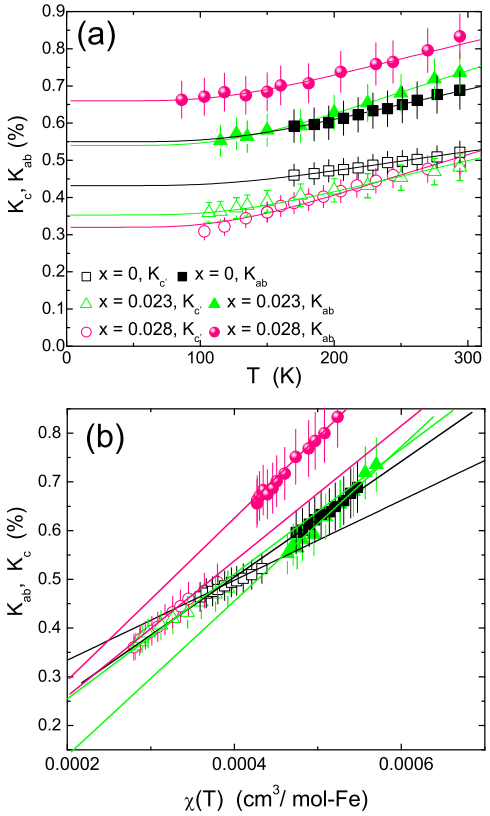

Figure 3.4 (a) Temperature T dependence of ^{75}As NMR shifts K_{ab} and K_c for $Ca(Fe_{1-x}Co_x)_2As_2$. The solid lines are fitting results with a thermal activation form $K \sim \exp(-\Delta/k_BT)$ with $\Delta/k_B = 510$ K for $x = 0$, and 490 K for $x = 0.023$ and 0.028, respectively. (b) K versus magnetic susceptibility $\chi(T)$ plots for the corresponding ab and c components of K in $Ca(Fe_{1-x}Co_x)_2As_2$ with T as an implicit parameter. The solid lines are linear fits.

The nearly x-independent $H_{\rm int}$ suggests that the ordered Fe magnetic moments are not suppressed drastically with the Co substitution, with a reasonable assumption of no drastic change in the hyperfine coupling constants as will be described below. Assuming that B_c is independent of x, $\langle s \rangle$ is estimated to be 0.72 μ_B and 0.71 μ_B for $x = 0.023$ and 0.028, respectively. On the other hand, if one assumes that the Fe moments decrease with Co substitution, the x independent $H_{\rm int}$ could be possible only if B_c increases drastically with Co substitution to compensate for the reduction of $\langle s \rangle$. However, this is highly unlikely because, as can be seen below, the K-χ plot analysis reveals a slight change in diagonal terms of the hyperfine coupling tensor with the Co substitution, and also $1/T_1T$, related to the square of hyperfine coupling

constants, are nearly x independent at high T suggesting no drastic change in hyperfine coupling constants. Thus we consider that Fe ordered moments are robust with the Co substitution. The robustness may be explained if "intrinsic" T_N were nearly independent of x. Here the "intrinsic" T_N is a Néel temperature in the orthorhombic phase and is considered to be much higher than T_S (or "observed" T_N) as expected from the temperature dependence of H_{int} shown in Fig. 3.3. Since the AFM ordering state can be established in only the orthorhombic phase, the suppression of the "observed" T_N with x can be due to the reduction of T_S. Assuming the Co substitution suppresses mainly the structural phase transition temperature but not "intrinsic" T_N, the nearly x-independent H_{int} can be expected, and thus the Fe ordered moments can be almost independent of x. These results are in sharply contrast to the case of $Ba(Fe_{1-x}Co_x)_2As_2$ where the neutron scattering measurements show a monotonic decrease in Fe ordered moments with Co substitution. [96] It will be interesting to perform neutron scattering and/or Mössbauer measurements to confirm the robustness of the Fe ordered moments in $Ca(Fe_{1-x}Co_x)_2As_2$.

Figure 3.4(a) shows the x and T dependence of the Knight shift, K_{ab} for H parallel to the ab plane and K_c for H perpendicular to the c axis, respectively, where the second order quadrupole shift was corrected in K_{ab}. [94, 239] With decreasing T, all Knight shifts decrease down to T_N for each crystal, similar to $\chi(T)$ data shown in Ref. [40] for these samples. It is noted that $K_c \sim 0.3$ – 0.5 % for $x = 0$, 0.023 and 0.028 is greater than $K_c = 0.2$ – 0.3 % for Sn-flux $CaFe_2As_2$. [87] The possible small misalignment of the crystal orientation, the deviation of H from $H \parallel c$ axis or ab plane, will results in additional corrections in second order quadrupole shifts for the central line position of ^{75}As NMR spectrum, which produces a small change in the absolute value of the K. Although we tried to set the crystal $H \parallel c$ or $H \parallel ab$ as precise as possible, a small misalignment of the crystal orientation is still possible. Since the temperature dependence of K will not be affected much, we focus on mainly on the temperature dependence of K's exhibiting the gradual decrease upon cooling. Similar temperature dependence of Knight shifts (or macroscopic magnetic susceptibility) were reported previously for various Fe based superconductors such as $Ba(Fe_{1-x}Co_x)_2As_2$ [90], $LaFeAsO_{1-x}F_x$ [66, 292] and FeSe [293]. The gradual decreases in K indicate gradual suppressions of the $q = 0$ component of the spin susceptibility on cooling and were fitted by a phenomenological thermal

activation form $K \propto \exp(-\Delta/k_{\rm B}T)$. Using the equation we estimate $\Delta/k_{\rm B} = 490-510$ K which is almost independent of x in the Co substituted compounds. The solid lines in the Fig. 3.4 are fitting results. This value is comparable to the previous estimates of 450 K in $Ba(Fe_{1-x}Co_x)_2As_2$ (Ref. [90]) and 435 K in $K_xFe_{2-x}Se_2$ [294]. We also tentatively fitted the data for $x = 0$ from Ref. [87] with the formula which produces a relatively large value of $\Delta \sim$ 650 K.

The diagonal terms of the hyperfine coupling tensor $A_{\rm hf}$ can be estimated by K-χ plot analysis. Since the spin part of K, $K_{\rm spin}$, is proportional to the spin susceptibility $\chi_{\rm spin}$ through the diagonal term of the hyperfine coupling tensor $A_{\rm hf}$ giving $K_{\rm spin} = \frac{A_{\rm hf}}{N_{\rm A}}\chi_{\rm spin}(T)$, where $N_{\rm A}$ is Avogadro's number, the slope of the K-χ plot gives an estimate of $A_{\rm hf}$. Figure 3.4(b) plots K_{ab} and K_c against the corresponding χ_{ab} and χ_c, respectively, for each sample with T as an implicit parameter. All K_{ab} and K_c are seen to vary linearly with the corresponding χ and the hyperfine coupling constants are estimated to be $A_c = (-12.2 \pm 2.0)$ kOe/$\mu_{\rm B}$/Fe, (-14.6 ± 1.4) kOe/$\mu_{\rm B}$/Fe and (-15.7 ± 1.4) kOe/$\mu_{\rm B}$/Fe and $A_{ab} = (-17.9 \pm 2.2)$ kOe/$\mu_{\rm B}$, (-19.0 ± 2.0) kOe/$\mu_{\rm B}$/Fe and (-20.5 ± 3.0) kOe/$\mu_{\rm B}$/Fe, for $x = 0$, 0.023 and 0.028, respectively. One does not observe a significant change in the diagonal term of the hyperfine coupling tensor in the Co substituted compounds within our experimental uncertainty, although both A_c and A_{ab} seems to be increased slightly with the Co substitution.

As shown in Fig. 3.5, we have observed that the ^{75}As quadrupole frequency, $\nu_{\rm Q}$ varies linearly with the spin part of Knight shift in the paramagnetic phase with the relation $\nu_Q = \nu_{Q0} + \alpha K_{\rm spin}$. As can be seen, α decreases from -46 MHz/% for $x = 0$ to -30 MHz/% for $x =$ 0.023 and to -25 MHz/% for $x = 0.028$, and ν_{Q0} of $\sim$26 MHz is nearly independent of x. Such linear relationship has also been reported in Co pnictides by Majumder *et al.* (Ref. [295]) and can be found in other itinerant magnetic systems such as the $BaFe_2As_2$ [86] and LiFeAs [296]. The α values estimated from the slopes of the ν_Q vs. K plot are ranged in $\sim$0.04 MHz/% for PrCoAsO, $\sim$ 4 MHz/% in LiFeAs, much less than that in $Ca(Fe_{1-x}Co_x)_2As_2$. According to self-consistent renormalization (SCR) theory, [297] temperature dependence of ν_Q can be influenced by the spin susceptibility due to the mode mode coupling between charge and spin density fluctuations. Thus the prominent α value indicates the strong coupling between charge

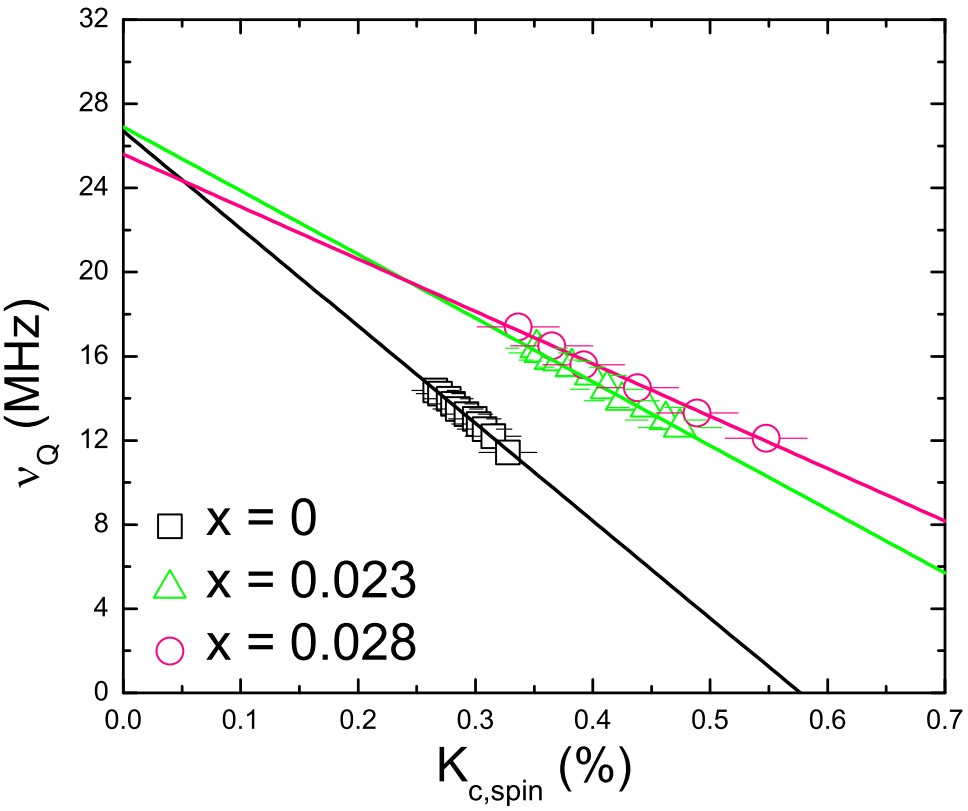

Figure 3.5 $\nu_{\rm Q}$ versus $K_{c,spin}$ plots for $x = 0$ (black), $x = 0.023$ (light green) and $x = 0.028$ (pink) in $Ca(Fe_{1-x}Co_x)_2As_2$ with T as an implicit parameter. The solid lines are linear fits.

and spin density fluctuations in $Ca(Fe_{1-x}Co_x)_2As_2$, consistent with the NMR spectrum data showing the strong coupling between lattice and magnetism.

3.4.2 ^{75}As spin lattice relaxation rates $1/T_1$

In order to investigate the evolution of the spin dynamics with Co substitution, we have measured ^{75}As spin lattice relaxation rates $1/T_1$ as a function of temperature. Figs. 3.6(a) and (b) show $1/T_1T$ versus T in $Ca(Fe_{1-x}Co_x)_2As_2$ for H perpendicular and parallel to the c axis at $H \sim 7.5$ T, respectively. For $x = 0.023$, above $T_{\rm N} = 106$ K, $1/T_1T$ for $H \parallel ab$ plane shows a monotonic increase with decreasing T, while $1/T_1T$ for $H \parallel c$ axis is nearly independent of T, similar to the case for $x = 0$ reported previously. [94] At $x = 0.028$, $1/T_1T$ for

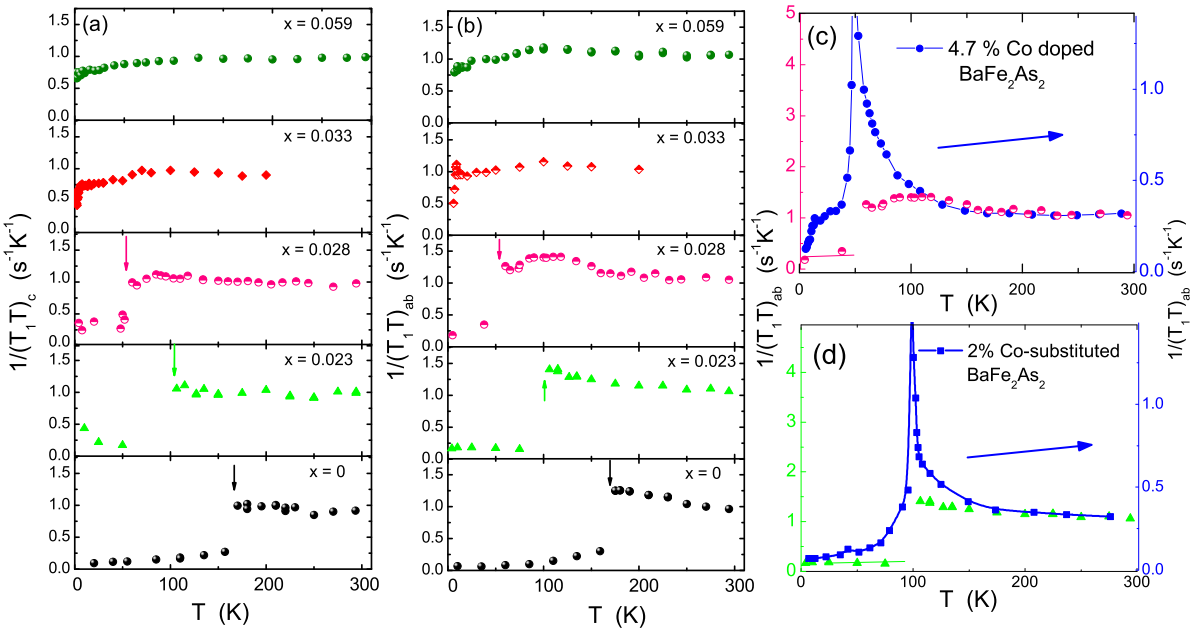

Figure 3.6 Temperature dependence of $1/T_1T$ in $Ca(Fe_{1-x}Co_x)_2As_2$. (a) $H \parallel c$ axis. (b) $H \parallel ab$ plane. The arrows indicate T_N for $x = 0$ (black), $x = 0.023$ (light green) and $x = 0.028$ (pink) determined by the magnetic susceptibility measurements. [40] In (c) and (d), we compare the temperature dependence of $(1/T_1T)_{ab}$ for $H \parallel ab$ plane in $Ca(Fe_{1-x}Co_x)_2As_2$ with that of $(1/T_1T)_{ab}$ in $Ba(Fe_{1-x}Co_x)_2As_2$. (c) $x = 0.047$ in $Ba(Fe_{1-x}Co_x)_2As_2$ with $T_N = 50$ K and $T_S = 15$ K (data from Ref. [305]), together with $x = 0.023$ in $Ba(Fe_{1-x}Co_x)_2As_2$ with $T_N = 53$ K. (d) $x = 0.02$ in $Ba(Fe_{1-x}Co_x)_2As_2$ with $T_N = 99$ K (data from Ref. [288]), together with $x = 0.028$ in $Ba(Fe_{1-x}Co_x)_2As_2$ with $T_N = 106$ K.

both H directions shows the similar behavior with those in $x < 0.023$ above ~80 K, but $1/T_1T$ starts to decrease below that temperature down to $T_N = 53$ K, suggesting a suppression of low energy spin excitations below ~80 K. In the case of superconducting samples with $x \geq 0.033$, $1/T_1T$ for both magnetic field directions is nearly constant above ~100 K but a suppression of the spin excitations can be observed below ~100 K. With a further decrease of T, $1/T_1T$ for $x = 0.033$ and 0.059 shows a sudden decrease below T_c [15 (10) K for $x = 0.033$ (0.059)] due to superconducting transitions, demonstrating not filamentary but bulk superconductivity in the system. This is consistent with the observation of clear jump at T_C in specific heat measurements. [40]

In order to see AFM spin fluctuation effects in the paramagnetic state, it is useful to re-

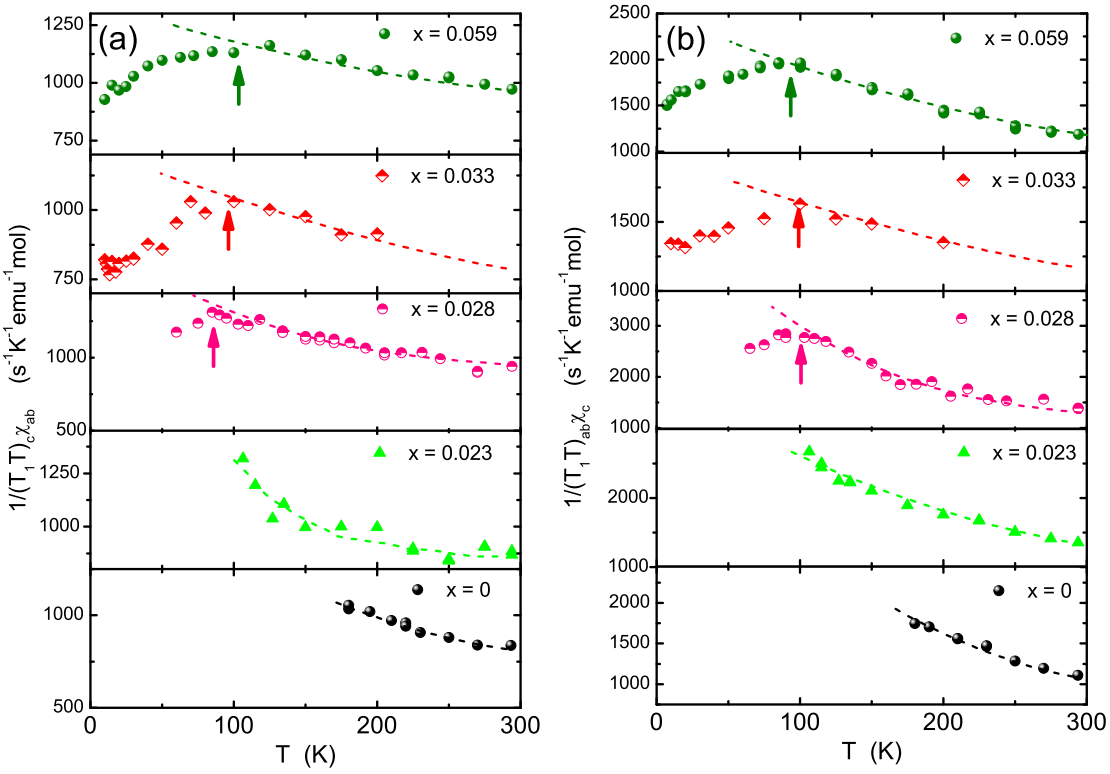

Figure 3.7 $1/T_1T\chi$ versus T in the paramagnetic state for both magnetic field directions, (a) $H \parallel c$-axis and (b) $H \parallel ab$-plane. The arrows indicate T^* as discussed in the text. The increases of $1/T_1T\chi$ observed above T^* indicates the growth of the stripe-type AFM spin correlations, while the decreases below T^* indicate the suppression of the AFM spin correlations. The dashed lines are guides for eyes.

plot the data by changing the vertical axis from $1/T_1T$ to $1/T_1T\chi$ as shown in Fig. 3.7, where the corresponding χ was used for each H direction. [40] $1/T_1T$ can be expressed in terms of the imaginary part of the dynamic susceptibility $\chi''(\vec{q},\omega_0)$ per mole of electronic spins as, [30, 298] $\frac{1}{T_1T} = \frac{2\gamma_N^2 k_B}{N_A}\sum_{\vec{q}}|A(\vec{q})|^2\frac{\chi''(\vec{q},\omega_0)}{\omega_0}$, where the sum is over the wave vectors $\vec{q}$ within the first Brillouin zone, $A(\vec{q})$ is the form factor of the hyperfine interactions and $\chi''(\vec{q},\omega_0)$ is the imaginary part of the dynamic susceptibility at the Larmor frequency ω_0.

On the other hand, the uniform χ corresponds to the real component $\chi'(\vec{q},\omega_0)$ with $q = 0$ and $\omega_0 = 0$. Thus a plot of $1/T_1T\chi$ versus T shows the T dependence of $\sum_{\vec{q}}|A(\vec{q})|^2\chi''(\vec{q},\omega_0)$ with respect to that of the uniform susceptibility $\chi'(0, 0)$. In order to eliminate effects due to impurity contributions in the magnetic susceptibilities in our analysis, we used the magnetic

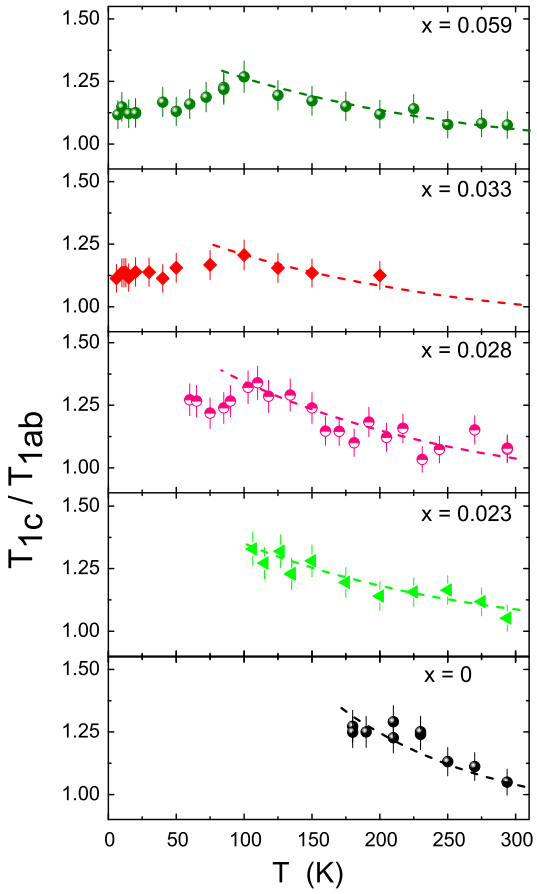

Figure 3.8 T dependence of the ratio $r \equiv T_{1,c}/T_{1,ab}$. The dashed lines are guides for eyes.

susceptibility data where impurity contributions were subtracted from the original χ data by using our Knight shift data as has been done in the $CaFe_2As_2$ (Ref. [94]). For above T_N, $1/T_1T\chi$ for $H \parallel c$-axis and $H \parallel ab$-plane in all five samples increase with decreasing temperature. The increase implies $\sum_{\vec{q}}|A(\vec{q})|^2\chi''(\vec{q},\omega_0)$ increases more than $\chi'(0,\,0)$, which is due to a growth of spin correlations with $q \neq 0$ stripe-type AFM wave vector $q = Q_{AF}$, as has been discussed in the $x = 0$ case. [42,94] However, $x \geq 0.028$, one can clearly see that $1/(T_1T\chi)$ are suppressed below a T^*-value marked by arrows. We attribute this behavior to a pseudogap phenomenon. The T^*s are nearly independent of Co substitution and are plotted in the phase diagram (Fig. 3.12). It is noted that the our definition of the pseudogap behavior is corresponding to suppressions of the spin fluctuations with only the stripe-type AFM wave vectors not from $q = 0$ components.

The suppressions in spin fluctuations with the $q = 0$ component can be seen in the temperature dependence of $K_{\rm spin}$ with nearly x-independent $\Delta/k_{\rm B} \sim 490$ K.

Based on these T_1 results, we can discuss more details of the Fe spin fluctuations in the pseudogap-like phase. According to previous NMR studies performed on Fe pnictides, [299–301] and $SrCo_2As_2$. [302] the ratio $r \equiv T_{1,c}/T_{1,ab}$ depends on AFM spin correlation modes as

$$r = \begin{cases} 0.5 + \left(\frac{S_{ab}}{S_c}\right)^2 & \text{for the stripe AFM fluctuations} \\ 0.5 & \text{for the Néel-type spin fluctuations} \end{cases} \tag{3.1}$$

where $\mathcal{S}_\alpha$ is the amplitude of the spin fluctuation spectral density at NMR frequency along the α direction. As plotted in Fig. 3.8, the r is greater than unity and, with decreasing T, r increases up to ~ 1.4 but never exceeds 1.5 even near $T_{\rm N}$ for $x < 0.028$. This means that the stripe-type AFM fluctuations along the c axis, $\mathcal{S}_c$, are stronger than the fluctuations in the ab plane, $\mathcal{S}_{ab}$, in the paramagnetic phase, although $\mathcal{S}_{ab}$ are more enhanced than $\mathcal{S}_c$ with decreasing temperature. An anisotropy in stripe-type AFM spin fluctuations is also observed in various Fe-based superconductors in the paramagnetic state [301, 303] and the r greater than 1.5 near $T_{\rm N}$ is observed in such as $SrFe_2As_2$ [299] and $LaFeAs(O_{1-x}F_x)$ [304]. This indicates that $\mathcal{S}_{ab}$ is greater than $\mathcal{S}_c$ near $T_{\rm N}$, in contrast to our results for $Ca(Fe_{1-x}Co_x)_2As_2$. In the case of $x \geq 0.028$, the r increases with decreasing temperature as in the case of $x < 0.023$, but one can see clear decrease in r below $\sim T^*$ which are due to the presence of the pseudogap-like phase: suppressions of the stripe-type AFM spin fluctuations. Interestingly, from the temperature dependence of r, the $\mathcal{S}_{ab}$ is found to be suppressed more than $\mathcal{S}_c$ in the pseudogap phase below T^*.

Finally, it is interesting to discuss magnetic fluctuations in the AFM state below $T_{\rm N}$ and compare with the case of $Ba(Fe_{2-x}Co_x)_2As_2$. As shown in Fig. 3.6, $1/T_1T$ suddenly dropped just below $T_{\rm N}$, indicating a sudden suppression of AFM magnetic fluctuations in the AFM state. This is in contrast to the case of Co-substituted $BaFe_2As_2$ where $1/T_1T$ shows divergence behaviors at $T_{\rm N}$ and, on lowering T, decreases gradually below $T_{\rm N}$ and levels off at low temperatures [see, Figs. 3.6(c) and (d)]. [288, 305] In addition, as can be seen in Fig. 3.6(c), clear suppressions of AFM spin fluctuations observed in the paramagnetic states for $x \geq 0.028$ in $Ca(Fe_{1-x}Co_x)_2As_2$ are not observed in $Ba(Fe_{1-x}Co_x)_2As_2$. [287, 288, 305] It is also

important to point out that the Fe ordered moments are robust with the Co substitution in $Ca(Fe_{1-x}Co_x)_2As_2$, contrast to the case in $Ba(Fe_{1-x}Co_x)_2As_2$. [96] Therefore, it is likely that these differences lead to these Co-substituted $CaFe_2As_2$ samples having no co-existence of AFM and SC.

3.4.3 Temperature-dependent anisotropic resistivity

In Figure 3.9, we study how the measurements in the two-probe configuration, revealing the most clear signatures of the pseudogap, as we discuss below, are affected by the two-probe technique measurements. For this purpose we compare measurements taken on samples of CaCo122 $x = 0.028$, T_a=350 °C, taken in standard four-probe contact configuration, $\rho_a(T)$, in two-probe configuration, $\rho_c(T)$ and in Montgomery technique measurements. In Montgomery technique, resistivity measurements are performed in four-probe contact scheme, as shown schematically in the left panel of Fig. 3.9. Two measurements are taken with current and potential drop along principal directions of conductivity tensor, a and c crystallographic directions. In the first measurement current is flowing between contacts 1 and 2, and potential drop is measured between contacts 3 and 4. The values determined in this way are used to calculate resistivity $R_{\rm MA} = V_{34}/I_{12}$, which is a weighted mixture of ρ_a and ρ_c, with dominant contribution of ρ_a depending on sample dimensions. Similar measurements along c-axis define resistance $R_{\rm MC} = V_{24}/I_{13}$ with dominant contribution of ρ_c. Direct comparison of measured ρ_a and $R_{\rm Ma}$ and ρ_c and $R_{\rm Mc}$ in Fig. 3.9, clearly shows that the features in $\rho_c(T)$ are observed at the same temperatures in both samples with full and partial coverage of the ab-plane with solder, thus showing that the effect of the contact stress are negligible. In the right panel we compare anisotropies determined and calculated from measurements on two different samples (ρ_a and ρ_c) and calculated in Montgomery technique measurements of the same sample. In both cases we obtain $\gamma_\rho = \rho_c/\rho_a \approx 4$ at 300 K and very similar temperature dependence with mild ≈ 4 times increase of anisotropy on cooling, clearly showing self-consistency of direct and Montgomery technique measurements of $\rho_c(T)$.

In the top three panels of Fig. 3.10 we plot temperature-dependent in-plane and inter-plane resistivity, using normalized value $\rho(T)/\rho(300K)$. These measurements were performed

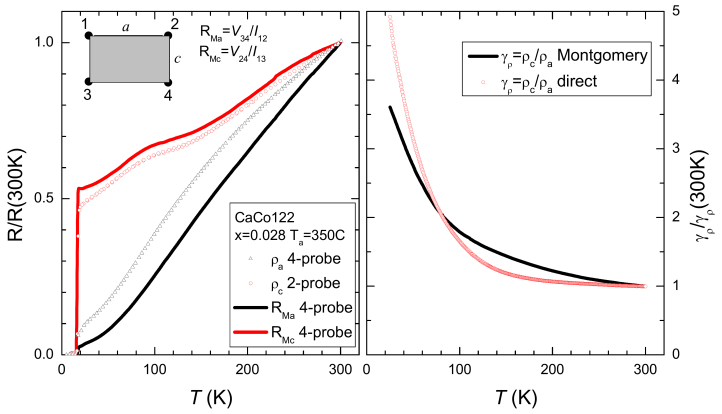

Figure 3.9 Temperature dependence of in-plane resistivity measured in CaCo122 samples of x=0.028, T_a = 350 °C in four-probe configuration (ρ_a, black triangles) and out--of-plane resistivity measured in two-probe configuration with contacts covering the whole ab-plane area (ρ_c, red open circles). For comparison we show temperature-dependent resistances measured in four-probe Montgomery configuration with contacts located at the corners of the sample as shown schematically in the left panel. $R_{\rm Ma} = V_{34}/I_{12}$ was measured with current (flowing between contacts 1 and 2) and potential difference (between contacts 3 and 4) along the a-axis in the plane, and $R_{\rm Mc} = V_{24}/I_{13}$ with current and potential drop along the c axis. All data are shown using normalized resistivity scale $R/R(300K)$. Raw Montgomery measurements represent weighted mixture of ρ_a and ρ_c with dominant contributions from respective current direction components. Comparison of $\rho_c(T)$ and $R_{MC}(T)$ directly shows that the features in the temperature dependent inter-plane resistivity are not affected by contacts covering the whole surface area of the sample. Right panel shows anisotropy ratio $\gamma_\rho \equiv \rho_c/\rho_a$, normalized to a room temperature value $\gamma_\rho \approx 4$, as determined from comparison of the direct resistivity measurements on two different samples in four- and two-probe configurations, and measurements taken in Montgomery configuration on the same sample. The data are truncated at 25 K due to noise appearing from partial contribution of superconductivity.

on samples from the same batches as used in NMR study. Both $\rho_a(T)$ and $\rho_c(T)$ show an initial metallic decrease on cooling at temperatures above the sharp, hysteretic, jump signaling first order structural-magnetic transition at $T_{\rm N}$. In the parent $x = 0$ compound, the $\rho_c(T)$ starts to increase above $T_{\rm N}$, and this increase of resistivity on cooling continues down to approximately 50 K, signaling opening of the partial gap on the Fermi surface. For $x > 0$, the increase of ρ_c starts significantly above $T_{\rm N}$ and is gradual. The sharp hysteretic feature, observed in $\rho_a(T)$ at $T_{\rm N}$, is smeared in $\rho_c(T)$ and instead gradual decrease of $\rho_c(T)$ is observed at low temperatures. The overall behavior of $\rho_c(T)$ in the $x = 0.023$ and $x = 0.028$ samples is strongly reminiscent

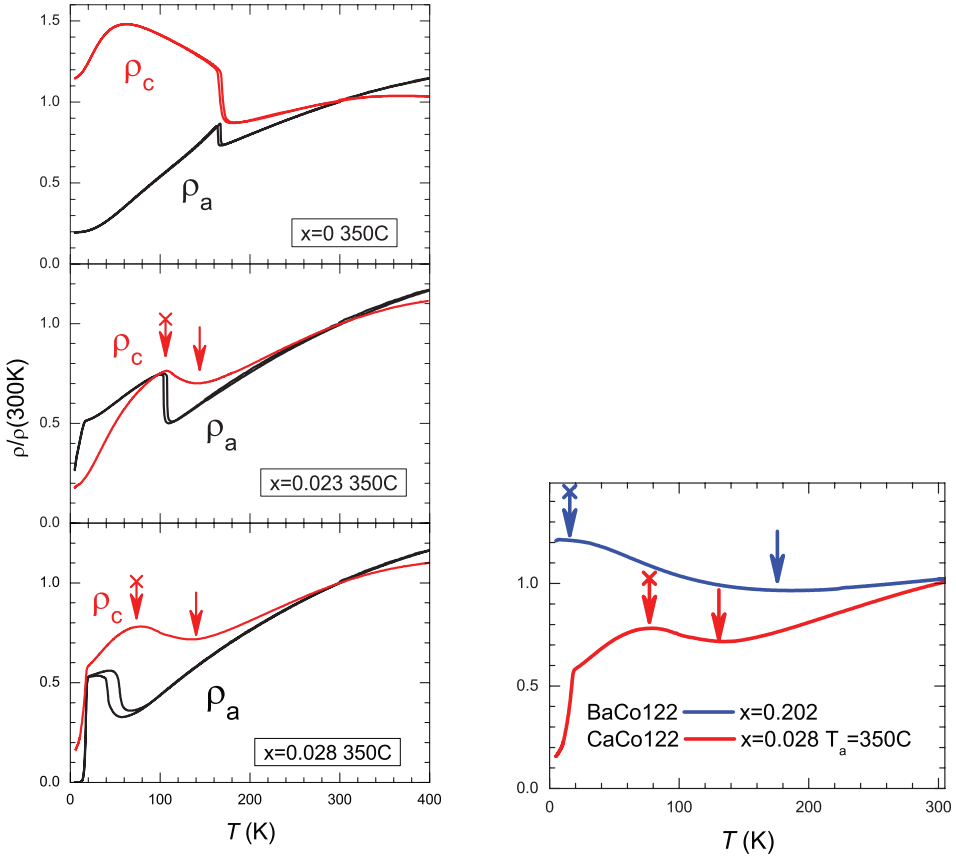

Figure 3.10 Temperature dependence of in-plane (ρ_a) and out-of-plane (ρ_c) resistivities for (top to bottom) $x = 0$ ($T_a = 400$ °C), 0.023 ($T_a = 350$ °C), and 0.028 ($T_a = 350$ °C), (same batches as used in NMR measurements). The inter-plane resistivity, $\rho_c(T)$, shows broad minimum, denoted by straight arrow, and maximum, shown with cross-arrow. In the bottom panel we compare $\rho_c(T)$ for sample $x = 0.028$ to that of the sample of $Ba(Fe_{1-x}Co_x)_2As_2$, $x = 0.202$ (non-superconducting heavily over-doped composition), showing similar features. [267]

of the dependence found in heavily over-doped $BaFe_2As_2$ compounds substituted with Co [267] and Rh [269]. Direct comparison of inter-plane resistivities for over-doped BaCo122 $x = 0.202$ and CaCo122 ($x = 0.028$, $T_a = 400$ °C) is shown in the bottom panel of Fig. 3.10. The two features on the overall metallic behavior of $\rho_c(T)$ correspond to opening of partial gap (resistivity minimum at T_{min}) and the end of carrier activation over partial gap and restoration of metallic properties at lower temperatures (resistivity maximum at T_{max}). [267, 269]

The minimum-maximum structure in the resistivity could be related to the stripe-type AFM spin fluctuations revealed by the NMR measurements. Electron scattering in the normal

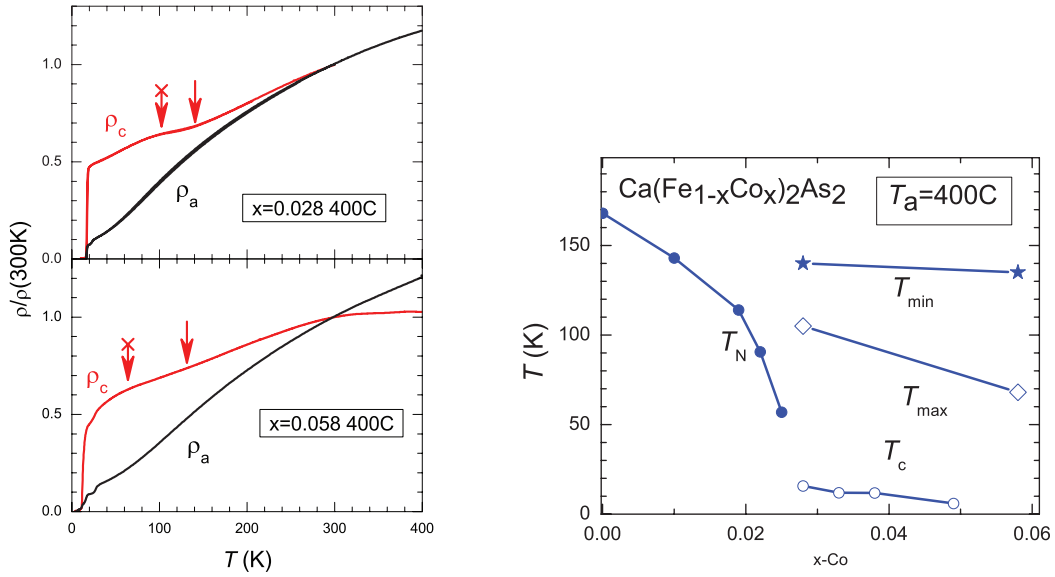

Figure 3.11 Temperature dependence of in-plane (ρ_a) and out-of-plane (ρ_c) resistivities for samples with $x = 0.028$ and 0.048 annealed at $T_a = 400$ °C. The samples are representative of superconducting and heavily over-doped non-superconducting regions. The $\rho_c(T)$ still shows minimum-maximum structure on cooling, suggesting the presence of pseudogap features through all the phase diagram. Bottom panel shows the phase diagram as determined from resistivity measurements on samples with 400 °C annealing. T_N and T_c for the samples with 400 °C annealing are from Ref. [40]

state of iron-based superconductors is predominantly magnetic [306], and transformations of magnetic correlations with temperature are reflected in temperature dependent resistivity in two ways. Since the stripe-type AFM spin fluctuations originate from interband correlations due to the multiband structure at the Fermi surface in the Fe pnictides, the opening of partial gap at the Fermi surface leading to the resistivity minimum may suppress the stripe-type AFM spin fluctuations with $q = (\pi, 0)$ or $(0, \pi)$ wavevectors as seen in the NMR measurements if the partial gap affects the interband correlations. On the other hand, a decrease of scattering at the other wavevectors would lead to a decrease in resistivity on further cooling (resistivity maximum).

NMR data suggest that pseudogap features are observed even in superconducting and heavily over-doped compositions. We were not able to find samples with $x > 0.028$, suitable for inter-plane resistivity measurements, with identical to NMR measurements annealing, $T_a = 350$

°C, conditions. Therefore we studied samples with different annealing temperature T_a = 400 °C, with $x = 0.028$ (bulk superconductivity region; T_c = 15.7 K) and $x = 0.058$ (heavily over-doped region of non-bulk superconductivity). The top panel in Fig. 3.11 shows temperature-dependent resistivity of these samples. For both compositions the minimum-maximum structure is preserved in $\rho_c(T)$, with no corresponding features in $\rho_a(T)$. In the bottom panel of Fig. 3.11 we plot phase diagram as determined from resistivity measurements on samples with T_a = 400 °C. This diagram suggests that the pseudogap features detected by the inter-plane resistivity measurements are observed in all substitution range from parent under-doped to heavily over-doped compositions. This is consistent with NMR data, though due to a broad cross-over character of the features and the ambiguity of the criteria for the definitions of the characteristic temperatures, there is no direct correspondence between the two. Additional source of discrepancy between two data sets can come from difference of characteristic time scale of the two measurements. Resistivity measurements see magnetic correlations on a time scale of scattering time (of order of 10^{-12} sec), while NMR measurements probe correlations at a much longer time scale (of order of 10^{-6} sec). It is natural then to expect that the appropriate features happen at somewhat lower temperatures in NMR measurements, which seems to be the case. Further studies for detail relationship between the resistivity minimum-maximum structure and the stripe-type AFM spin fluctuations are of clear interest.

3.5 Summary

Co substitution effects on static and dynamic magnetic properties of the single-crystalline $Ca(Fe_{1-x}Co_x)_2As_2$ (x = 0, 0.023, 0.028, 0.033, 0.059) have been investigated by ^{75}As nuclear magnetic resonance (NMR) and resistivity measurements. As in the case of $x = 0$ (T_N = 170 K), clear evidence for the first order structural and stripe-type antiferromagnetic (AFM) is observed from the sudden change in nuclear quadrupolar frequency (ν_Q) and internal field (H_{int}) at As sites in $x = 0.023$ (T_N = 106 K) and $x = 0.028$ (T_N = 53 K). In the stripe-type AFM state, for magnetic field H parallel to the c axis, the observed clear separations of ^{75}As NMR lines due to the internal field H_{int} indicate the commensurate stripe-type AFM state in the Co substituted crystals in $x = 0.023$ (T_N = 106 K) and $x = 0.028$ (T_N = 53 K), as in the

case of $x = 0$ ($T_N = 170$ K), similar to the case of Co/Ni substituted $BaFe_2As_2$. Although T_N is strongly suppressed from 170 K ($x = 0$) to $x = 0.023$ ($T_N = 106$ K) and $x = 0.028$ ($T_N = 53$ K) with Co substitution, H_{int} decreases only slightly from 2.64 T to 2.35 T and 2.25 T respectively, suggesting robustness of the Fe magnetic moments upon Co substitution in $Ca(Fe_{1-x}Co_x)_2As_2$. In the paramagnetic state, the temperature dependence of Knight shift K for all crystals shows similar temperature dependence of magnetic susceptibility, where the temperature dependent part of K can be fitted with a thermal activation behavior of $\exp(-\Delta/k_BT)$ with nearly x independent $\Delta/k_B \sim 490$ K. These results indicate that spin fluctuations with the $q = 0$ components are suppressed with $\Delta/k_B \sim 490$ K in the paramagnetic state.

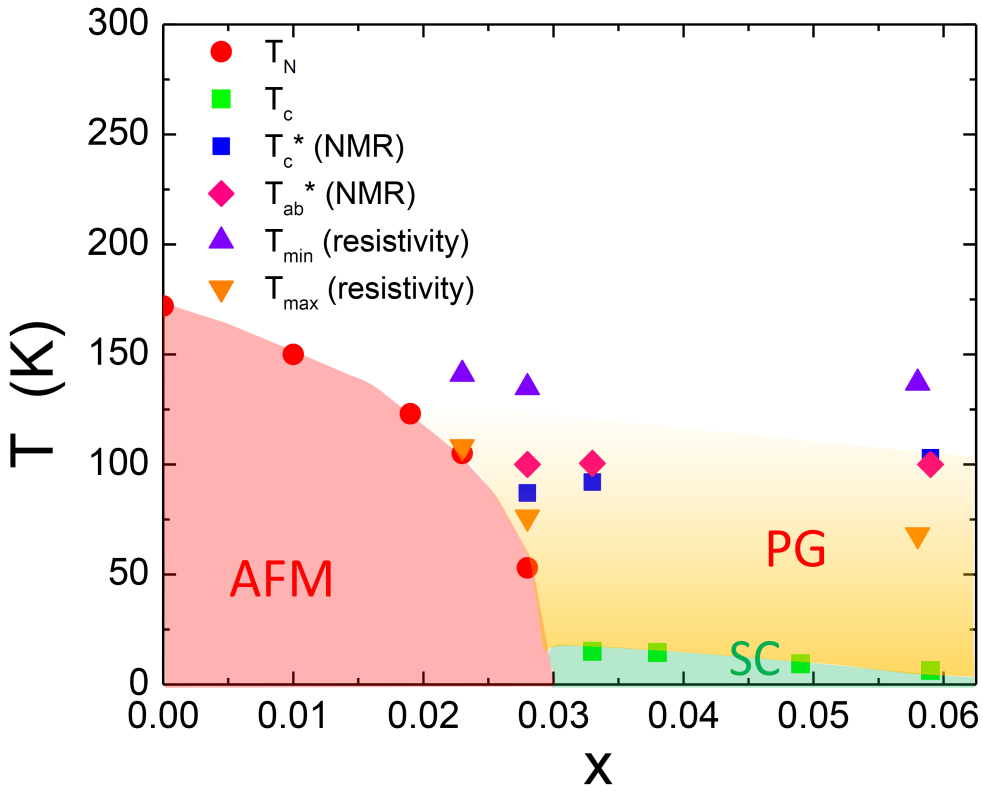

Figure 3.12 Phase diagram of $Ca(Fe_{1-x}Co_x)_2As_2$. T_N and T_c are from Ref. [40]. The crossover temperature T^*_{ab} and T^*_c are determined by NMR measurements for $H \parallel ab$ plane and $H \parallel c$ axis, respectively. T_{max} and T_{min} are estimated from the inter-plane resistivity measurements for the crystals annealed at $T_a = 350$ °C except for $x = 0.058$ with $T_a = 400$ °C. AFM, SC and PG stand for the antiferromagnetic ordered state, superconducting, and pseudogap-like phases, respectively.

On the other hand, the growth of the stripe-type AFM fluctuations with $q = (\pi, 0)$ or $(0, \pi)$ on lowering temperature in the paramagnetic state for all five crystals is evidenced by the temperature dependence of the nuclear spin lattice relaxation rates divided by temperature and magnetic susceptibility ($1/T_1T\chi$). In addition, above $x \geq 0.028$, $1/T_1T\chi$ is found to show a gradual decrease with decreasing T below T^*, a crossover temperature, corresponding to suppression of the stripe-type AFM fluctuations; attributed to the behavior of pseudogap-like phenomenon. As shown in Fig. 3.12, $T^* \sim 100$ K is almost independent of x. It is pointed out that the pseudogap-like phenomenon seems to affect on the temperature-dependent inter-plane resistivity, $\rho_c(T)$, but not with in-plane resistivity $\rho_a(T)$. The ratio of $1/T_1$ for magnetic fields H parallel to the ab plane and to the c axis, that is, $r = (T_1)_c/(T_1)_{ab}$, increases with decreasing T and starts to decreases below T^*. This indicates that the amplitude of stripe-type AFM fluctuations in the ab plane ($\mathcal{S}_{ab}$) is more enhanced than that along the c axis ($\mathcal{S}_c$) above T^*, but $\mathcal{S}_{ab}$ is more suppressed than $\mathcal{S}_c$ in the pseudogap-like phase. Further detailed studies on the pseudogap-like phase in $Ca(Fe_{1-x}Co_x)_2As_2$ will be required to shed the light on, using other experimental techniques such as inelastic neutron scattering measurements having different energy scale from NMR technique.

3.6 Acknowledgments

The work was supported by the U.S. Department of Energy (DOE), Office of Basic Energy Sciences, Division of Materials Sciences and Engineering. The research was performed at Ames Laboratory, which is operated for the U.S. DOE by Iowa State University under Contract No. DE-AC02-07CH11358.

CHAPTER 4. COEXISTENCE OF ANTIFERROMAGNETIC AND FERROMAGNETIC SPIN CORRELATIONS IN $CA(FE_{1-X}CO_X)_2AS_2$ REVEALED BY ^{75}AS NUCLEAR MAGNETIC RESONANCE

A paper published in Physical Review B **94**,174512 (2016)

J. Cui,[1,2] P. Wiecki,[1,3] S. Ran,[1,3] S. L. Bud'ko,[1,3] P. C. Canfield,[1,3] and Y. Furukawa[1,3]

1 Ames Laboratory, U.S. DOE, Ames, Iowa 50011, USA

2 Department of Chemistry, Iowa State University, Ames, Iowa 50011, USA

3 Department of Physics and Astronomy, Iowa State University, Ames, Iowa 50011, USA

4.1 Abstract

Recent nuclear magnetic resonance (NMR) measurements revealed the coexistence of stripe-type antiferromagnetic (AFM) and ferromagnetic (FM) spin correlations in both the hole- and electron-doped $BaFe_2As_2$ families of iron-pnictide superconductors by a Korringa ratio analysis. Motivated by the NMR work, we investigate the possible existence of FM fluctuations in another iron pnictide superconducting family, $Ca(Fe_{1-x}Co_x)_2As_2$. We re-analyzed our previously reported data in terms of the Korringa ratio and found clear evidence for the coexistence of stripe-type AFM and FM spin correlations in the electron-doped $CaFe_2As_2$ system. These NMR data indicate that FM fluctuations exist in general in iron-pnictide superconducting families and thus must be included to capture the phenomenology of the iron pnictides.

4.2 Introduction

Since the discovery of high T_c superconductivity in iron pnictides, [10] the interplay between spin fluctuations and the unconventional nature of superconductivity (SC) has been attracting

much interest. In most of the Fe pnictide superconductors, the "parent" materials exhibit antiferromagnetic ordering below the Néel temperature. [30, 254, 255] SC in these compounds emerges upon suppression of the stripe-type antiferromagnetic (AFM) phase by application of pressure and/or chemical substitution, where the AFM spin fluctuations are still strong. Therefore, it is believed that stripe-type AFM spin fluctuations play an important role in driving the SC in the iron-based superconductors, although orbital fluctuations are also pointed out to be important. [307]

Recently nuclear magnetic resonance (NMR) measurements revealed that ferromagnetic (FM) correlations also play an important role in both the hole- and electron-doped $BaFe_2As_2$ families of iron-pnictide superconductors. [30, 305, 308] The FM fluctuations are found to be strongest in the maximally-doped $BaCo_2As_2$ and KFe_2As_2, but are still present in the $BaFe_2As_2$ parent compound, consistent with its enhanced magnetic susceptibility χ. [30] These FM fluctuations are suggested to compete with superconductivity and are a crucial ingredient to understand the variation of T_c and the shape of the SC dome. [305] It is interesting and important to explore whether or not similar FM correlations exist in other iron pnictide systems.

The $CaFe_2As_2$ family has a phase diagram distinct from that for the $BaFe_2As_2$ family. Whereas for the $BaFe_2As_2$ materials the AFM and orthorhombic phase transitions become second order with Co substitution, the $CaFe_2As_2$ family continues to manifest a strongly first order, coupled, structural-magnetic phase transition even as Co substitution suppresses the transition temperature to zero. Another significant difference in the phase diagrams of the $CaFe_2As_2$ and $BaFe_2As_2$ systems is also found in superconducting phase. Although SC appears when the stripe-type AFM phase is suppressed by Co substitution for Fe in both cases, no coexistence of SC and AFM has been observed in $Ca(Fe_{1-x}Co_x)_2As_2$, whereas the coexistence has been reported in $Ba(Fe_{1-x}Co_x)_2As_2$. These results are consistent with the difference between a strongly first order versus second order phase transition. Recent NMR measurements revealed that the stripe-type AFM fluctuations are strongly suppressed in the AFM state in the Co-doped $CaFe_2As_2$ system, whereas sizable stripe-type AFM spin fluctuations still remain in the AFM state in the Co-doped $BaFe_2As_2$ system. [98] These results indicate that the residual AFM spin fluctuations play an important role for the coexistence of AFM and

SC in $Ba(Fe_{1-x}Co_x)_2As_2$. Furthermore, in the case of $Ca(Fe_{1-x}Co_x)_2As_2$, pseudogap-like behavior [98] has been observed in the temperature dependence of $1/T_1T$ and in-plane resistivity. The characteristic temperature of the pseudogap was reported to be nearly independent of Co substitution. [98]

In this paper, we investigated the possible existence of FM fluctuations in $Ca(Fe_{1-x}Co_x)_2As_2$ and found the clear evidence of coexistence of stripe-type AFM and FM correlations based on ^{75}As NMR data analysis. In contrast to the case of $Ba(Fe_{1-x}Co_x)_2As_2$ where the relative strength of FM correlations increases with Co substitution, that of the FM correlations is almost independent of the Co content in $Ca(Fe_{1-x}Co_x)_2As_2$ from $x = 0$ to 0.059. Although we have investigated a relatively small Co substitution region, the existence of the FM spin correlations would be consistent with the fact that $CaCo_2As_2$, the end member of the electron doped $Ca(Fe_{1-x}Co_x)_2As_2$ family of compounds, has an A-type antiferromagnetic ordered state below $T_N = 52$–76 K [309, 310] where the Co moments within the CoAs layer are ferromagnetically aligned along the c axis and the moments in adjacent layers are aligned antiferromagnetically. Since the coexistence of FM and AFM spin correlations are observed in both the hole- and electron-doped $BaFe_2As_2$ systems, [305] our results suggest that the FM fluctuations exist in general in iron pnictide superconductors, indicating that theoretical microscopic models should include FM correlations to incorporate all features of the iron pnictides.

4.3 Experimental

The single crystals of $Ca(Fe_{1-x}Co_x)_2As_2$ ($x = 0$, 0.023, 0.028, 0.033 and 0.059) used in the present study are from the same batches as reported in Ref. [98]. These single crystals were grown out of a FeAs/CoAs flux, [40, 261] using conventional high temperature growth techniques. [279, 280] Subsequent to growth, the single crystals were annealed at $T_a = 350$ °C for 7 days and then quenched. For $x = 0$, the single crystal was annealed at $T_a = 400$ °C for 24 hours. Details of the growth, annealing and quenching procedures have been reported in Refs. [261] and [40]. The stripe-type AFM states have been reported below the Néel temperatures $T_N =$ 170, 106, and 53 K for $x = 0$, 0.023, and 0.028, respectively. [42] The superconducting states are observed below the transition temperature of $T_c = 15$ and 10 K for $x = 0.033$ and 0.059,

respectively. [40]

NMR measurements were carried out on ^{75}As ($I = 3/2$, $\gamma/2\pi = 7.2919$ MHz/T, $Q = 0.29$ Barns) by using a lab-built, phase-coherent, spin-echo pulse spectrometer. The ^{75}As-NMR spectra were obtained at a fixed frequency $f = 53$ MHz by sweeping the magnetic field. The magnetic field was applied parallel to either the crystal c axis or the ab plane where the direction of the magnetic field within the ab plane was not controlled. The ^{75}As $1/T_1$ was measured with a recovery method using a single $\pi/2$ saturation rf pulse. The $1/T_1$ at each T was determined by fitting the nuclear magnetization M versus time t using the exponential function $1 - M(t)/M(\infty) = 0.1e^{-t/T_1} + 0.9e^{-6t/T_1}$, where $M(t)$ and $M(\infty)$ are the nuclear magnetization at time t after the saturation and the equilibrium nuclear magnetization at $t \to \infty$, respectively. Most of the NMR experimental results were published elsewhere. [94, 98]

4.4 Results and discussion

In this paper we discuss magnetic correlations in $Ca(Fe_{1-x}Co_x)_2As_2$ based on a Korringa ratio analysis of the NMR results. Fig. 4.1(a) shows the x and T dependence of the Knight shifts, K_{ab} for H parallel to the ab plane and K_c for H parallel to the c axis, where new Knight shift data for $x = 0.033$ and 0.059 are plotted in addition to the data ($x = 0$, 0.023 and 0.028) reported previously. [94, 98]

The NMR shift consists of a T-independent orbital shift K_0 and a T-dependent spin shift $K_{spin}(T)$ due to the uniform magnetic spin susceptibility $\chi(\mathbf{q} = 0)$ of the electron system. The NMR shift can therefore be expressed as $K(T) = K_0 + K_{spin}(T) = K_0 + A_{hf}\chi_{spin}/N$, where N is Avogadro's number, and A_{hf} is the hyperfine coupling constant, usually expressed in units of T/μ_B. As reported in Ref. [98], the temperature-dependent part of Knight shift K_{spin} was reproduced by thermally activated behavior$K_{spin} \sim \exp(-\Delta/k_BT)$ with a nearly x independent of $\Delta/k_B \sim 490 - 510$ K. In order to extract $K_{spin}(T)$, which is needed for the following Korringa ratio analysis, we plot $K(T)$ against the corresponding bulk static uniform magnetic susceptibility $\chi(T)$ with T as an implicit parameter as shown in Fig. 4.1(b). From the slope of the linear fit curve, the hyperfine coupling constant can be estimated. The hyperfine coupling constants for $H||c$ and $H||ab$ are estimated to be $A_c = (-12.2 \pm 2.0)$ kOe/μ_B/Fe,

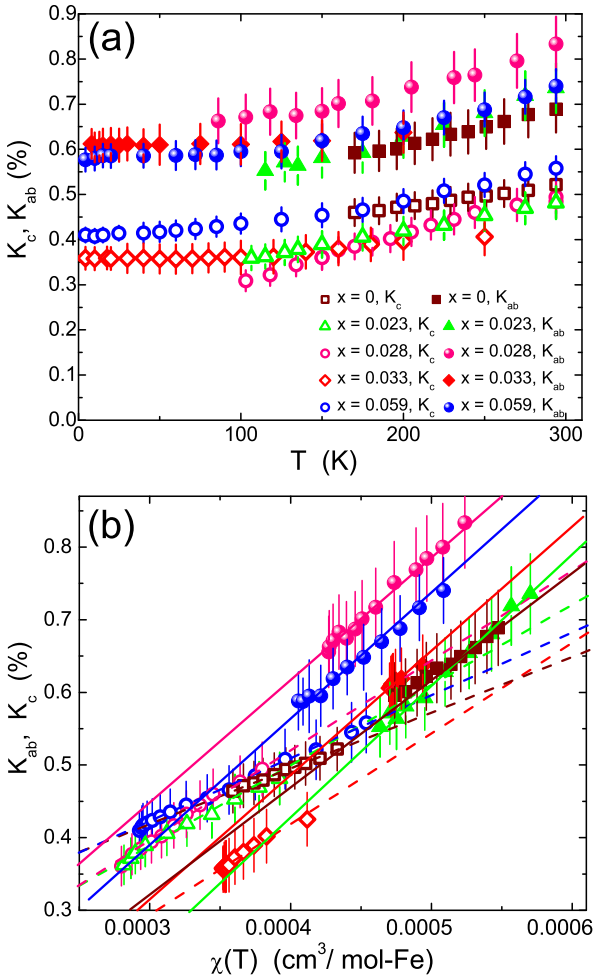

Figure 4.1 (a) Temperature dependence of ^{75}As NMR shifts of $Ca(Fe_{1-x}Co_x)_2As_2$. (b) $K(T)$ versus magnetic susceptibility $\chi(T)$ plots for the corresponding ab and c components of K in $Ca(Fe_{1-x}Co_x)_2As_2$ with T as an implicit parameter. The solid and broken lines are linear fits.

(-14.6 ± 1.4) kOe/μ_B/Fe, (-15.7 ± 1.4) kOe/μ_B/Fe, (-15.1 ± 1.5) kOe/μ_B/Fe, and (-13.3 ± 2.0) kOe/μ_B/Fe and $A_{ab} = (-17.9 \pm 2.2)$ kOe/μ_B, (-19.0 ± 2.0) kOe/μ_B/Fe, (-20.5 ± 3.0) kOe/μ_B/Fe, (-18.2 ± 1.8) kOe/μ_B/Fe and (-20.3 ± 2.7) kOe/μ_B/Fe for $x = 0$, 0.023, 0.028, 0.033 and 0.059, respectively. The nearly x independent hyperfine coupling constants have been reported in Ref. [98]. From the y-intercept of the linear fit curve, one can estimate the orbital shift K_0, and extract $K_{spin}(T)$ to discuss magnetic correlations.

A Korringa ratio analysis is applied to extract the character of spin fluctuations in $Ca(Fe_{1-x}Co_x)_2As_2$ from ^{75}As NMR data as has been carried out for both the electron-doped $Ba(Fe_{1-x}Co_x)_2As_2$

and hole-doped $Ba_{1-x}K_xFe_2As_2$ families of iron-pnictide SCs. [305] Within a Fermi liquid picture, $1/T_1T$ is proportional to the square of the density of states $\mathcal{D}(E_F)$ at the Fermi energy and $K_{spin}(\propto \chi_{spin})$ is proportional to $\mathcal{D}(E_F)$. In particular, $T_1TK^2_{spin} = \frac{\hbar}{4\pi k_B}\left(\frac{\gamma_e}{\gamma_N}\right)^2 = \mathcal{S}$, which is the Korringa relation. For the ^{75}As nucleus ($\gamma_N/2\pi = 7.2919$ MHz/T), $\mathcal{S} = 8.97 \times 10^{-6}$ Ks. The Korringa ratio $\alpha \equiv \mathcal{S}/(T_1TK^2_{spin})$, which reflects the deviations from $\mathcal{S}$, can reveal information about how electrons correlate in the material. [298, 311] $\alpha \sim 1$ represents the situation of uncorrelated electrons. On the other hand, $\alpha > 1$ indicates AFM correlations while $\alpha < 1$ for FM correlations. These come from the enhancement of $\chi(\mathbf{q} \neq 0)$, which increases $1/T_1T$ but has little or no effect on K_{spin}, since the latter probes only the uniform $\chi(\mathbf{q} = 0)$. Therefore, the predominant feature of magnetic correlations, whether AFM or FM, can be determined by the Korringa ratio α.

To proceed with the Korringa ratio analysis, one needs to take the anisotropy of K_{spin} and $1/T_1T$ into consideration. $1/T_1$ picks up the hyperfine field fluctuations at the NMR Larmor frequency, ω_0, perpendicular to the applied field according to $(1/T_1)_{H||i} = \gamma_N^2\left[|H_j^{hf}(\omega_0)|^2 + |H_k^{hf}(\omega_0)|^2\right]$, where (i, j, k) are mutually orthogonal directions and $|H_j^{hf}(\omega_0)|^2$ represents the power spectral density of the j-th component of the hyperfine magnetic field at the nuclear site. Thus, defining $H_{ab}^{hf} \equiv H_a^{hf} = H_b^{hf}$, which is appropriate for the tetragonal paramagnetic (PM) state, we have $(1/T_1)_{H||c} = 2\gamma_N^2|H_{ab}^{hf}(\omega_0)|^2 \equiv 1/T_{1,\perp}$. The Korringa parameter $\alpha_\perp \equiv \mathcal{S}/T_{1,\perp}TK^2_{spin,ab}$ will then characterize fluctuations in the ab-plane component of the hyperfine field. Similarly, we consider the quantity $1/T_{1,\parallel} \equiv 2(1/T_1)_{H||ab} - (1/T_1)_{H||c} = 2\gamma_N^2|H_c^{hf}(\omega_N)|^2$, since $(1/T_1)_{H||ab} = \gamma_N^2\left[|H_{ab}^{hf}(\omega_N)|^2 + |H_c^{hf}(\omega_N)|^2\right]$. We then pair $K_{spin,c}$ with $1/T_{1,\parallel}$, so that the Korringa parameter $\alpha_\parallel = \mathcal{S}/T_{1,\parallel}TK^2_{spin,c}$ characterizes fluctuations in the c-axis component of the hyperfine field.

Figure 4.2 shows the temperature dependence of $1/T_{1,\perp}T$ and $1/T_{1,\parallel}T$ in $Ca(Fe_{1-x}Co_x)_2As_2$ at $H \sim 7.5$ T, obtained from the $(1/T_1T)_{H||ab}$ and $(1/T_1T)_{H||c}$ data reported previously. [98] For $x = 0$ and 0.023, $1/T_{1,\parallel}T$s show a monotonic increase with decreasing T down to $T_N = 170$ K and 106 K for $x = 0$ and 0.023, respectively, while $1/T_{1,\perp}T$s are nearly independent of T although the slight increase can be seen near T_N for each sample. Since the increase of $1/T_{1,\parallel}T$s originates from the growth of the stripe-type AFM spin fluctuations, [98] the results indicate

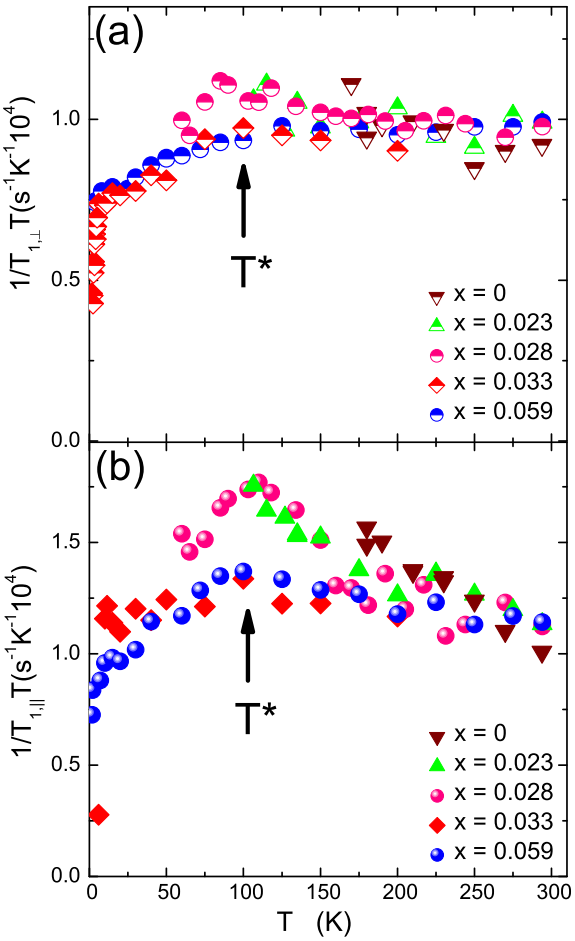

Figure 4.2 Temperature dependence of $1/T_1T$ with anisotropy in $Ca(Fe_{1-x}Co_x)_2As_2$. (a) $1/T_{1,\perp} = (1/T_1T)_{H||c}$. (b) $1/T_{1,\parallel}T = 2(1/T_1T)_{H||ab} - (1/T_1T)_{H||c}$. The arrows indicate a cross-over temperature $T^* \sim 100$ K. Below T^*, both $1/T_{1,\perp}$ and $1/T_{1,\parallel}T$ decrease due to the suppression of the stripe-type AFM spin correlations, pseudogap-like behavior defined in the text.

that the AFM spin fluctuations enhance the hyperfine fluctuations at the As sites along the c axis. At $x = 0.028$ ($T_N = 53$ K), both $1/T_{1,\parallel}T$ and $1/T_{1,\perp}T$ show similar behavior with those in $x = 0$ and 0.023 above $T^* \sim 100$ K (marked by arrows) from room temperature as shown in Fig. 4.2. However, below T^*, both $1/T_{1,\parallel}T$ and $1/T_{1,\perp}T$ decrease slightly upon cooling. The reduction in both $1/T_{1,\parallel}T$ and $1/T_{1,\perp}T$ below the crossover temperature T^* has been explained by the suppression of the stripe-type AFM spin fluctuations and has been ascribed to pseudogap-like behavior in Ref. [98]. In the case of the superconducting samples with $x \geq 0.033$, both $1/T_{1,\perp}T$ and $1/T_{1,\parallel}T$ show a slight increase or constant above $T^* \sim 100$ K on

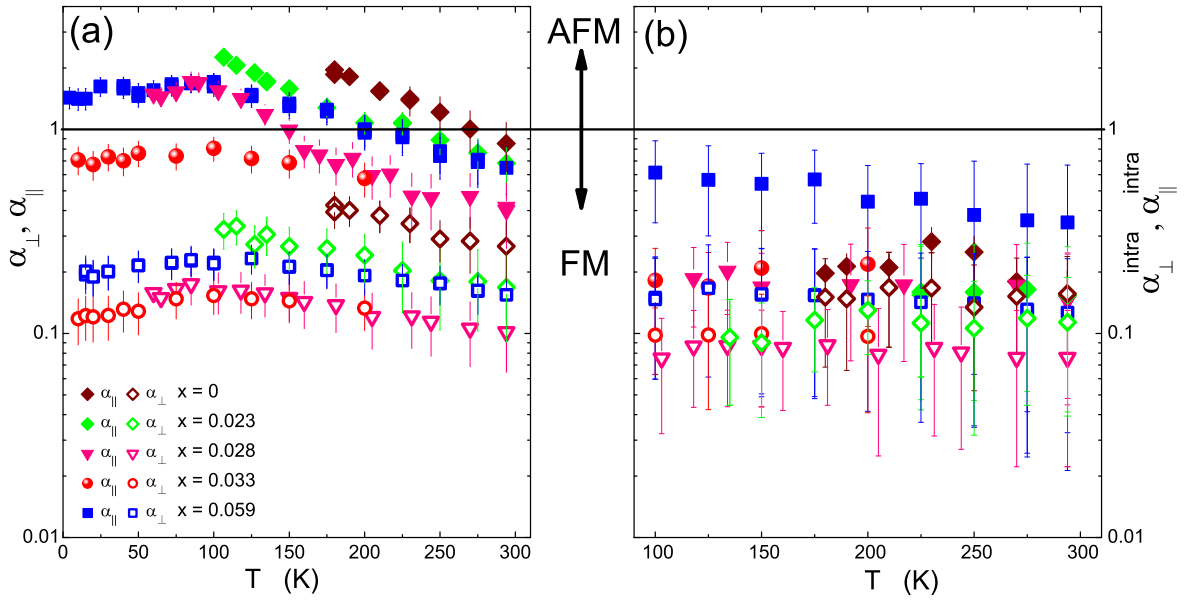

Figure 4.3 (a) T dependence of Korringa ratios, $\alpha_\perp$ and $\alpha_\parallel$. (b) T dependence of intraband Korringa ratios, $\alpha_\perp^{\rm intra}$and $\alpha_\parallel^{\rm intra}$, above $T_{\rm N}$ or T^*, obtained by subtracting a CW term from the temperature dependence of $1/T_{1,\perp}T$ and $1/T_{1,\parallel}T$ as described in the text.

cooling and then show the similar pseudogap-like behavior observed in $x = 0.028$ below T^*. As described in Ref. [98], the pseudogap-like behavior in $Ca(Fe_{1-x}Co_x)_2As_2$ is defined by the suppression of the stripe-type AFM spin fluctuations only. With a further decrease in T, both $1/T_{1,\parallel}T$ and $1/T_{1,\perp}T$ show sudden decreases below $T_{\rm c}$ [15 (10) K for $x = 0.033$ (0.059)] due to superconducting transitions.

Using the $1/T_{1,\perp}T$, $1/T_{1,\parallel}T$ data and Knight shift data, we discuss magnetic correlations in $Ca(Fe_{1-x}Co_x)_2As_2$ based on the Korringa ratios. The T dependences of the Korringa ratios $\alpha_\perp = \mathcal{S}/T_{1,\perp}TK^2_{{\rm spin},ab}$ and $\alpha_\parallel = \mathcal{S}/T_{1,\parallel}TK^2_{{\rm spin},c}$ are shown in Fig. 4.3(a). All $\alpha_\parallel$ and $\alpha_\perp$ increase with decreasing T down to $T_{\rm N}$ or T^*. The increase in α, which is the increase in $1/T_1TK^2$, clearly indicates the growth of the stripe-type AFM spin correlations as have been pointed out previously. [98] It is noted that $\alpha_\parallel$ is always greater than $\alpha_\perp$ for each sample, indicating that hyperfine field fluctuations parallel to the c axis at the As sites originated from the stripe-type AFM spin correlations (in-plane) are stronger than those perpendicular to the c axis, as described in more detail below. On the other hand, $\alpha_\perp$ values seem to be less than unity: the largest value of $\alpha_\perp$ can be found to be ~0.4 in $x = 0$. The even smaller values $\alpha_\perp$ of

0.1 – 0.2 in $x = 0.023$ and 0.028 at high temperatures are observed, suggesting dominant FM fluctuations in the normal state.

In the application of the Korringa ratio to the iron pnictides, the question arises as to the role of the hyperfine form factor, which can, in principle, filter out the AFM fluctuations at the As site. This filtering effect could affect the balance of FM vs. AFM fluctuations as measured by the Korringa ratio. [312] In order to discuss the filtering effects, it is convenient to express $1/T_1$ in terms of wave-number ($\mathbf{q}$) dependent form factors and $\mathbf{q}$ dependent dynamical spin susceptibility $\chi(\mathbf{q}, \omega_0)$. By an explicit calculation of the form factors (see Appendix A) using the methods of Ref. [313], we find that

$$\frac{1}{T_{1,\parallel}T} \sim \left[\left(2.7\frac{\mathrm{T}^2}{\mu_\mathrm{B}^2}\right)\frac{\chi''_{ab}(\mathbf{Q},\omega_0)}{\hbar\omega_0} + \left(1.5\frac{\mathrm{T}^2}{\mu_\mathrm{B}^2}\right)\frac{\chi''_c(\mathbf{0},\omega_0)}{\hbar\omega_0}\right], \tag{4.1}$$

$$\frac{1}{T_{1,\perp}T} \sim \left[\left(3.2\frac{\mathrm{T}^2}{\mu_\mathrm{B}^2}\right)\frac{\chi''_{ab}(\mathbf{0},\omega_0)}{\hbar\omega_0} + \left(1.4\frac{\mathrm{T}^2}{\mu_\mathrm{B}^2}\right)\frac{\chi''_c(\mathbf{Q},\omega_0)}{\hbar\omega_0}\right] \tag{4.2}$$

where $\chi''(\mathbf{0}, \omega_0)$ and $\chi''(\mathbf{Q}, \omega_0)$ represent the imaginary part of the dynamical susceptibility for $\mathbf{q} = 0$ ferromagnetic and $\mathbf{Q} = (\pi, 0)/(0, \pi)$ stripe-type AFM components, respectively. The numbers are calculated from the hyperfine coupling constants in units of $\mathrm{T}/\mu_\mathrm{B}$ for $CaFe_2As_2$ given in Ref. [98]. From these equations, it is clear that the stripe-type AFM fluctuations are not filtered out for either direction in the iron pnictides. It is also seen that for $1/T_{1,\parallel}T$, the form factor favors AFM fluctuations, which explains the larger (more AFM) values of $\alpha_\parallel$. On the other hand, for $1/T_{1\perp}T$, the ferromagnetic fluctuations dominate more than the AFM fluctuations as actually seen in Fig. 4.3(a) where $\alpha_\perp$ is less than $\alpha_\parallel$ for each sample.

Now we consider the origin of the hyperfine field at the ^{75}As site in order to further understand the physics associated with each term in Eqs. (4.1) and (4.2). The hyperfine field at the ^{75}As site is determined by the spin moments on the Fe sites through the hyperfine coupling tensor $\tilde{A}$, according to $\mathbf{H}^{\mathrm{hf}} = \tilde{A} \cdot \mathbf{S}$. In the tetragonal PM phase, the most general form for $\tilde{A}$ is [86, 301]

$$\tilde{A} = \begin{pmatrix} A_\perp & D & B \\ D & A_\perp & B \\ B & B & A_c \end{pmatrix}, \tag{4.3}$$

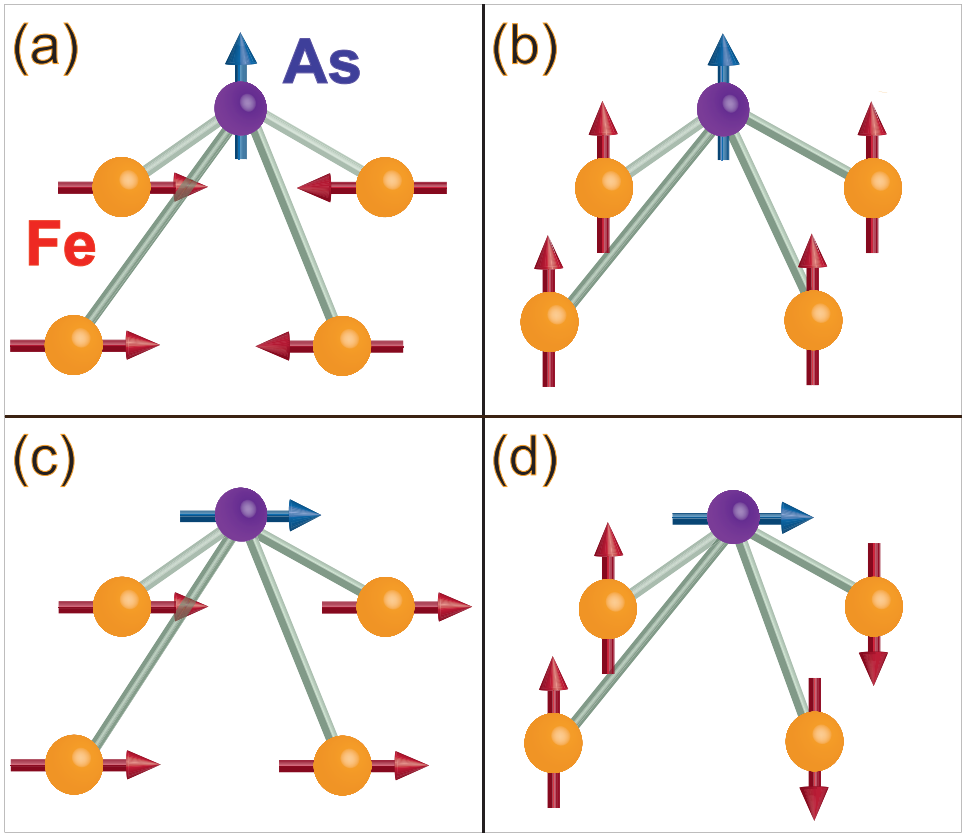

Figure 4.4 (a),(b): Sources of hyperfine field along the c-axis. (c),(d): Sources of hyperfine field in the ab-plane.

where A_i is the coupling for FM correlation, D is the coupling for in-plane Neél-type AFM correlation and B is coupling for stripe-type AFM correlations. Since there is no theoretical or experimental reason to expect Neél-type AFM correlation in the iron pnictides, below we simply set $D = 0$. We then obtain $H_{\perp}^{\rm hf} = A_{\perp}S_{\perp} + BS_{\rm c}$ and $H_{\rm c}^{\rm hf} = 2BS_{\perp} + A_{\rm c}S_{\rm c}$. There are therefore two sources of hyperfine field pointing along the c axis [86]: fluctuations at $\mathbf{q} = \mathbf{Q} = (\pi, 0)/(0, \pi)$ with the spins pointing in plane (as illustrated in Fig. 4.4(a)) or fluctuations at $\mathbf{q} = 0$ with the spins pointing along the c axis (Fig. 4.4(b)). The first and second fluctuations correspond to the first and second terms, respectively, in $1/T_{1,\parallel}T$ [Eq. (4.1)]. Similarly, hyperfine field fluctuations in the ab plane can result from fluctuations at $\mathbf{q} = 0$ with the spins pointing in plane (Fig. 4.4(c)), or from fluctuations at $\mathbf{q} = \mathbf{Q}$ with the spins pointing along the c axis (Fig. 4.4(d)). Again, the first and second fluctuations can be attributed to the first and second terms, respectively, in $1/T_{1,\perp}T$ [Eq. (4.2)]. In what follows, we will refer to the correlations

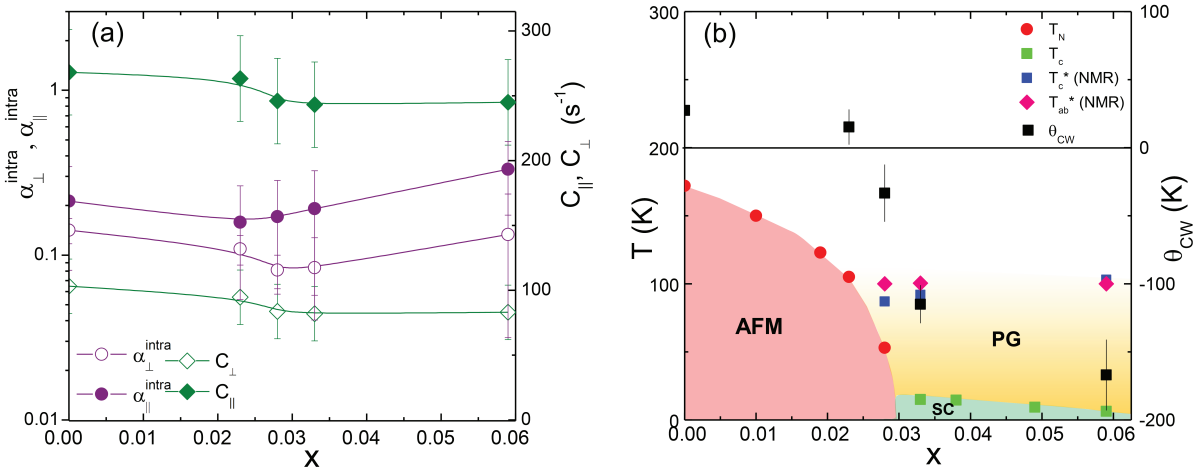

Figure 4.5 (a) Doping dependence of the T-independent values of $\alpha_{\perp}^{\rm intra}$, $\alpha_{\parallel}^{\rm intra}$ and Curie-Weiss parameters $C_{\perp}$, $C_{\parallel}$ The lines are guide for eyes. (b) Doping dependence of $\Theta_{\rm CW}$ together with phase diagram of $Ca(Fe_{1-x}Co_x)_2As_2$ reported in Ref. [98]. $T_{\rm N}$ and $T_{\rm c}$ are from Ref. [40]. The pseudogap crossover temperature T_{ab}^* and T_c^* are determined by NMR measurements for $H \parallel ab$ plane and $H \parallel c$ axis, respectively. The pseudogap-like behavior in the present paper is defined, as in Ref. [98], by the suppression of the spin fluctuations with only stripe-type AFM wave vectors, not from $q = 0$ component. AFM, SC and PG stand for the antiferromagnetic ordered state, superconducting, and pseudogap-like phases, respectively.

depicted in Fig. 4.4(a) as "(a)-type" correlations (similarly for the others). To summarize, the value of $\alpha_{\parallel}$ reflects the competition between (a)- and (b)-type correlations, while $\alpha_{\perp}$ reflects the competition between (c)- and (d)-type correlations.

Now, since $\alpha_{\parallel}$ reflects the character of hyperfine field fluctuations with a c-axis component, the strongly AFM $\alpha_{\parallel}$ in Fig. 4.3 can be attributed to stripe-type AFM correlations with the Fe spins in plane (i.e. (a)-type). These must dominate the (b)-type correlations in order to have an AFM value of $\alpha_{\parallel}$. Similarly, since $\alpha_{\perp}$ reflects the character of the ab-plane component of hyperfine field fluctuations, the strongly FM value of $\alpha_{\perp}$ in the high T region may be attributed to in plane FM fluctuations (Fig. 4.4(c)), while the increase of $\alpha_{\perp}$ as the temperature is lowered reflects the increasing dominance of stripe-type AFM correlations with a c-axis component to the spin (as in Fig. 4.4(d)). By examining the c-axis and ab-plane components of the hyperfine field fluctuations separately via $\alpha_{\parallel}$ and $\alpha_{\perp}$, we see the simultaneous coexistence of FM and AFM fluctuations in $Ca(Fe_{1-x}Co_x)_2As_2$. Furthermore, the dominance of (a)- and (c)-type spin fluctuations in the high temperature region suggests that both the AFM and FM fluctuations

are highly anisotropic, favoring the *ab*-plane. A similar feature of the coexistence of FM and AFM fluctuations [305] has been reported in $Ba(Fe_{1-x}Co_x)_2As_2$ and $Ba_{1-x}K_xFe_2As_2$.

It is interesting to separate the FM and the stripe-type AFM fluctuations and extract their T dependence, as has been performed in the hole- and electron-doped $BaFe_2As_2$. [305] According to the previous paper, [305] $1/T_1T$ was decomposed into inter- and intraband components according to $1/T_1T = (1/T_1T)_{\rm inter} + (1/T_1T)_{\rm intra}$, where the T dependence of the interband term is assumed to follow the Curie-Weiss (CW) form appropriate for two dimensional AFM spin fluctuations: $(1/T_1T)_{\rm inter} = C/(T-\Theta_{\rm CW})$. For T dependence of the intraband component, $(1/T_1T)_{\rm intra}$ was assumed to be $(1/T_1T)_{\rm intra} = \alpha + \beta{\rm exp}(-\Delta/k_{\rm B}T)$. Such a decomposition of $1/T_1T$ data has been performed in several iron based superconductors such as $BaFe_2(As_{1-x}P_x)_2$ (Ref. [314]), $Ba(Fe_{1-x}Co_x)_2As_2$ (Ref. [90]) and $LaFeAsO_{1-x}P_x$ (Ref. [315]). Here we also tried to decompose the present $1/T_{1,\parallel}T$ and $1/T_{1,\perp}T$ data following the procedure. We, however, found large uncertainty in decomposing our data, especially for the $1/T_{1,\perp}T$ case, due to the weak temperature dependence of $1/T_1T$. Nevertheless, we proceeded with our analysis to qualitatively examine the x dependence of Curie-Weiss parameter C, which measures the strength of AFM spin fluctuations, and $\Theta_{\rm CW}$ corresponding to the distance in T from the AFM instability point. [90,301,316] Here we fit the data above $T_{\rm N}$ or T^* for each sample. $\Theta_{\rm CW}$ decreases from 38 $\pm$ 17 K ($x = 0$) to 15 $\pm$ 13 K ($x = 0.023$), and to a negative values of -33 ± 21 K ($x = 0.028$). This suggests that compounds with $x = 0.023$ and 0.028 are close to the AFM instability point of $\Theta_{\rm CW} = 0$ K. A similar behavior of $\Theta_{\rm CW}$ is reported in $Ba(Fe_{1-x}Co_x)_2As_2$ (Refs. [90, 305]), $BaFe_2(As_{1-x}P_x)_2$ (Ref. [316]) $Ba_{1-x}K_xFe_2As_2$ (Ref. [301]) and $Ba(Fe_{1-x}Ni_x)_2As_2$ (Ref. [317]). The x dependences of CW parameters $C_\perp$, $C_\parallel$ and $\Theta_{\rm CW}$ are shown in Figs. 4.5(a) and (b) together with the phase diagram reported in Ref. [98]. Although these parameters have large uncertainty, $C_\parallel$ seems to be greater than $C_\perp$, consistent with that the in-plane AFM fluctuations are stronger than the *c*-axis AFM fluctuations. This result is same as in $Ba(Fe_{1-x}Co_x)_2As_2$ samples in Ref. [305]. On the other hand, the $C_\perp$ and $C_\parallel$ parameters are almost independent of x in $Ca(Fe_{1-x}Co_x)_2As_2$ in the range of $x = 0$ – 0.059, while the $C_\perp$ and $C_\parallel$ parameters decrease with Co substitution in $BaFe_2As_2$ where the *c*-axis component AFM spin fluctuations decrease and die out with $x \geq 0.15$. [90] It is interesting to point out that a similar x-independent behav-

ior is also observed in the crossover temperature T^* attributed to the pseudogap-like behavior in the spin excitation spectra where the stripe-type AFM spin correlations are suppressed in the $Ca(Fe_{1-x}Co_x)_2As_2$ system. [98] Although we do not have a clear explanation about the x dependence of T^* at present, it could be related to the x dependence of CW parameters as both the CW parameters and T^* are considered to be associated with the AFM interactions between Fe spins. Further detailed studies will be required to understand peculiar properties of pseudogap-like behavior in $Ca(Fe_{1-x}Co_x)_2As_2$. It is also interesting to mention nematic spin correlations which have been recently discussed in $Ba(Fe_{1-x}Co_x)_2As_2$ (Refs. [318] and [319]) and $BaFe_2(As_{1-x}P_x)_2$ (Ref. [320]) based on NMR-T_1 and spectrum measurements. In the case of $Ca(Fe_{1-x}Co_x)_2As_2$, the nuclear magnetization recovery curves in the tetragonal PM states were well fitted by the function shown in Sec. II within our experimental uncertainty, indicating no obvious distribution in T_1. This would suggest that nematic spin correlations are not significant in $Ca(Fe_{1-x}Co_x)_2As_2$.

Finally we show, in Fig. 4.3(b), the intra band Korringa ratios $\alpha_{\parallel}^{\rm intra}$ and $\alpha_{\perp}^{\rm intra}$ by subtracting the interband scattering term $C/(T-\Theta_{\rm CW})$. Both $\alpha_{\parallel}^{\rm intra}$ and $\alpha_{\perp}^{\rm intra}$ remain roughly constant above $T_{\rm N}$ or T^*. We plotted the average value of $\alpha_{\parallel}^{\rm intra}$ and $\alpha_{\perp}^{\rm intra}$ as a function of x in Fig. 4.5(a). We find that $\alpha_{\perp}^{\rm intra}$ is smaller than $\alpha_{\parallel}^{\rm intra}$ for all the samples, confirming again the dominant in-plane FM spin fluctuations. The calculated $\alpha_{\perp}^{\rm intra}$and $\alpha_{\parallel}^{\rm intra}$ in $Ca(Fe_{1-x}Co_x)_2As_2$ are almost same order with those in both the electron- and hole-doped $BaFe_2As_2$. FM values of α were also observed in different iron-based SCs such as $La_{0.87}Ca_{0.13}FePO$ ($\alpha = 0.37$) [321], $LaO_{0.9}F_{0.1}FeAs$ ($\alpha = 0.55$) [66], and $K_{0.8}Fe_2Se_2$ ($\alpha = 0.45$) [322]. These results indicate that the FM spin correlations exist in general and may be a key ingredient to a theory of superconductivity in the iron pnictides.

4.5 Summary

Motivated by the recent NMR measurements which revealed the coexistence of the stripe-type antiferromagnetic (AFM) and ferromagnetic (FM) spin correlations in both the hole- and electron-doped $BaFe_2As_2$ families of iron-pnictide superconductors [305], we have reanalyzed NMR data in $Ca(Fe_{1-x}Co_x)_2As_2$ and found clear evidence for the coexistence of the stripe-type

AFM and FM spin correlations. In contrast to the case of $Ba(Fe_{1-x}Co_x)_2As_2$ where the relative strength of FM correlations increases with Co substitution, the FM correlations are almost independent of Co substitution for our investigated range of $x = 0 - 0.059$ in $Ca(Fe_{1-x}Co_x)_2As_2$. The Curie-Weiss parameters $C_{\perp,\parallel}$ representing the strength of the stripe-type AFM correlations are almost independent of Co doping, close to a feature of T^* representing a characteristic temperature of the pseudogap-like behavior. The observed nearly x-independent behaviors of the AFM and FM spin correlations may be associated with the small change of T_C from 15 K for $x = 0.033$ to 10 K for $x = 0.059$ for the Co doping range investigated. Our analysis of the NMR data indicates that FM fluctuations exist in general in iron-pnictide superconducting families. A recent theoretical study using the dynamical mean field theory also pointed out an importance of FM fluctuations in iron pnictides. [323] Further systematic theoretical and experimental investigation on the role of the FM correlations in iron pnictide superconducting families are highly required.

4.6 Acknowledgments

We thank David C. Johnston for helpful discussions. The research was supported by the U.S. Department of Energy, Office of Basic Energy Sciences, Division of Materials Sciences and Engineering. Ames Laboratory is operated for the U.S. Department of Energy by Iowa State University under Contract No. DE-AC02-07CH11358.

4.7 Appendix: calculation of form factor

Here, we directly calculate the appropriate form factors for the PM state of the iron pnictides according to the theory of Ref. [313]. We make the assumption that the external applied field is much larger than the hyperfine field, which is certainly true in the PM state. We further assume that the wave-number q dependent dynamic susceptibility tensor $\chi^{\alpha\beta}(\mathbf{q}, \omega_0)$ is diagonal in the PM state. Under these assumptions, the spin-lattice relaxation rate in an external field $\mathbf{h}_{\rm ext}$ is given by

$$\frac{1}{T_1(\mathbf{h}_{\rm ext})} = \lim_{\omega_0 \to 0} \frac{\gamma_N^2}{2N} k_B T \sum_{\alpha,\mathbf{q}} \mathcal{F}_\alpha^{\mathbf{h}_{\rm ext}}(\mathbf{q}) \frac{\mathrm{Im}[\chi^{\alpha\alpha}(\mathbf{q}, \omega_0)]}{\hbar\omega_0}, \tag{4.4}$$

where $\alpha = (a, b, c)$ sums over the crystallographic axes. The general expression for the q dependent form factor is

$$\mathcal{F}_{\alpha}^{\mathbf{h}_{\text{ext}}}(\mathbf{q}) = \sum_{\gamma,\delta}[R_{\mathbf{h}_{\text{ext}}}^{x\gamma} R_{\mathbf{h}_{\text{ext}}}^{x\delta} + (x \leftrightarrow y)]\mathcal{A}_{\mathbf{q}}^{\gamma\alpha}\mathcal{A}_{-\mathbf{q}}^{\delta\alpha}, \tag{4.5}$$

where $R_{\mathbf{h}_{\text{ext}}}$ is a matrix which rotates a vector from the crystallographic (a, b, c) coordinate system to a coordinate system (x, y, z) whose z axis is aligned with the total magnetic field at the nuclear site. For details we refer the reader to Ref. [313]. When $\mathbf{h}_{\text{ext}} \| c$, the two coordinate systems coincide so that

$$R_{\mathbf{h}_{\text{ext}}\|c} = \begin{pmatrix} 1 & 0 & 0 \\ 0 & 1 & 0 \\ 0 & 0 & 1 \end{pmatrix}. \tag{4.6}$$

For $\mathbf{h}_{\text{ext}} \| a$, the appropriate matrix is

$$R_{\mathbf{h}_{\text{ext}}\|a} = \begin{pmatrix} 0 & 0 & 1 \\ 0 & 1 & 0 \\ -1 & 0 & 0 \end{pmatrix}. \tag{4.7}$$

For the case of the As site in the iron pnictides, the matrix $\mathcal{A}_{\mathbf{q}}$ in Eq. 4.5 is given by [313]

$$\mathcal{A}_{\mathbf{q}} = 4\begin{pmatrix} \mathcal{A}^{aa}c_a c_b & -\mathcal{A}^{ab}s_a s_b & i\mathcal{A}^{ac}s_a c_b \\ -\mathcal{A}^{ba}s_a s_b & \mathcal{A}^{bb}c_a c_b & i\mathcal{A}^{bc}c_a s_b \\ i\mathcal{A}^{ca}s_a c_b & i\mathcal{A}^{cb}c_a s_b & \mathcal{A}^{cc}c_a c_b \end{pmatrix}, \tag{4.8}$$

where $\mathcal{A}^{\alpha\beta}$ are the components of the hyperfine coupling tensor and

$$c_a = \cos\frac{q_a a_0}{2} \qquad c_b = \cos\frac{q_b b_0}{2}$$
$$s_a = \sin\frac{q_a a_0}{2} \qquad s_b = \sin\frac{q_b b_0}{2}.$$

Here a_0 and b_0 are lattice constants. Of course, $a_0 = b_0$ in the PM state. Combining Eqs. 4.5-4.8, we obtain

$$\mathcal{F}_{a}^{\mathbf{h}_{\text{ext}}\|a}(\mathbf{q}) = 16(\mathcal{A}^{ca}s_a c_b)^2 + 16(\mathcal{A}^{ba}s_a s_b)^2 \tag{4.9}$$

$$\mathcal{F}_{b}^{\mathbf{h}_{\text{ext}}\|a}(\mathbf{q}) = 16(\mathcal{A}^{cb}c_a s_b)^2 + 16(\mathcal{A}^{bb}c_a c_b)^2 \tag{4.10}$$

$$\mathcal{F}_{c}^{\mathbf{h}_{\text{ext}}\|a}(\mathbf{q}) = 16(\mathcal{A}^{cc}c_a c_b)^2 + 16(\mathcal{A}^{bc}c_a s_b)^2 \tag{4.11}$$

$$\mathcal{F}_a^{\mathbf{h}_{\rm ext}\|c}(\mathbf{q}) = 16(\mathcal{A}^{aa}c_a c_b)^2 + 16(\mathcal{A}^{ba}s_a s_b)^2 \tag{4.12}$$

$$\mathcal{F}_b^{\mathbf{h}_{\rm ext}\|c}(\mathbf{q}) = 16(\mathcal{A}^{bb}c_a c_b)^2 + 16(\mathcal{A}^{ab}s_a s_b)^2 \tag{4.13}$$

$$\mathcal{F}_c^{\mathbf{h}_{\rm ext}\|c}(\mathbf{q}) = 16(\mathcal{A}^{ac}s_a c_b)^2 + 16(\mathcal{A}^{bc}c_a s_b)^2. \tag{4.14}$$

To calculate $1/T_1$ from Eq. 4.4, we assume for simplicity that $\chi^{\alpha\beta}(\mathbf{q},\omega_0)$ is non-zero only near the wavevectors $\mathbf{q}=0$, $\mathbf{q}=\mathbf{Q}_a \equiv (\pm\pi/a_0, 0)$ and $\mathbf{q}=\mathbf{Q}_b \equiv (0, \pm\pi/b_0)$. By tetragonal symmetry we have $a \leftrightarrow b$. In particular, $\mathbf{Q}_a = \mathbf{Q}_b \equiv \mathbf{Q}$ and $\mathrm{Im}[\chi^{\rm aa}(\mathbf{q},\omega_0)] = \mathrm{Im}[\chi^{\rm bb}(\mathbf{q},\omega_0)] \equiv \chi''_{\rm ab}(\mathbf{q},\omega_0)$. We also now write $\mathrm{Im}[\chi^{\rm cc}(\mathbf{q},\omega_0)] \equiv \chi''_{\rm c}(\mathbf{q},\omega_0)$. We thus obtain

$$\frac{1}{T_1(\mathbf{h}_{\rm ext}\|c)} = \lim_{\omega_0\to 0}\frac{8\gamma_N^2}{N}k_{\rm B}T\left[2(\mathcal{A}^{aa})^2\frac{\chi''_{ab}(\mathbf{0},\omega_0)}{\hbar\omega_0} + 4(\mathcal{A}^{ac})^2\frac{\chi''_{c}(\mathbf{Q},\omega_0)}{\hbar\omega_0}\right] \tag{4.15}$$

and

$$\frac{1}{T_1(\mathbf{h}_{\rm ext}\|a)} = \lim_{\omega_0\to 0}\frac{8\gamma_N^2}{N}k_{\rm B}T\left[4(\mathcal{A}^{ca})^2\frac{\chi''_{ab}(\mathbf{Q},\omega_0)}{\hbar\omega_0} + (\mathcal{A}^{aa})^2\frac{\chi''_{ab}(\mathbf{0},\omega_0)}{\hbar\omega_0} + (\mathcal{A}^{cc})^2\frac{\chi''_{c}(\mathbf{0},\omega_0)}{\hbar\omega_0} + 2(\mathcal{A}^{ac})^2\frac{\chi''_{c}(\mathbf{Q},\omega_0)}{\hbar\omega_0}\right]. \tag{4.16}$$

We have summed over four AFM wavevectors $\mathbf{Q} = (\pm\pi/a_0, 0)$ and $\mathbf{Q} = (0, \pm\pi/a_0)$, which have the same value of $\chi''(\mathbf{Q},\omega_0)$ in the PM state. Notice that, for both field directions, AFM flucutations at $\mathbf{q}=\mathbf{Q}$ are completely filtered out if $\mathcal{A}^{ac}=0$, as pointed out in Ref. [30]. However, in the iron pnictides $\mathcal{A}^{ac}\neq 0$, [86] and therefore AFM fluctuations are not filtered out. From Eqs. 4.15 and 4.16 we can easily calculate $1/T_{1,\|} \equiv 2/T_1(\mathbf{h}_{\rm ext}\|a) - 1/T_1(\mathbf{h}_{\rm ext}\|c)$ and $1/T_{1,\perp} \equiv 1/T_1(\mathbf{h}_{\rm ext}\|c)$

$$\frac{1}{T_{1,\perp}} = \lim_{\omega_0\to 0}\frac{16\gamma_N^2}{N}k_B T\left[(\mathcal{A}^{aa})^2\frac{\chi''_{ab}(\mathbf{0},\omega_0)}{\hbar\omega_0} + 2(\mathcal{A}^{ac})^2\frac{\chi''_{c}(\mathbf{Q},\omega_0)}{\hbar\omega_0}\right] \tag{4.17}$$

$$\frac{1}{T_{1,\parallel}} = \lim_{\omega_0 \to 0} \frac{16\gamma_N^2}{N} k_B T \left[4(\mathcal{A}^{ca})^2 \frac{\chi''_{ab}(\mathbf{Q}, \omega_0)}{\hbar\omega_0} + (\mathcal{A}^{cc})^2 \frac{\chi''_c(\mathbf{0}, \omega_0)}{\hbar\omega_0} \right] \tag{4.18}$$

Notice that the fluctuations probed by $1/T_{1,\parallel}$ and $1/T_{1,\perp}$ are consistent with the qualitative arguments used in the main text. For the case of $CaFe_2As_2$, Ref. [98] gives $\mathcal{A}^{aa} = 1.8$ T/μ_B, $\mathcal{A}^{cc} = 1.2$ T/μ_B and $\mathcal{A}^{ca} = \mathcal{A}^{ac} = 0.82$ T/μ_B. $\mathcal{A}^{aa}$ and $\mathcal{A}^{cc}$ are determined by Knight shift measurements and $\mathcal{A}^{ac}$ is found by comparing the measured internal field in the AFM state to the value of the ordered moment obtained by neutron scattering.

CHAPTER 5. ELECTRONIC PROPERTIES OF GETE AND AG- OR SB-SUBSTITUTED GETE STUDIED BY LOW TEMPERATURE ^{125}TE NMR

A paper published in Physical Review B **94**, 085203 (2016)

J. Cui,[1,2] E. M. Levin,[1,3] Y. Lee,[1] and Y. Furukawa,[1,3]

1 Ames Laboratory, U.S. DOE, Ames, Iowa 50011, USA

2 Department of Chemistry, Iowa State University, Ames, Iowa 50011, USA

3 Department of Physics and Astronomy, Iowa State University, Ames, Iowa 50011, USA

5.1 Abstract

We have carried out ^{125}Te nuclear magnetic resonance (NMR) in a wide temperature range of 1.5 – 300 K to investigate electronic properties of $Ge_{50}Te_{50}$, $Ag_2Ge_{48}Te_{50}$ and $Sb_2Ge_{48}Te_{50}$ from a microscopic point of view. From the temperature dependence of NMR shift (K) and nuclear spin lattice relaxation rate ($1/T_1$), we found that two bands contribute to the physical properties of the materials. One band overlaps the Fermi level providing the metallic state where no strong electron correlations are revealed by Korringa analysis. The other band is separated from the Fermi level by an energy gap of E_g/k_B ~67 K, which gives rise to the semiconductor-like properties. First-principle calculation reveals that the metallic band originates from the Ge vacancy while the semiconductor-like band is related to the fine structure of the density of states near the Fermi level. Low-temperature ^{125}Te NMR data for the materials studied here clearly show that the Ag substitution increases hole concentration while Sb substitution decreases it.

5.2 Introduction

Complex tellurides have been studied extensively due to their intriguing fundamental properties and their application as thermoelectric materials, [104, 114, 115, 324–326] which directly convert heat into electricity. The efficiency is characterized by the dimensionless figure of merit $zT = S^2\sigma T/\kappa$ (S the Seebeck coefficient, σ the electrical conductivity, T the absolute temperature, and κ the thermal conductivity). The well-known group of thermoelectric materials, the complex tellurides based on GeTe, [327–329] TAGS-m materials $(GeTe)_m(AgSbTe_2)_{100-m}$, have a thermoelectric figure of merit zT above 1. [114, 137, 330, 331] According to band calculations, GeTe is a narrow-band-gap semiconductor whose band gap is calculated to be 0.3 $\sim$ 0.5 eV. [332–335] On the other hand, electrical resistivity measurements show metallic behavior [327, 336–339] although a small gap also has been observed by optical measurements. [340] This is believed to be due to high hole concentrations generated by Ge vacancies, forming a self-dopant system with p-type conductivity. [327, 336, 341] Therefore, depending on the samples' composition, they may have different concentrations of Ge vacancies resulting in different physical properties. This makes it very difficult to understand physical properties of GeTe-based materials. In fact, there is a significant discrepancy between the electronic and thermal transport data for GeTe-based materials reported in the literature. [114, 140, 342, 343]

To avoid such confusion, one needs to study the physical properties using well characterized samples. We have conducted systematic characterization of GeTe by using x ray diffraction (XRD), scanning electron microscopy (SEM), energy dispersive spectroscopy (EDS), Seebeck coefficient, electrical resistivity, Hall effect, thermal conductivity, and ^{125}Te nuclear magnetic resonance (NMR) measurements. [327] Hereafter, we will use notation $Ge_{50}Te_{50}$ for GeTe with the coefficients shown in atomic percent.

In our previous paper, [327] we concluded that the discrepancy in the data for $Ge_{50}Te_{50}$ reported in literature can be attributed to the variation in the Ge/Te ratio of solidified samples as well as to different conditions of measurements. It is well established that NMR is a powerful tool to investigate carrier concentrations in semiconductors from a microscopic point of view. The Hall and Seebeck effects show only bulk properties, which can be affected by small amounts

of a second phase. [344, 345] Nuclear spin lattice relaxation rates ($1/T_1$) have been measured at room temperature, and were found to increase linearly with carrier concentrations. [346] However, to our knowledge, no systematic NMR investigation of $Ge_{50}Te_{50}$ has been carried out over a wide temperature range.

In this paper, we report the first ^{125}Te NMR measurements of $Ge_{50}Te_{50}$ over a wide temperature range of T = 1.5 - 300 K. We found that the NMR shift K and $1/T_1T$ data are nearly temperature-independent at temperatures below ~50 K and both increase slightly with increasing temperature at high temperatures. These behaviors can be explained well by a two-band model where one band overlaps the Fermi level and the other band is separated from the Fermi level by an energy gap of E_g/k_B ~67 K. First-principle calculations indicate that the first band originates from the Ge vacancy while the second band is related to the fine structure of the density of states near the Fermi level. We also carried out ^{125}Te NMR measurements of $M_2Ge_{48}Te_{50}$ (M = Ag, Sb) to study carrier doping effects on electronic properties. Clear changes in carrier concentration upon Ag or Sb substitutions were observed: the Ag substitution increases the hole concentration whereas Sb substitution decreases the concentration, which is consistent with our previous report. [347]

5.3 Experimental

Polycrystalline samples of $Ge_{50}Te_{50}$, $Ag_2Ge_{48}Te_{50}$ and $Sb_2Ge_{48}Te_{50}$ were prepared by direct reaction of the constituent elements of Ge, Te, Ag or Sb in fused silica ampoules, as described in Ref. [327] and Ref. [347]. The samples were well characterized by XRD, Seebeck coefficient, electrical resistivity, Hall effects, and room temperature ^{125}Te NMR measurements. The coarsely powdered samples were loosely packed into 6-mm quartz tubes for NMR measurements. NMR measurements of ^{125}Te ($I = \frac{1}{2}$; $\frac{\gamma_N}{2\pi}$ = 13.464 MHz/T) were conducted using a homemade phase-coherent spin-echo pulse spectrometer. ^{125}Te NMR spectra were obtained either by Fourier transform of the NMR echo signal at a constant magnetic field of 7.4089 T or by sweeping the magnetic field at a frequency of 99.6 MHz in the temperature range of T = 1.5 - 300 K. The NMR echo signal was obtained by means of a Hahn echo sequence with a typical $\pi/2$ pulse length of 7.5 μs which produces an oscillation field (so-called H_1) of ~25 Oe.

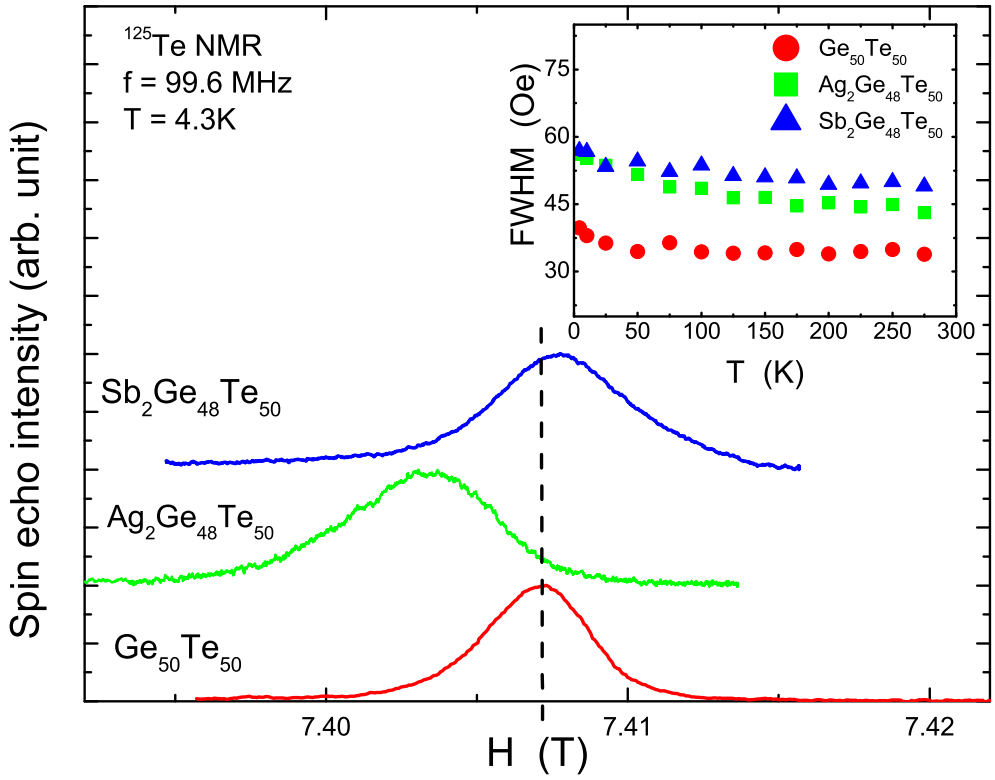

Figure 5.1 Magnetic field-swept ^{125}Te-NMR spectra for $Ge_{50}Te_{50}$, $Ag_2Ge_{48}Te_{50}$, and $Sb_2Ge_{48}Te_{50}$ at f = 99.6 MHz and T = 4.3 K. The dotted vertical line is a guide for eyes. The inset shows the temperature dependence of FWHM for the samples.

5.4 Results and discussion

Figure 5.1 shows field-swept ^{125}Te NMR spectra measured at 4.3 K for $Ge_{50}Te_{50}$, $Ag_2Ge_{48}Te_{50}$ and $Sb_2Ge_{48}Te_{50}$. The full width at half maximum (FWHM) for $Ge_{50}Te_{50}$ is 40.0(5) Oe at T = 4.3 K which is almost independent of temperature although a slight increase can be observed below ~25 K as shown in the inset of Fig. 5.1. This FWHM is slightly smaller than 43 Oe at room temperature reported previously. [347] With Ag substitution the peak position shifts to lower magnetic field, while the peak position slightly shifts to higher magnetic field with Sb substitution. The FWHM shows a slight increase to 56.0(5) Oe and 54.0(5) Oe at T = 4.3 K for Ag- or Sb-substituted samples, respectively. The FWHM is also found to increase slightly with decreasing temperature for Ag- or Sb-substituted samples. These observed values are also close to the values (~50 Oe) at room temperature reported previously. [347]

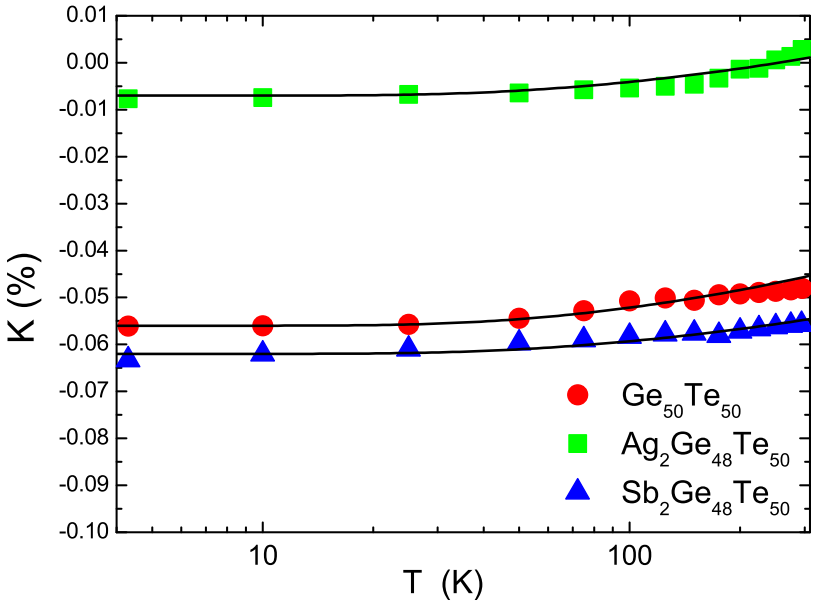

Figure 5.2 Temperature dependence of NMR shift K for for $Ge_{50}Te_{50}$ (red circles), $Ag_2Ge_{48}Te_{50}$ (green squares) and $Sb_2Ge_{48}Te_{50}$ (blue triangles). The solid lines are best fits using Eq. 5.2.

The temperature dependence of K is shown in Fig. 6.2 where K is determined by the peak position of the spectrum. Although the absolute values of K depend on the sample composition, their temperature dependencies exhibit qualitatively the same behavior: K slightly decreases with decreasing temperature, then levels off at low temperatures. The temperature dependence of K can be analyzed by a two-band model where the first band overlaps the Fermi level and the second band is separated from the Fermi level by an energy gap (E_g). The nearly temperature-independent behavior observed at low temperatures is a typical characteristic of metals (due to Pauli paramagnetic susceptibility) originated from the first band. The increase of K at high temperatures originates from the second band, similar to the case of semiconductors. Thus, the total NMR shift is given by

$$K = K_{\text{Pauli}} + K_{\text{semi}} + K_{\text{orb}} \tag{5.1}$$

where K_{Pauli} is the temperature-independent NMR shift related to the the Pauli paramagnetic susceptibility χ_{Pauli} due to self-doping/substitution effects and K_{semi} originates from the semiconducting-like nature giving rise to the temperature-dependent contribution because of

thermal excitations across an energy gap E_g. The temperature-independent K_{orb} includes chemical shift, orbital and Landau diamagnetic contributions. As is shown below, K_{orb} is estimated to be $-0.142(10)\%$. As the temperature-dependent K_{semi} has been calculated as $K_{semi} \propto \sqrt{T}e^{-E_g/k_BT}$, [348,349] the total K is given as

$$K = K_{Pauli} + a\sqrt{T}e^{-E_g/k_BT} + K_{orb} \tag{5.2}$$

Using the $K_{orb} = -0.142(10)\%$ and $E_g/k_B = 67(4)$ K [5.8(3) meV] estimated from the temperature dependence of $1/T_1$ shown below, the experimental data are reasonably reproduced as shown by the solid lines with $K_{Pauli} = 0.084$ %, $a = 0.00075$ %/$\sqrt{\text{K}}$ for $Ge_{50}Te_{50}$, $K_{Pauli} = 0.135$ %, $a = 0.00057$ %/$\sqrt{\text{K}}$ for $Ag_2Ge_{48}Te_{50}$, and $K_{Pauli} = 0.081$ %, $a = 0.00052$ %/$\sqrt{\text{K}}$ for $Sb_2Ge_{48}Te_{50}$, respectively. Since K_{Pauli} is proportional to the Pauli paramagnetic susceptibility which is proportional to the density of states $\mathcal{N}(E_F)$ at the Fermi level, the increase of K_{Pauli} from $Ge_{50}Te_{50}$ to the Ag doped material indicates an increase of $\mathcal{N}(E_F)$ while Sb doping reduces $\mathcal{N}(E_F)$ at the Fermi level. These results are consistent with the previous report. [347] The $\mathcal{N}(E_F)$ discussed here is due to unavoidable self-doping and/or Ag(Sb)-substitution effects not including the effects of thermally activated carriers from the second band.

Figure 5.3(a) shows the temperature dependence of $1/T_1T$ for the three samples. T_1 values reported here were measured by the single saturation pulse method at the peak position of the NMR spectrum. As shown in Fig. 5.3(b), the nuclear recovery data can be fitted by a single exponential function $1 - M(t)/M(\infty) = e^{-t/T_1}$, where $M(t)$ and $M(\infty)$ are the nuclear magnetizations at time t after the saturation and the equilibrium nuclear magnetization at $t \rightarrow \infty$, respectively. Similar to the case of K, $1/T_1T$s for all samples exhibit qualitatively the same behavior: $1/T_1T$ decreases slightly with decreasing temperature, then levels off at low temperatures. The temperature dependence of $1/T_1T$ can also be explained by the two-band model.

In this case, $1/T_1T$ is given by

$$1/T_1T = (1/T_1T)_{const} + ATe^{-E_g/k_BT} \tag{5.3}$$

where $(1/T_1T)_{const}$ is the temperature-independent constant value originated from the conduction carriers and the second term is due to thermal excitation effects from the second band.

[349,350] Here we assumed in the simple model (Eq. 5.3) that a cross-relaxation effect originated from mixing of the two bands is negligible for simplicity. A similar analysis of the temperature dependence of $1/T_1T$ without the cross-relaxation process has been reported in the semimetal $CaAl_{2-x}Si_{2+x}$ [351] and in the Heusler-type compound $Fe_{2+x}V_{1-x}Al$ [352]). Using Eq. 5.3, the magnitude of E_g is estimated to be 67(4) K for $Ge_{50}Te_{50}$ and $Ag_2Ge_{48}Te_{50}$, although the experimental data are somewhat scattered, as shown in Fig. 5.3(c) where $[(1/T_1T) - (1/T_1T)_{const}]/T$ is plotted against to $1/T$ on a semi-log scale. It is difficult to estimate E_g for $Sb_2Ge_{48}Te_{50}$ due to a large scattering of the data. The black solid line in the figure is the best fit with a assumption of $E_g/k_B = 67$ K, which seems to reproduce the data reasonably although we cannot determine E_g. It is noted that 67 K is too small to attribute to the semiconducting gap energy of $0.3 - 0.5$ eV reported from optical measurements for GeTe. [340]

The solid lines in Fig. 5.3(a) are best fits to Eq. 5.3, using $E_g/k_B = 67$ K, with $(1/T_1T)_{const} = 0.37$ $(sK)^{-1}$, $A = 0.0013$ $(sK^2)^{-1}$ for $Ge_{50}Te_{50}$, $(1/T_1T)_{const} = 0.90$ $(sK)^{-1}$, $A = 0.0010$ $(sK^2)^{-1}$ for $Ag_2Ge_{48}Te_{50}$, and $(1/T_1T)_{const} = 0.33$ $(sK)^{-1}$, $A = 0.00068$ $(sK^2)^{-1}$ for $Sb_2Ge_{48}Te_{50}$, respectively. Within a Fermi liquid picture, $(1/T_1T)_{const}$ is proportional to the square of the density of states at the Fermi level $\mathcal{N}(E_F)$ and K_{Pauli} is proportional to $\mathcal{N}(E_F)$. Therefore, as K_{Pauli} is expected to be proportional to $(1/T_1T)^{1/2}_{const}$, one can estimate the temperature-independent K_{orb} by plotting $(1/T_1T)^{1/2}_{const}$ as a function of the temperature-independent $K = K_{Pauli} + K_{orb}$ at low temperatures for different samples. As shown in Fig. 5.4, we actually found a linear relation between $(1/T_1T)^{1/2}_{const}$ and K in the plot of $(1/T_1T)^{1/2}_{const}$ vs. the temperature-independent K, from which K_{orb} is estimated to be $-0.142(10)\%$.

Using the NMR data, we can discuss electron correlations through the Korringa ratio analysis. As described, both $(1/T_1T)_{const}$ and K_{Pauli} are determined primarily by $\mathcal{N}(E_F)$. This leads to the general Korringa relation

$$T_1TK^2_{spin} = \frac{\hbar}{4\pi k_B}\left(\frac{\gamma_e}{\gamma_N}\right)^2 \equiv R \tag{5.4}$$

where K_{spin} denotes the spin part of the NMR shift. For the ^{125}Te nucleus, $R = 2.637 \times 10^{-6}$ Ks. Deviations from R can reveal information about electron correlations in materials, which are conveniently expressed via the Korringa ratio $\alpha \equiv R/(T_1TK^2_{spin})$. [298, 311] For

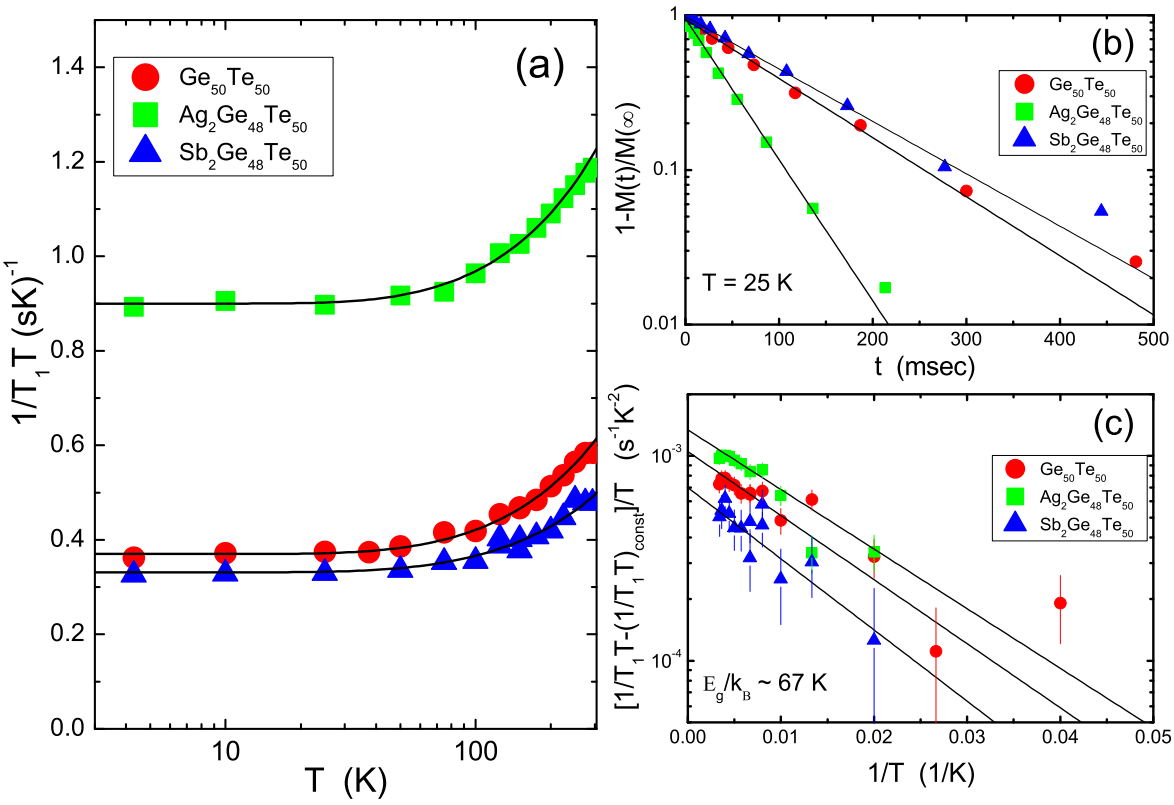

Figure 5.3 (a) Temperature dependence of ^{125}Te $1/T_1T$ for $Ge_{50}Te_{50}$ (red circles), $Ag_2Ge_{48}Te_{50}$ (green squares) and $Sb_2Ge_{48}Te_{50}$ (blue triangles). The solid lines are best fits with the equation of $1/T_1T = (1/T_1T)_{\rm const} + ATe^{-E_{\rm g}/k_{\rm B}T}$ for each sample. (b) Typical nuclear recovery curves for the three samples at $T = 25$ K. (c) Semi-log plot of $(1/T_1T - (1/T_1T)_{\rm const})/T$ versus $1/T$. The solid lines are fitting results with $E_{\rm g}/k_{\rm B} = 67(4)$ K.

uncorrelated metals, one has $\alpha \sim 1$. For antiferromagnetic spin correlation, $\alpha >> 1$; in contrast, $\alpha << 1$ for ferromagnetic spin correlations. The Korringa ratio α, then, reveals how electrons correlate in materials. Fig. 5.5 shows the temperature dependence of α for the three samples. We found the values of α for all samples are similar, $\alpha \sim 1.25$ at low temperatures, where the temperature-independent $(1/T_1T)_{\rm const}$ and $K_{\rm Pauli}$ dominate, indicative of no strong correlations for conduction carriers originated from self-doping/substitution effects in the samples. With increasing temperature, α slightly increases above ~ 50 K. If we assume that the Korringa relation holds at high temperatures, the increase suggests a tiny enhancement of antiferromagnetic spin correlations for carriers. Since the temperature dependence of α

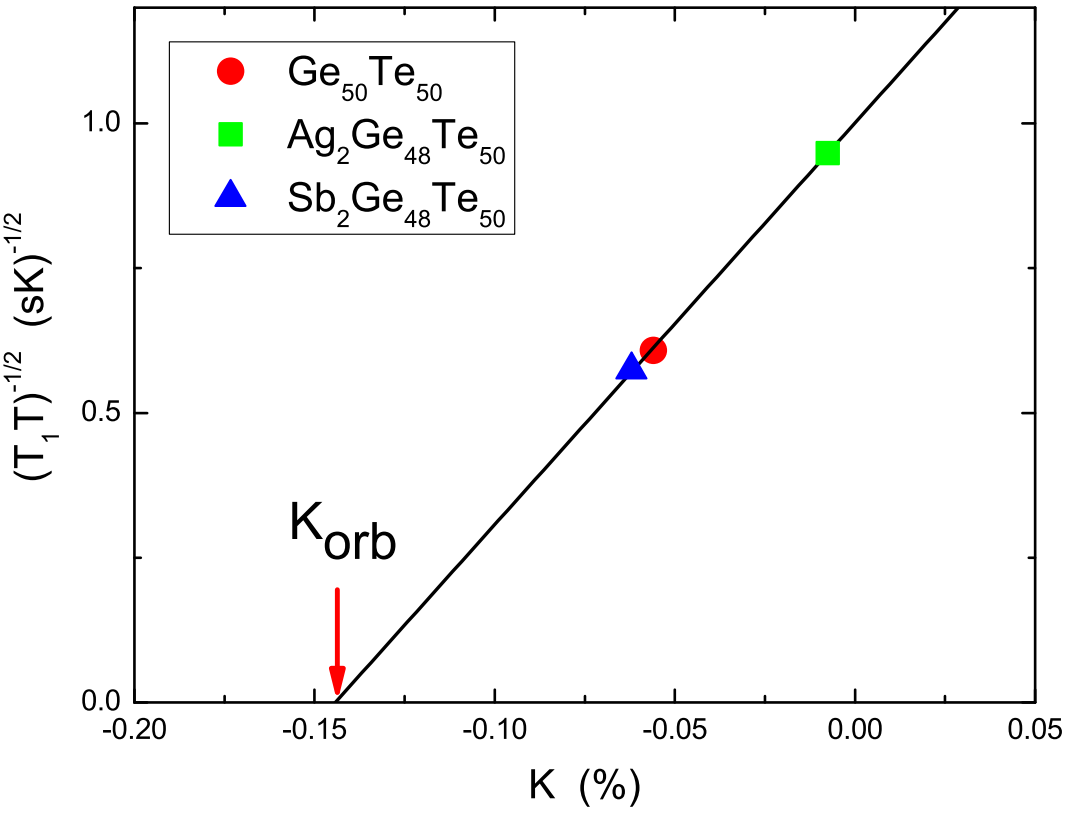

Figure 5.4 $(1/T_1T)^{0.5}_{\rm const}$ versus the T-independent $K = K_{\rm Pauli} + K_{\rm orb}$ for three samples. The solid line is a linear fit giving rise to $K_{\rm orb}$=−0.142(10)%

originates from the second band having semiconducting nature, these results may suggest that thermally excited carriers play an important role in electron correlation effects in the system. As electron correlations have been pointed out to be significant for a figure of merit (zT values) [353], it is interesting if the increase of zT in $Ge_{50}Te_{50}$ at high temperatures above 300 K [327] is related to the electron correlations. Further NMR studies at high temperatures above 300 K are required in shedding light on the relationship between electron correlations and zT, which is currently in progress.

We now discuss how the carrier concentration changes by Ag or Sb substitution based on $\mathcal{N}(E_{\rm F})$ obtained from NMR data. In a parabolic band for noninteracting carriers, $\mathcal{N}(E_{\rm F})$ is given by $\mathcal{N}(E_{\rm F}) = \frac{4\pi}{h^3}(2m^*)^{3/2}E_{\rm F}^{1/2}$ where $E_{\rm F} = \frac{h^2}{2m^*}(3\pi^2 n)^{2/3}$. Here n is the carrier concentration and m^* the renormalized effective carrier mass. Therefore, one can get a simple

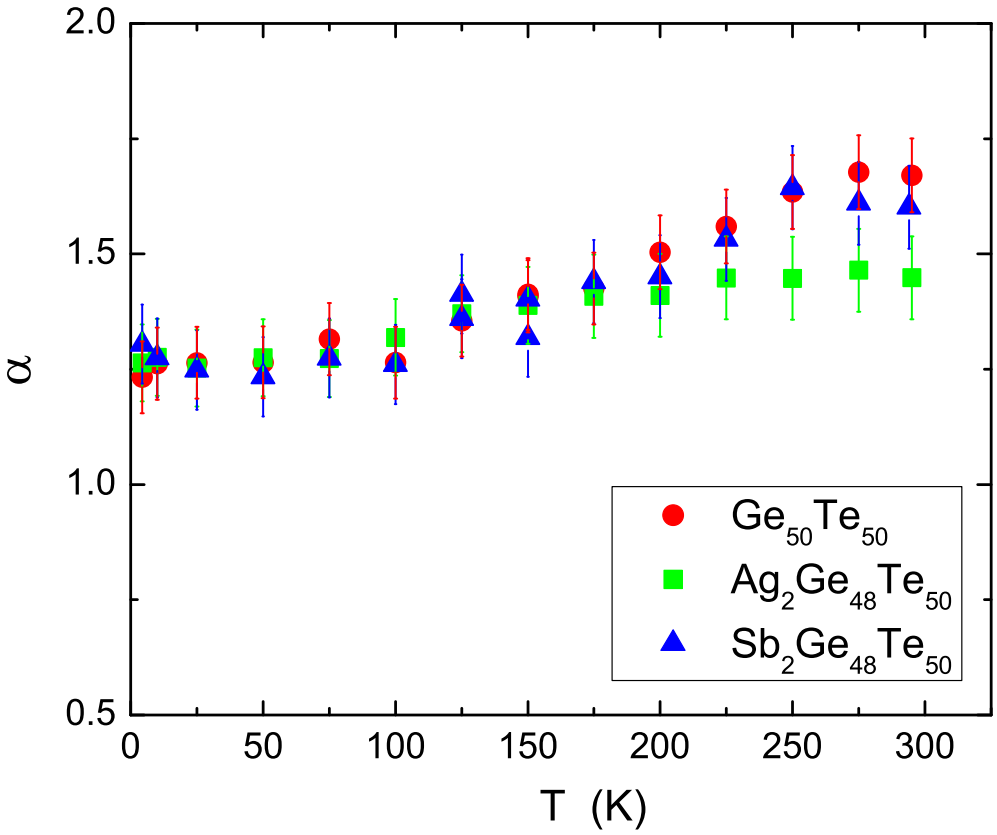

Figure 5.5 Temperature dependence of the Korringa ratio α for $Ge_{50}Te_{50}$ (red circles), $Ag_2Ge_{48}Te_{50}$ (green squares) and $Sb_2Ge_{48}Te_{50}$ (blue triangles)

relation of $\mathcal{N}(E_F) \propto (m^* n^{1/3})$. From the values of $(1/T_1T)_{const}$ and/or K_{Pauli} where the effect from m^* can be negligible, the carrier concentration in $Ag_2Ge_{48}Te_{50}$ is found to increase about 380% from that of $Ge_{50}Te_{50}$ while the carrier concentration in $Sb_2Ge_{48}Te_{50}$ is reduced only by ~16%. Since there are 1.85×10^{22} cm^{-3} Ge atoms in $Ge_{50}Te_{50}$, the replacement of two Ag atoms for two Ge atoms out of 50 provides additional 7.4×10^{20} cm^{-3} holes into the system. On the other hand, the substitution of two Sb atoms should reduce the same amount of carrier concentration (7.4×10^{20} cm^{-3}). Therefore, the large increase of the carrier concentration by Ag substitution and the slight decrease of that by Sb substitution cannot be explained by the simple substitution effect. These results strongly indicate that the number of Ge vacancies must be different for Ag or Sb substitutions. A similar conclusion has been pointed out in our previous paper. [347]

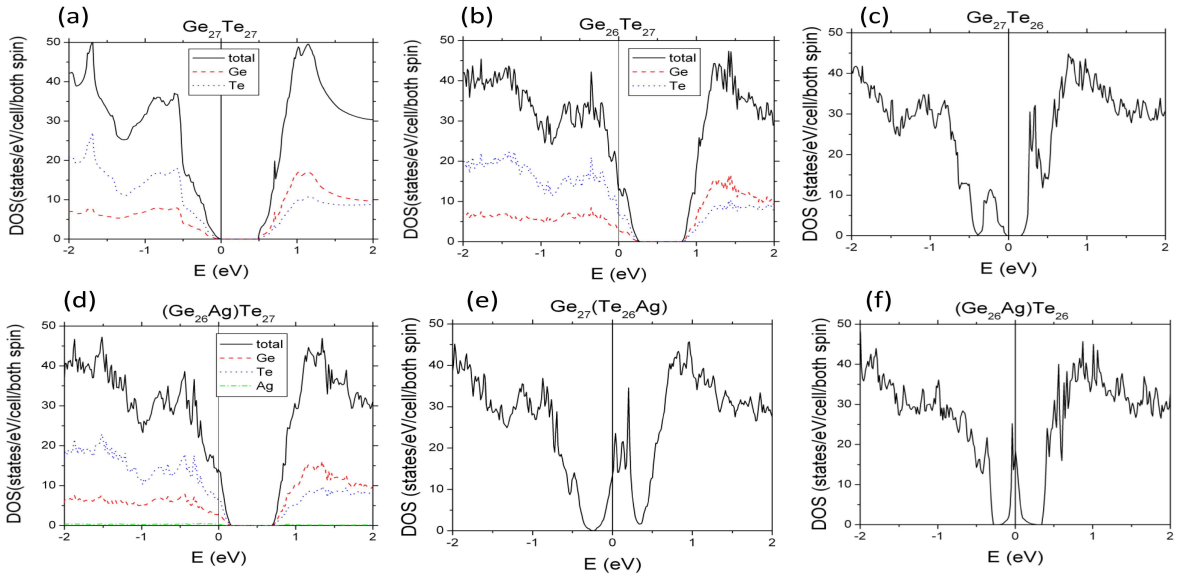

Figure 5.6 Density of states (DOS) near the Fermi level (E_F). Black line is the total DOS. In some figures, atomic decomposed DOS is shown where the blue and red dotted lines show DOS from Te $5p$ and Ge $4p$ electrons, respectively: (a) $Ge_{27}Te_{27}$, (b) $Ge_{26}Te_{27}$, (c) $Ge_{27}Te_{26}$, (d) $(Ge_{26}Ag)Te_{27}$, (e) $Ge_{27}(Te_{26}Ag)$, and (f) $(Ge_{26}Ag)Te_{26}$.

To obtain insight into the origin of the metallic conductivity in $Ge_{50}Te_{50}$, particularly the vacancies effects on electronic structure of $Ge_{50}Te_{50}$, we performed first-principles calculations where we employed a full-potential linear augmented plane wave method (FP-LAPW) [354] with a generalized gradient approximation (GGA) functional. [355] We constructed supercells which are composed of 27 Ge atoms and 27 Te atoms and randomly chose sites for vacancies or for Ag substituted site. For obtaining self-consistent charge density, we employed $R_{\mathrm{MT}}k_{\max} = 7.0$ and $R_{\mathrm{MT}} = 2.3$ and 2.8 a.u. for Ge and Te atoms respectively. We selected 828 **k**-points in irreducible brillouin zone for obtaining self-consistent charge and density of states (DOS). As convergence criteria, we used energy difference 0.0001 Ry/cell, charge difference 0.0001 e, and force difference 1.0 mRy/a.u. between self-consistent steps. To get an optimized structure, we relaxed atoms around the vacancy or the substituted atom so that forces on each atom are less than 2.0 mRy/a.u.

Figure 5.6(a) shows the calculated DOS for a perfect $Ge_{27}Te_{27}$ without any defect, with a band gap of ∼0.5 eV (semiconductor nature). This agrees well with previous reports. [334,

335, 339] Here we show atomic decomposed DOS of the perfect $Ge_{27}Te_{27}$, where the black line shows the total DOS. The red and blue dotted lines show DOS from Te $5p$ and Ge $4p$ electrons, respectively. Figs. 5.6(b) and (c) show the vacancy effect on DOS. In the case of a vacancy at the Ge site ($Ge_{26}Te_{27}$), the Fermi level E_F moves to lower energy while keeping a similar gap structure to the case of $Ge_{27}Te_{27}$. This produces a finite DOS at E_F, giving rise to metallic character. The most part of DOS at E_F originates from Te $5p$ and Ge $4p$ electrons. On the other hand, a vacancy at the Te site ($Ge_{27}Te_{26}$) keeps semiconducting states although some isolated states are developed in the gap. We conclude that a vacancy at the Ge site gives rise to p-type metallic conductivity in $Ge_{50}Te_{50}$ as has been observed in experiments. A similar conclusion based on electronic structure calculations has been reported by Edwards *et al.* [339] We further investigate the Ag substitution effect on electronic states. Figs. 5.6(d) and (e) show a Ag atom substitution effect on DOS. While replacing a Ge atom by a Ag atom lowers the Fermi level and gives metallic character as in the case of a Ge vacancy, replacing a Te atom develops some isolated states in the gap and places E_F on the isolated states. Finally, Fig. 5.6(f) shows DOS for a case that a Ag atom replaces a Ge atom and a vacancy on a the Te atom site. In this case the impurity states are sharper than other cases and E_F is located at the center of isolated states. As we discussed, our NMR data were well explained by the two-band model where one band overlaps the Fermi level giving metallic nature and the other band is separated from the Fermi level by an energy gap of $E_g/k_B = 67(4)$ K. It is clear that the metallic band can be attributed to the Ge vacancy effect, while the second band cannot be explained by the effect. We found that a vacancy at the Te sites produces an isolated state in the gap, and one may think that it could be the origin of the second band. However, our observation of a gap magnitude of 67(4) K [5.8(3) meV] is much smaller than the gap energy of order (0.1 eV) even if we take the isolated states created by the Te defects into consideration. Therefore, we consider that the observed semiconducting nature cannot be attributed to the Te-defect effects but probably fine structures of DOS near the Fermi level.

Finally it is interesting to point out the inhomogeneity of the electronic states in the samples. According to Levin *et al.*, [346] electronic inhomogeneity has been observed in some semiconductors such as PbTe from $1/T_1$ measurements. We investigate homogeneity of elec-

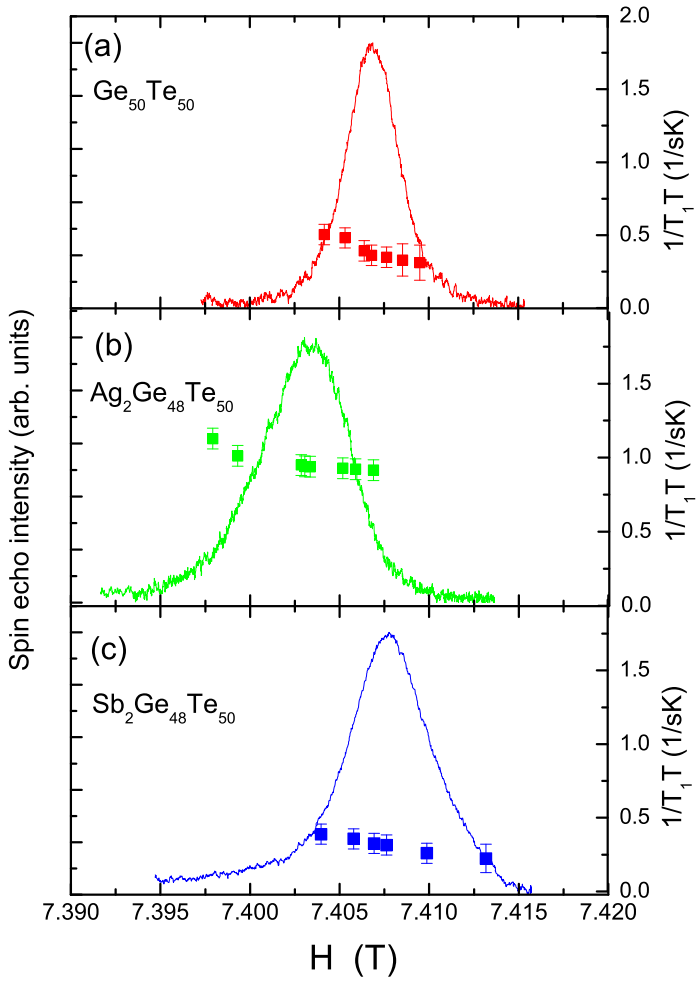

Figure 5.7 Position dependence of $1/T_1T$ at $T = 4.3$ K for (a) $Ge_{50}Te_{50}$, (b) $Ag_2Ge_{48}Te_{50}$ and (c) $Sb_2Ge_{48}Te_{50}$, together with corresponding NMR spectrum.

tronic states in the samples by measuring T_1 at $T = 4.3$ K and different positions in the spectra for the three samples. Since our H_1 for T_1 measurements is ~25 Oe which is much smaller than the line widths of the observed spectra, we can determine T_1 for different positions in the spectra where a nearly single exponential behavior in nuclear recovery was observed for each position because a distribution of T_1 values for a part of the line irradiated by the rf pulses. As shown in Figs. 5.7(a)-(c), $1/T_1$ seems to depend on the position in the spectrum, where we plotted $1/T_1T$ together with the corresponding spectrum. One can see that $1/T_1$ has a trend of a slight increase at lower magnetic field positions indicating a greater $K_{\rm spin}$. For example, the $1/T_1T$ at the peak position of $Ge_{50}Te_{50}$ is ~0.36 $(\mathrm{sK})^{-1}$, while the $1/T_1T$ ~0.50

$(\mathrm{sK})^{-1}$at a lower field position (H = 7.4033 T). The enhancement of $1/T_1T$ and the larger K_{spin} at lower magnetic fields are consistent with an increased carrier concentration. Since $1/T_1T$ and K_{spin} values are related to $\mathcal{N}(E_{\mathrm{F}})$, this result indicates that the electronic state in $Ge_{50}Te_{50}$ is likely inhomogeneous. Similar behaviors have been observed in $Ag_2Ge_{48}Te_{50}$ and $Sb_2Ge_{48}Te_{50}$. These results indicate electronic states of all GeTe-based materials investigated here are inhomogeneous which could originate from a possible inhomogeneous distribution of defects creating areas with differing carrier concentrations in $Ge_{50}Te_{50}$ and $M_2Ge_{48}Te_{50}$ (M = Ag, Sb). The distributions of the local carrier concentration $\Delta n/n$ at low temperatures can be estimated from the distribution of NMR shift, $\Delta K/K$, where ΔK was estimated from the line width of the NMR spectrum at T = 4.3 K. The estimated $\Delta n/n$ are 0.25, 0.17, and 0.67, for $Ge_{50}Te_{50}$, $Ag_2Ge_{48}Te_{50}$, and $Sb_2Ge_{48}Te_{50}$, respectively. Using the average local carrier concentration $n = 8.0 \times 10^{20}$ cm^{-3} ($Ge_{50}Te_{50}$), 1.7×10^{20} cm^{-3} ($Ag_2Ge_{48}Te_{50}$) and 4.0×10^{20} cm^{-3} ($Sb_2Ge_{48}Te_{50}$) obtained from the Hall coefficient measurement, [347] Δn are estimated to be 2.0×10^{20} cm^{-3}, 2.9×10^{20} cm^{-3}, and 2.7×10^{20} cm^{-3}, respectively.

5.5 Conclusion

We have carried out ^{125}Te NMR measurements to microscopically investigate the electronic properties of $Ge_{50}Te_{50}$, $Ag_2Ge_{48}Te_{50}$ and $Sb_2Ge_{48}Te_{50}$. For $Ge_{50}Te_{50}$, the NMR shift K and $1/T_1T$ data are nearly temperature independent at low temperatures below ~50 K and both increase slightly with increasing temperature at high temperatures. These behaviors are well explained by a two-band model where one band overlaps the Fermi level and the other band is separated from the Fermi level by an energy gap of $E_{\mathrm{g}}/k_{\mathrm{B}}$ = 67(4) K. Korringa analysis indicates that the conduction carriers can be considered as free carriers with no significant electron correlations at low temperatures. On the other hand, Korringa ratio increases slightly at high temperature, suggesting the slight enhancement of the electron correlation. A first-principle calculation revealed that the metallic band originates from the Ge vacancy while the semiconductor-like band may be related to the fine structure of the density of states near the Fermi level. Low-temperature ^{125}Te NMR data for $Ag_2Ge_{48}Te_{50}$ and $Sb_2Ge_{48}Te_{50}$ clearly demonstrate that the carrier concentration changes by Ag or Sb substitutions where the Ag

substitution increases hole concentration while Sb substitution decreases the concentration.

5.6 Acknowledgments

The research was supported by the U.S. Department of Energy, Office of Basic Energy Sciences, Division of Materials Sciences and Engineering. Ames Laboratory is operated for the U.S. Department of Energy by Iowa State University under Contract No. DE-AC02-07CH11358.

CHAPTER 6. QUANTIFICATION OF C=C AND C=O SURFACE CARBONS IN DETONATION NANODIAMOND BY NMR

A paper published in J. Phys. Chem. C, **118**, 9621 (2014)

J.-F. Cui, X.-W. Fang, and K. Schmidt-Rohr

Ames Laboratory-DOE and Department of Chemistry, Iowa State University, Ames, Iowa 50011, United States

6.1 Abstract

The ability of solid-state ^{13}C NMR to detect and quantify small amounts of sp^2-hybridized carbon on the surface of ∼5 nm diameter nanodiamond particles is demonstrated. The C=C carbon fraction is only 1.1 ± 0.4% in pristine purified detonation nanodiamond, while a full single-layer graphitic or "bucky diamond" shell would contain ca. 25% of all C in a 5 nm diameter particle. Instead of large aromatic patches repeatedly proposed in the recent literature, sp^3-hybridized CH and COH carbons cover most of the nanodiamond particle surface, accounting for ∼5% each. C=O and COO groups also seen in X-ray absorption near-edge structure spectroscopy (XANES) but not detected in previous NMR studies make up ca. 1.5% of all C. They are removed by heat treatment at 800 °C, which increases the aromatic fraction. ^{13}C{^{1}H} NMR demonstrates that the various sp^2-hybridized carbons are mostly not protonated, but cross-polarization shows that they are separated from ^{1}H by only a few bond lengths, which proves that they are near the protonated surface. Together, the observed C–H, C–OH, C=O, and C=C groups account for 12-14% of all C, which matches the surface fraction expected for bulk- terminated 5 nm diameter diamond particles.

6.2 Introduction

Detonation nanodiamond consists of partially crystalline, approximately spherical nanoparticles made up mostly of carbon, with a fairly reproducible diameter of ∼5nm. [162,163,356–358] It is produced in quantities of tens of tons annually, [156] having found various applications based mostly on the hardness or surface properties of the nanoparticles. Nanodiamond in lubricants can reduce the fuel consumption of internal combustion engines by 5%, [147] while blending it into polymers produces nanocomposites with improved hardness and stiffness. [144, 148, 205, 359] Favorable catalytic properties have also been reported. [150] Given that individual nanodiamond particles have low toxicity and the size of 50 kDa globular proteins, surface-functionalized nanodiamond is also promising for drug delivery. [147, 214, 360]

Surface functional groups are crucial for the interactions of nanodiamond particles with their surroundings, whether biological targets, catalysis substrates, or a polymer matrix. [190, 215] Some years ago, we studied the chemical and nanometer-scale structure of nanodiamond by $^{13}C\{^1H\}$ NMR and proposed a model with an ordered diamond core and a disordered shell of sp^3-hybridized carbon. [194] Most importantly, we reported that the fraction of aromatic carbons is $< 1\%$, which refuted models with an aromatic surface layer, including"bucky diamond"; [220, 361] we showed that instead the surface layer consists of sp^3-hybridized C–H (∼6%) and C–OH (∼4% of all C). Our model has been confirmed by XPS, which shows signals assigned to crystalline and disordered sp^3-hybridized carbon but no sp^2-hybridized C, in pristine detonation nanodiamond. [181, 362–364] In addition, other ^{13}C NMR studies of purified detonation nanodiamond also have not shown signals of aromatic carbons (i.e, peaks between 115 and 150 ppm that are not spinning sidebands). [230, 232–235]

Nevertheless, models of detonation nanodiamond with more than 40% of the particle surface covered by an aromatic shell, containing $> 10\%$ of all C (see calculation below), are still being put forward even by experts in carbon materials. [147, 150] This appears to be mostly based on small pre-edge X-ray absorption near-edge structure spectroscopy (XANES) peaks. However, some of this signal is from C=O rather than C=C, and even bulk diamond showed XANES pre-edge signal interpreted as representing 2% sp^2-hybridized C. [157] Furthermore, the theory

of XANES is complex, [365–367] and unlike direct-polarization NMR, XANES does not provide peaks whose areas are directly proportional to the numbers of carbons in the various functional group; [366,367] therefore, external standards (e.g., graphite) very different from nanodiamond have been used for calibration, which may be unreliable.

Still, it is a weakness of the previous ^{13}C NMR analyses of detonation nanodiamond [194, 227,230–235] that an aromatic-carbon signal was not identified and that signals of C=O groups seen in XANES and IR spectra were not detected. In this paper, we overcome this shortcoming and show that NMR can detect a few percent of sp^2-hybridized and ~1% aromatic carbon in nanodiamond. The aromatic-carbon signal is detected most clearly in a reference material where such carbon has been generated by heat treatment at 800 °C, generally consistent with Raman, XPS, and NMR studies of slightly pyrolyzed detonation nanodiamond. [224,235,362–364,368,369] The location of the sp^2-hybridized carbons at the nanodiamond particle surface is confirmed by probing their distance to ^{1}H. The signals of C=O and COO carbons, not detected in previous NMR studies [194, 227, 230–235] and therefore not considered in NMR-based models of nanodiamond, [194, 231] are also observed. By quantifying the ^{13}C NMR signals of sp^3-hybridized C–H and C–OH surface carbons, we provide a complementary upper limit to the sp^2-hybridized surface carbon fraction.

6.3 Experimental

Materials. Nanodiamond powder (> 97% purity) produced by the detonation method was purchased from Sigma-Aldrich and used as received ("pristine nanodiamond"). In addition, a reference material with a larger aromatic fraction, which is easier to detect by NMR, was produced by partial pyrolysis of the original nanodiamond at 800 °C for 6 h under an argon atmosphere ("800 °C-heat-treated nanodiamond").

NMR Spectroscopy. Solid-state NMR experiments were carried out at room temperature using a 400 MHz Bruker Biospin Avance spectrometer with a ^{13}C resonance frequency of 100 MHz, in ^{13}C{^{1}H} double-resonance probe heads for magic angle spinning (MAS) of 7 mm and 4 mm outer-diameter rotors. Samples were placed into 4 mm rotors for direct-polarization experiments with a Hahn echo before detection at MAS frequencies of 14 kHz, with 5 s recycle

delays for the pristine nanodiamond and 2 s recycle delays for the 800 °C-treated reference sample. Spectra with 2.5 times higher signal per unit time were obtained using 7 mm rotors, at 6 to 6.8 kHz MAS with total suppression of spinning sidebands (TOSS) using four 180° pulses and recycle delays of 4 and 2 s for the pristine nanodiamond and the heat-treated reference material, respectively. To achieve the required signal-to-noise ratios, between 4300 and 53000 scans were averaged, resulting in measuring times between 6 and 15 h per spectrum. Cross-polarization experiments were performed at 6.5 to 6.8 kHz MAS with TOSS and 1 s recycle delays, averaging ≥65500 scans per spectrum. ^{1}H decoupling of sufficiently high power and with two-pulse phase modulation (TPPM) [370] was applied during detection. Selective spectra of nonprotonated carbons were obtained by dipolar dephasing under the same conditions, with proton decoupling gated off for 40 and 68 μs [371] at ∼6 kHz and 14 kHz MAS, respectively. The difference between the full and dipolar dephased spectra shows signals mostly of protonated carbons. Chemical shifts were referenced to neat TMS at 0 ppm using α-glycine COO at 176.5 ppm and the methylene peak of adamantane at 38.5 ppm as secondary references; [372] the peak maximum of our detonation nanodiamond is at 35.1 ± 0.2 ppm.

6.4 Results and discussion

Detection of sp^2-Hybridized C in Nanodiamond. Figure 1(a) shows quantitative, direct-polarization ^{13}C NMR spectra of pristine detonation nanodiamond (thin line) and of nanodiamond after 800 °C heat treatment (thick line). The position and shape of the main peak near 35 ppm, from the crystalline diamond core, [194] and the broad foot up to 100 ppm from surface carbons and the disordered alkyl shell [194] are very similar in the two spectra, showing that most of nanodiamond has not been altered by the heat treatment. The main difference is a reduction of the small signal near 70 ppm, which is due to loss of most alkyl C–OH groups as a result of the heat treatment.

The signals of sp^2-hybridized carbons at >100 ppm are too small to be visible on the scale of Fig. 6.1(a), but they can be seen after the spectra have been scaled vertically by a factor of 34 (Fig. 6.1(b)(c)). The C=C band is particularly clear in Fig. 6.1(b), the spectrum of the heated material, which shows just the band centered near 135 ppm. In pristine nanodiamond,

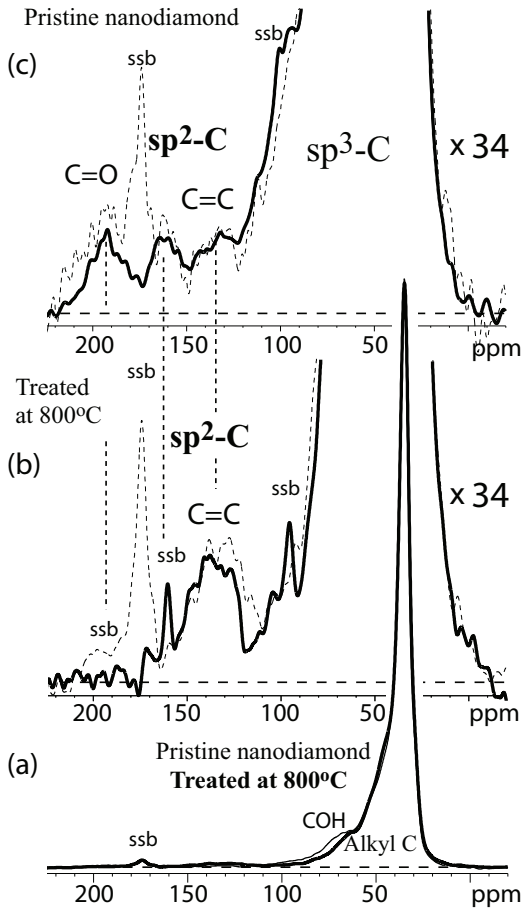

Figure 6.1 Quantitative, direct-polarization ^{13}C NMR spectra of detonation nanodiamond and a heat-treated reference sample. (a) Spectra of pristine nanodiamond (thin line) and of the 800 °C heat-treated material (thick line), taken at 14 kHz MAS. (b) Spectra after 800 °C heat treatment, expanded 34 times vertically, taken at 14 kHz MAS (dashed line) and at 6 kHz with TOSS (full line). A broad C=C band is clearly visible. (c) Same as (b) for pristine nanodiamond (except higher spinning frequency of 6.5 kHz for TOSS spectrum). "ssb": Spinning sideband.

additional signals near 163 and 193 ppm are detected (see Fig. 6.1(c)). Detection of these signals, which are small not only in absolute terms but also relative to the two-orders-of-magnitude larger peak at 35 ppm, requires careful spectroscopy. They are visible only after sufficient signal averaging and with minimal baseline distortions, achieved by use of a Hahn echo and careful phasing of the spectrum. Residual spinning sidebands of the 35 ppm peak, which occur at nr from the main peak, are comparable to the sp^2-carbon signals, even at high spinning frequencies or after TOSS, and must not be included in the quantification of the sp^2-hybridized carbon signals. By comparing spectra taken at $v_r \approx 6$ kHz with TOSS (full lines)

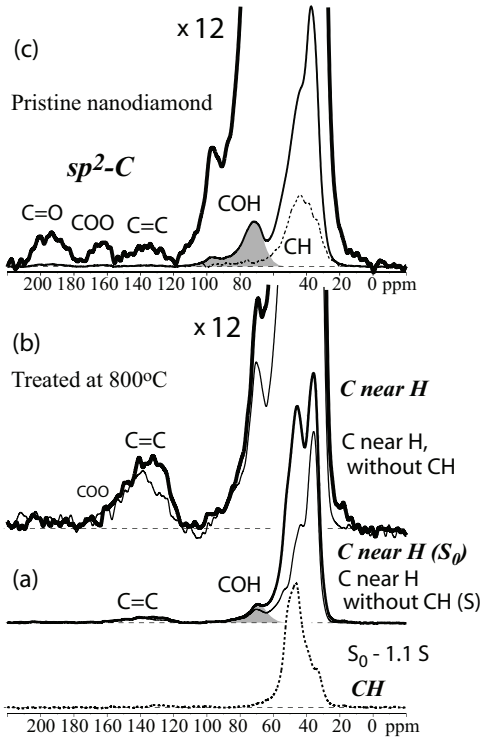

Figure 6.2 Surface-selective spectra: ^{13}C NMR of pristine detonation nanodiamond and of heat-treated nanodiamond after 1 ms cross-polarization from ^{1}H. (a) Spectra of 800 °C heated material with enhanced C=C fraction, taken at 6.5 kHz MAS with TOSS. Thick line: C near H; thin line: C near H but not bonded to H (after dipolar dephasing of CH signals); dashed line: CH signal obtained by difference from the two previous spectra. (b) Same spectra as in the top part of (a), expanded 12 times vertically. The broad C=C band is clearly visible. (c) Same as the thick line in (b) for pristine nanodiamond; the unscaled full CP spectrum and dashed spectrum of CH as in (a) are also shown. The area of the COH carbon signal has been highlighted by shading and is comparable to that of CH (under the dashed line).

and at $\nu_r = 14$ kHz (dashed lines), real signals can be distinguished from spinning sidebands, whose position can be predicted exactly. The signals of the sp^2-hybridized carbons are seen even more clearly in cross-polarization spectra (see Fig. 6.2), which are free of detectable spinning sidebands since the intense peak at 35 ppm, from the nonprotonated interior diamond carbons, is suppressed by cross-polarization from ^{1}H. The spectra of the sample treated at 800 °C are particularly clear. They show one broad band between 150 and 110 ppm, which can be attributed to C=C, including aromatic carbons.

The band near 130 ppm in the spectra of Figs. 6.1(c) and 6.2(c) provides the first reliable

detection of C=C signals in pristine purified detonation nanodiamond by NMR. A sharp peak at 111 ppm previously claimed to be from aromatic C [227] has never been reproduced, [194, 230, 232, 233] not even in spectra published by some of the same authors, [234, 235] and was most likely due to a spinning sideband or signal of Teflon tape used to balance the rotor.

In pristine nanodiamond (see Fig. 6.1(c) and Fig. 6.2(c)), signals of sp^2-hybridized C other than C=C are clearly observed near 163 and 193 ppm. These can be assigned to COO and C=O functional groups, respectively. The complexity of this spectrum and the small intensity of each peak, also relative to spinning sidebands, prevented the identification of these signals in earlier studies. [194, 227, 230, 232–235] As a result, COO and C=O groups were missing from previous NMR-based models of detonation nanodiamond. [194, 231]

Quantification of C=O, COO, and Aromatic C in Nanodiamond. The peak areas in the direct-polarization spectra of Fig. 6.1 are quantitative, apart from minor differential signal loss due to incomplete relaxation during the recycle delay or due to undetected spinning sidebands. The good match (outside of the spinning sidebands) of the spectra acquired under different conditions in Figure 1b,c indicates that these corrections are quite small. To account for incomplete relaxation and spinning sidebands, a correction factor of 1.1 (i.e., +10%) was applied to the integrals of the small C=O and COO peaks, and the C=C intensity was corrected by 1.3; the uncorrected values are within the error margins given in Table 6.1.

Table 6.1 Amounts of Functional Groups at the Nanodiamond Particle Surface, as Percent of All C, From Quantitative ^{13}C NMR Spectra of Pristine Detonation Nanodiamond (Top Row) and Nanodiamond after Heat Treatment at 800 °C (Bottom Row)

sample	**alkyl CH**	**alkyl C–OH**	**C=O**	**COO**	**C=C**	**total surface groups**
Pristine	5.3 ± 0.5%	4.9 ± 0.7%	0.7 ± 0.1%	0.6 ± 0.1%	1.1 ± 0.4%	12.6 ± 0.9%
800 °C	6.8 ± 0.5%	2 ± 1%	0 ± 0.1%	0.2 ± 0.1%	2.7 ± 0.6%	11.7 ± 1.3%

Integration shows that the signals between 220 and 120 ppm, which are assigned to sp^2-hybridized C, account for 2.4 ± 0.5% of all C in pristine detonation nanodiamond and 2.9 ± 0.5% after 800 °C heat treatment. This includes clear signals from C=O and COO groups around 193 and 163 ppm, respectively. The signal fraction between 150 and 115 ppm, which is

an upper limit to the aromaticity, is 1.1 ± 0.4% in pristine nanodiamond and 2.7 ± 0.6% after our heat treatment.

Carbon Fraction of a Complete Aromatic Shell. The small experimentally observed aromatic fractions should be compared with the value of 25% in a complete aromatic shell of 4.6 nm average diameter, derived in the following. To calculate the surface fraction, one can refer to Figure 3a, which shows that the area A1 per carbon atom in graphene is half of the single ring area of $3b^2\cos(30^\circ) = 0.052nm^2$, where b is the bond length. The number of carbons in a complete aromatic shell of radius R and area $A = 4\pi R^2$ is then obtained as

$$N_{arom} = A/A_1 = 4\pi R^2/(0.026nm^2) \tag{6.1}$$

which gives $N_{arom} = 2800$ carbons for R = 2.3 nm, out of approximately 10000 in the nanodiamond particle.

Alternatively, the average nucleus-to-nucleus diameter of 0.71 nm of the fullerene C60 and the scaling of the surface area with the square of the diameter can be used to estimate that there are approximately (4.6 nm/0.71 nm)2 × 60 = 2500 C atoms in a 4.6 nm diameter aromatic shell. We can also consider C540, with a reported 1.03 nm outer radius, [373] which after correction for the 0.077 nm atomic radius of carbon gives the center-to-nucleus radius of 1.03 nm − 0.077 nm = 0.953 nm; again, the surface area scales with the square of the radius, so a 2.3 nm radius aromatic shell would contain (2.3/0.953)2 × 540 = 3145 atoms out of ca. 10000.

These estimates consistently show that the fraction of carbons, and therefore of the NMR signals, from an aromatic or bucky-diamond shell would be at least 25%, which is higher than previously estimated. [231] The small aromatic signals in NMR and XANES (1–2% of all C, see below) thus rule out a significant aromatic surface coverage in pristine detonation nanodiamond, disproving the "bucky diamond" [220, 361] and several partial aromatic-shell models [147, 150] in the literature.

Fraction of Carbons in the Surface Layer. As a starting point for the quantification of sp^3-hybridized carbons at the nanodiamond particle surface, we need to estimate the fraction of carbon atoms in the surface layer (i.e., those with three or fewer bonds to other C) of a 4.8 nm diameter bulk-terminated nanodiamond particle. To a good approximation, this is equal

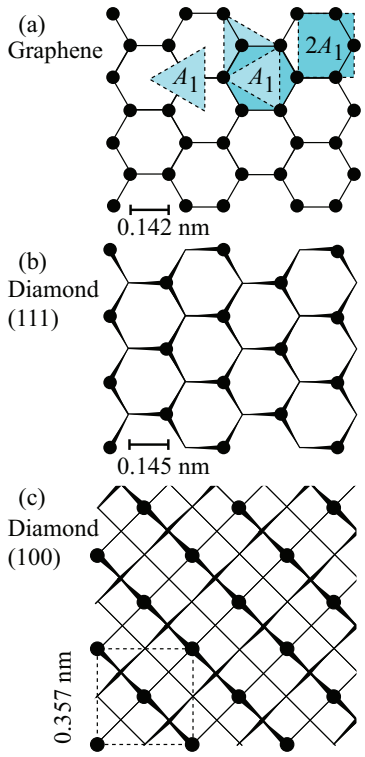

Figure 6.3 Distribution of surface carbons (filled circles) for (a) graphene; (b) the bulk-terminated diamond (111) surface, where one broken bond per surface carbon points perpendicular to the surface; and (c) the bulk-terminated diamond (100) surface, with two broken bonds per surface carbon (projected onto the thinnest diagonal lines). The three structures are drawn on the same scale. A carbon atom is located wherever full lines meet or intersect, but only carbons at the surface (i.e., with fewer than four bonding partners) are shown as circles. Out-of-plane orientations of bonds near the surface are indicated by "wedges". In (a), the area A1 per carbon and its relation to the area of a six-membered ring are indicated. The figures highlight the >2-fold higher density of surface carbons in graphene (in a) compared to bulk-terminated diamond (in b,c).

to the volume fraction v_{surf} of the surface layer. For a spherical particle, it is obtained from the radius R of the nanoparticle and the thickness L of the surface layer according to

$$v_{surf} = \frac{4/3\pi R^3 - 4/3\pi(R-L)^3}{4/3\pi R^3} = 1 - (1 - L/R)^3 \tag{6.2}$$

Inspection of the diamond crystal structure [374] shows that parallel to the (100) surface there are four carbon layers per 0.357 nm, so the layer spacing is $L = 0.09$ nm, which yields v_{surf} = 11% for a particle with a diameter of 2R = 4.8 nm. Parallel to the diamond (111) surface, a slightly more complex analysis yields v_{surf} = 11.5%. Figure 3b,c displays the distribution of carbon atoms on these two surfaces. Comparison with Figure 3a shows that an aromatic layer

has a 2.2-fold larger surface-carbon density than bulk-terminated diamond, which is consistent with the 25% and 11% surface fractions, respectively, that we have predicted for these two structures.

Deviations from perfect spherical shape, such as faceting, increase the surface fraction only slightly relative to eq 2. For instance, for a cubic particle of the same diameter as the sphere (i.e., with side length 2R), v_{surf} is also given by eq (6.1); for a cubic particle of the same volume as the sphere, the surface fraction is only 1.24-fold larger. Including such effects and some surface roughness, a surface fraction of v_{surf} = 12–14% is a reasonable estimate for our nanodiamond samples with 4.8 nm particle diameter. If the diameter was somewhat larger, [364] the surface fraction would be proportionally smaller.

In a recent review of NMR of nanodiamond, [231] it was proposed that 19% of all carbons are in the surface layer of a bulk-terminated 4.5 nm nanodiamond particle. This erroneously high value was the result of the unrealistic assumption [231] that the surface layer thickness L is equal to the diameter of a carbon atom (0.154 nm). This is the bond length in nanodiamond, while for a realistic estimate of L the bond length must be projected onto the surface normal. Bursill and Fullerton, [375] who were quoted in ref. [231], determined the number of carbons in a 0.125 nm thick shell, not just the carbons at the surface. For instance, in Figure 3b all the carbons (unmarked vertices and black circles) near the (111) surface are less than 0.125 nm from the surface, but only half of them are surface carbons (i.e., not bonded to four other sp^3-hybridized carbons).

Just based on this faulty surface fraction, [231] our structural model of nanodiamond was explicitly rejected in ref [231]. At the same time, ref [231] did not account for the NMR signal or the structure of the putative remaining ~1/3 of the surface carbons. In other respects, ref [231] seems to agree with our structural conclusions, [194] given that the model in Figure 10 of ref [231] is essentially a copy of ours (Figure 11 of ref [194]), with two "sp^2 flakes" and possibly some ill-defined bare spots added. We have now detected and characterized the small fraction of sp^2 carbons, most of which are C=O or COO groups.

Reference [231] referred to bare spots on the nanodiamond particle surface without specifying their structure. A simple calculation shows that these cannot be significantly terminated

by dangling bonds: Even if all of the 15 [231] to 40 [194] unpaired electrons per 10000-carbon particle were at the surface, less than 40/10000 = 0.4% among the ∼12% surface carbons would be terminated by a dangling bond. In addition, we have shown by NMR relaxation analysis, [194] and others have confirmed by EPR, [376] that most unpaired electrons are not at the nanoparticle surface. With <20% of the unpaired electrons at the surface, the fraction of surface C with a dangling bond is reduced to <0.1%, which is negligible.

Alternatively, one could consider reconstruction of clean diamond surfaces, but this would result in carbons with only three bonding partners and significant π-bonding, [377] which should exhibit characteristic downfield (high ppm) chemical shifts. Our data show no evidence (<5%) of such unusual structures, and we can explain most, if not all, of the surface structure in terms of conventional functional groups (see next section).

Quantification of Surface Groups: CH and COH. In the present study, we have confirmed that only a minor part of the nanodiamond surface layer is sp^2-hybridized; therefore, we must account for the majority of surface atoms in terms of sp^3-hybridized carbons.

We had previously identified CH and COH surface groups in pristine purified detonation nanodiamond by NMR and estimated their amounts. [194] In the following, we refine these estimates. Fig. 6.2 shows that in pristine detonation nanodiamond and still after 800 °C heat treatment cross-polarization from ^{1}H to ^{13}C gives strong signals. ^{1}H–^{13}C dipolar dephasing after cross-polarization destroys the signals of CH carbons while retaining those of C near H but not bonded to it (thin line in Fig. 6.2(a)). The spectrum of the CH carbons (dashed line in Fig. 6.2(a) and (c)) is obtained as the difference between the full spectrum and the dipolar dephased spectrum, scaled by 1.1 to account for slight long-range dephasing of the nonprotonated carbons; note that this scaling decreases the signal fraction assigned to CH.

The spectra in Fig. 6.2(a) also exhibit a peak near 70 ppm, which are assigned to C–OH groups. This peak is most pronounced in the spectrum of pristine nanodiamond (Fig. 6.2(c)); a secondary peak at 98 ppm can be attributed to O–C–OH groups (also sp^3-hybridized C). The total area of these C–OH signals (shaded in Fig. 6.2(c)) is almost as large as that of the CH groups (dashed line in Fig. 6.2(c)) selected by the dipolar-dephasing difference. Taking into account the slightly lower cross-polarization efficiency of C–OH groups due to the larger

^{1}H–^{13}C distance, this shows that the C–OH and CH fractions are similar.

While cross-polarization and dipolar-dephasing difference provides the spectrum of the CH groups with good signal-to-noise ratio, this approach does not lend itself to CH quantification. Instead, we combine direct polarization, which gives a quantitative spectrum, with dipolar dephasing, [371, 378] which selectively suppresses the signal of CH groups; the difference from the full spectrum is mostly the spectrum of CH carbons, and its area fraction out of the total signal is slightly larger than the fraction of C bonded to H. This is shown for 800 °C-treated nanodiamond in Figure 4a. On the basis of this dipolar-dephasing difference approach, the C–H fraction is found to be 5.3 ± 0.5% in pristine nanodiamond and 6.8 ± 0.5% after 800 °C heat treatment.

The direct-polarization spectrum can also confirm the COH quantification. The spectrum of pristine nanodiamond shows a pronounced shoulder near 75 ppm, which is mostly lost during heat treatment (see Fig. 6.1(a)). The same loss of COH signal is also seen when comparing the CP spectra in Fig. 6.1(a) and (c). The shoulder between 65 and 110 ppm in the DP spectrum of Fig. 6.4(b) accounts for ca. 9% of all C, with signal contributions from C–OH as well as carbons in the disordered shell. [194] Fig. 6.4(b) also compares the quantitative DP spectrum of pristine nanodiamond with the CP spectrum, where the C–OH resonance (highlighted by gray shading) is better resolved. When the CP spectrum is scaled to give a smooth, nonnegative difference spectrum, as in Figure 4b, a C–OH fraction (between 60 and 110 ppm) of ∼5% is obtained.

Table 6.1 summarizes the amounts of the various surface functional groups in the two samples. Within the error margins, the total fractions of surface groups match the expected range of 12–14% of all C (see above), which shows that NMR has not missed a major fraction of surface groups. In other words, this result excludes the presence of a significant fraction of aromatic rings that might be invisible to NMR for some reason.

Location of sp^2-Hybridized C at the Nanodiamond Surface. The cross-polarization spectra of nanodiamond selectively show signals of C near the protonated particle surface. The relatively strong signals of most of the sp^2-hybridized carbons after cross-polarization from ^{1}H (see Figure 2) prove that the C=O, COO, and C=C groups are near that surface. They also

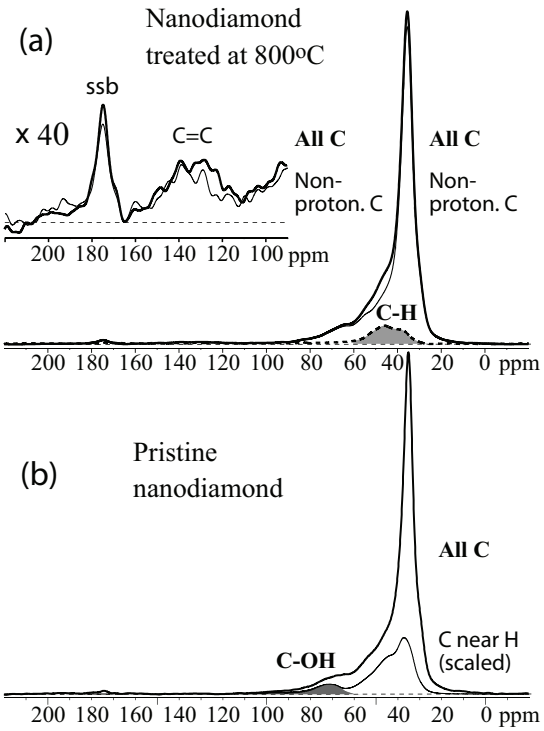

Figure 6.4 Quantification of nanodiamond CH and COH fractions: (a) Quantitative, direct-polarization ^{13}C NMR spectra of 800 °C heat-treated nanodiamond acquired without (thick line) and with (thin line) 68 μs of recoupled ^{13}C–^{1}H dipolar dephasing, which suppresses signals of CH groups. The difference spectrum (dashed line), whose shaded area at <60 ppm accounts for 8.3% of the total, is mostly the signal of CH groups. The inset shows the spectral region from 80 to 220 ppm scaled vertically by a factor of 40. (b) Quantitative, direct-polarization ^{13}C NMR spectra of pristine nanodiamond (thick line) and the selective cross-polarization spectrum of surface C near H (thin line), superimposed with the scaling factor adjusted to give a smooth difference spectrum. The area of the COH signals between 60 and 110 ppm, which corresponds to ca. 5% of the total, has been highlighted by shading.

exclude large patches of a bucky-diamond aromatic termination of the diamond surface, where many aromatic carbons would be distant from H. Similarly, the easy polarization transfer from ^{1}H to sp^2-hybridized ^{13}C shows that most of the sp^2-hybridized carbons are not incorporated into reconstructed, H-free "bare spots" [231] on the nanodiamond surface. Recoupled ^{13}C{^{1}H} dipolar dephasing [194] of the aromatic C after 800 °C heating was very fast (data not shown), confirming the small distance to H.

The same conclusion is obtained from complementary data, the significant aromatic C–H fraction revealed by dipolar dephasing of the aromatic-carbon signals in both CP (Fig. 6.2) and

DP (Fig. 6.4) spectra. The spectra indicate that ∼1/3 of the C=C or aromatic C is bonded to H. In large patches of aromatic surface sheets, which do not contain H in their interior, the protonated-carbon fraction would be smaller.

Comparison with Other Studies. Aromatic carbons account for ∼10% of all carbons in the Mochalin-Gogotsi model [147] of pristine detonation nanodiamond at room temperature, apparently based on reported 6% of sp^2-hybridized C in pristine detonation nanodiamond from XANES. [157] Nevertheless, a closer analysis of the original XANES data [157] reveals a much smaller discrepancy with NMR. In XANES of pristine purified detonation nanodiamond, as in IR [150] and our NMR spectra, the most pronounced peaks among all sp^2-hybridized C are from C=O groups, not from aromatic C. [157] In addition, even bulk diamond shows a pre-edge background corresponding to 2% of sp^2-hybridized C, [157] which must be considered as an artifact of the XANES method. Subtracting this background from the XANES-derived 4% of aromatic C in typical pristine purified detonation nanodiamond [157] gives an aromatic fraction of 2%, equal to the C=O fraction. This aromatic fraction represents less than 1/11 of a full aromatic shell, which would contain ca. 25% of all C (see above). Given that XANES peaks are not inherently quantitative, [366,367] the XANES data are quite consistent with the 1.1 ± 0.4% of aromatic C from our direct-polarization NMR spectra, where peak areas are directly proportional to the numbers of carbons.

Our NMR spectra of pristine purified detonation nanodiamond are in good agreement with those in the literature [230,232–235] acquired with the same excitation method (direct polarization or cross-polarization), apart from operational differences in signal-to-noise ratio, baseline, and spinning sideband artifacts. Thus, any significant disagreement between conclusions from NMR data cannot be attributed to differences in samples obtained from different sources but must be due to a difference in analysis, for instance assuming different surface-carbon fractions as discussed above. The ∼5% sp^2-hybridized in pristine detonation nanodiamond claimed in a recent NMR study [371] is clearly not from aromatic carbons: The considerable noise between 110 and 150 ppm (i.e., in the aromatic-carbon region) in their Figure 4 ("UD90Ox") is as indistinguishable from the baseline as the pure noise between 200 and 250 ppm. The only detectable signal in the sp^2-carbon range, the peak at ∼156 ppm, is most likely the 12 kHz

spinning-sideband artifact of the main sp^3-carbon peak, similar to that seen in our Figure 1a at 14 kHz offset. This artifact has to be excluded from the quantification of the sp^2-hybridized carbons, but ref [371] gives no indications that this was done.

The text and graphical abstract of ref [150] represented the surface of pristine detonation nanodiamond mostly as an sp^2-hybridized graphitic shell. [220, 229] It was reported that an sp^2-carbon peak was observed at 287.4 eV in C 1s XPS, but inspection of the XP spectra in ref 12 does not support this claim for nanodiamond before heat treatment. Butenko et al.(48) were quoted in ref 12 for support of this claim, but in fact Butenko et al. reported the "absence of a pronounced sp^2 component" in their XPS spectra even after heating to ~830 °C and concluded that "annealing of ND at 1170 K is insufficient to produce appreciable graphitization". [379]

The moderate aromatic-carbon fraction after heating to 800 °C observed in this study is generally consistent with the literature, although the reported data show significant scatter, possibly due to different pyrolysis protocols. A Raman spectrum showed spectral changes but no graphitic peak, [224] while C 1s XPS studies found no detectable, [379] 7%, [363] or 12–25% [364] sp^2-hybridized carbon. Similarly, the broad and featureless sp^2-carbon NMR signal from nanodiamond annealed at 800 °C in ref 28 is much stronger than the aromatic-carbon signal of our corresponding heat-treated sample.

6.5 Conclusions

We have shown that ^{13}C NMR can detect and quantify small amounts of aromatic or other C=C carbons on the surface of nanodiamond particles. Applying this approach to pristine purified detonation nanodiamond, we have detected sp^2-hybridized C=O, COO, and aromatic/C=C carbons totaling only 2.4 ± 0.5% of all C. The aromatic fraction is only ~1.1%, which corresponds to less than 1/20 of an aromatic surface layer, as we have shown by a careful analysis of the carbon density in the surface layer. Not only have we detected and quantified the small amounts of C=C/aromatic carbons but also we have shown that other surface functional groups (CH, COH, COO, and C=O) make up ~11.5% of all C in pristine nanodiamond, which accounts for most of the surface sites; this is complementary evidence that excludes a dominant aromatic or bucky-diamond surface layer. A sample of nanodiamond heat-treated at 800 °C

was studied similarly for reference. Efficient cross-polarization from ^{1}H to most sp^2-hybridized carbons proves that the sp^2-hybridized carbons are close to hydrogen, which places them near the nanoparticle surface. The unique ability of NMR, demonstrated here, to accurately analyze the surface composition of nanodiamond particles will be useful for guiding rational functionalization of nanodiamond materials.

6.6 Acknowledgments

We would like to thank Y. Gogotsi and V. Mochalin for stimulating discussions. This work was supported by the U.S. Department of Energy, Office of Basic Energy Science, Division of Materials Sciences and Engineering. It was performed at the Ames Laboratory, which is operated for the U.S. Department of Energy by Iowa State University under Contract No. DE-AC02-07CH11358.

CHAPTER 7. QUANTIFICATION OF SURFACE FUNCTIONAL GROUPS, THE DISORDERED SHELL, AND N NEAR THE CORE OF OXIDATION-PURIFIED NANODIAMOND BY NMR

A paper to be submitted to Solid-State NMR

J-F. Cui,[1] V. Mochalin,[3] Y. Gogotsi,[2] K. Schmidt-Rohr[4]

1 Ames Laboratory - DOE and Department of Chemistry, Iowa State University, Ames IA 50011, USA

2 Department of Materials Science and Engineering, Drexel University, Philadelphia, PA 19104, USA

3 Department of Chemistry, Missouri University of Science and Technology, Rolla, MO 65409

4 Department of Chemistry, Brandeis University, Waltham MA 02453, USA

7.1 Abstract

We have confirmed and carefully quantified the main features of the nonaromatic core-shell model of nanodiamond, applying ^{13}C NMR spectra editing and long-range $^{13}C\{^1H\}$ dephasing to a sample of nanodiamond thoroughly purified by air oxidation. Various surface functional groups account for 10.9 ± 0.7 % of all C. They include alkyl C–OH, alkyl C–H, alkyl O–C–OH, C=O, COO, and C=C at 4.5, 2.4, 1.5, 0.8, 0.6, and 1.1 % levels, respectively. CH_3 and CH_2 groups are not detectable (<0.3%), but the O–C–OH groups must be located at edge sites previously proposed as CH_2 groups. Signals of carbons bonded to O and N are identified by their downfield chemical shifts and lower bonding symmetry, with resulting larger chemical-shift anisotropy. The majority of nitrogen atoms are not near the protonated particle surface,

since most of the ∼5% of C bonded to N is detected below the surface layers, using long-range $^{13}C\{^1H\}$ REDOR dephasing. The small width of the 65-ppm C–N peak indicates a uniform, crystalline environment; a similarly sharp and ca. 3 times more intense peak at 29.5 ppm is tentatively assigned to the ∼15% of all carbons that are separated from N by two bonds. The chemically distinct two carbon layers closest to the particle surface account for 22% of all C, and an additional >12% in the broad shoulder detected at >40 ppm must also be attributed to a third layer of distinctly noncrystalline sp^3-hybridized C. The ordered crystalline core far from the surface ^1H and with a typical diamond chemical shift of 35 ppm, accounts for ∼20% of all C. The remaining ∼40% of all C, which are closer to the surface than is the core, are detected in a twice-broader slightly asymmetric resonance displaced by +0.6 ppm from the crystalline-diamond peak.

7.2 Introduction

Nanodiamond is an attractive material for a variety of applications. Its hardness is desirable in composites, while its biocompatibility allows applications in high-end cosmetics. Nanodiamond particles, having diameters of ∼5 nm, are similar in size as for globular proteins, and a high surface-to-volume ratio [225] in combination with their functionalizable surface enables attachment of drug molecules for biomedical applications. [380] Nanodiamond is produced in ton quantities by detonation of carbon-containing explosives, such as TNT and hexogen, in the absence of oxygen. [147] The yield of nanodiamond in the detonation residue can reach 75%. One of the most expensive steps in the preparation of nanodiamond is removal of carbonaceous soot, metals, and other impurities. [156] Traditionally, this has been achieved by treatment with concentrated oxidizing acids [381]. However, it requires expensive corrosion-resistant equipment and costly waste disposal processes while barely providing sufficient purity for commercially available nanodiamond. More recently, air-oxidation [157] has been introduced as a more benign and less costly purification approach without any additional oxidizers, [178] catalysts, [382] or inhibitors [383] that may lead to significant losses of the diamond phase.

While air-oxidization shows little effects on lattice defects in the crystalline core [384] of nanodiamond, it is reported that various species can be etched from the surface of nanodia-

mond, including water and physically absorbed organic impurities, graphitic layers, amorphous carbon and ultimately the sp^3-hybridized carbons6, depending on the temperature of oxidation. In addition, a higher content of carboxyl groups (COOH) was observed in air-oxidized nanodiamond than in as-received samples. [385]

Here we report detailed investigations of the surface, shell, and core of air-oxidized nanodiamond using advanced solid-state NMR methods with recoupled dipolar and chemical-shift-anisotropy (CSA) dephasing. We have been able to obtain selective and quantitative direct-polarization spectra of the surface layers, of the rest of the disordered shell, and of the crystalline core, using C-H dipolar dephasing. The local deviations from local tetrahedral symmetry due to bonding of carbon to heteroatoms has been probed by ^{13}C CSA dephasing. Combined with ^{1}H-^{13}C dipolar dephasing, this can probe the location of nitrogen relative to the particle surface. The signal at -5.5 ppm from the main diamond signal is shown to arise from carbon in the core and is tentatively assigned to C separated from N by two bonds. The quantification of sp^2-hybridized carbon signals could be used to calibrate the corresponding signals observed in XANES. Both methods find consistently that the amount of C=O exceeds that of aromatic C. Through careful spectroscopy and spectral editing, close to a dozen different ^{13}C NMR peaks have been resolved. We critically evaluate claims in the literature such as the surface location of N. [231]

7.3 Experimental

NMR spectroscopy. Solid-state NMR experiments were performed at ambient temperature using a 400-MHz Bruker Biospin (Billerica, MA) Avance spectrometer at a ^{13}C resonance frequency of 100 MHz, in ^{13}C{^{1}H} double-resonance probe heads with 6.8-kHz magic angle spinning (MAS) of samples in 7-mm outer-diameter rotors. Direct-polarization spectra were measured with recycle delays of 8 s and total suppression of spinning sidebands (TOSS) using four 180° pulses. ^{1}H decoupling of sufficiently high power and with two-pulse phase modulation (TPPM) was applied during detection. To achieve the required signal-to-noise ratios, between 4,000 and 53,000 scans were averaged, resulting in measuring times between 6 and 15 hours per spectrum. Cross-polarization experiments were performed at 6.8-kHz MAS with TOSS and

1-s recycle delays, averaging ≥65,500 scans per spectrum. Selective spectra of nonprotonated carbons were obtained by dipolar dephasing under the same conditions, with proton decoupling gated off for 40 s. The difference between the full and dipolar dephased spectra shows signals mostly of protonated carbons. Chemical shifts were referenced to neat TMS at 0 ppm using α-glycine COO at 176.5 ppm and the methylene peak of adamantane at 38.5 ppm as secondary references. [372]

^{13}C{^{1}H} REDOR. Recoupled ^{13}C{^{1}H} dipolar dephasing (REDOR) experiments were performed with an 8.2-μs ^{1}H 180° composite pulse per half rotation period at 6.8 kHz spinning frequency. The ^{13}C 90° and 180° pulse lengths were 4.5 and 9 μs, respectively. The purpose is to distinguish nonprotonated carbons at different distances from the nearest protons by enhancing the differential dephasing of nonprotonated carbon signals, compared to standard dipolar dephasing without recoupling. [378] Applying REDOR after direct polarization (DP) ensures the observation of dephasing of nonprotonated carbons separated from the nearest proton by three or more bonds, while used after cross polarization (CP) it helps to monitor the dephasing of nonprotonated carbons close to protons.

Intermediate-depth ^{13}C{^{1}H} REDOR. In a regular ^{13}C{^{1}H} REDOR experiment on nanodiamond, one obtains the signal S of the core below a certain depth from the surface, and the signal ΔS of the shell within a certain depth. In order to select the spectrum of carbons at an intermediate depth, i.e. a depth slice, a first dephasing period is added to the regular ^{13}C{^{1}H} REDOR pulse sequence so the signals near the surface are dephased in both the reference and the additional-dephasing experiment. The difference $\Delta S'$ between the pre-dephased reference intensity S'_0 and the intensity S' after pre-dephasing and additional dephasing is from carbons at an intermediate depth from the surface.

^{13}C chemical-shift anisotropy dephasing. The ^{13}C chemical-shift anisotropy (CSA) reflects the bonding symmetry around different ^{13}C sites. It vanishes if the symmetry is perfectly tetrahedral, as in the case of carbon in an extended, undistorted diamond lattice without unpaired electrons. In this case, there is no decay of the signal during recoupling of the chemical shift anisotropy. [240] If the local symmetry is reduced, for instance by bonding of the observed carbon to oxygen or nitrogen, the chemical-shift anisotropy is nonzero and signals will dephase,

the faster the larger the chemical-shift anisotropy. We applied CSA dephasing with three ^{13}C 9-μs 180° pulses spaced by 70-μs, which refocus the isotropic chemical shift, and two 4.5-μs 90° pulses flanking a z-filter that is incremented in four steps of $t_r/4$ providing the γ-average. This enables four-pulse total suppression of sidebands (TOSS) applied before detection to suppress sidebands up to fourth order. [386] The experiment was performed with magnetization generated by CP from ^{1}H, and with direct polarization by a 90° pulse on ^{13}C; the recycle delays were 1 and 2 s, respectively. The CSA dephasing time $t_{CSA} = 70\mu$s produces 50% dephasing for relatively small chemical-shift anisotropies of $\Delta\sigma = |\sigma 33 - \sigma 11| = 40$ ppm. [371] In the analysis of the CSA dephasing and of spinning sidebands, the paramagnetic shift anisotropy due to the unpaired electrons must be taken into account.

7.4 Results and Discussion

Core vs. shell. Fig. 7.1(c) shows quantitative, direct-polarization ^{13}C NMR spectra of air-oxidized nanodiamond. The main peak at 35 ppm is assigned to the crystalline diamond core, and the shaded broad signals (including the low intensity between 210 and 115 ppm from sp^2-hybridized carbons, see Fig. 7.1(d) with 24-fold vertical expansion) come from the noncrystalline alkyl shell. [194] Fig. 7.1(b) exhibits only the signal of carbons far from the hydrogen-covered surface of nanodiamond, i.e. of the particle core, as selected by long, 8.8-ms ^{13}C{^{1}H} REDOR dephasing. The sharp peak of the core signal centered at 35 ppm matches the position of the main peak of all carbons in Fig. 7.1(c).

It has been shown by NMR [194] and confirmed by XPS [362, 363, 379] that a 4.8-nm diameter detonation nanodiamond particle has a complex structure consisting of ordered core and a disordered shell also made up mostly of sp^3-hybridized carbon atoms. The shaded area in Fig. 7.1(c) corresponds to 38% of all carbons, which represents a lower limit to the disordered shell component. Conversely, an upper limit of the core fraction, obtained from the area of signal at $\leq$ 40 ppm, is 41% of all C. The thickness of the shell may vary with the detonation conditions and chemical purification process. [387]

Selective spectra of the core and subsurface shell. Figure 7.2 presents expanded views of the sp^3-carbon signals of spectra from Fig. 7.1 and related data. Fig. 7.2(a) compares the

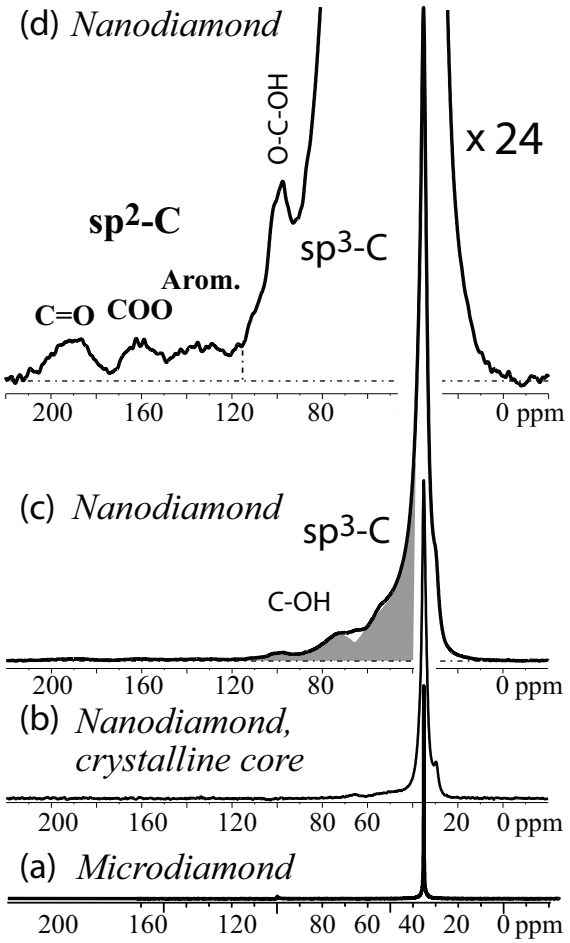

Figure 7.1 Direct-polarization ^{13}C NMR spectra of (a) microdiamond; (b) core of air-oxidized nanodiamond, selected by 8-ms ^{13}C{^{1}H} REDOR dephasing; (c) all carbon of air-oxidized nanodiamond; the signals of the disordered shell (excluding those of C-N near 66 ppm) shaded in gray account for 38% of the total area. (d) Same as c) with 24-fold vertical expansion, making small signals of sp^2-hybridized C visible (at >115 ppm).

full-echo ^{13}C{^{1}H} REDOR spectrum (S_0, dashed line), which shows signal associated with all carbon atoms in the nanodiamond, with some distortion due to differential relaxation. The reduced-echo spectrum (S, thin line) obtained with ^{1}H recoupling pulses characterizes carbon signals far away from hydrogen, i.e. mostly from the core of nanodiamond. The difference spectrum (ΔS, thick line) is complementary to the spectrum S and therefore contains substantial contributions from carbons that are in the nanodiamond shell.

Comparing the S_0 spectrum in Fig. 7.2(a) with the regular DP spectrum in Fig. 7.2(b), an increase in the sharp peak of the core, or conversely a decrease of the broad signal of the

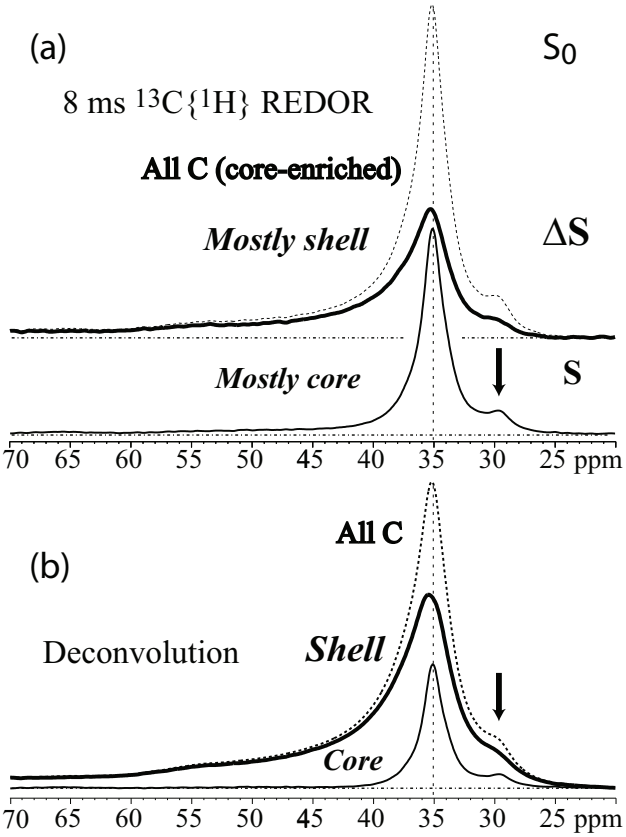

Figure 7.2 Estimation of core and shell contributions to the ^{13}C NMR spectrum. (a) Signals selected by 8-ms long-range $^{13}C\{^1H\}$REDOR dephasing. Dashed line: Spectrum without dephasing; thin solid line: Spectrum after dephasing, mostly from the particle core; thick line: signal lost due to dephasing, mostly associated with the shell near ^1H on the particle surface. (b) Same as a) but rescaled to correct for differential loss of shell intensity due to T_2 relaxation during $^{13}C\{^1H\}$REDOR. The signal at 29.5 ppm, tentatively assigned to C separated from N by two bonds, is marked with an arrow.

shell is observed. This indicates that shell signal has been lost due to differential T_2 relaxation, presumably due to the influence of unpaired electrons.

The core signal without distortion from T_2 relaxation is obtained by utilizing a series of dephasing1+decoupling − dephasing1+dephasing2 when performing the REDOR experiment. The first part, dephasing1+decoupling defines the signal of core with a shorter cut-off; the second part, dephasing1+dephasing2 indicates the shell signal scaled by a longer cut-off factor; Combining the two parts of the series, as displayed in Figure 2(b) select the signal of the ordered core in the nanodiamond; this also indicates an upper limit to the amount of carbon in the crystalline diamond core.

One can also see Fig. 7.4(b) for the expanded views of the signals between 20 and 70 ppm. The dashed line ΔS is the difference spectrum of two REDOR experiments, with short and intermediate dephasing pulse, respectively. $\Delta S = S/0.5\text{-ms} - S'/1.5\text{-ms}$, allows us to identify only the subsurface layers in the diamond shell.

C=O and COO. Signals of sp^2-hybridized carbons in the quantitative direct-polarization spectra of nanodiamond (Fig. 7.1(d)) at 193 ppm and 164 ppm are assigned to carbon with a double bond to oxygen, specifically C=O and COO groups, respectively. Dipolar dephasing has confirmed that these carbons are not bonded to hydrogen. As found before, the C=O and COO groups must be near the hydrogen-covered surface [388] of nanodiamond since their signals are clearly observed in cross-polarization spectra (Fig. 7.3(b)). Additionally, C=O and COO group in the $^{13}C\{^1H\}$ REDOR experiment dephase very fast even with short 0.6-ms dephasing time duration (Fig. 7.3(a)), which verifies their small distance from ^1H.

Aromatic C. The cross-polarization spectrum of nanodiamond (Fig. 7.3(b)) shows a broad band of low intensity between 160 and 120 ppm, which can be attributed to aromatic carbons. We observed a very similar small aromatic carbon signals at 130 ppm in purified pristine detonation nanodiamond. [388] In Fig. 7.1(d), the direct-polarization spectrum again displays the same peak position in the air-oxidized nanodiamond.

No CH_3 groups. Methyl groups at the nanodiamond particle surface are easy to imagine and have been proposed in a model of nanodiamond. [147] CH_3 groups have distinctive resonances at the right end of the ^{13}C NMR spectral range, with little overlap from other moieties. In addition, they can be observed selectively after cross polarization and dipolar dephasing: On the one hand, due to the three attached hydrogens, ^1H to ^{13}C cross polarization is efficient in a methyl group. On the other hand, the fast rotational jumps of a CH_3 group around it $C3$ symmetry axis reduce the C-H dipolar coupling and therefore lead to slower dipolar dephasing of CH_3 signals. As a result, after standard 40-μs dipolar dephasing, about 57% of the methyl signal remain. In the CP spectrum after dipolar dephasing, Fig. 7.3, no significant signal is observed between 0 and 25 ppm. Therefore, we conclude that fewer than 0.3% of all carbons in the air-oxidized nanodiamond are in CH_3 groups.

Alkyl C bonded to OH. The signal observed at 72 ppm in DP spectra in Fig. 7.1(d)

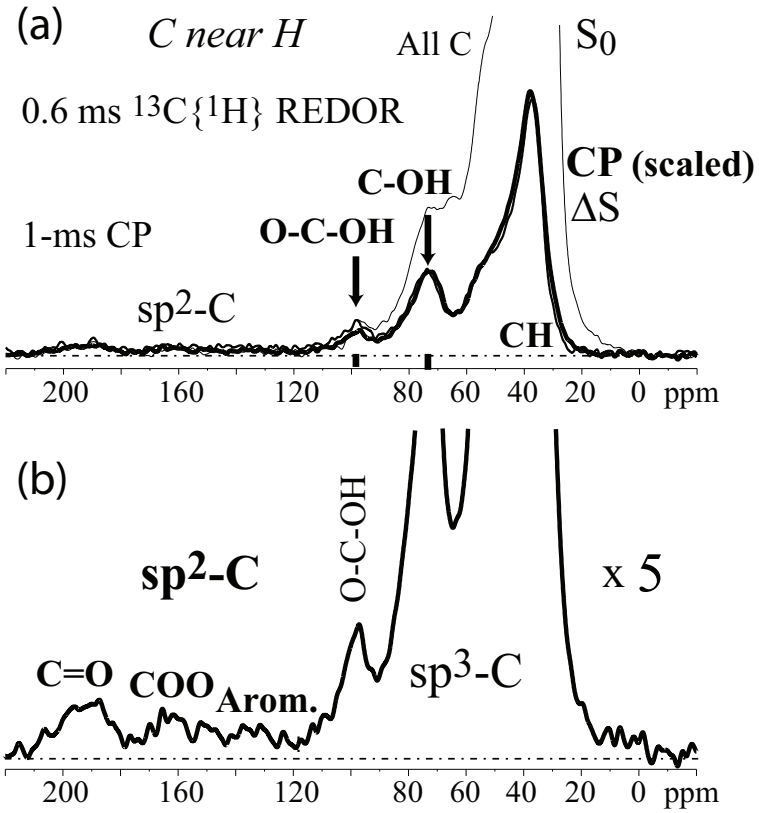

Figure 7.3 Selective ^{13}C NMR spectra of C within ca. two bonds from hydrogen, observed using ^{13}C{^{1}H} REDOR dephasing of short (0.6-ms) duration, after direct polarization. (a) Thin line: Full spectrum S_0. Thick line: difference spectrum of ^{13}C within a few bonds from ^{1}H, which matches closely with the suitably scaled cross polarization spectrum. (b) The CP spectrum scaled up by a factor of 5, which makes C=O and C=C signals visible.

and CP spectra in Fig. 7.3(a) (thin line) of the pristine detonation nanodiamond sample has been assigned to C–OH groups. The hydroxyl group are generated by the oxidative treatment3 of nanodiamond and have also been detected in FTIR and XPS spectra. [157, 363, 389, 390]

The short CP spectra shows not only signals of carbon atoms directly bonded to protons but also of carbons separated from the nearest proton by two or more bonds. The signal of each of these more distant is weaker than that of a carbon directly bonded to H, but since there are at least three times more of the more distant carbons, their signals are not negligible. Therefore we performed recoupled C-H dipolar dephasing (^{13}C{^{1}H} REDOR) experiments with different dephasing times to distinguish nonprotonated carbons at different distances to the nearest protons.

Figure 7.3(a) shows the $^{13}C\{^1H\}$ REDOR spectra obtained with a short dephasing time of 0.6-ms after direct polarization. The full spectrum S_0 (thin line) was obtained without dephasing pulses, the signal of ^{13}C near ^1H as the difference ΔS (thick line) where $\Delta S = S_0 - S$ with the signal S after rotor-synchronized dephasing pulses. Since S represents only the signals of nonprotonated carbon atoms close to the surface, the difference spectrum ΔS is then the carbons bonded to protons on the surface. The good match of ΔS and the 1-ms CP spectrum (thick line, scaled) confirmed that C–OH groups on the surface of nanodiamond, contrary to a claim in the literature that this signal is from the core12. The core is separated from the surface layer by more than 0.8 nm and will therefore not contribute significantly to the current difference spectrum ΔS.

One may also notice that the shoulder at 55 ppm dephases significantly within 1.5-ms, which indicates that the signals are from C near the protonated surface. It might be from C–C–O, i.e. carbons with a two-bond distance from O.

Alkyl O–C–OH and H–C–OH. The signal at 98 ppm in Fig. 7.3(a) and Fig. 7.4(a) can be assigned to O–C–OH sites. These account for 20% of all alkyl C bonded to OH. Their slow dipolar dephasing identifies these as nonprotonated carbons.

To saturate carbons at the edges of faceted nanodiamond particles, two bonds are required. Traditionally, CH_2 groups have been proposed for these edge sites [391–393], but we have not detected any [194]. However, C=O, O–C–OH and H–C–OH groups can similarly occupy edge sites, and these have been detected at 0.8%, 1.5%, and ∼0.5% levels. Similarly, carbon at the bulk-terminated diamond (100) surface [390, 394] would also need two external bonding partners.

The reduction of the signal at 72 ppm and 100 ppm in the REDOR experiment with short 0.6-ms dephasing duration (Fig. 7.3(a)) is due to dephasing of C–OH and O–C–OH groups. In the direct-polarization spectrum in 7.1(c) of nanodiamond, peaks at 72 ppm is well presented, and with the scaled spectrum (d), a secondary resonance at 100 ppm can be observed clearly, which is assigned to O–C–OH bonding. With a longer 1.5-ms recoupled ^{13}C–^1H dipolar dephasing, one can gain extensive sight at the layers below the surface of nanodiamond. Fig. 7.4(a, thick line) shows the difference spectrum ΔS of carbons within a few bonds from protons,

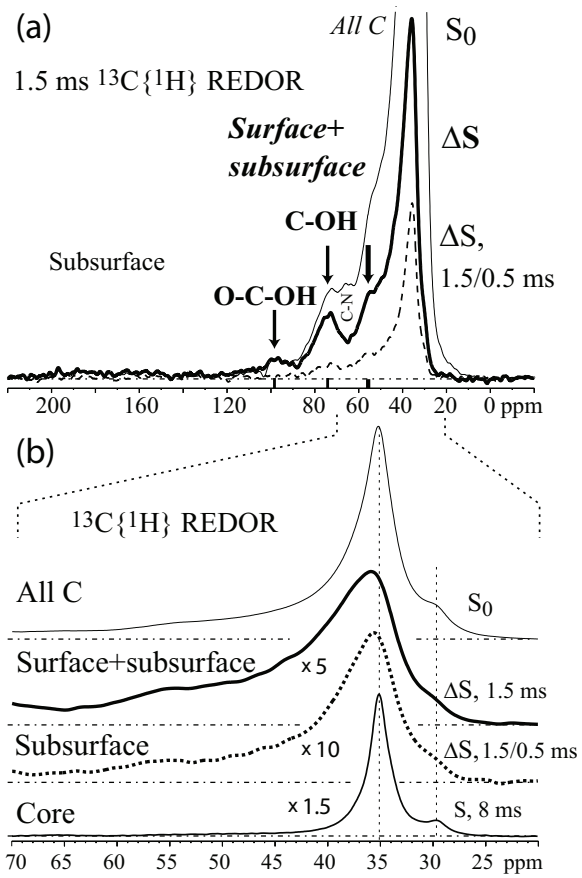

Figure 7.4 Selective ^{13}C NMR spectra of surface and subsurface layers, observed using $^{13}C\{^1H\}$ REDOR dephasing of intermediate (1.5-ms) duration, after direct polarization. (a) Thin line: Full spectrum S_0; thick line: difference spectrum of ^{13}C within a few bonds from ^1H. Dashed line: Signals from carbons at an intermediate depth from the surface, selected by REDOR with pre-dephasing of the surface signals. The three spectra are shown without scaling. (b) Expanded views of the signals between 20 and 70 ppm; at the bottom, the spectrum of the core obtained after long $^{13}C\{^1H\}$ dephasing is shown for reference.

which denotes the signal of surface and subsurface of the alkyl shell of nanodiamond. With estimation based on the dipolar dephasing approach, the area fraction of C–O out of the total alkyl carbon signal between 0 and 110 ppm, is 20% in air-oxidized nanodiamond.

Pervasive deviations of chemical shifts. The observed ^{13}C isotropic chemical shifts of most of the signals of nanodiamond are by 11 to 17 ppm lower than expected for the corresponding chemical environments in organic compounds. This is small enough, given the ∼200-ppm range of ^{13}C chemical shifts, that the assignments are not in doubt, in particular given that the protonation (or mostly lack thereof) of the carbon in question can be reliably determined

by dipolar dephasing. Nevertheless, it is a pervasive trend that should be pointed out.

To start with, the chemical shift of the diamond core is 35 ppm rather than 52 ppm; note that 35 ppm is also found in microdiamond, so this is not specific to nanodiamond. According to traditional increment rules [395],the diamond core has an expected chemical shift of at least 54 ppm, while the C-H surface signals would be predicted at 55 ppm. However, we observed these two carbon types at 35 ppm and 40 ppm, respectively, (see Fig. 7.2 (a)). Nonprotonated C–OH resonates not at the regular 85 [396] but at 72 ppm. Nonprotonated C-N not at 75 but at 66 ppm [397]. Similarly, the chemical shifts of C=O and COO signals, 193 ppm and 164 ppm, are about 11 ppm lower than the expected positions, 205 ppm [396, 398] and 175 ppm [396, 399] respectively. The observed upfield shift indicates an increase in charge density at the carbon nuclei. It is interesting to note that the experimental chemical shift of diamond has been reproduced in ab-initio calculations [400], where the bond length was shown to have a systematic influence.

Sites with reduced local symmetry: CSA dephasing. The magnitude of the chemical shift anisotropy (CSA) can provide information about the symmetry of the bonding environment around the carbon observed and therefore about bonding to heteroatoms and local structure. Carbons with highly symmetric tetrahedral bonding have much smaller ^{13}C CSAs than those in a lower-symmetry environment. After recoupling of the chemical shift anisotropy for a certain period $2t_{CSA}$, the signals of the lower-symmetry sites will be suppressed.

Fig. 7.5(a) shows a CSA-filtered CP/TOSS spectrum (red line) of surface carbons in air-oxidized nanodiamond obtained with 2 $t_{CSA} = 140$-μs filtering duration, the spectrum scaled up by a factor of 1.9 (dashed blue line), and the unfiltered CP spectrum (black line) for reference. After the filter, the C-OH groups show differential signal suppression by a factor of $\sim$4 relative to other alkyl signals. This is the result of oxygen breaking the tetrahedral bonding symmetry. The corresponding spectra obtained after direct polarization shows additional components with large CSA resonating between 50 and 70 ppm. The signals of these low-symmetry sites are seen most clearly in the scaled-difference spectrum of Fig. 7.5(c), where a peak near 55 ppm becomes visible. The presence of lattice distortions in the shell of nanodiamond particles [401] has also been evidenced in compressibility experiments.

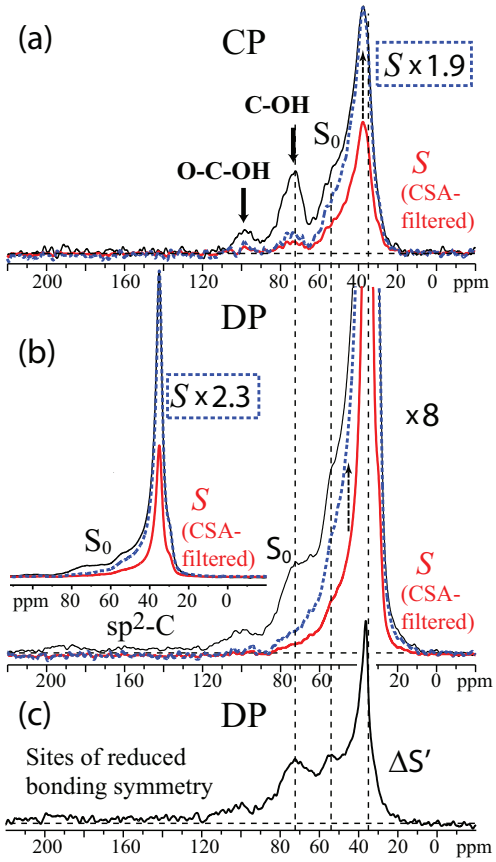

Figure 7.5 Characterization of the distortion of the local tetrahedral bonding symmetry by chemical-shift anisotropy (CSA) dephasing, using CSA recoupling after (a) cross polarization from ^{1}H; (b) direct polarization. Thin black line: Full spectrum S_0; thick red line: CSA-filtered spectrum of surface carbons. The dephased spectra after scaling by a factor close to 2 to match the biggest peak in the full spectrum S_0 are shown dashed. (c) Signals of sites with fast CSA dephasing, in a difference of the DP spectra in b) of the full spectrum S_0 and the scaled-up dephased spectrum 2.3 S.

C bonded to N. Since there is ∼2% nitrogen in nanodiamond and each is bonded to up to three carbons, we should anticipate signals of 4–6% C bonded to N. We previously detected the signal of ^{15}N in natural abundance in nanodiamond, so most N is not close to unpaired electrons that prevent NMR detection. This is in agreement with EPR of nanodiamond, which does not show the triplet due to the three nuclear spin states of ^{14}N. Nonprotonated C bonded to N is expected to resonate between 62 and 75 ppm. [402] While the unselective spectrum shows only a broad shoulder in this region, ^{13}C{^{1}H} REDOR dephasing reveals a peak at 66 ppm, see Fig. 7.6. The relatively small width of the peak strongly suggests a specific chemical

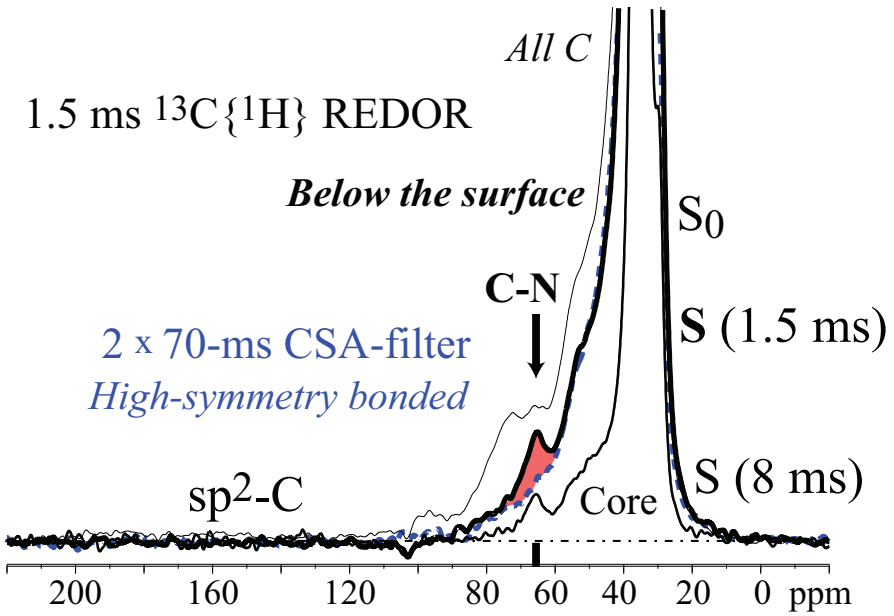

Figure 7.6 Identification of signals from carbon bonded to nitrogen, and of the depth of N from the protonated surface. Top spectrum (thin line): Full direct-polarization spectrum as reference for REDOR (S_0). Thick line: Spectrum remaining after ^{13}C{^{1}H} REDOR dephasing of intermediate duration (1.5-ms duration). Dashed line: Spectrum after CSA dephasing scaled to match the spectral intensity outside the distinct peak at 66 ppm. The absence of this peak after the CSA dephasing shows that it must be associated with a relatively large CSA (low bonding symmetry). Combined with the peak position, this results in an assignment to nitrogen-bonded carbon (C–N). Lowest spectrum (thin line): Remaining (core) signal after long ^{13}C{^{1}H}REDOR dephasing, scaled to match the C–N peak in the top two spectra.

environment.

The bonding to nitrogen is further strongly supported by the reduced local symmetry of the site associated with the 66-ppm peak, compared to C tetrahedrally surrounded by 4 other carbons. Bonding to the more electronegative N distorts the local tetrahedral symmetry. This reduced symmetry is proven by its fast chemical-shift anisotropy dephasing (see dashed line in Fig. 7.6, the spectrum after 70 μs of CSA dephasing). This dashed-line spectrum provides an experimentally determined baseline and enables estimation of an area fraction of 3–5 %. The main uncertainty arises from residual C-N signal in the CSA-dephased "baseline" spectrum.

The slow dipolar dephasing of the peak at 66 ppm shows that the nitrogen-bonded carbons are not at the surface; some are in the ordered core. This is a nontrivial result, which is contrary

to the expectations in ref. [231], where it was declared that "such a situation does not seem to be realistic".

C two bonds from N. Bonding to nitrogen does not only shift the resonance position of the directly bonded carbons, but also perturbs the chemical shift of carbons separated by two bonds from nitrogen ("C–C–N"). The electron-withdrawing effect of nitrogen, which is more electronegative than carbon, reduces the electron density and increases the chemical shift at the carbon to which it is bonded, but usually results in a slight increase in the electron density and a decrease in the chemical shift at the next-nearest neighbor. We can also predict the relative intensity of the C–C–N signal: Each carbon bonded to nitrogen is in turn bonded to three other carbons, so the signals of such carbons two bonds from N should account for $\sim 3 \times 5\% = 15\%$ of all C.

A signal that matches all these predictions is observed at 29.5 ppm. Its slow dipolar dephasing and cross polarization proves that it is not from a protonated C (e.g. CH), but from a partially crystalline nonprotonated C far from H, partially in the core.

Quantification of surface groups. We have verified that the majority of surface carbons (i.e. those bonded to three or fewer other carbons) are sp^3-hybridized. We identified CH, C–OH and O–C–OH in previous sections and earlier studies. [194, 388] We had also summarized the amounts of the various surface functional groups in pristine purified detonation nanodiamond and nanodiamond after 800 °C heat treatment. [388] Here we will quantify the fraction of surface groups in the air-oxidized sample and compare it with the other two samples.

The spectrum of the CH carbons (see line in Fig. 7.5(a) and Fig. 7.5(g)) in the air-oxidized nanodiamond is obtained as the difference between the full spectrum and the dipolar dephased spectrum and further confirmed by dipolar DEPT method. To obtain the quantitative result, direct polarization with 40-s gated decoupling [371, 378] was conducted, the C–H fraction is found to be 2.4 ± 0.4 % in air-oxidized nanodiamond, lower than 5.3 ± 0.5% in pristine nanodiamond (Fig. 7.7(h)) and 6.8 ± 0.5% in sample after 800 °C heat treatment (Fig. 7.5(i)). The increasing of amount of alkyl carbon bonded to H has also been illustrated by XANES and FTIR spectra. [157]

One can clearly observed dephasing of C–OH group in the CSA filtered spectrum (Fig.

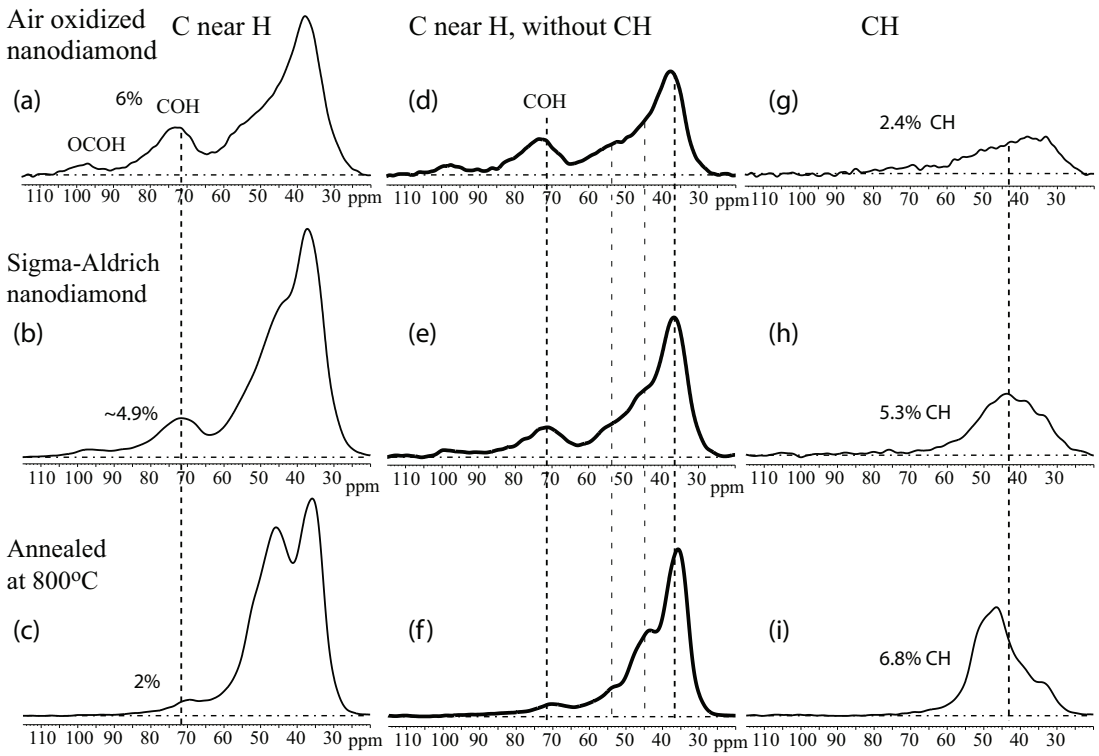

Figure 7.7 Comparison of spectra from surface and subsurface components of three samples. (a, d, g) Air-oxidized nanodiamond; (b, e, h) Sigma-Aldrich nanodiamond; (c, f, i) Sigma-Aldrich nanodiamond heat treated at 800 °C for 2 h.

7.5(a)), consistent with ΔS that overlaps C–OH in the REDOR experiment with 1.5-ms dephasing duration. Based on the recoupled dipolar dephasing difference, the C–O fraction is found to be 6 ± 0.7% in air-oxidized nanodiamond (Fig. 7.5(a)), slightly higher than the fraction of 4.9 ± 0.7% in the pristine nanodiamond (Fig. 7.7(b)) and 2 ± 1% in 800 °C heat treated samples (Fig. 7.5(c)).

The integral of peak areas in the direct-polarization spectra of Fig. 7.1(d) leads to the quantitative fraction of the sp^2-hybridized carbon, including C=C, C=O and COO. We have summarized the amounts of the various surface functional groups in the three samples in Table 7.1. The value is 2.4 ± 0.3% in pristine purified detonation nanodiamond [388] while for the air-oxidized nanodiamond, this value is 2.5 ± 0.5% with a correction factor of 1.3 applied to account for incomplete relaxation and spinning sidebands of the sp^2 carbons.

The long REDOR dephasing experiment can select the signal of the crystalline core of nanodiamond. As displayed in Fig. 7.1(b), the sharp peak at 35 ppm is assigned to the ordered

Table 7.1 Amounts of Functional Groups at the Nanodiamond Surface, From Quantitative ^{13}C NMR Spectra of Air-oxidized Detonation Nanodiamond (Top Row), Sigma-Aldrich ("SA") Detonation Nanodiamond [387] (Middle Row) and Nanodiamond after Heat Treatment at 800 °C [388] (Bottom Row).

Sample	**Alkyl CH**	**Alkyl C–OH**	**C=O**	**COO**	**C=C**	**total surface groups**
Air-oxidized	$2.4 \pm 0.4\%$	$6 \pm 0.7\%$	$0.8 \pm 0.1\%$	$0.6 \pm 0.1\%$	$1.1 \pm 0.3\%$	$10.9 \pm 0.7\%$
SA	$5.3 \pm 0.5\%$	$4.9 \pm 0.7\%$	$0.7 \pm 0.1\%$	$0.6 \pm 0.1\%$	$1.1 \pm 0.4\%$	$12.6 \pm 0.9\%$
800 °C	$6.8 \pm 0.5\%$	$2 \pm 1\%$	$0 \pm 0.1\%$	$0.2 \pm 0.1\%$	$2.7 \pm 0.6\%$	$11.7 \pm 1.3\%$

core in the nanodiamond, accounting for 20% of all carbon atoms.

7.5 Conclusions

The structure of air-oxidized nanodiamond has been analyzed by advanced solid-state NMR. While the regular ^{13}C spectrum of nanodiamond shows only one apparent peak (see Fig. 7.1(b)), careful spectroscopy and spectral editing has resolved ten peaks, of C=O, COO, C=C, O–C–O, C–OH, C–N, CH, subsurface C, core C, and C–C–N. The signal of carbon bonded to nitrogen has been observed selectively based on the breaking of the local symmetry and the resulting increased chemical-shift anisotropy, in conjunction with an upfield chemical shift. A three-times more intense signal at 29.5 ppm has been tentatively assigned to carbon with nitrogen as a second-nearest neighbor. The nitrogen is far from the protonated surface, according to $^{13}C\{^1H\}$ long-range dipolar dephasing. Signals from carbons at different depths from the protonated surface have been observed selectively through regular and modified $^{13}C\{^1H\}$ REDOR experiments, and their quantities estimated.

7.6 Acknowledgements

This work was supported by the U.S. Department of Energy, Office of Basic Energy Science, Division of Materials Sciences and Engineering. It was performed at the Ames Laboratory, which is operated for the U.S. Department of Energy by Iowa State University under Contract No. DE-AC02-07CH11358.

CHAPTER 8. GENERAL CONCLUSIONS

In this thesis, we have used the microscopic tool of NMR to study three different families of complex materials, namely the 122 Fe-based superconductors $Ca(Fe_{1-x}Co_x)_2As_2$, thermoelectric tellurides GeTe, Ag- and Sb-doped GeTe and detonation nanodiamond. NMR enables the investigation of the local magnetic properties of compounds. This becomes hugely important because practically bulk property measurement techniques like magnetization, heat capacity, Hall effect, diffraction or microscopy experiments are unable to conclusively detect intrinsic contribution alone. Also NMR is a great tool for gaining an insight into microscopic aspects of the materials.

In Chapter 3, we investigated the Co substitution effects on static and dynamic magnetic properties of the single-crystalline $Ca(Fe_{1-x}Co_x)_2As_2$ (x = 0, 0.023, 0.028, 0.033, 0.059) via ^{75}As NMR and resistivity measurements. We have shown clear evidence for the first order structural and stripe-type AFM from sudden change in ν_Q and internal field H_{int} at As sites in parent undoped CaFe2Fe$_2$As$_2$, samples with substituting concentration of x = 0.023 and x = 0.028. In the AFM state, clear separations of ^{75}As NMR lines due to H_{int} indicate the commensurate stripe-type AFM state in above samples. In addition, we observed only slight decreases of H_{int} although T_N is strongly suppressed with Co substitution, suggesting robustness of the Fe magnetic moments upon Co substitution in $Ca(Fe_{1-x}Co_x)_2As_2$.

In the paramagnetic state, the temperature dependence of Knight shift K for all crystals shows similar T-dependence of magnetic susceptibility χ, where the K_{spin} can be fitted with a thermal activation behavior of $\exp(-\Delta/k_BT)$ with nearly x independent Δ/k_B ~490 K, indicating that spin fluctuations with the q = 0 components are suppressed with Δ/k_B in the paramagnetic state. On the other hand, the growth of the stripe-type AFM fluctuations with $q = (\pi, 0)$ or $(0, \pi)$ upon cooling in the paramagnetic state for all samples is evidenced by

the T-dependence of $(1/T_1T\chi)$. We also found a gradual decrease of $1/T_1T\chi$ with decreasing T below a x-independent T^* ($\sim$100 K) in samples with $x \geq 0.028$. We attributed this suppression of the AFMSF to the behavior of pseudogap-like phenomenon. This pseudogap-like phenomenon seems to affect on the temperature-dependent inter-plane resistivity, $\rho_c(T)$, but not with in-plane resistivity $\rho_a(T)$. Furthermore, the ratio $(T_1)_c/(T_1)_{ab}$ increases with decreasing T and starts to decreases below T^*. This indicates that the amplitude of AFMSF in the ab plane is more suppressed than that along the c axis in the pseudogap-like phase.

In Chapter 4, we have reanalyzed NMR data in $Ca(Fe_{1-x}Co_x)_2As_2$ and found clear evidence for the coexistence of the stripe-type AFM and FM spin correlations. In contrast to the case of $Ba(Fe_{1-x}Co_x)_2As_2$ where the relative strength of FM correlations increases with Co substitution, the FM correlations are almost independent of Co substitution for our investigated range of $x = 0 - 0.059$ in $Ca(Fe_{1-x}Co_x)_2As_2$. The Curie-Weiss parameters $C_{\perp,\parallel}$ representing the strength of AFMSF are almost independent of Co doping, close to a feature of T^* representing a characteristic temperature of the pseudogap-like behavior.

In Chapter 5, we have carried out ^{125}Te NMR measurements to study the electronic properties of $Ge_{50}Te_{50}$, $Ag_2Ge_{48}Te_{50}$ and $Sb_2Ge_{48}Te_{50}$. We found that NMR shift K and $1/T_1T$ of $Ge_{50}Te_{50}$ are nearly temperature independent at T $<$ 50 K and both increase slightly with increasing temperature at high temperatures. We have explained these behaviors using a two-band model where one band overlaps the Fermi level and the other band is separated from the Fermi level by an energy gap. The first-principle calculation revealed that the metallic band originates from the Ge vacancy while the semiconductor-like band may be related to the fine structure of the density of states near the Fermi level.

At low temperature, we found conduction carriers are free carriers with no significant electron correlations, while Korringa ratio increases slightly at high temperature, suggesting the slight enhancement of the electron correlation. Our low-temperature ^{125}Te NMR data for $Ag_2Ge_{48}Te_{50}$ and $Sb_2Ge_{48}Te_{50}$ clearly shows that Ag substitution increases the hole concentration while Sb substitution decreases the concentration.

In Chapter 6, we have used ^{13}C NMR to accurately analyze the surface composition of pristine purified detonation nanodiamond and nanodiamond with heat-treatment at 800 °C

for reference. We have detected sp^2-hybridized C=O, COO, and aromatic/C=C carbons with a fraction of only 2.4 ± 0.5% of all carbons. The aromatic fraction is only ∼1.1%, which corresponds to less than 1/20 of an aromatic surface layer. We have also shown that other surface functional groups (CH, COH, etc.) accounts for most of the surface sites, making up ∼11.5% of all C in pristine nanodiamond. This is an clear evidence to exclude the dominant "bucky-diamond" model.

In Chapter 7, we have used ^{13}C spectral editing technique to analyze the air-oxidized nanodiamond. We have resolved ten peaks of C=O, COO, C=C, O–C–O, C–OH, C–N, CH, subsurface C, core C, and C–C–N. In addition, we have observed the signal of carbon bonded to nitroge selectively based on increased chemical-shift anisotropy due to breaking of the local symmetry. The nitrogen is far from the protonated surface, according to ^{13}C{^{1}H} long-range dipolar dephasing. Furthermore, we used modified ^{13}C{^{1}H} REDOR experiments to observe the signals from carbons at different depths from the surface and estimate their quantities.

BIBLIOGRAPHY

[1] H. K. Onnes, Commun. Phys. Lab. Univ. Leiden, **12**, 1 (1911).

[2] W. Meissner and R. Ochsenfeld, Naturwissenschaften, **21**, 787 (1933).

[3] J. Bardeen, L. N. Cooper and J. R. Schrieffer, Phys. Rev., **108**, 1175 (1957).

[4] F. Steglich, J. Aarts, C. Bredl, W. Lieke, D. Meschede, W. Franz and H. Schäfer, Phys. Rev. Lett., **43**, 1892 (1979).

[5] J. G. Bednorz and K. A. Mller, Ten Years of Superconductivity: 19801990, **267** (1986).

[6] D. J. Scalapino, Rev. Mod. Phys., **84**, 1383 (2012).

[7] M.-K. Wu, J. R. Ashburn, C. J. Torng, P. H. Hor, R. L. Meng, L. Gao, Z. J. Huang, Y. Wang and a. Chu, Phys. Rev. Lett., **58**, 908 (1987).

[8] D. J. Scalapino, Phys. Rep., **250**, 329 (1995).

[9] D. Pines, Physica B Condens Matter, **199**, 300 (1994).

[10] Y. Kamihara, T. Watanabe, M. Hirano and H. Hosono, J. Am. Chem. Soc, **130**, 3296 (2008).

[11] H. Takahashi, K. Igawa, K. Arii, Y. Kamihara, M. Hirano and H. Hosono, Nature, **453**, 376 (2008).

[12] X. Chen, T. Wu, G. Wu, R. Liu, H. Chen and D. Fang, Nature, **453**, 761 (2008).

[13] C. Wang, L. Li, S. Chi, Z. Zhu, Z. Ren, Y. Li, Y. Wang, X. Lin, Y. Luo and S. Jiang, EPL-Europhys. Lett., **83**, 67006 (2008).

[14] C. de La Cruz, Q. Huang, J. Lynn, J. Li, W. Ratcliff Ii, J. L. Zarestky, H. Mook, G. Chen, J. Luo and N. Wang, Nature, **453**, 899 (2008).

[15] J. Paglione and R. L. Greene, Nat. Phys., **6**, 645 (2010).

[16] H. Okabe, N. Takeshita, K. Horigane, T. Muranaka and J. Akimitsu, Phys. Rev. B, **81**, 205119 (2010).

[17] C.-H. Lee, A. Iyo, H. Eisaki, H. Kito, M. Teresa Fernandez-Diaz, T. Ito, K. Kihou, H. Matsuhata, M. Braden and K. Yamada, J. Phys. Soc. Jpn., **77**, 083704 (2008).

[18] S. A. Kimber, A. Kreyssig, Y.-Z. Zhang, H. O. Jeschke, R. Valent, F. Yokaichiya, E. Colombier, J. Yan, T. C. Hansen and T. Chatterji, Nat. Mater., **8**, 471 (2009).

[19] Y. Guo, X. Wang, J. Li, Y. Sun, Y. Tsujimoto, A. A. Belik, Y. Matsushita, K. Yamaura and E. Takayama-Muromachi, Phys. Rev. B, **86**, 054523 (2012).

[20] A. E. Taylor, *Magnetic dynamics in iron-based superconductors probed by neutron spectroscopy*. PhD diss., University of Oxford (2013).

[21] C. Varma, Nature, **468**, 184 (2010).

[22] D. J. Singh, Physica C Supercond, **469**, 418 (2009).

[23] A. Charnukha, P. Popovich, Y. Matiks, D. L. Sun, C. T. Lin, A. N. Yaresko, B. Keimer and A. V. Boris, Nat. Commun., **2**, 219 (2011).

[24] I. Mazin and J. Schmalian, Physica C Supercond, **469**, 614 (2009).

[25] D. Basov and A. V. Chubukov, Nat. Phys., **7**, 272 (2011).

[26] J. Zhao, Q. Huang, C. De La Cruz, S. Li, J. Lynn, Y. Chen, M. A. Green, G. Chen, G. Li and Z. Li, Nat. Mater., **7**, 953 (2008).

[27] P. Dai, J. Hu and E. Dagotto, Nat. Phys., **8**, 709 (2012).

[28] V. Zabolotnyy, D. Inosov, D. Evtushinsky, A. Koitzsch, A. Kordyuk, G. Sun, J. Park, D. Haug, V. Hinkov and A. Boris, Nature, **457**, 569 (2009).

[29] Y. Xia, D. Qian, L. Wray, D. Hsieh, G. Chen, J. Luo, N. Wang and M. Hasan, Phys. Rev. Lett., **103**, 037002 (2009).

[30] D. C. Johnston, Adv. Phys., **59**, 803 (2010).

[31] S. Chi, A. Schneidewind, J. Zhao, L. W. Harriger, L. Li, Y. Luo, G. Cao, Z. a. Xu, M. Loewenhaupt and J. Hu, Phys. Rev. Lett., **102**, 107006 (2009).

[32] D. Inosov, J. Park, P. Bourges, D. Sun, Y. Sidis, A. Schneidewind, K. Hradil, D. Haug, C. Lin and B. Keimer, Nat. Phys., **6**, 178 (2010).

[33] P. Popovich, A. Boris, O. Dolgov, A. Golubov, D. Sun, C. Lin, R. Kremer and B. Keimer, Phys. Rev. Lett., **105**, 027003 (2010).

[34] G. Lee, H. S. Ji, Y. Kim, C. Kim, K. Haule, G. Kotliar, B. Lee, S. Khim, K. H. Kim and K. S. Kim, Phys. Rev. Lett., **109**, 177001 (2012).

[35] E. Gati, S. Köhler, D. Guterding, B. Wolf, S. Knöner, S. Ran, S. L. Bud'ko, P. Canfield and M. Lang, Phys. Rev. B, **86**, 220511 (2012).

[36] H. Luetkens, H.-H. Klauss, M. Kraken, F. Litterst, T. Dellmann, R. Klingeler, C. Hess, R. Khasanov, A. Amato and C. Baines, Nat. Mater., **8**, 305 (2009).

[37] A. J. Drew, C. Niedermayer, P. Baker, F. Pratt, S. Blundell, T. Lancaster, R. Liu, G. Wu, X. Chen and I. Watanabe, Nat. Mater., **8**, 310 (2009).

[38] J.-H. Chu, J. G. Analytis, C. Kucharczyk, and I. R. Fisher, Phys. Rev. B **79**, 014506 (2009).

[39] N. Ni, M. E. Tillman, J. Q. Yan, A. Kracher, S. T. Hannahs, S. L. Bud'ko, and P. C. Canfield, Phys. Rev. B, **78**, 214515 (2008).

[40] S. Ran, S. L. Bud'ko, W. E. Straszheim, J. Soh, M. G. Kim, A. Kreyssig, A. I. Goldman and P. C. Canfield, Phys. Rev. B, **85**, 224528 (2012).

[41] K. Hashimoto, K. Cho, T. Shibauchi, S. Kasahara, Y. Mizukami, R. Katsumata, Y. Tsuruhara, T. Terashima, H. Ikeda and M. Tanatar, Science, **336**, 1554 (2012).

[42] A. I. Goldman, D. N. Argyriou, B. Ouladdiaf, T. Chatterji, A. Kreyssig, S. Nandi, N. Ni, S. L. Bud'ko, P. C. Canfield, and R. J. McQueeney, Phys. Rev. B **78**, 100506(R) (2008).

[43] N. Ni, S. Nandi, A. Kreyssig, A. I. Goldman, E. D. Mun, S. L. Bud'ko, and P. C. Canfield, Phys. Rev. B **78**, 014523 (2008).

[44] J.-Q. Yan, A. Kreyssig, S. Nandi, N. Ni, S. L. Budko, A. Kracher, R. McQueeney, R. McCallum, T. Lograsso and A. Goldman, Phys. Rev. B, **78**, 024516 (2008).

[45] J. Loudon, C. Bowell, J. Gillett, S. Sebastian and P. Midgley, Phys. Rev. B, **81**, 214111 (2010).

[46] E. Blomberg, M. Tanatar, A. Kreyssig, N. Ni, A. Thaler, R. Hu, S. BudKo, P. Canfield, A. Goldman and R. Prozorov, Phys. Rev. B, **83**, 134505 (2011).

[47] J.-H. Chu, J. G. Analytis, K. De Greve, P. L. McMahon, Z. Islam, Y. Yamamoto and I. R. Fisher, Science, **329**, 824 (2010).

[48] M. Tanatar, E. Blomberg, A. Kreyssig, M. Kim, N. Ni, A. Thaler, S. BudKo, P. Canfield, A. Goldman and I. Mazin, Phys. Rev. B, **81**, 184508 (2010).

[49] J.-H. Chu, H.-H. Kuo, J. G. Analytis and I. R. Fisher, Science, **337**, 710 (2012).

[50] S. Kasahara, H. Shi, K. Hashimoto, S. Tonegawa, Y. Mizukami, T. Shibauchi, K. Sugimoto, T. Fukuda, T. Terashima and A. H. Nevidomskyy, Nature, **486**, 382 (2012).

[51] R. M. Fernandes, E. Abrahams and J. Schmalian, Phys. Rev. Lett., **107**, 217002 (2011).

[52] R. Fernandes, A. Chubukov, J. Knolle, I. Eremin and J. Schmalian, Phys. Rev. B, **85**, 024534 (2012).

[53] M. Yi, D. Lu, J.-H. Chu, J. G. Analytis, A. P. Sorini, A. F. Kemper, B. Moritz, S.-K. Mo, R. G. Moore and M. Hashimoto, Proc. Natl. Acad. Sci., **108**, 6878 (2011).

[54] Y. Ishikawa, Y. Noda, Y. Uemura, C. Majkrzak and G. Shirane, Phys. Rev. B, **31**, 5884 (1985).

[55] D. Inosov, J. Park, A. Charnukha, Y. Li, A. Boris, B. Keimer and V. Hinkov, Phys. Rev. B, **83**, 214520 (2011).

[56] I. Mazin, D. J. Singh, M. Johannes and M.-H. Du, Phys. Rev. Lett., **101**, 057003 (2008).

[57] D. Parker, O. Dolgov, M. Korshunov, A. Golubov and I. Mazin, Phys. Rev. B, **78**, 134524 (2008).

[58] M. Korshunov and I. Eremin, Phys. Rev. B, **78**, 140509 (2008).

[59] C. W. Hicks, T. M. Lippman, M. E. Huber, J. G. Analytis, J.-H. Chu, A. S. Erickson, I. R. Fisher and K. A. Moler, Phys. Rev. Lett., **103**, 127003 (2009).

[60] J. Fletcher, A. Serafin, L. Malone, J. Analytis, J.-H. Chu, A. Erickson, I. Fisher and A. Carrington, Phys. Rev. Lett., **102**, 147001 (2009).

[61] K. Hashimoto, M. Yamashita, S. Kasahara, Y. Senshu, N. Nakata, S. Tonegawa, K. Ikada, A. Serafin, A. Carrington and T. Terashima, Phys. Rev. B, **81**, 220501 (2010).

[62] J. P. Reid, M. A. Tanatar, A. Juneau-Fecteau, R. T. Gordon, S. R. de Cotret, N. Doiron-Leyraud, T. Saito, H. Fukazawa, Y. Kohori, K. Kihou, C. H. Lee, A. Iyo, H. Eisaki, R. Prozorov and L. Taillefer, Phys. Rev. Lett., **109**, 087001 (2012).

[63] I. I. Mazin, Nature, **464**, 183 (2010).

[64] L. Hebel and C. P. Slichter, Phys. Rev., **113**, 1504 (1959).

[65] M. Sigrist and K. Ueda, Rev. Mod. Phys., **63**, 239 (1991).

[66] H.-J. Grafe, D. Paar, G. Lang, N. Curro, G. Behr, J. Werner, J. Hamann-Borrero, C. Hess, N. Leps and R. Klingeler, and B. Büchner, Phys. Rev. Lett., **101**, 047003 (2008).

[67] K. Matano, Z. Ren, X. Dong, L. Sun, Z. Zhao and G.-q. Zheng, EPL-Europhys. Lett., **83**, 57001 (2008).

[68] H. Mukuda, N. Terasaki, H. Kinouchi, M. Yashima, Y. Kitaoka, S. Suzuki, S. Miyasaka, S. Tajima, K. Miyazawa and P. Shirage, J. Phys. Soc. Jpn., **77**, 093704 (2008).

[69] Y. Nakai, K. Ishida, Y. Kamihara, M. Hirano and H. Hosono, J. Phys. Soc. Jpn., **77**, 073701 (2008).

[70] H. Fukazawa, T. Yamazaki, K. Kondo, Y. Kohori, N. Takeshita, P. M. Shirage, K. Kihou, K. Miyazawa, H. Kito and H. Eisaki, J. Phys. Soc. Jpn., **78**, 033704 (2009).

[71] H. Ding, P. Richard, K. Nakayama, K. Sugawara, T. Arakane, Y. Sekiba, A. Takayama, S. Souma, T. Sato and T. Takahashi, EPL-Europhys. Lett., **83**, 47001 (2008).

[72] X. Luo, M. Tanatar, J.-P. Reid, H. Shakeripour, N. Doiron-Leyraud, N. Ni, S. L. Bud'ko, P. Canfield, H. Luo and Z. Wang, Phys. Rev. B, **80**, 140503 (2009).

[73] T. Kondo, A. Santander-Syro, O. Copie, C. Liu, M. Tillman, E. Mun, J. Schmalian, S. BudKo, M. Tanatar and P. Canfield, Phys. Rev. Lett., **101**, 147003 (2008).

[74] A. Christianson, E. Goremychkin, R. Osborn, S. Rosenkranz, M. Lumsden, C. Malliakas, I. Todorov, H. Claus, D. Chung and M. G. Kanatzidis, Nature, **456**, 930 (2008).

[75] M. D. Lumsden, A. D. Christianson, D. Parshall, M. B. Stone, S. E. Nagler, G. MacDougall, H. Mook, K. Lokshin, T. Egami and D. Abernathy, Phys. Rev. Lett., **102**, 107005 (2009).

[76] Y. Kobayashi, A. Kawabata, S. Chul Lee, T. Moyoshi and M. Sato, J. Phys. Soc. Jpn., **78**, 073704 (2009).

[77] S. Kawasaki, K. Shimada, G. Chen, J. Luo, N. Wang and G.-q. Zheng, Phys. Rev. B, **78**, 220506 (2008).

[78] F. Ning, K. Ahilan, T. Imai, A. S. Sefat, R. Jin, M. A. McGuire, B. C. Sales and D. Mandrus, J. Phys. Soc. Jpn., **77**, 103705 (2008).

[79] N. Terasaki, H. Mukuda, M. Yashima, Y. Kitaoka, K. Miyazawa, P. M. Shirage, H. Kito, H. Eisaki and A. Iyo, J. Phys. Soc. Jpn., **78**, 013701 (2008).

[80] H. Fukazawa, Y. Yamada, K. Kondo, T. Saito, Y. Kohori, K. Kuga, Y. Matsumoto, S. Nakatsuji, H. Kito and P. M. Shirage, J. Phys. Soc. Jpn., **78**, 083712 (2009).

[81] K. Matano, Z. Li, G. Sun, D. Sun, C. Lin, M. Ichioka and G.-q. Zheng, EPL-Europhys. Lett., **87**, 27012 (2009).

[82] S. Zhang, L. Ma, Y. Hou, J. Zhang, T.-L. Xia, G. Chen, J. Hu, G. Luke and W. Yu, Phys. Rev. B, **81**, 012503 (2010).

[83] A. V. Chubukov, D. Efremov and I. Eremin, Phys. Rev. B, **78**, 134512 (2008).

[84] Y. Bang, H.-Y. Choi and H. Won, Phys. Rev. B, **79**, 054529 (2009).

[85] M. Yashima, H. Nishimura, H. Mukuda, Y. Kitaoka, K. Miyazawa, P. M. Shirage, K. Kihou, H. Kito, H. Eisaki and A. Iyo, J. Phys. Soc. Jpn., **78**, 103702 (2009).

[86] K. Kitagawa, N. Katayama, K. Ohgushi, M. Yoshida, and M. Takigawa, J. Phys. Soc. Jpn., **77**, 114709 (2008).

[87] S.-H. Baek, N. J. Curro, T. Klimczuk, E. Bauer, F. Ronning and J. Thompson, Phys. Rev. B, **79**, 052504 (2009).

[88] T. Iye, Y. Nakai, S. Kitagawa, K. Ishida, S. Kasahara, T. Shibauchi, Y. Matsuda and T. Terashima, J. Phys. Soc. Jpn., **81**, 033701 (2012).

[89] Z. Li, R. Zhou, Y. Liu, D. Sun, J. Yang, C. Lin and G.-q. Zheng, Phys. Rev. B, **86**, 180501 (2012).

[90] F. L. Ning, K. Ahilan, T. Imai, A. S. Sefat, M. A. McGuire, B. C. Sales, D. Mandrus, P. Cheng, B. Shen and H. -H. Wen, Phys. Rev. Lett., **104**, 037001 (2010).

[91] A. Kreyssig, M. A. Green, Y. B. Lee, G. D. Samolyuk, P. Zajdel, J. W. Lynn, S. L. Bud'ko, M. S. Torikachvili, N. Ni, S. Nandi, J. B. Leõ, S. J. Poulton, D. N. Argyriou, B. N. Harmon, R. J. McQueeney, P. C. Canfield, and A. I. Goldman, Phys. Rev. B **78**, 184517 (2008).

[92] M. S. Torikachvili, S. L. Bud'ko, N. Ni, and P. C. Canfield, Phys. Rev. Lett. **101**, 057006 (2008).

[93] P. C. Canfield, S. L. Bud'ko, N. Ni, A. Kreyssig, A. I. Goldman, R. J. McQueeney, M. S. Torikachvilli, D. N. Argyriou, G. Luke, and W. Yu, Physica C **469**, 404 (2009).

[94] Y. Furukawa, B. Roy, S. Ran, S. L. Bud'ko, and P. C. Canfield, Phys. Rev. B **89**, 121109 (2014).

[95] S. -H. Baek, H. J. Grafe, L. Harnagea, S. Singh, S. Wurmehl, and B. Büchner, Phys. Rev. B **84**, 094510 (2011).

[96] R. M. Fernandes, D. K. Pratt, W. Tian, J. Zarestky, A. Kreyssig, S. Nandi, M. G. Kim, A. Thaler, N. Ni, P. C. Canfield, R. J. McQueeney, J. Schmalian, and A. I. Goldman, Phys. Rev. B **81**, 140501(R) (2010).

[97] J. Teng, C. Chen, Y. Xiong, J. Zhang, R. Jin and E. W. Plummer, Proc. Natl. Acad. Sci., **110**, 898 (2013).

[98] J. Cui, B. Roy, M. A. Tanatar, S. Ran, S. L. Bud'ko, R. Prozorov, P. C. Canfield, and Y. Furukawa, Phys. Rev. B **92**, 184504 (2015).

[99] A. Shakouri, Annu. Rev. Mater. Res, **41**, 399 (2011).

[100] C. B. Vining, Nat. Mater., **8**, 83 (2009).

[101] D. M. Rowe, ed. *Thermoelectrics Handbook: Macro to Nano.* (CRC press, 2005).

[102] M. Zebarjadi, K. Esfarjani, M. Dresselhaus, Z. Ren and G. Chen, Energy Environ Sci., **5**, 5147 (2012).

[103] L. E. Bell, Science, **321**, 1457 (2008).

[104] G. J. Snyder and E. S. Toberer, Nature Mater. **7**, 105 (2008).

[105] T. Narasimhan, Phys. Today, **63**, 36 (2010).

[106] C. Kittel, *Introduction to Solid State Physics* (John Wiley & Sons, Inc., 1996).

[107] J. R. Szczech, J. M. Higgins and S. Jin, J. Mater. Chem., **21**, 4037 (2011).

[108] C. Bhandari in *CRC Handbook of Thermoelectrics* (ed. D. M. Rowe) pp.49 (CRC Press, Boca Raton, 1995).

[109] G. A. Slack, in *CRC Handbook of Thermoelectrics* (ed. D. M. Rowe) pp.407 (CRC Press, Boca Raton, 1995).

[110] R. R. Heikes and R. W. Ure, *Thermoelectricity: Science and Engineering* (Interscience, New York, 1961).

[111] F. Rosi, E. Hockings and N. Lindenblad, RCA (Radio Corporation of America) Review (US), **22**, (1961).

[112] C. Wood, Rep. Prog. Phys., **51**, 459 (1988).

[113] Y. Gelbstein, Z. Dashevsky and M. P. Dariel, Physica B Condens Matter, **363**, 196 (2005).

[114] E. A. Skrabek and D. S. Trimmer, in *CRC Handbook of Thermoelectrics* (ed. D. M. Rowe) pp.267 (CRC Press, Boca Raton, 1995).

[115] J. P. Heremans, V. Jovovic, E. S. Toberer, A. Saramat, K. Kurosaki, A. Charoenphakdee, S. Yamanaka and G. J. Snyder, Science, **321**, 554 (2008).

[116] H. Wang, A. Charoenphakdee, K. Kurosaki, S. Yamanaka and G. J. Snyder, Phys. Rev. B, **83**, 024303 (2011).

[117] L. D. Hicks and M. S. Dresselhaus, Phys. Rev. B, **47**, 12727 (1993).

[118] M. S. Dresselhaus, G. Chen, M. Y. Tang, R. G. Yang, H. Lee, D. Z. Wang, Z. F. Ren, J. P. Fleurial and P. Gogna, Adv. Mater., **19**, 1043 (2007).

[119] K. Biswas, J. He, I. D. Blum, C.-I. Wu, T. P. Hogan, D. N. Seidman, V. P. Dravid and M. G. Kanatzidis, Nature, **489**, 414 (2012).

[120] J. P. Heremans, M. S. Dresselhaus, L. E. Bell and D. T. Morelli, Nat. Nano., **8**, 471 (2013).

[121] G. S. Nolas, J. Poon and M. Kanatzidis, MRS bulletin, **31**, 199 (2006).

[122] C. Uher, Semiconduc. Semimet., **69**, 139 (2001).

[123] J. L. Feldman, D. J. Singh, I. I. Mazin, D. Mandrus and B. C. Sales, Phys. Rev. B, **61**, R9209 (2000).

[124] S. M. Kauzlarich, S. R. Brown and G. J. Snyder, Dalton Trans., **2099** (2007).

[125] W. Koshibae and S. Maekawa, in *Properties and Applications of Thermoelectric Materials: The Search for New Materials for Thermoelectric Devices*, pp. 69 (Springer Science & Business Media, 2009).

[126] L. Zhao, D. Berardan, Y. Pei, C. Byl, L. Pinsard-Gaudart and N. Dragoe, Appl. Phys. Lett., **97**, 092118 (2010).

[127] M. G. Kanatzidis, Chemistry of Materials, **22**, 648 (2010).

[128] D. T. Morelli, V. Jovovic and J. P. Heremans, Phys. Rev. Lett., **101**, 035901 (2008).

[129] S. N. Guin, A. Chatterjee, D. S. Negi, R. Datta and K. Biswas, Energy Environ Sci., **6**, 2603 (2013).

[130] E. M. Levin, B. A. Cook, K. Ahn, M. G. Kanatzidis and K. Schmidt-Rohr, Phys. Rev. B, **80**, 115211 (2009).

[131] A. Willig and B. Sapoval, J. Phys. Lett-Paris, **38**, L57 (1977).

[132] I. Orion, J. Rocha, S. Jobic, V. Abadie, R. Brec, C. Fernandez and J.-P. Amoureux, J. Chem. Soc., Dalton Trans., **3741** (1997).

[133] C. M. Jaworski, J. Tobola, E. M. Levin, K. Schmidt-Rohr and J. P. Heremans, Phys. Rev. B, **80**, 125208 (2009).

[134] S. D. Senturia, A. C. Smith, C. R. Hewes, J. A. Hofmann and P. L. Sagalyn, Phys. Rev. B, **3**, 4045 (1970).

[135] C. R. Hewes, M. S. Adler and S. D. Senturia, Phys. Rev. B, **7**, 5195 (1973).

[136] M. N. Alexander, P. L. Sagalyn, S. D. Senturia and C. R. Hewes, J. Nonmetals., **1**, 251 (1973).

[137] E. M. Levin, S. L. Bud'ko and K. Schmidt-Rohr, Adv. Funct. Mater., **22**, 2766 (2012).

[138] J. R. Salvador, J. Yang, X. Shi, H. Wang and A. A. Wereszezak, J. Solid State Chem., **182**, 2088 (2009).

[139] S. H. Yang, T. J. Zhu, T. Sun, J. He, S. N. Zhang and X. B. Zhao, Nanotechnology, **19**, 245707 (2008).

[140] Y. Gelbstein, O. Ben-Yehuda, E. Pinhas, T. Edrei, Y. Sadia, Z. Dashevsky and M. P. Dariel, J. Electron. Mater., **38**, 1478 (2009).

[141] J. D. Venables, *Status and Applications of Diamond and Diamond-like Materials: An Emerging Technology: Report of the Committee on Superhard Materials.* (National Academy Press, 1990).

[142] E. H. Falcao and F. Wudl, J. Chem. Technol. Biotechnol., **82**, 524 (2007).

[143] D. Pech, M. Brunet, H. Durou, P. Huang, V. Mochalin, Y. Gogotsi, P.-L. Taberna and P. Simon, Nat Nano, **5**, 651 (2010).

[144] I. Neitzel, V. Mochalin, I. Knoke, G. R. Palmese and Y. Gogotsi, Compos. Sci. Technol., **71**, 710 (2011).

[145] O. Shenderova, Diamond Relat. Mater., **16**, 1213 (2007).

[146] O. Shenderova, Phys. Status Solidi A, **205**, 2245 (2008).

[147] V. N. Mochalin, Shenderova O., Ho D. and Gogotsi Y., Nat. Nanotechnol., **7**, 11 (2012).

[148] K. D. Behler, ACS Nano, **3**, 363 (2009).

[149] V. N. Mochalin, ACS Nano, **5**, 7494 (2011).

[150] J. Zhang, D. S. Su, R. Blume, R. Schlögl, R. Wang, X. Yang and A. Gajović, Angew. Chem. Int. Ed., **49**, 8640 (2010)

[151] K. B. Holt, Phil. Trans. Roy. Soc. A, **365**, 2845 (2007).

[152] V. Vaijayanthimala and H. C. Chang, Nanomedicine, **4**, 47 (2009).

[153] Y. R. Chang, Nat. Nanotechnol., **3**, 284 (2008).

[154] A. Krüger, Y. J. Liang, G. Jarre and J. Stegk, J. Mater. Chem., **16**, 2322 (2006).

[155] O. Shenderova, Diamond Relat. Mater., **15**, 1799 (2006).

[156] V. Y. Dolmatov, Russ. Chem. Rev., **70**, 607 (2001).

[157] S. Osswald, G. Yushin, V. Mochalin, S. O. Kucheyev and Y. Gogotsi, J. Am. Chem. Soc., **128**, 11635 (2006).

[158] A. E. Aleksenskiy, E. D. Eydelman and A. Y. Vul, Nanosci. Nanotechnol. Lett., **3**, 68 (2011).

[159] V. Y. Dolmatov, Russ. Chem. Rev., **76**, 339 (2007).

[160] O. Shenderova, J. Phys. Chem. C, **115**, 9827 (2011).

[161] A. Krueger, M. Ozawa, G. Jarre, Y. Liang, J. Stegk and L. Lu, Phys. Status Solidi A, **204**, 2881 (2007).

[162] A. Krüger, F. Kataoka, M. Ozawa, T. Fujino, Y. Suzuki, A. E. Aleksenskii, A. Y. Vul' and E. Osawa, Carbon, **43**, 1722 (2005).

[163] M. Ozawa, M. Inaguma, M. Takahashi, F. Kataoka , A. Krüger and E. Osawa, Adv. Mater., **19**, 1201 (2007).

[164] E. D. Eidelman, V. I. Siklitsky, L. V. Sharonova, M. A. Yagovkina, A. Y. Vul, M. Takahashi, M. Inakuma, M. Ozawa and E. Osawa, Diamond and Related Materials, **14**, 1765 (2005).

[165] D. P. Mitev, A. T. Townsend, B. Paull and P. N. Nesterenko, Carbon, **60**, 326 (2013).

[166] K. Turcheniuk, C. Trecazzi, C. Deeleepojananan and V. N. Mochalin, ACS Appl. Mater. Interfaces, **8**, 25461 (2016).

[167] T. Meinhardt, D. Lang, H. Dill and A. Krueger, Adv. Funct. Mater., **21**, 494 (2011).

[168] O. A. Shenderova and D. M. Gruen, *Ultrananocrystalline Diamond: Synthesis, Properties and Applications.* (William Andrew, 2006).

[169] B. V. ', Diamond Relat. Mater., **15**, 296 (2006).

[170] Y. Liu, Z. N. Gu, J. L. Margrave and V. N. Khabashesku, Chem. Mater., **16**, 3924 (2004).

[171] Y. Liu, V. N. Khabashesku and N. J. Halas, J. Am. Chem. Soc., **127**, 3712 (2005).

[172] G. V. Lisichkin, I. I. Kulakova, Y. A. Gerasimov, A. V. Karpukhin and R. Y. Yalkovlev, Mendeleev Commun., **19**, 309 (2009).

[173] V. L. Kuznetsov, A. L. Chuvilin, Y. V. Butenko, I. Y. Malkov and V. M. Titov, Chem. Phys. Lett., **222**, 343 (1994).

[174] C. Portet, G. Yushin and Y. Gogotsi, Carbon, **45**, 2511 (2007).

[175] N. Matsumoto, L. Joly-Pottuz, H. Kinoshita and N. Ohmae, Diamond Relat. Mater., **16**, 1227 (2007).

[176] G. Jarre, Y. J. Liang, P. Betz, D. Lang and A. Krueger, Chem. Commun., **47**, 544 (2011).

[177] A. Krueger, J. Stegk, Y. J. Liang, L. Lu and G. Jarre, Langmuir, **24**, 4200 (2008).

[178] L. Li, J. L. Davidson and C. M. Lukehart , Carbon, **44**, 2308 (2006).

[179] L. Lai and A. S. Barnard, Nanoscale, **3**, 2566 (2011).

[180] L. Lai and A. S. Barnard, J. Phys. Chem. C, **115**, 6218 (2011).

[181] V. L. Kuznetsov and Y. V. Butenko, Nanodiamond graphitization and properties of onion-like carbon. In *Synthesis, Properties and Applications of Ultrananocrystalline Diamond* pp. 199 (Springer Netherlands, 2005)

[182] O. A. Williams, ACS Nano, **4**, 4824 (2010).

[183] T. L. Jiang, K. Xu and S. F. Ji, J. Chem. Soc. Faraday Trans., **92**, 3401 (1996).

[184] J.-Y. Raty, G. Galli, C. Bostedt, T. W. van Buuren and L. J. Terminello, Phys. Rev. Lett., **90**, 037401 (2003).

[185] B. Palosz, C. Pantea, E. Grzanka, S. Stelmakh, T. Proffen, T. W. Zerda and W. Palosz, Diamond and Related Materials, **15**, 1813 (2006).

[186] A. Aleksenskii, M. Baidakova, A. Y. Vul and V. Siklitskii, Phys. Solid State, **41**, 668 (1999).

[187] I. Kulakova, Phys. Solid State, **46**, 636 (2004).

[188] A. M. Schrand, S. A. C. Hens and O. A. Shenderova, Crit. Rev. Solid State Mater. Sci., **34**, 18 (2009).

[189] Q. Zou, M. Z. Wang and Y. G. Li, J. Exp. Nanosci , **5**, 319 (2010).

[190] A. Krueger and D. Lang, Adv. Funct. Mater., **22**, 890 (2012).

[191] A. P. Dement'ev and K. I. Maslakov, Phys. Solid State, **46**, 678 (2004).

[192] V. Mochalin, S. Osswald and Y. Gogotsi, Chem. Mater., **21**, 273 (2009).

[193] T. S. Varley, M. Hirani, G. Harrison and K. B. Holt, Farad. Discuss , **172**, 349 (2014).

[194] X. Fang, J. Mao, E. M. Levinand K. Schmidt-Rohr, J. Am. Chem. Soc., **131**, 1426 (2009).

[195] C. Presti, A. S. L. Thankamony, J. G. Alauzun, P. H. Mutin, D. Carnevale, C. d. Lion, H. Vezin, D. Laurencin and O. Lafon, J. Phys. Chem. C, **119**, 12408 (2015).

[196] T. Kobayashi, O. Lafon, A. S. Lilly Thankamony, I. I. Slowing, K. Kandel, D. Carnevale, V. Vitzthum, H. Vezin, J.-P. Amoureux, G. Bodenhausen and M. Pruski, Phys. Chem. Chem. Phys., **15**, 5553 (2013).

[197] Y. Ishii, N. P. Wickramasinghe and S. Chimon, J. Am. Chem. Soc, **125**, 3438 (2003).

[198] N. P. Wickramasinghe and Y. Ishii, J. Magn. Reson., **181**, 233 (2006).

[199] M. J. Duijvestijn, C. van der Lugt, J. Smidt, R. A. Wind, K. W. Zilm and D. C. Staplin, Chem. Phys. Lett., **102**, 25 (1983).

[200] E. C. Reynhardt and G. L. High, Prog. Nucl. Magn. Reson. Spectrosc., **38**, 37 (2001).

[201] P. Dutta, G. V. Martinez and R. J. Gillies, J. Phys. Chem. Lett., **5**, 597 (2014).

[202] V. Jacques, P. Neumann, J. Beck, M. Markham, D. Twitchen, J. Meijer, F. Kaiser, G. Balasubramanian, F. Jelezko and J. Wrachtrup, Phys. Rev. Lett., **102**, 057403 (2009).

[203] R. Fischer, C. O. Bretschneider, P. London, D. Budker, D. Gershoni and L. Frydman, Phys. Rev. Lett., **111**, 057601 (2013).

[204] M. G. Ivanov, S. V. Pavlyshko, D. M. Ivanov, I. Petrov and O. Shenderova, J Vac. Sci. Technol. B, **28**, 869 (2010).

[205] U. Maitra, K. E. Prasad, U. Ramamurty and C. N. R. Rao, Solid State Commun., **149**, 1693 (2009).

[206] A. Stravato, R. Knight, V. Mochalin and S. C. Picardi, J. Therm. Spray Technol., **17**, 812 (2008).

[207] J. Y. Lee, D. P. Lim and D. S. Lim, Composites B, **38**, 810 (2007).

[208] O. Shenderova, S. Hens and G. McGuire, Diamond Relat. Mater., **19**, 260 (2010).

[209] P. Neumann, Science, **329**, 542 (2010).

[210] O. Faklaris, ACS Nano, **3**, 3955 (2009).

[211] R. A. Shimkunas, Biomaterials, **30**, 5720 (2009).

[212] H. Huang, E. Pierstorff, E. Osawa and D. Ho, Nano Lett., **7**, 3305 (2007).

[213] X.-Q. Zhang, R. Lam, X. Xu, E. K. Chow, H.-J. Kim and D. Ho, Adv. Mater., **23**, 4770 (2011).

[214] E. K. Chow, X.-Q. Zhang, M. Chen, R. Lam, E. Robinson, H. Huang, D. Schaffer, E. Osawa, A. Goga and D. Ho, Sci. Transl. Med., **3**, 73ra21 (2011).

[215] A. Krueger, J. Mater. Chem., **18**, 1485 (2008).

[216] Y. Qi, E. Konca and A. T. Alpas, Surface Science, **600**, 2955 (2006).

[217] A. R. Konicek, D. S. Grierson, P. U. P. A. Gilbert, W. G. Sawyer, A. V. Sumant and R. W. Carpick, Phys. Rev. Lett., **100**, 235502 (2008).

[218] A. N. Andriotis, G. Mpourmpakis, E. Richter and M. Menon, Phys. Rev. Lett., **100**, 106801 (2008).

[219] K. Hirama, H. Takayanagi, S. Yamauchi, J. H. Yang, H. Kawarada and H. Umezawa, Appl. Phys. Lett., **92**, 112107 (2008).

[220] A. S. Barnard and M. Sternberg, J. Phys. Chem. B, **109**, 17107 (2005).

[221] A. L. Vereshchagin and G. S. Yur'ev, Inorg. Mater., **39**, 247 (2003).

[222] A. S. Barnard and M. Sternberg, J. Mater. Chem., **17**, 4811 (2007).

[223] M. V. Baidakova, A. Y. Vul', V. I. Siklitskii and N. N. Faleev, Phys. Solid State, **40**, 715 (1998).

[224] J. Chen, S. Z. Deng, J. Chen, Z. X. Yu and N. S. Xu, Appl. Phys. Lett., **74**, 3651 (1999).

[225] O. A. Shenderova, V. V. Zhirnov and D. W. Brenner, Crit. Rev. Solid State Mater. Sci., **27**, 227 (2002).

[226] E. Osawa, Diamond and Related Materials, **16**, 2018 (2007).

[227] A. M. Panich, A. I. Shames, H. M. Vieth, E. Osawa, M. Takahashi and A. Y. Vul', Eur. Phys. J. B, **52**, 397 (2006).

[228] A. I. Shames, A. M. Panich, W. Kempiński, A. E. Alexenskii, M. V. Baidakova, A. T. Dideikin, V. Y. Osipov, V. I. Siklitski, E. Osawa, M. Ozawa and A. Y. Vul', J. Phys. Chem. Solids, **63**, 1993 (2002).

[229] J. Y. Raty and G. Galli, J. Electroanal. Chem., **584**, 9 (2005).

[230] T. M. Alam, Mater. Chem. Phys., **85**, 310 (2004).

[231] A. M. Panich, Crit. Rev. Solid State Mater. Sci., **37**, 276 (2012).

[232] M. Dubois, K. Guerin, E. Petit, N. Batisse, A. Hamwi, N. Komatsu, J.Giraudet, P. Pirotte and F. Masin, J. Phys. Chem. C, **113**, 10371 (2009).

[233] M. Dubois, K. Guerin, N. Batisse, E. Petit, A. Hamwi, N. Komatsu, H. Kharbache, P. Pirotte and F. Masin, Solid State Nucl. Magn. Reson., **40**, 144 (2011).

[234] O. Shenderova, A. M. Panich, S. Moseenkov, S. C. Hens, V. Kuznetsovand H. M.Vieth, J. Phys. Chem. C, **115**, 19005 (2011).

[235] A. M. Panich, A. I. Shames, N. A. Sergeev, M. Olszewski, J. K. McDonough, V. N. Mochalin and Y.Gogotsi, J. Phys. Cond. Matt., **25**, 245303 (2013).

[236] E. M. Purcell, H. C. Torrey and R. V. Pound, Phys. Rev., **69**, 37 (1946).

[237] F. Bloch, W. W. Hansen and M. Packard, Phys. Rev., **69**, 127 (1946).

[238] F. Bloch, Phys. Rev., **70**, 460 (1946).

[239] C. P. Slichter, *Principles of Magnetic Resonance*, (Springer Science & Business Media, 1990).

[240] K. Schmidt-Rohr and H. W. Spiess, *Multidimensional solid-state NMR and polymers* (Elsevier, 1994).

[241] M. H. Levitt, *Spin Dynamics: Basics of Nuclear Magnetic Resonance* (John Wiley & Sons2001).

[242] G. C. Carter, L. H. Bennett and D. J. Kahan, *Metallic Shifts in NMR* (Pergamon Press, England, 1977).

[243] W. D. Knight, Phys. Rev., **76**, 1259 (1949).

[244] C. H. Townes, C. Herring and W. D. Knight, Phys. Rev., **77**, 852 (1950).

[245] R. Kubo and Y. Obata, J. Phys. Soc. Jpn. **11**, 547 (1956).

[246] T. P. Das and E. H. Sondheimer, Phil. Mag. **5**, 529 (1960).

[247] J. Korringa, Physica **16**, 601 (1950).

[248] L. C. Hebel, Phys. Rev., **116**, 79 (1959).

[249] N. J. Curro, Rep. Prog. Phys , **72**, 026502 (2009).

[250] R. Kubo, Rep. Prog. Phys, **29**, 255 (1966).

[251] E. Fukushima and S. B. Roeder, *Experimental Pulse NMR: A Nuts and Bolts Approach* (Addison-Wesley Reading, 1981).

[252] E. L. Hahn, Phys. Rev., **80**, 580 (1950).

[253] H. Y. Carr and E. M. Purcell, Phys. Rev. **94**, 630 (1954).

[254] P. C. Canfield and S. L. Bud'ko, Annu. Rev. Condens. Matter Phys. **1**, 27 (2010).

[255] G. R. Stewart, Rev. Mod. Phys. **83**, 1589 (2011).

[256] N. Kumar, R. Nagalakshmi, R. Kulkarni, P. L. Paulose, A. K. Nigam, S. K. Dhar, and A. Thamizhavel, Phys. Rev. B **79**, 012504 (2009).

[257] N. Kumar, S. Chi, Y. Chen, K. G. Rana, A. K. Nigam, A. Thamizhavel, W. Ratcliff, S. K. Dhar, and J. W. Lynn, Phys. Rev. B **80**, 144524 (2009).

[258] H. Lee, E. Park, T. Park, V. A. Sidorov, F. Ronning, E. D. Bauer, and J. D. Thompson, Phys. Rev. B **80**, 024519 (2009).

[259] W. Yu, A. A. Aszel, T.J. Williams, S. L. Bud'ko, N. Ni, P. C. Canfield, and G. M. Luke, Phys. Rev. B **79**, 020511 (2009).

[260] A. I. Goldman, A. Kreyssig, K. Prokeš, D. K. Pratt, D. N. Argyriou, J. W. Lynn, S. Nandi, S. A. J. Kimber, Y. Chen, Y. B. Lee, G. D. Samolyuk, J. B. Leão, S. J. Poulton, S. L. Bud'ko, N. Ni, P. C. Canfield, B. N. Harmon, and R. J. McQueeney, Phys. Rev. B **79**, 024513 (2009).

[261] S. Ran, S. L. Bud'ko, D. K. Pratt, A. Kreyssig, M. G. Kim, M. J. Kramer, D. H. Ryan, W. N. Rowan-Weetaluktuk, Y. Furukawa, B. Roy, A. I. Goldman, and P. C. Canfield, Phys. Rev. B **83**, 144517 (2011).

[262] K. Ishida, Y. Nakai, and H. Hosono, J. Phys. Soc. Jpn. **78** 062001 (2009).

[263] L. Ma, G.-F. Ji, J. Dai, S. R. Saha, T. Drye, J. Paglione, and W.-Q. Yu, Chin. Phys. B **22**, 057401 (2013).

[264] S.-H. Baek, H. Lee, S. E. Brown, N. J. Curro, E. D. Bauer, F. Ronning, T. Park, and J. D. Thompson, Phys. Rev. Lett. **102**, 227601 (2009).

[265] N. J. Curro, A. P. Diguardi, N. ApRoberts-Warren, A. C. Schockley, and P. Klavins, New J. Phys. **11** 075004 (2009).

[266] S. Kawasaki, T. Tabuchi, X. F. Wang, X. H. Chen, G-q. Zheng, Supercond. Sci. Technol. **23**, 054004 (2010).

[267] M. A. Tanatar, N. Ni, A. Thaler, S. L. Bud'ko, P. Canfield, and R. Prozorov, Phys. Rev. B **82**, 134528 (2010).

[268] M. A. Tanatar, M. S. Torikachvili, A. Thaler, S. L. Bud'ko, P. C. Canfield and R. Prozorov, Phys. Rev. B **90**, 104518 (2014).

[269] M. A. Tanatar, N. Ni, A. Thaler, S. L. Bud'ko, P. C. Canfield, and R. Prozorov, Phys. Rev. B **84** 014519 (2011).

[270] M. A. Tanatar, W. E. Straszheim, Kim, Hyunsoo, J. Murphy, N. Spyrison, E. C. Blomberg, K. Cho, J. -Ph Reid, B. Shen, L. Taillefer, H. Wen and R. Prozorov, Phys. Rev. B **89**, 144514 (2014).

[271] Y.-M. Xu, P. Richard, K. Nakayama, T. Kawahara, Y. Sekiba, T. Qian, M. Neupane, S. Souma, T. Sato, T. Takahashi, H.-Q. Luo, H.-H. Wen, G.-F. Chen, N.-L. Wang, Z. Wang, Z. Fang, X. Dai, and H. Ding, Nat. Commun. **2**, 392 (2011).

[272] T. Shimojima, T. Sonobe, W. Malaeb, K. Shinada, A. Chainani, S. Shin, T. Yoshida, S. Ideta, A. Fujimori, H. Kumigashira, K. Ono, Y. Nakashima, H. Anzai, M. Arita, A. Ino, H. Namatame, M. Taniguchi, M. Nakajima, S. Uchida, Y. Tomioka, T. Ito, K. Kihou, C. H. Lee, A. Iyo, H. Eisaki, K. Ohgushi, S. Kasahara, T. Terashima, H. Ikeda, T. Shibauchi, Y. Matsuda, and K. Ishizaka, Phys. Rev. B **89**, 045101 (2014).

[273] S. J. Moon, A. A. Schafgans, S. Kasahara, T. Shibauchi, T. Terashima, Y. Matsuda, M. A. Tanatar, R. Prozorov, A. Thaler, P. C. Canfield, A. S. Sefat, D. Mandrus, and D. N. Basov, Phys. Rev. Lett. **109**, 027006 (2012).

[274] C. Liu, A. D. Palczewski, R. S. Dhaka, T. Kondo, R. M. Fernandes, E. D. Mun, H. Hodovanets, A. N. Thaler, J. Schmalian, S. L. Bud'ko, P. C. Canfield, and A. Kaminski, Phys. Rev. B **84**, 020509 (2011).

[275] R. S. Dhaka, R. Jiang, S. Ran, S. L. Bud'ko, P. C. Canfield, B. N. Harmon, A. Kaminski, M. Tomič, R. Valentí, and Y. Lee, Phys. Rev. B **89**, 020511(R) (2014).

[276] L. Harnagea, S. Singh, G. Friemel, N. Leps, D. Bombor, M. Abdel-Hafiez, A. U. B.Wolter, C. Hess, R. Klingeler, G. Behr, S. Wurmehl, and B. Büchner, Phys. Rev. B **83**, 094523 (2011).

[277] M. Matusiak, Z. Bukowski, and J. Karpinski, Phys. Rev. B **81**, 020510(R) (2010).

[278] R. Hu, S. Ran, W. E. Straszheim, L. Sergey, S. L. Bud'ko and P. C. Canfield, Philos. Mag. **92**, 3113 (2012).

[279] P. C. Canfield, *in Properties and Applications of Complex Intermetallics*, edited by E. Belin-Frré (World Scientific Co. Pte. Ltd, Singapore, 2010).

[280] P. C. Canfield and Z. Fisk, Philos. Mag. B **65**, 1117 (1992).

[281] S. L. Bud'ko, S. Ran, and P. C. Canfield, Phys. Rev. B **88**, 064513 (2013).

[282] M. A. Tanatar, N. Ni, C. Martin, R. T. Gordon, H. Kim, V. G. Kogan, G. D. Samolyuk, S. L. Bud'ko, P. C. Canfield, and R. Prozorov, Phys. Rev. B **79**, 094507 (2009).

[283] M. A. Tanatar, N. Ni, S. L. Bud'ko, P. C. Canfield, and R. Prozorov, Supercond. Sci. Technol. **23**, 054002 (2010).

[284] M. A.Tanatar, R.Prozorov, N. Ni, S. L. Bud'ko, and P. C. Canfield, U.S. Patent 8450246 (2011).

[285] H. C. Montgomery, J. Appl. Phys. **42**, 2971 (1971).

[286] B. F. Logan, S. O. Rice, and R.F.Wick, J. Appl. Phys. **42**, 2975 (1971).

[287] F. L. Ning, K. Ahilan, T. Imai, A. S. Sefat, R. Jin, M. A. McGuire, B. C. Sales, and D. Mandrus, Phys. Rev. B **79**, 140506(R) (2009).

[288] F. L. Ning, M. Fu, D. A. Torchetti, T. Imai, A. S. Sefat, P. Cheng, B. Shen, and H. H. Wen, Phys. Rev. B **89**, 214511 (2014).

[289] A. P. Dioguardi, N. apRoberts-Warren, A. C. Shockley, S. L. Bud'ko, N. Ni, P. C. Canfield, and N. J. Curro, Phys. Rev. B **82**, 140411 (2010).

[290] S. O. Diallo, D. K. Pratt, R. M. Fernandes, W. Tian, J. L. Zarestky, M. Lumsden, T. G. Perring, C. L. Broholm, N. Ni, S. L. Bud'ko, P. C. Canfield, H. F. Li, D. Vaknin, A. Kreyssig, A. I. Goldman, and R. J. McQueeney, Phys. Rev. B **81**, 214407 (2010).

[291] H. Xiao,T. Hu, A. P. Dioguardi, N. apRoberts-Warren, A. C. Shockley, J. Crocker, D. M. Nisson, Z. Viskadourakis, X. Tee, I. Radulov, C. C. Almasan, N. J. Curro, and C. Panagopoulos, Phys. Rev. B **85**, 024530 (2012).

[292] R. Klingeler, N. Leps, I. Hellmann, A. Popa, U. Stockert, C. Hess, V. Kataev, H. J. Grafe, F. Hammerath, G. Lang, S. Wurmehl, G. Behr, L. Harnagea, S. Singh, and B. Büchner, Phys. Rev. B, **81**, 024506 (2010).

[293] H. Kotegawa, S. Masaki, Y. Awai, H. Tou, Y. Mizuguchi, and Y. Takano, J. Phys. Soc. Jpn. **77**, 113703 (2008).

[294] D. A. Torchetti, M. Fu, D. C. Christensen, K. J. Nelson, T. Imai, H. C. Lei, and C. Petrovic, Phys. Rev. B, **83**, 104508 (2011).

[295] M. Majumder, K. Ghoshray, A. Ghoshray, A. Pal, and V. P. S. Awana, J. Phys.: Condes. Matter **25**, 196002 (2013).

[296] S.-H. Baek, H.-J. Grafe, F. Hammerath, M. Fuchs, C. Rudisch, L. Harnagea, S. Aswartham, S. Wurmehl, J. van den Brink, and B. Büchner, Eur. Phys. J. B **85**, 159 (2012).

[297] Y. Takahashi and T. Moriya, J. Phys. Soc. Jpn., **44** 850 (1978).

[298] T. Moriya, J. Phys. Soc. Jpn. **18**, 516 (1963).

[299] K. Kitagawa, N. Katayama, K. Ohgushi, and M. Takigawa, J. Phys. Soc. Jpn. **78**, 063706 (2009).

[300] S. Kitagawa, Y. Nakai, T. Iye, K. Ishida, Y. Kamihara, M. Hirano, and H. Hosono, Phys. Rev. B **81**, 212502 (2010).

[301] M. Hirano, Y. Yamada, T. Saito, R. Nagashima, T. Konishi, T. Toriyama, Y. Ohta, H. Fukazawa, Y. Kohori, Y. Furukawa, K. Kihou, C-H Lee, A. Iyo and H. Eisaki, J. Phys. Soc. Jpn. **81**, 054704 (2012).

[302] A. Pandey, D. G. Quirinale, W. Jayasekara, A. Sapkota, M. G. Kim, R. S. Dhaka, Y. Lee, T. W. Heitmann, P. W. Stephens, V. Ogloblichev, A. Kreyssig, R. J. McQueeney, A. I. Goldman, Adam Kaminski, B. N. Harmon, Y. Furukawa, and D. C. Johnston, Phys. Rev. B. **88**, 014526 (2013).

[303] Z. Li, D.L. Sun, C.T. Lin, Y.H. Su, J.P. Hu, and G.-q. Zheng, Phys. Rev. B **83**, 140506(R) (2011).

[304] Y. Nakai, S. Kitagawa, T. Iye, K. Ishida, Y. Kamihara, M. Hirano, and H. Hosono, Phys. Rev. B **85**, 134408 (2012).

[305] P. Wiecki, B. Roy, D. C. Johnston, S. L. Bud'ko, P. C. Canfield, and Y. Furukawa, Phys. Rev. Lett. **115**, 137001 (2015).

[306] E.C.Blomberg, M.A.Tanatar, R.M.Fernandes, I.I.Mazin, B.Shen, Hai-Hu Wen, M.D. Johannes, J. Schmalian, and R. Prozorov, Nat. Commun. **4**, 1914 (2013).

[307] Y. K. Kim, W. S. Jung, G. R. Han, K.-Y. Choi, C.-C. Chen, T. P. Devereaux, A. Chainani, J. Miyawaki, Y. Takata, Y. Tanaka, M. Oura, S. Shin, A. P. Singh, H. G. Lee, J.-Y. Kim, and C. Kim, Phys. Rev. Lett. **111**, 217001 (2013).

[308] P. Wiecki, V. Ogloblichev, A. Pandey, D. C. Johnston, and Y. Furukawa, Phys. Rev. B **91**, 220406 (R) (2015).

[309] B. Cheng, B. F. Hu, R. H. Yuan, T. Dong, A. F. Fang, Z. G. Chen, G. Xu, Y. G. Shi, P. Zheng, J. L. Luo, and N. L. Wang, Phys. Rev. B **85**, 144426 (2012).

[310] D. G. Quirinale, V. K. Anand, M. G. Kim, Abhishek Pandey, A. Huq, P. W. Stephens, T. W. Heitmann, A. Kreyssig, R. J. McQueeney, D. C. Johnston, and A. I. Goldman, Phys. Rev. B **88**, 174420 (2013).

[311] A. Narath and H. T. Weaver, Phys. Rev. **175**, 373 (1968).

[312] P. Jeglič, A. Potočnik, M. Klanjšek, M. Bobnar, M. Jagodič, K. Koch, H. Rosner, S. Margadonna, B. Lv, A. M. Guloy, and D. Arčon, Phys. Rev. B **81**, 140511(R) (2010).

[313] A. Smerald and N. Shannon, Phys. Rev. B **84**, 184437 (2011).

[314] Y. Nakai, T. Iye, S. Kitagawa, K. Ishida, S. Kasahara, T. Shibauchi, Y. Matsuda, H. Ikeda, and T. Terashima, Phys. Rev. B **87**, 174507 (2013).

[315] T. Oka, Z. Li, S. Kawasaki, G.F. Chen, N.L. Wang, and G.-q. Zheng, Phys. Rev. Lett. **108**, 047001 (2012).

[316] Y. Nakai, T. Iye, S. Kitagawa, K. Ishida, H. Ikeda, S. Kasahara, H. Shishido, T. Shibauchi, Y. Matsuda, and T. Terashima, Phys. Rev. Lett. **105**, 107003 (2010).

[317] R. Zhou, Z. Li, J. Yang, D. L. Sun, C. T. Lin, and G.-q. Zheng, Nat. Commun. **4**, 2265 (2013).

[318] A. P. Dioguardi, M. M. Lawson, B. T. Bush, J. Crocker, K. R. Shirer, D. M. Nisson, T. Kissikov, S. Ran, S. L. Bud'ko, P. C. Canfield, S. Yuan, P. L. Kuhns, A. P. Reyes, H.-J. Grafe, and N. J. Curro, Phys. Rev. B **92**, 165116 (2015).

[319] T. Kissikov, A. P. Dioguardi, E. I. Timmons, M. A. Tanatar, R. Prozorov, S. L. Bud'ko, P. C. Canfield, R. M. Fernandes, and N. J. Curro, Phys. Rev. B **94**, 165123 (2016).

[320] T. Iye, M.-H. Julien, H. Mayaffre, M. Horvati, C. Berthier, K. Ishida, H. Ikeda, S. Kasahara, T. Shibauchi, and Y. Matsuda, J. Phys. Soc. Jpn. **84**, 043705 (2015).

[321] Y. Nakai, K. Ishida, Y. Kamihara, M. Hirano, and H. Hosono, Phys. Rev. Lett. **101**, 077006 (2008).

[322] H. Kotegawa, Y. Hara, H. Nohara, H. Tou, Y. Mizuguchi, H. Takeya, and Y. Takano, J. Phys. Soc. Jpn. **80**, 043708 (2011).

[323] J. Ishizuka, T. Yamada, Y. Yanagi, and Y. Ōno, J. Phys. Soc. Jpn. **85**, 114709 (2016).

[324] R. A. Hein, J. W. Gibson, R. Mazelsky, R. C. Millerand, and J. K. Hulm, Phys. Rev. Lett. **12**, 320 (1964).

[325] E. F. Steigmeier and G. Harbeke, Solid State Commun. **8**, 1275 (1970).

[326] J. Akola and R. O. Jones, Phys. Rev. Lett. **100**, 205502 (2008).

[327] E. M. Levin, M. F. Besser, and R. Hanus, J. Appl. Phys. **114**, 083713 (2013).

[328] D. Wu, L.-D. Zhao, S. Hao, Q. Jiang, F. Zheng, J.W. Doak, H. Wu, H. Chi, Y. Gelbstein, C. Uher, C. Wolverton, M. Kanatzidis and J. He, J. Am. Chem. Soc. **136**, 11412 (2014).

[329] R. Sankar, D.P. Wong, C.-S. Chi, W.-L. Chien, J.-S. Hwang, F.-C. Chou, L.-C. Chen and K.-H. Chen, CrystEngComm. **17**, 3440 (2015).

[330] S.K. Plachkova, Phys. Status Solidi A **83** 349 (1984).

[331] B.A. Cook, M.J. Kramer, X. Wei, J.L. Harringa, E.M. Levin, J. Appl. Phys. **101**, 053715 (2007).

[332] F. Herman, R.L. Kortum, I.B. Ortenburger, J. P. Van Dyke, J. Phys. Colloq. **29**, C4-62 (1968).

[333] M. L. Cohen, Y. Tung, and P. B. Allen, J. Phys. Colloq. **29**, C4-163 (1968).

[334] H. M. Polatoglou, G. Theodorou, and N. A. Economou. *Physics of Narrow Gap Semiconductors.* pp. 221 (Springer Berlin Heidelberg, 1982).

[335] D.J. Singh, J. Appl. Phys., **113**, 203101 (2013).

[336] D. H. Damon, M. S. Lubeli, and R. M. Mazelsky, J. Phys. Chem. Solids **28**, 520 (1967).

[337] N. V. Kolomoets, E. Y. Lev, and L. M. Sysoeva, Sov. Phys. Solid State **5**, 2101 (1964).

[338] N. V. Kolomoets, E. Y. Lev, and L. M. Sysoeva, Sov. Phys. Solid State **6**, 551 (1964).

[339] A.H. Edwards, A.C. Pineda, P.A. Schultz, M.G. Martin, A.P. Thompson, H.P. Hjalmarson and C.J. Umrigar, Phys. Rev. B **73** , 045210 (2006).

[340] P. M. Nikolic, J. Phys. D **2**, 383 (1969).

[341] M. S. Lubell and R. Mazelskyl, J. Electrochem. Soc. **110**, 520 (1963).

[342] Y. Gelbstein, B. Daro, O. Ben-Yehuda, Y. Sadia, Z. Dashevsky, and M. P. Dariel, J. Electron. Mater. **39**, 2049 (2010).

[343] L. Zhang, W. Wang, B. Ren, and Y. Yan, J. Electron. Mater. **40**, 1057 (2011).

[344] R. Wolfe, J. H. Wernick, and S. E. Haszko, J. Appl. Phys. **31**, 1959 (1960).

[345] J. P. Heremans and C. M. Jaworski, Appl. Phys. Lett. **93**, 122107 (2008).

[346] E.M. Levin, J.P. Heremans, M.G. Kanatzidis, K. Schmidt-Rohr, Phys. Rev. B **88**, 115211 (2013).

[347] E. M. Levin, Phys. Rev. B **93**, 045209 (2016).

[348] D. Wolf, *Spin Temperature and Nuclear Spin Relaxation in Matter*, (Clarendon, Oxford, 1979).

[349] N. Bloembergen, Physica **20**, 1130 (1954).

[350] G. Al, G. Frosali and O. Morandi, *Scientific Computing in Electrical Engineering, Mathematics in Industry*, **9**, 271 (2004).

[351] C.S. Lue, S.Y. Wang, C.P. Fang, Phys. Rev. B **75**, 235111 (2007).

[352] O. Kiyoshi, Jpn. J. Appl. Phys. **39**, 407 (2000).

[353] A. V. Joura, D. O. Demchenko, and J. K. Freericks, Phys. Rev. B **69**, 165105 (2004)

[354] P. Blaha, K. Schwarz, G. K. H. Madsen, D. Kvasnick, and J. Luitz, WIEN2K, an Augmented Plane Wave + Local Orbitals Program for Calculation Crystal Properties (Karlheinz Schwarz, Technical Universität Wien, Austria), 2001.

[355] J. P. Perdew, K. Burke and M. Ernzerhof, Phys. Rev. Lett. **77**, 3865 (1996).

[356] N. R. Greiner, D. S. Phillips, J. D. Johnson and F. Volk, Nature, **333**, 440 (1988).

[357] K. Iakoubovskii, M. V. Baidakova, B. H. Wouters , A. Stesmans, G. J. Adriaenssens, A. Y. Vul and P. J. Grobet, Diamond Relat. Mater., **9**, 861 (2000).

[358] K. Iakoubovskii, K. Mitsuishi and K. Furuya, Nanotechnology, **19**, 155705/1 (2008).

[359] Q. Zhang, I. Neitzel, V. N. Mochalin, I. Knoke, D. M. Wotton, Y. Gogotsi, P. I. Lelkes and J. G. Zhou, Proc. ASME Global Congr. NanoEng. Med. Biol., **241** (2010).

[360] K.-K. Liu, W.-W. Zheng, C.-C. Wang, Y.-C. Chiu, C.-L. Cheng, Y.-S. Lo, C. Chen and J.-I. Chao, Nanotechnol., **21**, 315106/1 (2010).

[361] J. Y. Raty and G. Galli, Journal, **192**, 15 (2005).

[362] Y. V. Butenko, V. L. Kuznetsov, E. A. Paukshtis, A. I. Stadnichenko, I. N. Mazov, S. I. Moseenkov, A. I. Boronin and S. V. Kosheev, Fuller Nanotub Carbon Nanostruct., **14**, 557 (2006).

[363] T. Petit, J.-C. Arnault, H. A. Girard, M. Sennour and P. Bergonzo, Phys. Rev. B Condens. Matter Mater. Phys., **84**, 233407/1 (2011).

[364] T. Petit, J.-C. Arnault, H. A. Girard, M. Sennour, T.-Y. Kang, C.-L. Cheng and P. Bergonzo, Nanoscale, **4**, 6792 (2012).

[365] P. J. Durham, Chem. Anal. (N. Y.), **92**, 53 (1988).

[366] J. E. Penner-Hahn, Coord. Chem. Rev., **190**, 1101 (1999).

[367] M. Newville, Fundamentals of XAFS, Consortium for Advanced Radiation Sources: Chicago (2004).

[368] S. Zeppilli, J. C. Arnault, C. Gesset, P. Bergonzo and R. Polini, Diamond Relat. Mater., **19**, 846 (2010).

[369] V. N. Mochalin, S. Osswald, C. Portet, G. Yushin, C. Hobson, M. Havel and Y. Gogotsi, Mater. Res. Soc. Symp. Proc., **1039**, 1011 (2008).

[370] A. E. Bennett, C. M. Rienstra, M. Auger, K. V. Lakshmi and R. G. Griffin, J. Chem. Phys., **103**, 6951 (1995).

[371] J. D. Mao and K. Schmidt-Rohr, Environ. Sci. Technol., **38**, 2680 (2004).

[372] C. R. Morcombe and K. W. Zilm, J. Magn. Reson., **162**, 479 (2003).

[373] X. B. Zhang, X. F. Zhang, D. Bernaerts, G. Van Tendeloo, S. Amelinckx, J. Van Landuyt, V. Ivanov, J. B. Nagy, P. Lambin and A. A. Lucas, EPL-Europhys. Lett., **27**, 141 (1994).

[374] Y. Aoki, Y. Mitsuoka and Y. Nakamuta, Diamond Relat. Mater., **8**, 1310 (1999).

[375] L. A. Bursill, A. L. Fullerton and L. N. Bourgeois, Int. J. Mod. Phys. B, **15**, 4087 (2001).

[376] A. I. Shames, V. Y. Osipov, A. E. Aleksenskiy, E. Osawaand A. Y. Vul, Diamond Relat. Mater., **20**, 318 (2011).

[377] A. Scholze, W. G. Schmidt and F. Bechstedt, Phys. Rev. B, **53**, 13725 (1996).

[378] J. D. Mao and K. Schmidt-Rohr, J. Magn. Reson., **162**, 217 (2003).

[379] Y. V. Butenko, S. Krishnamurthy, A. K. Chakraborty, V. L. Kuznetsov, V. R. Dhanak, M. R. C. Hunt and L. Šiller, Phys. Rev. B **71**, 075420 (2005).

[380] V. Vaijayanthimala, D. K. Lee, S. V. Kim, A. Yen, N. Tsai, D. Ho, H.-C. Chang and O. Shenderova, Expert Opin. Drug Deliv., **12**, 735 (2015).

[381] D. M. Gruen, O. A. Shenderova and A. Y. Vul, *Synthesis, Properties and Applications of Ultrananocrystalline Diamond* (Springer: Dordrecht, The Netherlands, 2005).

[382] T. Gubarevich, R. Sataev and V. Y. Dolmatov, 5th All-Union Meeting on Detonation, Krasnoyarsk USSR, **1**, pp135 (1991).

[383] A. S. Chiganov, Phys. Solid State, **46**, 620 (2004).

[384] D. E. Waddington, M. Sarracanie , H. Zhang, N. Salameh, D. R. Glenn, E. Rej, T. Gaebel, T. Boele, R. L. Walsworth and D. J. Reilly, arXiv preprint arXiv:1611.05167, (2016).

[385] M. Alishiri, A. Shojaei and M. J. Abdekhodaie, RSC Adv., **6**, 8743 (2016).

[386] E. R. deAzevedo, T. J. Bonagamba and K. Schmidt-Rohr, J. Magn. Reson., **142**, 86 (2000).

[387] M. V. Baidakova, V. I. Siklitsky and A. Y. Vul, Chaos. Soliton. Fract., **10**, 2153 (1999).

[388] J. F. Cui, X. W. Fang and K. Schmidt-Rohr , J. Phys. Chem. C, **118**, 9621 (2014).

[389] H. A. Girard, T. Petit, S. Perruchas , T. Gacoin, C. Gesset , J. C. Arnault and P. Bergonzo, Phys. Chem. Chem. Phys., **13**, 11517 (2011).

[390] A. Krueger, *Carbon materials and nanotechnology* (John Wiley & Sons, 2010).

[391] J.-S. Tu, E. Perevedentseva , P.-H. Chung and C.-L. Cheng, J. Chem. Phys., **125**, 174713 (2006).

[392] J. Scholz, A. J. McQuillan and K. B. Holt , Chem. Commun., **47**, 12140 (2011).

[393] G. A. Inel, E.-M. Ungureau , T. S. Varley , M. Hirani and K. B. Holt, Diamond Relat. Mater., **61**, 7 (2016).

[394] S. H. Yang, D. A. Drabold and J. B. Adams , Phys. Rev. B, **48**, 5261 (1993).

[395] F. A. Bovey, P. A. Mirau and H. Gutowsky, *Nuclear Magnetic Resonance Spectroscopy* (Elsevier, 1988).

[396] E. Pretsch, P. Buehlmann and C. Affolter, *Structure Determination of Organic Compounds: Tables of Spectral Data, 3rd Completely Revised and Enlarged Edition* (Springer-Verlag, 2000).

[397] X. Fang and K. Schmidt-Rohr, J. Agric. Food Chem., **57**, 10701 (2009).

[398] T. J. Cornish and T. Baer, J. Am. Chem. Soc., **110**, 6287 (1988).

[399] G. A. Webb, *Modern Magnetic Resonance Part 3: Applications in Materials Science and Food Science* (Springer, 2007).

[400] F. Mauri, B. G. Pfrommer and S. G. Louie, Phys. Rev. Lett., **77**, 5300 (1996).

[401] C. Pantea, J. Zhang, J. Qian,Y. Zhao, A. Migliori, E. Grzanka, B. Palosz, Y. Wang, T. Zerda and H. Liu. In 2006 NSTI Nanotechnology Conference and Trade Show, pp 823. (2006).

[402] D. L. Sparks, *Soil physical chemistry* (CRC press, 1998).